UNIVERSITY OF GENOVA

PHD PROGRAM IN BIOENGINEERING AND ROBOTICS

Advanced signal processing and machine learning tools for non-invasive foetal electrocardiography and intracardiac electrophysiology

by

Giulia Baldazzi

Thesis submitted for the degree of *Doctor of Philosophy* (34° cycle)

March 2022

Prof. Danilo Pani	Supervisor
Prof. Giorgio Cannata	Head of the PhD program

Dibris

Department of Informatics, Bioengineering, Robotics and Systems Engineering

"Nothing in life is to be feared, it is only to be understood.
Now is the time to understand more, so that we may fear less."

Marie Skłodowska Curie

Declaration

I hereby declare that except where specific reference is made to the work of others, the contents of this dissertation are original and have not been submitted in whole or in part for consideration for any other degree or qualification in this, or any other university. This dissertation is my own work and contains nothing which is the outcome of work done in collaboration with others, except as specified in text and Acknowledgements. This dissertation contains fewer than 66,000 words including appendices, bibliography, footnotes, tables and equations and has fewer than 95 figures.

Giulia Baldazzi

March 2022

Acknowledgements

I sincerely wish to thank my supervisor, Prof. Danilo Pani, that always constituted a scientific, motivational and personal guide for me, and that made this research work possible from the beginning.

I would like to thank Prof. Hau-Tieng Wu (Department of Mathematics and Statistical Science, Duke University, Durham, NC, USA), for his valuable supervision and suggestions in the development of part of this work.

I also wish to acknowledge the team headed by Dr. Roberto Tumbarello (Division of Paediatric Cardiology, AOB Hospital, Cagliari, Italy) and Dr. Graziana Viola (Division of Cardiology, San Francesco Hospital, Nuoro, Italy) for their clinical support, but also Prof. Giuliana Solinas (Department of Biomedical Sciences, University of Sassari, Sassari, Italy) and Eng. Mirko Matraxia (Medical Concept Lab, Sassari, Italy) for their professional and technical contribution. I thank Prof. Luca Mainardi (Department of Bioengineering, Polytechnic University of Milano, Milan, Italy) and Prof. Paolo Bifulco (Department of Electrical Engineering and Information Technology, University of Naples Federico II, Naples, Italy) for their relevant comments and effort in reviewing this PhD thesis.

I gratefully wish to thank my research group and all my colleagues, that allowed me to go forward in a stimulating atmosphere. Special thanks to Eleonora Sulas and Elisa Gusai, that made our climate collaborative and friendly.

I finally acknowledge all the BSc and Msc students that I supervised during their thesis works, especially Marco Orrù, Giorgia Ibba, and Martina Corda, who contributed to my personal and professional growth and added small but important pieces to this dissertation.

Abstract

In the last decades, bioengineering research promoted the improvement in human health and wellbeing through the development, optimization and evaluation of innovative technologies and medical devices for both diagnosis and therapy. In this context, the exploitation of biomedical technology advances plays a key role in the study and treatment of heart disorders.

This PhD thesis focuses on two main application areas: on one hand, foetal cardiac physiology and electrocardiography and, on the other, intracardiac electrophysiology, substrate mapping and radiofrequency ablation. There, it aims at providing new instruments and insights to improve the knowledge and go beyond the current state of the art by the development of novel signal processing and machine learning tools that aim at supporting the diagnosis and treatment of cardiac diseases.

Non-invasive foetal ECG (fECG) is a long-standing niche research topic characterized by the continuous demand of improved solutions to solve the problem of recovering high-quality fECG signals from non-invasive trans-abdominal recordings. This PhD thesis focused on the development of algorithms for non-invasive fECG extraction and enhancement. Specifically, in collaboration with the Prof. Hau-Tieng Wu (Department of Mathematics and Statistical Science, Duke University, Durham, NC, USA), a novel algorithm for the extraction of morphologically preserved multi-channel fECG signals was conceived. Furthermore, wavelet denoising was deeply investigated for the post-processing of the fECG recordings, to quantitatively evaluate the noise-removal and morphology-preservation effects of different wavelet denoising approaches, expressly tailored for this application domain.

Intracardiac electrophysiology is a branch of interventional cardiology aimed at the diagnosis and treatment of arrhythmias by catheter-based techniques exploiting electroanatomic substrate mapping and ablation. In this exciting scenario, this PhD thesis focused on post-ischemic ventricular tachycardia, which is a life-threatening arrhythmia. Being the electrophysiological studies and ablations very time-consuming and operator-dependent, the first applied-research goal was the development of an effective tool able to support clinical experts in the recognition of the ablation targets during clinical procedures. Moreover, a detailed spectral characterization of post-ischaemic signals was performed, thus paving the way to the development of novel approaches in terms of advanced signal analysis, automatic recognition of the arrhythmogenic substrates, study of the substrate and, in general, to a deeper understanding of the arrhythmogenic mechanisms.

Beyond the scientific content, this PhD thesis gives an important contribution from an industrial perspective in both fields. In fact, automated signal processing tools for the non-invasive fECG signals can improve the detection capabilities of current tools, to be clinically exploited for low-cost antenatal screening. At the same time, novel methods for ablation targets recognition in cardiac electrophysiology could be embedded in future medical electroanatomic mapping systems as plug-in to enhance current computer-aided methods.

Table of contents

List of figures

List of tables

Introduction

Technological advances in cardiovascular health are strongly fostered by the need to help solving some relevant clinical conditions. In fact, according to the American Heart Association [1], cardiovascular diseases represent the first cause of death and their prevalence is globally increasing, causing more than 18 million deaths globally in 2019 [2]. This evidence gave birth to the strong scientific motivation and research-based drive for providing innovative health technologies aiming to improve the clinical care and assessment, not only in terms of diagnosis and treatment, but also monitoring and prevention. The scientific objective of this PhD thesis belongs to this context, and as such it aimed to study and conceive novel approaches supporting the diagnosis and treatment of cardiac diseases. These innovative techniques, employing advanced signal processing and machine learning tools, were conceived to address some critical issues affecting two clinical areas: on one hand, foetal cardiac physiology and electrocardiography and, on the other one, intracardiac electrophysiology, substrate-guided mapping and radiofrequency ablation.

As regards the foetal electrocardiography, non-invasive foetal electrocardiogram (NI-fECG) could play a key role for the prenatal screening and diagnosis of all pathologies inducing changes in foetal electrocardiogram (fECG) morphology, like some forms of congenital heart diseases and foetal arrhythmias, thus enabling a prompt in-utero treatment or intervention in early pregnancy. However, NI-fECG is not typically adopted in the clinical practice, mainly because of its complex setup and relatively low signal-to-noise ratio (SNR)[3]. Several physiological and instrumental noise sources hamper its acquisition, even after that powerful signal processing methods have been applied. Furthermore, despite the huge number of techniques developed in the literature, the identification of a clean and undistorted fECG signal still remains an open research issue [4]. As such, one goal of this PhD project was the development of algorithms for NI-fECG extraction and enhancement. Specifically, as regards the fECG extraction, a novel algorithm for the recovery of morphologically preserved multi-channel NI-fECG signals was introduced, in collaboration with the Prof. Hau-Tieng Wu (Department of Mathematics and Statistical Science, Duke University, Durham, NC, USA). On the other hand, for the post-processing of the NI-fECG recordings, different wavelet denoising (WD) methods were studied and assessed, to quantitatively evaluate the noise-removal and morphology-preservation effects of different implementation approaches in this application field.

As regards the intracardiac electrophysiology, the main focus of the thesis concerns the electrophysiological substrate mapping in post-ischaemic ventricular tachycardia (VT). Specifically, in this regard, this PhD thesis deals with signal processing and machine learning tools for the analysis of bipolar endocardial electrograms (EGMs) acquired from patients affected by post-ischemic VT undergoing substrate mapping and catheter ablation procedures. In this sense, the research activity had two main goals, which are tightly linked and required by the high VT recurrence after ablation procedures [5]. The first goal was the improvement of the clinical outcome and the reduction of clinical procedure times, by developing an effective tool able to support the cardiologist in the recognition of the ablation targets during electrophysiological procedures. Therefore, in the light of this first scientific objective, a novel tool for the automatic recognition of abnormal ventricular potentials (AVPs) has been proposed, by comparing different features and classification strategies. The other goal was a basic characterisation of the AVPs, thus paving the way to the introduction of innovative and targeted approaches for their detection and, in this perspective, supporting a deeper understanding of the arrhythmogenic mechanisms, such as re-entry circuits within the damaged myocardial substrate. As such, a spectral investigation of bipolar EGM has been carried out, in order to identify the main frequency contributions of both post-ischaemic physiological potentials and AVPs, along with some spectral signatures for these EGMs. Both aspects are extremely relevant, since electrophysiological studies and their outcomes strongly depend on the cardiologist's expertise, who is asked to visually inspect a huge amount of signals when targeting ablation sites, thus making the clinical procedure time-consuming, prone to errors and intrinsically operator-dependent.

Thesis outline

This thesis is divided in two parts, according to the two application areas under investigation. In Part I, the focus is on NI-fECG research, introducing the physiological and scientific background and the motivation behind the development of algorithms for NI-fECG extraction and enhancement. In Part II, the intracardiac electrophysiology research is presented, along with a preliminary description of electrophysiological substrates, the scientific context and the main issues that led to the proposed investigation.

In Chapter 1, the physiology and the electrophysiological basis of the foetal cardiac activity are described, with an overview on available foetal cardiac monitoring tools. Chapter 2 introduces the NI-fECG signal processing issues and the state-of-the-art methods developed for fECG analysis. Chapter 3 focuses on the description of the novel fECG extraction algorithm conceived in this thesis, detailing its processing stages and results, also in comparison with other effective NI-fECG extraction algorithms from the scientific literature. Chapter 4 and 5 illustrate the effectiveness of WD methods for the post-processing of the NI-fECG recordings, presenting and comparing different implementation approaches and algorithms in terms of the noise reduction and morphology preservation, while introducing a real and synthetic dataset for post-processing benchmarking. Remarkably, the proposed fECG extraction algorithm has been conceived independently from the NI-fECG post-processing investigations, thus they are presented separately. Conclusions on Part I are presented in Chapter 6.

Part II starts with Chapter 7, which gives an overview of cardiac arrhythmias, their electrophysiological substrates and currently available tools for the electrophysiological studies and treatment. Chapter 8 deepens the investigation on scar-related VTs, focusing on their arrhythmogenic substrates and illustrating the main targeting strategies and background tools guiding catheter ablation. Moreover, this Chapter details several issues related to the current clinical substrate-guided ablation procedures. In Chapter 9, some novel insights on VT arrhythmogenic signals are given, by presenting a spectral investigation on the power contents of post-ischaemic physiological and abnormal potentials, along with some spectral features, to highlight specific signatures for these signals. Chapter 10 presents the adoption of artificial intelligence tools for the automatic recognition of ablation target in substrate-guided mapping procedures, thus supporting the clinicians in targeting arrhythmogenic sites. In Chapter 11 the conclusion on Part II is presented, whereas Chapter 12 closes this PhD thesis work, with possible hints on future works and industrial exploitation of the results.

The scientific dissemination of my research is reported at the end of this PhD thesis. Remarkably, some publications about different research field, i.e. mainly neural signal processing and wearable electronics in the context of the DoMoMEA project, have been produced under remunerative research grants, and as such they are just listed without providing any deeper exploration in this thesis, in order to keep the focus on the two main research topics.

Part I

Non-invasive foetal ECG monitoring

Chapter 1

Foetal cardiac monitoring

1.1 Physiology of foetal cardiovascular system

During the embryogenesis process, the heart is one of the first originated organs, starting to fulfil its function since the earliest stages of gestation [6], [7]. In fact, foetal heart first beats at around the 22nd day of gestation, when it starts to actively participate in the oxygen and nutrients distribution [8]. The embryology of the developing heart and its different structures is based on several sequential stages and genetic expressions [9]. More generally, the foetal cardiac development starts at the 2nd week of gestation, when the cardiogenic mesodermal cells form the first and second heart fields progenitor cells leading to the four-chambered structure by the end of the 7th week, though different stages (Figure 1.1) [10].

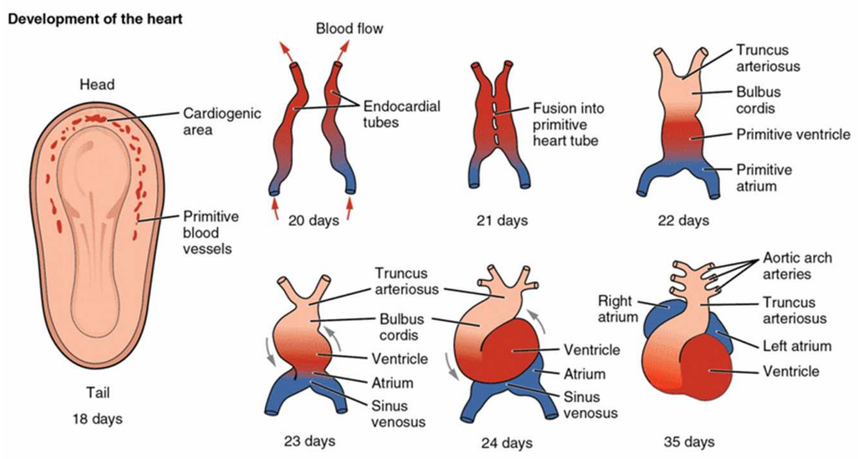

Figure 1.1. Different stages of foetal heart development.

However, despite the anatomical similitude, the foetal circulation significantly differs from neonatal one, both structurally and functionally [11]. In fact, in the foetal circulation gas exchange does not occur in lungs but is governed by the placenta, which acts predominantly by the 10th week of gestation [8]. Moreover, the foetal cardiovascular system function is guaranteed also by other anatomical adaptations: the ductus venosus, the ductus arteriosus or ductus Botalli, and the foramen ovale. Specifically, blood flows from the placenta to the foetus via the umbilical vein, providing the oxygen and all the nutrients needed. At this stage, a minimal part of this blood provides the liver with oxygen and nutrients, whereas the largest part arrives in the right atrium, through the ductus venosus and the inferior vena cava. Oxygenated blood entering the right atrium mostly reaches the left atrium through the foramen ovale. Then, it flows to the left ventricle, the ascending aorta and subsequently to all the foetal upper body, in particular the head and brain, thus guaranteeing optimal oxygen and nutrients for their functioning [10], [11]. The residual poorly oxygenated blood entering the right atrium, both from inferior and superior vena cava, flows into the right ventricle and then to the pulmonary artery. Here, only a small blood proportion reaches the lungs, to satisfy their limited metabolic needs, whereas most of the blood flow arrives in the descending aorta by the ductus arteriosus, thus irrorating the foetal lower body. Finally, the partially-oxygenated blood from the aorta returns to the placenta by the umbilical arteries [8], [10], [12].

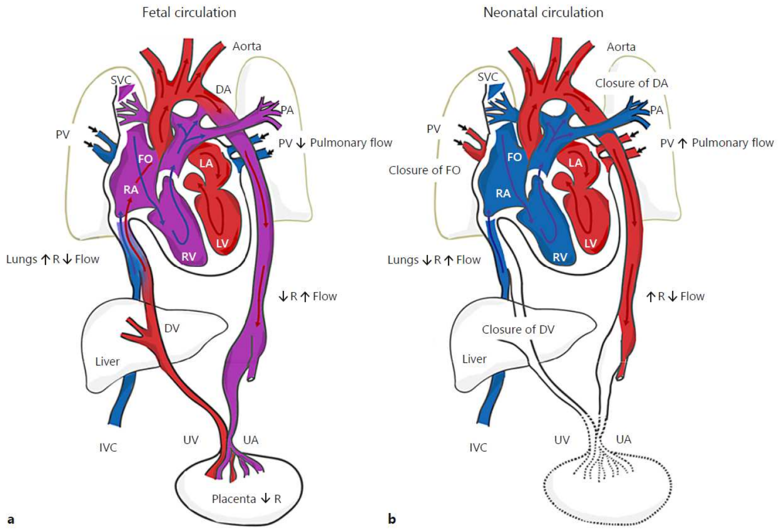

Figure 1.2. Schematic representation of foetal and neonatal circulation from [10].

DV, ductus venosus; UV, umbilical vein; IVC, inferior vena cava; RA, right atrium; RV, right ventricle; LA, left atrium; FO, foramen ovale; SVC, superior vena cava; PA, pulmonary artery; DA, ductus arteriosus; UA, umbilical arteries; PV, pulmonary veins. At birth, the umbilical cord is clamped and the shunts occlude, thus resulting in a separation of the pulmonary and systemic circulations.

However, the unique cardiac circulation characterizing foetal physiology is lost when the transition from intrauterine to extrauterine life occurs, which relies on several complex physiological changes involving cardiovascular, respiratory and other organ systems. At birth, all the shunts (i.e., the foramen ovale, the ductus arteriosus and the ductus venosus) are closed by the combined action of postnatal oxygenation, increased systemic vascular resistance and lower pulmonary vascular resistance, which are induced by pulmonary ventilation and the umbilical cord clamping [11], [12]. From now on, in the after-birth physiology, the pulmonary and systemic circulations are separated, as detailed hereinafter. However, any alteration in foetal heart development or in its transition to the extrauterine life can determine adverse consequences for the baby [10].

After birth, the physiology of human heart is based on two pumps: the right heart, mainly composed of the right atrium, the tricuspid valve, the right ventricle and the pulmonary valve, and the left heart, given by the left atrium, the mitral valve, the left ventricle and the aortic valve. They provide the pulmonary and systemic circulations respectively. In fact, in the pulmonary circulation, the deoxygenated blood from the right ventricle is passed to the lungs, and returns as oxygenated blood to the left side of the heart. Conversely, the pumping action of the left heart transports oxygenated blood from the pulmonary circulation through the left atrium, the left ventricle, the aorta and to the rest of the body, which then returns as oxygen-depleted to the right heart [13], [14].

1.2 Electrophysiological basis of cardiac electrical activity

The basis for normal mechanical pumping function of heart is given by the sequential generation and propagation of the cardiac electrical impulses [15]. However, despite the differences between foetal and adult hearts are significant from a mechanical perspective, their electrical activity is similar [4].

The fundamental unit of the cardiac electrical activity is given by the excitable cells, which are able to generate the so-called *action potentials*. Action potentials are found to be rapid changes in the membrane potential [14], whose typical waveform is depicted in Figure 1.3.

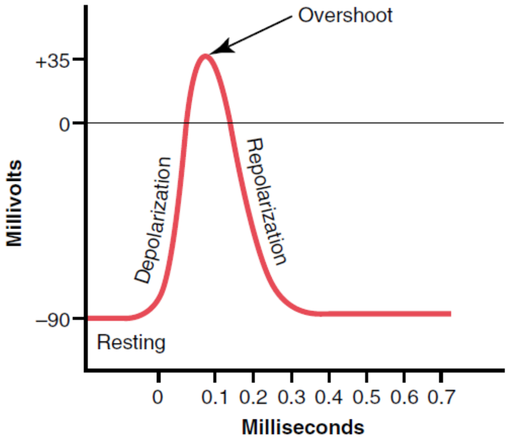

Figure 1.3. Schematic representation of a typical action potential in nerve cells [14].

The normal resting trans-membrane potential is about -90 mV, which is determined by the potassium (K^+) and sodium (Na^+) diffusion and the action of the electrogenic Na^+-K^+ pump. In this condition, the K^+ conductance is 50-100 times higher than the Na^+ one. When the membrane potential rises from -90 mV towards 0 mV because of an external stimulus, the voltage-gated Na^+ channels are opened and Na^+ ions start to pour into the cell. This fact causes a 5000-fold increase of the Na^+ conductance of the membrane, and as such allowing the inflow of other positive Na^+ ions. In this phase, the trans-membrane potential depolarises and overshoot, even reaching positive voltage values. Then, the Na^+ channels start to inactivate and close, while the delayed voltage-gated K^+ channels open even more, because of the potential rise. These simultaneous events lead to the decrease of the Na^+ ions inflow and a substantial outflow of K^+ ions, thus resulting in the sharp repolarization and recovery of the resting membrane potential [14].

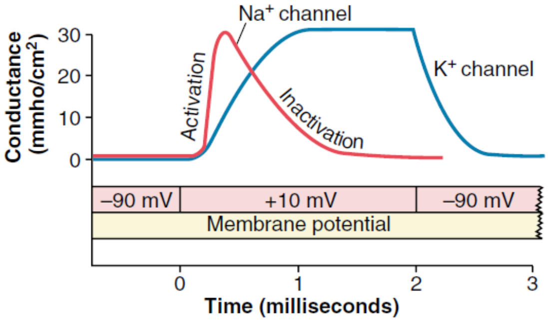

Figure 1.4. Schematic representation of conductance changes for Na^+ and K^+ ion channels generating the action potential in nerve cells [14].

However, the action potential is initially generated only when a threshold voltage for elicitation is reached by the membrane potential, which typically constitutes a sudden rise of 15 to 30 mV. Once generated, it propagates in excitable tissues following the all-or-nothing principle [14].

Different types of excitable cells co-exist in the human heart. Focusing on heart muscle fibres, the waveform of the action potential is quite different, as shown in Figure 1.5. In this case, the depolarization phase is governed by the opening of the fast voltage-gated Na^+ channels. The depolarization phase is followed by a plateau portion of about 200-300 ms, which is mainly caused by the inflow of calcium (Ca^{2+}) ions through the prolonged opening the Ca^{2+}-K^+ channels and, partly, by the slower opening of the voltage-gated K^+ channels, which delay the repolarization phase. The presence of the plateau has a functional role in these excitable cells, delaying the repolarization phase and as such prolonging the contraction of the heart muscle for the whole period [14]. Remarkably, a new action potential cannot be generated until the membrane is depolarized, since the voltage-gated Na^+ channels are inactivated until the resting membrane potentials level is reached. Therefore, the plateau also influences the duration of the refractory period of the cardiac fibre, which is normally around 250-300 ms for the ventricles and 150 ms for the atria.

This action potential waveform is typically found in Purkinje fibres, but also in atrial and ventricular myocytes [16].

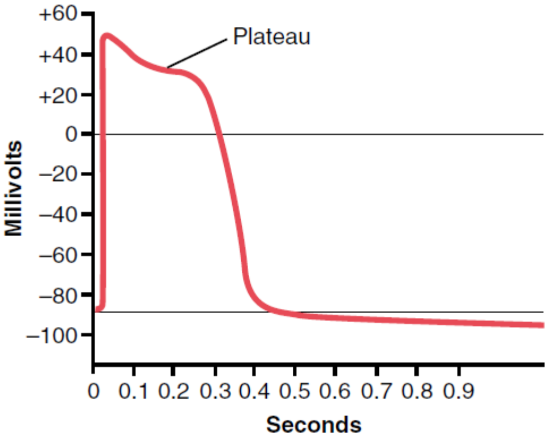

Figure 1.5. Action potential in a Purkinje fibre [14].

Another characteristic action potential waveform is that occurring in cardiac pacemaker cells (see Figure 1.6), like those in the sinoatrial and atrioventricular nodes [16], whose self-induced discharges determine the rhythmical heartbeat. In these excitable cells, the automatic re-excitation is due to the resting membrane potential, which is around -60 to -70 mV. In this condition, the Na^+ and Ca^{2+} can easily flow inward, determining a further increase of the membrane permeability and inflow of other positive ions, eliciting the action potential. Remarkably, at the end of the membrane repolarization and for some milliseconds after, the membrane shows a higher permeability to K^+ ions, causing a hyperpolarization of the trans-membrane potential which impede the instantaneous self-induced re-excitation of the pacemaker cell. When the permeability to K^+ is restored, the resting potential is reached and the re-excitation can occur again.

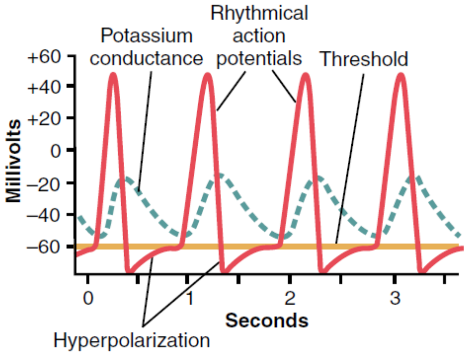

Figure 1.6. Example of rhythmical action potentials and the corresponding K^+ conductance changes [14].

Therefore, different action potential waveforms can be detected from different cardiac tissues (and then regions), as shown in Figure 1.7. Specifically, the sequential generation and propagation of these potentials leads to the typical waveform detected in surface electrocardiograms [16]. Normally, the pacemaker cells in the sinoatrial node generate the cardiac electrical impulse, thus determining the electrical pattern also known as sinus rhythm. The impulse propagates across the atria through the anterior, middle and posterior internodal pathways and Bachmann's bundle, moving toward the atrioventricular node. At this point, the impulse propagation is slightly delayed, i.e. the atrioventricular node depolarizes after some milliseconds, allowing the atrial cardiomyocytes to complete their contraction and pump the residual blood into the ventricles before their depolarization [14]. Then, the impulse is propagated to the bundle of His, the left and right bundle branches, the Purkinje fibres and finally to the ventricular muscle [16]. As such, in the cardiac cycle, each cardiac chamber is depolarized and repolarized rhythmically, alternating systolic and diastolic phases. Overall, each sequence of a systole and a diastole constitute a cardiac cycle, whose duration is found to be as the reciprocal of the heart rate [14].

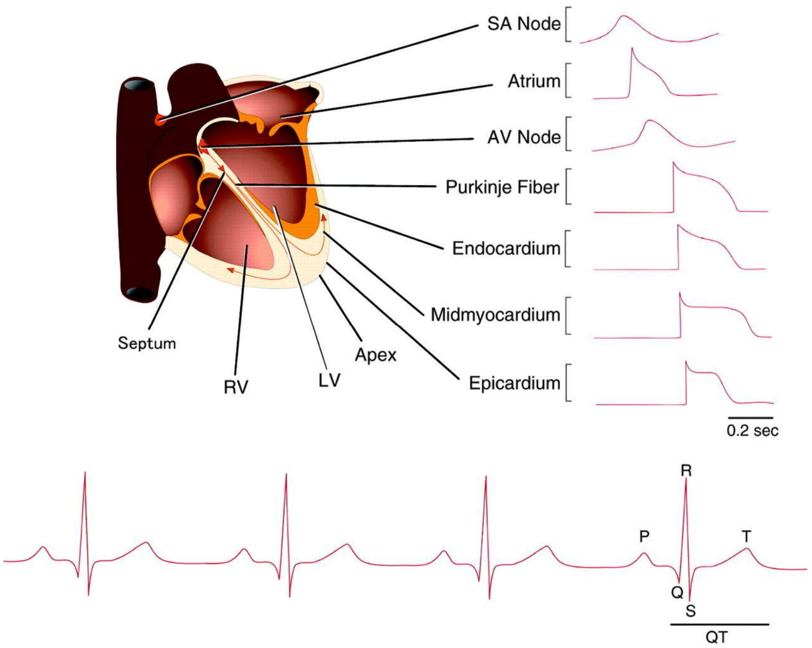

Figure 1.7. Action potentials arising from the different cardiac regions and the resulting electrocardiogram waveform [16].

1.3 Electrocardiography and ECG acquisition

The ECG is the time-domain representation of the cardiac electrical activity. In healthy subjects, each cardiac cycle is depicted in the ECG by several deflections, mainly the P wave, the QRS complex and the T wave. Adults and foetuses have ECG patterns that are very similar in their morphology, despite they show significant differences in amplitudes [4], [17].

The P wave reflects the depolarization of the atria preceding the atrial systole, whose amplitude and duration are typically below 0.25 mV and 120 ms, respectively, in adults [18], [19]. After about 0.15 to 0.20 s from the end of the P wave, the atria repolarize. However, the so-called atrial T wave is rarely recorded in the ECG since it is buried by the simultaneous QRS complex [14]. The isoelectric interval between the end of the P wave and the onset of the consecutive QRS complex is called as P-R segment, whereas the time between the onset of the atrial and ventricular depolarizations is called P-Q interval (or P-R interval) [18], [19]. In this phase, between 0.12 and 0.2 s, the electrical impulse travels through the atrioventricular node, the bundle of His and bundle branches, and the Purkinje fibres. The QRS complex is caused by the ventricular depolarization, occurring at the beginning of the ventricular contraction; it typically lasts less than 100 ms with a peak-to-peak amplitude between 1 and 1.5 mV. The end of the QRS complex is defined at the J point. The segment between the J point and the onset of the consecutive T wave is called S-T segment, representing the temporal interval between the end of depolarisation and the beginning of repolarisation occurring in ventricles. Finally, the T wave represents the ventricular repolarization and, as such, anticipates the ventricular diastole. Its normal morphology is asymmetrical, with a duration of less than 250 ms and an amplitude below 0.3 mV. However, from a clinical perspective, the most interesting measure concerns the Q-T interval, representing the total time for the complete ventricular depolarization and repolarization. A minor deflection may occur after the T wave, known as the U wave, which seems to result from the repolarisation of mid-myocardial cells and His-Purkinje fibres, but its significance is still debated [18], [19]. Figure 1.8 summarizes the electrophysiological events of the cardiac cycle and their corresponding ECG waves.

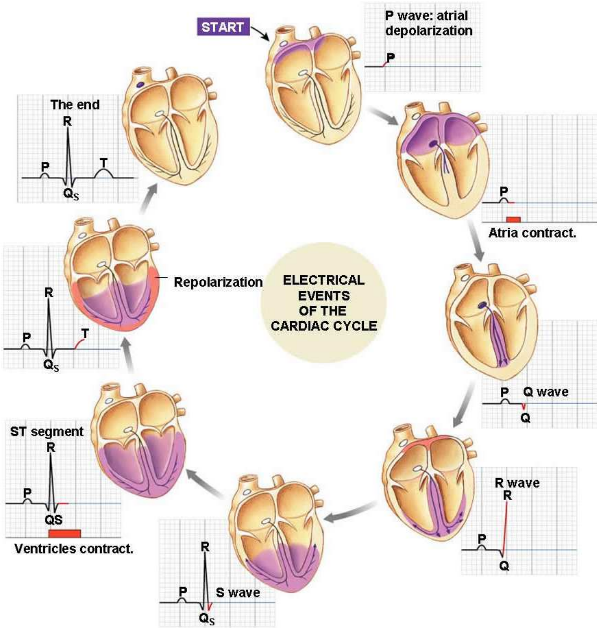

Figure 1.8. The P, QRS and T waves constituting the ECG and their corresponding electrophysiological events occurring in the cardiac cycle.

In adults, the electrocardiogram can be acquired non-invasively, by placing surface electrodes on the chest and the limbs. In fact, the cardiac electrical activity determines the spread of an electrical depolarization through the heart but also in the surrounding conductive tissues, generating electrical potentials that can be recorded on the body surface [14].

Actually, the ECG recording is based on an original assumption that models the cardiac electrical activity as a single two-dimensional dipole, with a fixed location at the centre of the heart, located in an infinite, homogeneous, resistive, passive volume conductor [20]. The dipole is represented by its time-varying dipole moment, also known as cardiac vector, which rotates in accordance with the cardiac depolarization and repolarizations. As such, the ECG signal recorded on the body surface can be seen as a linear projection of the cardiac vector. On these assumptions, the Einthoven's lead system identified the right arm, the left arm and the left leg as the vertices of an equilateral triangle, whose sides correspond to the so-called lead vectors. As such, when performing a bipolar recording by placing two measuring electrodes, one positive and one negative, in correspondence of two of these anatomical points, it is possible to observe the projection of the cardiac vector onto the chosen lead vector [20].

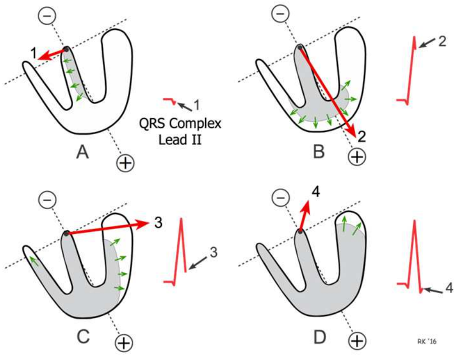

Figure 1.9. The cardiac vector resulting from the different phases of ventricular depolarization and the corresponding ECG trace recorded on lead II.

The Einthoven electrode configuration allows the recording of the three bipolar leads, i.e. lead I, lead II, lead III, but also the three Goldberger unipolar augmented leads, i.e. aVR, aVL and aVF. In the unipolar leads, the recording is performed between each limb electrode and the Wilson central terminal reference. All these leads, along with the six precordial leads on the chest, which measure the electrical activity closer to the heart, constitute the standard 12-lead ECG system, which is the one of major clinical adoption [20]. The 12-lead ECG system requires the placement of ten recording electrodes and a ground/right leg drive electrode on the right leg, as shown in Figure 1.10. Since each lead examines the cardiac electrical activity from a different perspective, the electrode positioning is standardized for adults (Figure 1.10) but not for the foetuses, as better detailed in Section 2.1, considering that it is not possible to directly apply the electrodes on the foetal body.

Nonetheless, also the foetal cardiac electrical activity can be model by the single dipole theory effectively [4]. However, due to the different cardiac output of the ventricles in foetus and adult, their electrical axes point towards different directions, i.e. towards the right and the left side of the heart respectively, thus resulting in different vectorcardiograms (VCG) representations [21]. Based on these premises and the dynamical ECG model proposed in [22], a synthetic model for the NI-fECG was introduced [23] and later extended to be included in the *fecgsyn* open-source toolbox [24], [25] for foetal-maternal mixture simulation. Moreover, due to the anatomic differences and changes in media properties and distributions, this modelling has been recently optimized [26].

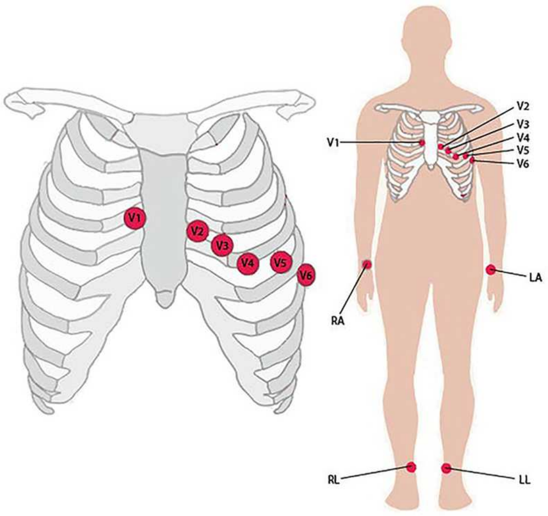

Figure 1.10. Electrode positioning for the standard ECG 12-lead configuration. V1-V6: precordial leads; RA: right arm; LA: left arm; LL: left leg; RL: right leg.

1.4 Monitoring the foetal cardiac well-being

Different technologies can be exploited for foetal heart monitoring, depending on the gestational age and the goal of the examination [27], [28]. They can rely on different principles and approaches, both invasive and non-invasive, and mainly include phonocardiography, one-dimensional Doppler ultrasound, cardiotocography, foetal echocardiography, magnetocardiography and electrocardiography. However, other methodologies have been rarely exploited for the same purpose, such as pulse oximetry [29], [30], photoplethysmography [31] and near-infrared spectroscopy [32]–[35].

Foetal phonocardiography (fPCG) estimates the foetal cardiac performance non-invasively from the foetal heart sounds produced by the closure of the cardiac valves [36]. This technique can be used from the 20th week of gestation, but can be exploited also in labour [37]. fPCG employs a piezoelectric or optical sensor placed on the maternal abdomen that transduces the acoustic information into an electrical signal [28]. It currently provides only the antenatal analysis of foetal heart rate (fHR) and foetal breathing movement [38], [39] but, although it could provide important diagnostic information, the considerable difficulties related to the signal acquisition and processing limit its adoption [40], [41].

One-dimensional Doppler ultrasound performs the fHR measure by estimating the Doppler shift between the transmitted and received ultrasound beams. The ultrasound wave is sent by the piezoelectric crystal, pass through the different maternal tissues and is reflected by the foetal heart, thus guaranteeing a non-invasive foetal cardiac assessment. Specifically, in the hand-held Doppler transducers, which are used for intrapartum and antenatal heart rate variability (HRV) measures, two distinct piezoelectric crystals manage the transmission and the detection of the echo, respectively. However, beyond HRV, one-dimensional Doppler ultrasound techniques have proven to be useful also for foetal development and wellbeing assessment by the analysis of foetal cardiac valve opening intervals [42]–[44].

Cardiotocography (CTG) is an ultrasound-based technology allowing the foetal heart monitoring by the continuous fHR recording along with the simultaneous monitoring of uterine mechanical contractions. It is performed from the 20th week of gestation, by using two transducers: an ultrasound transducer detecting the foetal heart activity, and a pressure transducer, called tocodynamometer, monitoring the uterine contractions [4]. Despite they can be internally placed, transducers are typically applied externally, thus enabling a non-invasive monitoring. As regards the ultrasound technology, CTG is mainly based on a single piezoelectric crystal performing both the sending and the receiving of the ultrasound wave, thus exploiting the so-called pulsed-wave Doppler mode [28]. CTG constitutes a standard care methodology for the foetal well-being assessment, in antenatal [45] and intrapartum settings [46]. Despite the advantages introduced by CTG are still debated [47], many studies focused on the automatic analysis of CTG recordings in order to reduce inter- and intra-expert variability and enable the identification of risky or pathological conditions [48]–[55]. However, although CTG is relatively cheap and easy to implement, it does not provide a beat-to-beat fHR assessment since, due to its low SNR, fHR averaging in a time window is often required [37], [56], [57].

Foetal echocardiography is an ultrasound imaging technique that enables clinicians to monitor the foetal heart both structurally and functionally from the 18th week of gestation. Foetal echocardiography ultrasound systems should exhibit several imaging capabilities, as 2D or grey-scale, M-mode, colour and pulsed-wave Doppler (PWD) [3]. Doppler echocardiography has been found to be particularly useful for the detection of congenital heart diseases (CHD) and the assessment of the foetal cardiac rhythm [3]. Specifically, it allows evaluating the anatomy and function of cardiac chambers, the cardiac timings but also the direction, volume and velocity of the blood flow in vessels and cardiac chambers. In this regard, PWD allows the evaluation of additional important information, as the foetal blood flow across the main cardiac valves along with its direction and velocity, and a complete assessment of the diastolic and systolic function in the apical five-chamber view. Specifically, this latter methodology allows the inspection of the four chambers and the first part of the aorta, leading to a characteristic PWD velocity waveform [58], [59], as shown in Figure 1.11, by which different cardiac intervals and performance indexes can be deduced [60].

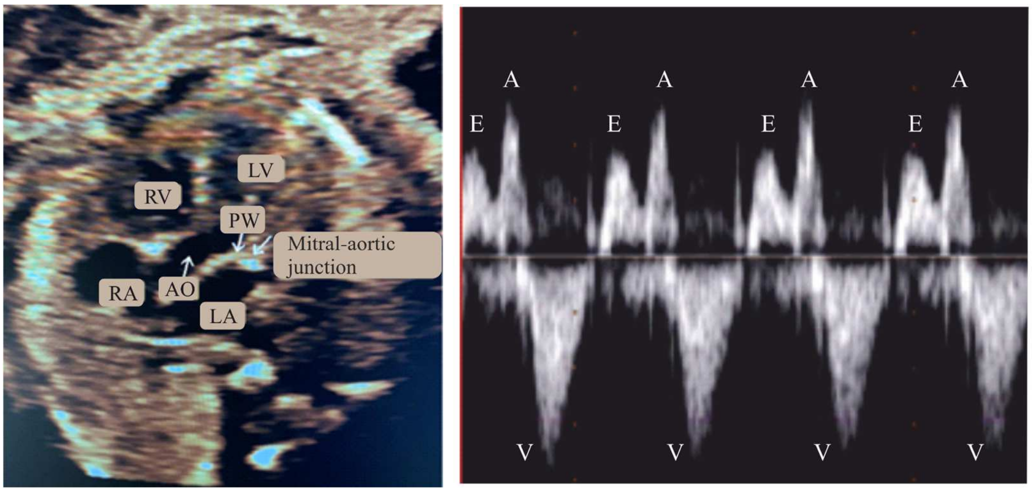

Figure 1.11. An apical five-chamber view of a foetal heart (on the left) along with an example of PWD velocity trace with the characteristic waveform (on the right) reflecting the mitral inflow due to the passive filling of the LV and atrial contraction (i.e., the E and A peaks, respectively) and the aortic outflow (i.e., the V peak) in different cardiac cycles. In the apical five-chamber view, the right and left ventricles (RV and LV, respectively), the left and right atria (LA and RA), the aortic region (AO) and the sample volume adopter for PWD acquisition (PW) are indicated. Adapted from [59].

Despite foetal echocardiographic methods represent a standard tool for antenatal screening and care [3], they need expensive technologies and qualified clinicians to be performed [37], [61], thus restricting their adoption only in case of risky conditions [28]. Remarkably, they measure the mechanical consequences of the electrical activity. As such, they are not able to provide information about cardiac electrical waveforms and beat-to-beat variability of the fHR[1] [4], [62], [63]. Nonetheless, these aspects are of peculiar importance since several CHD and foetal arrhythmias have morphological reflections on the cardiac electrical signal [27], but also in pre-eclampsia [64], intrauterine growth restriction (IUGR) [65] and foetal distress abnormal conditions [17]. Moreover, they cannot allow continuous monitoring, thus missing transitory arrhythmias and fHR changes over time [66]. As such, new technologies were introduced and studied: magnetocardiography and foetal electrocardiography [4], [63], [66].

Foetal magnetocardiography (fMCG) can measure the magnetic fields associated to the foetal cardiac electrical activity non-invasively from the 20th week of gestation. It requires high-performance sensors as the superconductive quantum interference device (SQUID) to be employed in a magnetically shielded room. Despite fMCG may provide cardiac electrical signals with accurate morphology, proven to be useful for CHD and foetal arrhythmias identification [67] and the assessment of foetal neurodevelopment [68], it cannot be adopted for long-term monitoring and suffers from the expensive, complex and cumbersome equipment needed [27], [37]. All these limitations relegate the use of the fMCG in only a limited number of clinical centres [3].

---

[1] Although an accurate estimate of fHR can be obtained by foetal pulsed-wave Doppler or M-mode echocardiography, the complexity of the exam hampers its use for general screening, and, in any case, the analysis can be only limited to a short time.

Foetal electrocardiography is based on the acquisition of the foetal cardiac electrical activity. Given the topic of the first part of this thesis, it is deeply explored in the next section.

1.4.1 Foetal electrocardiography

Foetal cardiac electrical activity has been firstly recorded as ECG in the early 20th century [69]. From that moment on, several works focused on this research topic, but many fundamental aspects are still under investigation and discussion.

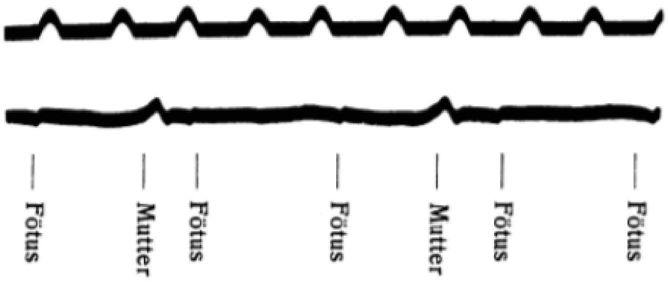

Figure 1.12. First fECG recording [69].

The acquisition of fECG can be performed either invasively or non-invasively.

The **invasive fECG** (I-fECG) is performed by introducing an intra-uterine electrode in the cervix, after the rupture of the membrane, and attaching it in direct contact with the presenting portion of the foetal scalp. The reference electrode is placed on the maternal thigh [70]. Due to the invasiveness of the procedure, this technique can be performed only during labour and in presence of risk factors, thus impeding its adoption for prenatal screening. I-fECG allows the recording of high-quality fECG signals, thus enabling accurate fHR monitoring with beat-to-beat accuracy, fECG morphology analysis [37], [71], and especially the S-T analysis (STAN) based on the S-T segment and T/QRS ratio [72]–[75]. In intrapartum foetal monitoring, I-fECG may be clinically combined with CTG monitoring [70], [76] and performed by commercially-available devices as the STAN S31 monitor (Neoventa Medical, Molndal, Sweden) [77], but its clinical usage is uncommon [78]. Nonetheless, the main drawbacks of this monitoring technique concern its invasiveness, which exposes both the mother and the foetus to infection risks, the possibility of being exploited only at the last stage of pregnancy, and the unavailability of a three-dimension assessment of the foetal cardiac electrical activity [4], [76], [78].

Non-invasive fECG (or NI-fECG) is a promising tool for continuous foetal monitoring and prenatal diagnostics [17], [56], [79]. NI-fECG examines the foetal cardiac electrical activity from the maternal abdomen, by applying surface electrodes on the mother's belly, which record the potentials associated with the depolarizations and repolarizations occurring in the foetal heart [27]. Typically, in order to optimise the skin-electrode contact impedance, a gentle abrasion is performed on the maternal skin and then, a conductive gel is applied before electrode placement. NI-fECG can be exploited starting from the 18th week of gestation [4]. As such, it could allow a prenatal, low-cost and risk-free monitoring, and thanks to its non-invasiveness, it could be exploited also for long-term applications [27], [37]. Moreover, NI-fECG could also enable the assessment of all pathological states inducing changes in ECG waveform morphology [56] and, in worst cases, premature diagnosis of foetal defects. As such, it could be a powerful tool enabling possible therapeutic interventions antenatally or immediately after-birth.

NI-fECG provides accurate estimate of fHR and its beat-to-beat variability [80], even outperforming standard ultrasound methods [81], [82] especially in case of high maternal body mass indexes [83], [84]. This is an important aspect since fHR patterns are related to the foetal well-being, the gestational age, but also the autonomic nervous system (ANS) development and, as such, allow the ANS functionality assessment in the prenatal period [85]. Moreover, NI-fECG technique has been found to be particularly useful also in cases of pre-eclampsia [86], [87], IUGR [88] and for the antenatal screening and diagnosis of CHD [79] and foetal arrhythmias [89]. However, NI-fECG suffers from several problems, as better described in the next chapter, which lead to low-quality fECG recordings [3], [4], [27], [78], thus preventing the adoption of this technique for the fECG morphological analysis and, generally, in the clinical practice. In fact, NI-fECG is mainly exploited for fHR estimation [37], while fECG morphological analyses are enabled by I-fECG technology [56]. Despite the huge scientific effort and results on simulated data [25], [90]–[93], some useful morphological information has been rarely extracted from real NI-fECG recordings, as for detection of foetal arrhythmias [89], [94], S-T segment analysis [80], [95], altered morphology of the QRS complex [96], T-wave alternans [97] and some cardiac intervals [79], [90], [98], deserving further clinical validation. As such, further research is needed to address this specific issue [99].

1.4.2 Commercially available monitoring devices based on non-invasive foetal ECG

In recent years, several fHR monitoring devices based on NI-fECG were proposed and approved for clinical use [30], [56], [100]. The first commercially available system was the wireless Monica AN24 monitor by Monica Healthcare (Nottingham, UK), adopting several electrodes placed on the maternal abdomen. Then, several technologies exploiting disposable patch-systems were introduced, as the Novii Wireless Patch System by GE Healthcare (Chicago, Illinois, USA), the MERIDIAN M110 system by MindChild Medical (North Andover, Massachusetts, USA), the PUREtrace and the Nemo Fetal Monitoring System by Nemo Healthcare (Veldhoven, The Netherlands). Moreover, in order to guarantee long-term continuous assessment of foetal well-being, many at-home monitoring technologies have been proposed as the wearable 5-channel monitor system by Bloomlife (San Francisco, California, USA and Genk, Belgium) and Imec (Leuven, Belgium and Eindhoven, The Netherlands), the FDA-cleared Invu device [101] by Nuvo (Tel Aviv, Israel) and the Owlet Band (Lehi, UT, USA).

Figure 1.13. Some examples of most recent monitoring devices based on NI-fECG. On top, the Owlet Band (left side) and the Invu device by Nuvo (right side) are reported, whereas on bottom, the Nemo Fetal Monitoring System by Nemo Healthcare (left side) and the wearable 5-channel monitor system by Bloomlife and Imec (right side) are depicted.

Chapter 2

Overview of non-invasive foetal ECG signal processing

2.1 Non-invasive foetal ECG signal processing issues

As discussed in the previous Chapter 1, several issues affect the recording of NI-fECG signals, preventing them to reach diagnostic reliability and to be clinically exploited [27]. At first, the recorded NI-fECG signals are very weak, whose magnitude is in the order of a few dozen of microvolts [17], [27] and as such several times lower than maternal ECG (mECG). Moreover, NI-fECG recordings are characterized by low SNR [3], [4], [27], [78], which can be ascribed to different causes. In fact, the source of NI-fECG signals, i.e. the foetal heart, is small [78] and the foetal cardiac electrical signal must pass through different propagating media before being acquired on the maternal abdomen by the measuring electrodes [4]. In their entirety, the layers and interposed tissues constitute the so-called volume conductor, whose shape and electrical properties change during the whole gestation period [102], hampering the NI-fECG acquisition. In fact, these biological media exhibit different electrical conductivities during the gestation and, specifically, an electrically insulating layer grows during gestation, which is able to mask the fECG signal completely between about the 28th and the 32nd week of gestation [102]. It is a protective waxy substance covering the foetus, called *vernix caseosa*, which acts as a complete electrical shield and, as such, changes the conductive propagation pathways, potentially inducing significant variations in NI-fECG morphology [102]. Nonetheless, this insulating layer gradually disappears from some parts of the foetal body, in particular the face and head that come in tight contact with the maternal pelvis, in the last phase of gestation, i.e. normally starting from the 32nd week of gestation. After this stage, NI-fECG can be acquired again with more consistent magnitude, but it is strongly influenced by the size and the unpredictable locations of the vernix caseosa holes [103]. In fact, the biological dissolving process may cause gaps in the vernix caseosa, which could alter the signal conduction pathways and make them inhomogeneous, thus distorting the NI-fECG and impeding morphological analysis from that moment on [103].

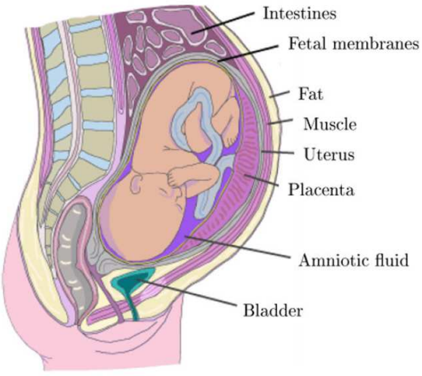

Figure 2.1. Main foeto-maternal compartments [4].

Besides the source and the propagation issues related to the foetal cardiac electrical activity, the low SNR of NI-fECG is also ascribed to the different biological and technical interferences [17], [76]. Many bioelectrical interferences are derived from the mother, particularly mECG, but also maternal respiration, electromyogram, the uterine contractions. Moreover, additional non-physiological noises can be identified as interferences related to improper skin-electrode interface and cable shielding, or instrumentation noise, such as powerline interference and baseline wander.

Noises and interferences overlap with the weaker fECG in various domains [4], [17], and especially in both time and frequency domains (see Figure 2.2) thus requiring powerful signal processing methods [37], as better detailed in the next section.

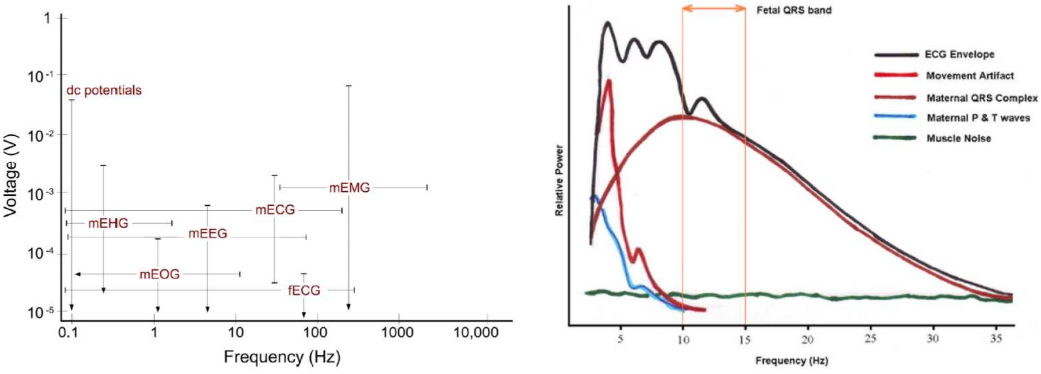

Figure 2.2. Amplitude and frequency range of different overlapping bioelectrical interferences to the fECG signals [4]. Labels are indicating maternal electrocardiogram (mECG), electroencephalogram (mEEG), electrooculogram (mEOG), electromyogram (mEMG), electrohystrogram (mEHG), and the foetal ECG (fECG).

Moreover, NI-fECG acquisition is challenged even more considering that the foetus can show different presentations during the recording, and can move a lot in the maternal abdomen especially in the first two trimesters [4], when the signal is not distorted. Foetal presentation is typically unpredictable and can substantially influence the recorded fECG from the maternal belly, as different dipole projections are exposed on the measuring electrodes. In this regard, time-varying foetal orientation and movement prevent the adoption of a standard electrode configuration, as foetal body coordinates may vary with respect to the maternal body coordinates and as such to the surface electrodes. Moreover, electrodes are placed on the maternal abdomen, thus different anisotropic media are interposed between the source and the measuring systems, limiting the exploitability of the conventional dipole model and leads. This is the reason why, despite the different positioning proposed in the literature, an optimal electrode configuration cannot be achieved [17]. Overlapping interferences, foetus' behavioural states and time-varying presentations comprehensively make the NI-fECG a non-stationary signal, thus hampering even more its processing and analysis. Moreover, multiple pregnancies are possible, therefore challenging more and more the NI-fECG tools because multiple foetal ECG sources are recorded.

Based on all these premises, despite the huge number of techniques developed in the scientific literature for fECG processing, the identification of a clinically-interpretable and morphologically preserved fECG signal is still an open research issue [4], [17].

2.2 Background on signal processing methods for non-invasive foetal ECG analysis

Given the promising advantages and potentialities in the adoption of NI-fECG for the antenatal screening, a great scientific effort has been put into the development of signal processing and analysis techniques, but also of innovative technologies, in order to recover high-quality and reliable fECG from non-invasive recordings [57], [78].

Typically, NI-fECG recording first undergo a *pre-processing* stage in order to mainly remove noises which are out of the fECG band [17]. In this stage, the main low-frequency artifacts, as baseline wandering and drift due to maternal respiration and electrode motion, are attenuated by adopting different signal processing approaches such as FIR and IIR high-pass filtering, moving median filtering with different window sizes [78], but also exploiting wavelet-based approaches [104]. At this stage, also the powerline noise and the high-frequency noise components due to electromyographic activity are suppressed, by selecting typical FIR and IIR low-pass and notch filters [78] or non-linear denoising approaches such as wavelet-based ones [105].

Then, the *fECG extraction* process is typically performed to retrieve the fECG component from the pre-processed NI-fECG recordings. This step mainly aims to remove the mECG component, which is stronger than the fECG in amplitude and overlaps with the fECG not only in the time domain but also in the frequency domain [4], [17]. Being a challenging task, a huge number of fECG extraction algorithms have been proposed in the literature for this purpose [37], [56], [76], [106]. According to the specific implementation, only abdominal recordings can be required, either single or multichannel, or both abdominal and thoracic signals can be recorded, to have a clean mECG reference. Many different fECG extraction approaches have been proposed in the literature, such as blind source separation algorithms, mainly exploiting independent component analysis (ICA)[107]–[109], but also as principal component analysis (PCA) [109], [110], periodic component analysis (πCA) [111] and nonstationary component analysis (NSCA) [112], template-subtraction methods [81], [110], [113], Kalman filtering and its different extended versions [114], [115], wavelet-based algorithms [116], [117], adaptive filtering [118], [119] and neural networks [120]–[123], de-shape algorithm [93], [124] and many other hybrid approaches as reported in [37], [56].

After the fECG extraction process is performed, an additional *post-processing* stage may be needed in order to remove the residual background noise and enhance the fECG content [106]. In this regard, despite the scientific effort put into the NI-fECG post-processing stage is substantially lower than that related to fECG extraction, different NI-fECG enhancement methods may be mentioned. The first post-processing approach is the synchronized averaging of consecutive foetal QRS complexes, which has been proposed for fECG noise reduction for a long time [125], [126]. This approach has been frequently exploited in the field [127]–[129], also with improvements as the optimal tuning of the number of foetal beats to be averaged in NI-fECG traces [21], [130] or by looking at similar foetal beats in a different N-dimensional space [93] before averaging. Other works based the NI-fECG enhancement on spatio-temporal filtering [131], time-sequenced adaptive filtering [132] or deep neural network models [133]–[135]. Nonetheless, different authors exploited wavelet denoising methods for the same purpose [104], [136]–[151], as better explored in Chapter 4 and 5.

2.3 Conclusion

It is clear that, although NI-fECG is widely identified as a promising tool for antenatal screening and diagnosis, several issues hamper the achievement of high-quality fECG signals from abdominal recordings to be exploited for clinically useful morphological analyses. In this regard, as briefly illustrated in the previous paragraph, a huge number of signal processing techniques have been developed and published in the scientific literature, but nowadays NI-fECG is still mainly relegated to fHR estimation.

In the light of all these premises that limit the NI-fECG development and consequently its clinical adoption, this PhD thesis aims to describe novel advanced signal processing tools for morphologically preserved fECG recovery. As such, this PhD work presents, at first, a novel algorithm for fECG extraction. Moreover, different wavelet-based strategies for the NI-fECG post-processing are proposed, and then compared with state-of-the-art wavelet denoising approaches developed for this specific application, in order to guarantee an optimal fECG enhancement and background noise removal.

Chapter 3

A novel algorithm for non-invasive foetal ECG extraction

3.1 Rationale

As already explained in Chapter 2, many different issues hinder the attainment of clinically useful NI-fECG signals for antenatal screening and diagnosis. These aspects can be ascribed to the difficulties encountered when trying to extract high-quality and morphology-preserved fECG signals from abdominal recordings, even when introducing more advanced signal processing techniques and modelling tools. Therefore, in order to address this issue, in this chapter a novel algorithm for fECG extraction is introduced. This algorithm has been conceived in collaboration with Prof. Hau-Tieng Wu (Department of Mathematics and Statistical Science, Duke University, Durham, NC, USA). Specifically, considering the work by Su and Wu [90] in which a fECG extraction algorithm for both fHR and morphology analysis has been presented for two or three transabdominal recordings, and other previous works [93], [124], [152] introducing several advanced signal processing tools allowing for an efficient fECG extraction, a multi-channel fECG extraction approach was developed, which exploits the nonlocal Euclidean median algorithm, the de-shape short-time Fourier transform (STFT) technique and optimal shrinkage denoising algorithm. The performance obtained by this novel algorithm has been quantitatively assessed both in terms of foetal R-peak detection, including the evaluation of the foetal QRS complex detection accuracy (Acc), the true positive rate (TPR) and the positive predictive value (PPV), but also looking at the recovered foetal beats morphology on synthetic signals, by evaluating its preservation through the estimation of the root-mean-square error (RMSE), the Spearman's rank correlation coefficient (r_s) and Pearson's correlation coefficient (ρ).

3.2 Materials and methods

The proposed fECG extraction algorithm fundamentally relies on the so-called adaptive non-harmonic (ANH) model [93], [152], by which each abdominal ECG signal $x(t)$ can be assumed as the combination of different time-varying non-sinusoidal oscillatory components with time-varying amplitude and frequency, i.e., the mECG ($x_m(t)$), the fECG ($x_f(t)$) and the non-stationary noise ($n(t)$):

$$x(t) = x_m(t) + x_f(t) + n(t) \qquad (3.1)$$

On this basis, the novel algorithm exploits several recent state-of-the-art signal processing tools, i.e. the optimal shrinkage algorithm, the de-shape STFT-based R-peak detection, and the nonlocal Euclidean median technique, which are briefly detailed hereinafter.

3.2.1 Background on optimal shrinkage, nonlocal Euclidean median and de-shape STFT tools

3.2.1.1 Optimal shrinkage

Optimal shrinkage is a SVD-based denoising approach introduced in [153] and later exploited in [90] for an effective estimation of mECG. Indeed, considering the mECG contribution in a typical non-invasive abdominal recording, it is mixed with several instrumental and biological noisy interferences, particularly the fECG components, which must be removed for a robust mECG recovery. Thus, this can be treated as a matrix denoising problem, which can be mathematically expressed as [90], [153]:

$$Y = X + W \tag{3.2}$$

where $X = [x_1, x_{2,} \ldots, x_n] \in R^{z \times n}$ represents the mECG matrix including n noiseless mECG segments of length z, W is the noise matrix of the same size, and $Y = [y_1, y_{2,} \ldots, y_n] \in R^{z \times n}$ is the matrix containing the corresponding noisy segments in the abdominal recording. By assuming a low-rank matrix X and a zero-mean independent and identical noise N with unit variance, and considering large n and z with $z/n \leq 1$, the optimal denoised matrix estimate of X, i.e. Y, can be retrieved as [90], [153]:

$$\hat{X} = U \Lambda^{*} V^{T} \tag{3.3}$$

where

$$Y = U \mathit{\Lambda} V^{T} \tag{3.4}$$

whereas $\mathit{\Lambda}^{*} \in R^{z \times n}$ is computed from the optimal shrinker $\eta^{*}(\lambda)$, that for an operator-norm loss function can be defined as [90], [153]:

$$\eta^{*}(\lambda) = \begin{cases} \frac{1}{\sqrt{2}} \sqrt{\lambda^2 - \beta - 1 + \sqrt{(\lambda^2 - \beta - 1)^2 - 4\beta}} & if\ \lambda \geq 1 + \beta \\ 0 & otherwise \end{cases} \tag{3.5}$$

in which λ represents each singular value of Y and β the asymptotic aspect ratio of the Y matrix, defined as z/n, respectively [90], [153].

In this way, the optimal shrinkage allows for a better estimation of the mECG contribution, thus guaranteeing a subsequent, more suitable mECG cancellation and, therefore, a more reliable fECG recovery [90]. However, since the above-mentioned assumption of unit variance cannot be satisfied in this context, a normalization is required according to the noise level. This is accomplished by introducing a constant parameter chosen by the user, hereinafter called so_p [90].

3.2.1.2 Nonlocal Euclidean median

Despite the nonlocal Euclidean median has been introduced as an image denoising algorithm [154], [155], it has been successfully applied in one-dimensional denoising contexts, and remarkably for single-lead and two-channel fECG extraction [90], [93], [124]. Specifically, in its application for mECG recovery in a single-channel abdominal ECG signal, around each maternal beat, different segments of L samples can be extracted, which can be considered overall as the noisy collection of the pure mECG segments to be retrieved. In this regard, each noisy beat can be considered as a single entity in a L-dimensional manifold.

Considering that two consecutive cardiac cycles may have different morphologies, i.e., may be distant in the manifold, and assuming the collection of maternal cardiac cycles to be independent from foetal ones [93], the underlying wave-shape function can be recovered for each noisy maternal beat by including its K nearest neighbours in the median, with $K \in N$. Mathematically, taking into account the i-th maternal beat in the abdominal ECG signal, i.e. $x_m^{(i)} \in M^{1\times L}$, and considering its Euclidean distance from each j-th maternal beat $x_m^{(j)} \in M^{1\times L}$ as

$$d_{i,j} = \sqrt{\sum_{h=1}^{L} (x_{m,h}^{(i)} - x_{m,h}^{(j)})^2} \qquad (3.6)$$

its K neighbours may be identified by considering the beats showing the smallest relative Euclidean distances in the manifold, leading to the neighbour's matrix $x_{Nm}^{(i)} \in M^{K\times L}$ of the i-th maternal beat, where K is a user-defined parameter. On this basis, the noiseless version of the $x_m^{(i)}$, namely $\tilde{x}_m^{(i)}$, can be computed as [93]:

$$\tilde{x}_m^{(i)} = median(x_{Nm}^{(i)} \in M^{K\times L}) \qquad (3.7)$$

However, considering the abovementioned basic concepts, it is clear that the nonlocal Euclidean median algorithm can be applied not only for maternal beats, but also for fECG denoising whenever foetal R-peak locations are available [93].

3.2.1.3 De-shape STFT

The de-shape STFT is a time-frequency analysis technique allowing for an enhancement of the fundamental frequency contribution while performing a nonlinear adaptive filtering on the spectral interferences related to its harmonics [93], [152]. For a general signal $x(t)$, de-shape STFT is performed by combining the STFT ($V_x^{(h)}$) and the inverse short-time cepstral transform ($U_x^{(h,\gamma)}$), as [93], [152]:

$$W_x^{(h,\gamma)}(t,\xi) = V_x^{(h)}(t,\xi)\, U_x^{(h,\gamma)}(t,\xi) \qquad (3.8)$$

where h is the chosen window function and $\xi > 0$ describes the frequency, while $V_x^{(h)}$ and $U_x^{(h,\gamma)}$ are respectively defined as:

$$V_x^{(h)}(t,\xi) = \int x(\tau)h(\tau - t)e^{-i2\pi\xi(\tau-t)}\, d\tau \qquad (3.9)$$

$$U_x^{(h,\gamma)}(t,\xi) = C_x^{(h,\gamma)}(t, 1/\xi) \qquad (3.10)$$

with q defined as quefrency, and

$$C_x^{(h,\gamma)}(t,q) = \int \left|V_x^{(h)}(t,\xi)\right|^{\gamma} e^{-i2\pi q\xi}\, d\xi \quad (3.11)$$

As such, by applying the de-shape STFT algorithm under the ANH model [152], it is possible to obtain a time-frequency representation of the signal, from which it is possible to extract the time-domain trend of the instantaneous frequency by dynamic programming curve extraction algorithm and then the R peak locations by the beat tracking technique, as deeply described in [93], [124], [152].

3.2.2 Proposed algorithm

In this section, a novel multi-channel fECG extraction algorithm is introduced. Then, the dataset adopted for its evaluation and the performance metrics are described.

The algorithm is graphically described in Figure 3.1 and better detailed below.

Step 1: Pre-processing

At first, each abdominal ECG signals was pre-processed by removing high frequency noise through a 5th-order bidirectional IIR Butterworth low-pass filter with a cut-off frequency of 100 Hz, as in [90]. Then, low-frequency interferences as baseline wandering were suppressed in each abdominal ECG channel by detrending. Specifically, low-frequency noise was estimated by a moving median filter with window of 500 ms, and then subtracted. As such, in the following sections, each p-th pre-processed abdominal ECG signal is denoted as $\boldsymbol{x}_p(t) \in R^{1\times N}$, and the multi-channel recording set as $\boldsymbol{x}(t) \in R^{P\times N}$, with P the total number of available channels and N the number of samples.

Step 2: Maternal R-peak detection

Then, an accurate R-peak detection of maternal beats was performed. To this aim, on each pre-processed abdominal recording $\boldsymbol{x}_p(t)$, maternal R peaks were detected by using the de-shape STFT along with the dynamic programming curve extraction algorithm and the beat tracking technique, following [90], [93], [124]. At this stage, a collection of maternal R-peak locations for each of the P available channels is obtained, which however may differ because of background noise or fECG contributions. In order to select the most robust maternal R-peak annotation, each collection was compared with all the others in terms of F1 score, by imposing a very strict tolerance window (i.e., 5 or 10 ms). In this way, for each channel, the number of other channels showing a significant detection coherence (i.e., F1 score above a user-defined threshold, e.g. 0.95 or 0.999) was computed and the channels were ranked according to this metric. Finally, the two top channels were considered to determine the final maternal R-peak locations, hereinafter denoted as:

$$\boldsymbol{R_m} = \{R_m^{(k)}\}_{k=1}^{M} \quad (3.12)$$

where M identifies the total number of maternal cardiac cycles. Specifically, the maternal R-peak locations belonging to the two collections of R peaks exhibiting the highest number of consistent detections were compared in terms of distance, and then only the R-peak annotations falling into an acceptable window of temporal distance (i.e., 5 or 10 ms) were retained in order to obtain $\boldsymbol{R_m}$. However, in those cases in which the collections of maternal R-peak locations were not strictly coherent (i.e., the collection selected as second for its high consistency showed a high F1 only when compared with another channel annotation), the $\boldsymbol{R_m}$ was considered as the maternal R-peak

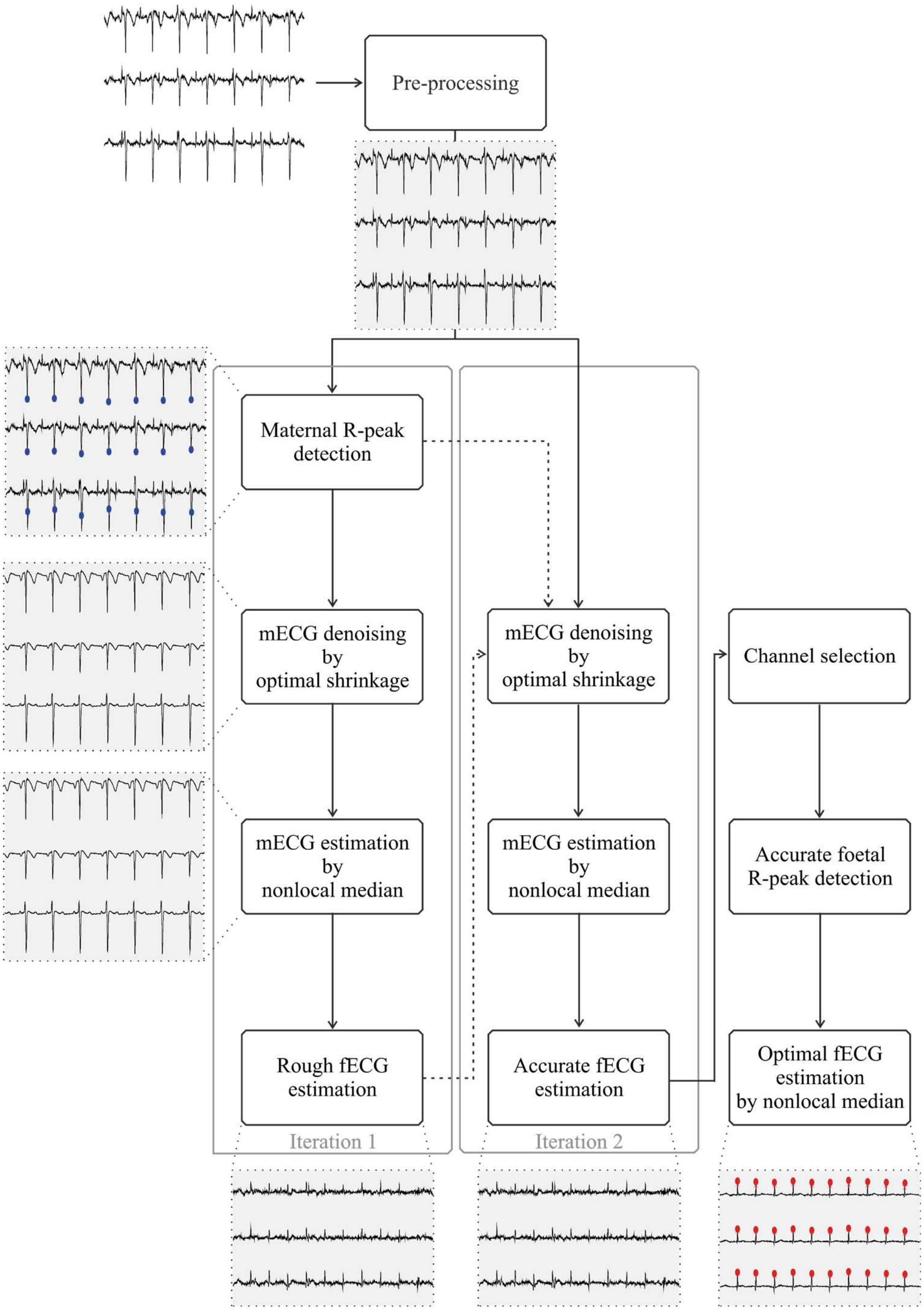

Figure 3.1. Schematic representation of the different steps involved in the proposed algorithm. After a pre-processing stage, abdominal ECGs are subjected to maternal R-peak detection and, then, to a two-steps denoising stage by optimal shrinkage and nonlocal median approaches. Then, a rough estimate of the multi-channel fECG is available and exploited for a more reliable estimation of the mECG content. At this point, an accurate multi-channel fECG is recovered by subtraction. On this basis, a channel selection approach is implemented, and an accurate foetal R-peak detection is adopted, in order to estimate an optimal fECG multi-channel set by nonlocal median.

locations belonging to the abdominal channel exhibiting the highest number of coherent channels in terms of F1 score.

Step 3: Maternal ECG estimation by optimal shrinkage and nonlocal median

Based on the maternal R-peak locations in $\boldsymbol{R_m}$, abdominal traces were denoised in order to retrieve a good estimate of the mECG contributions. As such, from each $\boldsymbol{x}_p(t)$, all segments including the maternal R peaks (i.e., $\boldsymbol{x}_{p,m}$) were firstly extracted by considering a window centred on the R peak and with a duration equal to the quantile 0.95 of all the RR intervals ($RR_{0.95}$).

Mathematically,

$$\boldsymbol{x}_{p,m} = \{\boldsymbol{x}_{p,m}{}^{(k)}\}_{k=1}^{M} \tag{3.13}$$

with

$$\boldsymbol{x}_{p,m}{}^{(k)} = [\boldsymbol{x}_p(R_m^{(k)} - 0.5RR_{0.95}), \ldots, \boldsymbol{x}_p(R_m^{(k)} + 0.5RR_{0.95})] \tag{3.14}$$

and $p = 1, \ldots, P$.

Considering each channel separately, in order to attenuate both noise and fECG contents, all segments were denoised by optimal shrinkage by assuming, in this phase, an a-priori value of the parameter so_p equal to 4.5, according to the supposed noise level and a preliminary fine-tuning based on visual inspection. At this point, in the multi-channel case, a set of matrices $\hat{\boldsymbol{x}}_{p,m}$ was defined, with $p = 1, \ldots, P$:

$$\hat{\boldsymbol{x}}_{p,m} = \{\hat{\boldsymbol{x}}_{p,m}{}^{(k)}\}_{k=1}^{M} \tag{3.15}$$

$$\hat{\boldsymbol{x}}_{p,m}{}^{(k)} = [\hat{\boldsymbol{x}}_p(R_m^{(k)} - 0.5RR_{95\%}), \ldots, \hat{\boldsymbol{x}}_p(R_m^{(k)} + 0.5RR_{95\%})] \tag{3.16}$$

where $\hat{\boldsymbol{x}}_{p,m}{}^{(k)}$ indicates the k-th segment in the p-th abdominal ECG channel after optimal shrinkage denoising.

Then, in order to remove any uncorrelated residual noise, the nonlocal median algorithm was applied. However, since the nonlocal median has been adopted in single-channel applications only [90], [93], in this work it was adapted to a multi-channel set of abdominal recordings. Specifically, in the multi-channel approach, the similarity between each pair of maternal cardiac cycles was evaluated by summing their squared Euclidean distances across all available channels, as:

$$d^2(\hat{\boldsymbol{x}}_{p,m}{}^{(k)}, \hat{\boldsymbol{x}}_{p,m}{}^{(j)}) = \sum_{p=1}^{P} \left\| \hat{\boldsymbol{x}}_{p,m}{}^{(k)} - \hat{\boldsymbol{x}}_{p,m}{}^{(j)} \right\|_2^2 \tag{3.17}$$

Then, the abovementioned distance was used to determine the K nearest neighbours for each $\hat{\boldsymbol{x}}_{p,m}{}^{(k)}$, which were further exploited for the proper median template estimate. In this context the squared Euclidean distance, which is frequently adopted in clustering and cluster compactness applications [156], was preferred to the standard Euclidean distance, in order to emphasize the distance between the neighbours [157]. Furthermore, K was imposed equal to 60 for both real and synthetic dataset investigations, in order to include a reasonable percentage of closest beats with respect to the total maternal beats in each median template, according to the signal duration and the supposed maternal heart rate.

After all nonlocal medians were computed, the noiseless multi-channel mECG $\tilde{\boldsymbol{x}}_{mECG}(t)$ was reconstructed by introducing each median template in its proper location. However, in order to handle overlapping cases during mECG reconstruction, all beat extremes were tapered by multiplying each template by a window function $w(n)$, defined as:

$$w(n) = \begin{cases} sin^2(i_s), & i_s \in \{0, (\pi/2)/(l_{overlap} - 1) \; , \ldots , \pi/2\} \\ sin^2(i_s), & i_s \in \{\pi/2 \, , \pi/2 + (\pi/2)/(r_{overlap} - 1) \ldots , \pi\} \\ 1 & otherwise \end{cases} \quad (3.18)$$

where $l_{overlap}$ and $r_{overlap}$ identify any eventual overlap between two consecutive beats on the left and right side, respectively. Nonetheless, in order to avoid any step due to the introduction of median beats, even when two consecutive beats did not overlap, all templates were tapered in the construction of $\tilde{\boldsymbol{x}}_{mECG}(t)$, simply by introducing in $w(n)$ a fixed overlap of two samples.

Step 4: Rough fECG estimation by mECG subtraction

After the recovery of the mECG by denoising and tapering, a rough multi-channel fECG signal can be extracted. This can be achieved by subtracting the estimated mECG, i.e., $\tilde{\boldsymbol{x}}_{mECG}(t)$, from $\boldsymbol{x}(t)$:

$$\tilde{\boldsymbol{x}}_{fECG}(t) = \boldsymbol{x}(t) - \tilde{\boldsymbol{x}}_{mECG}(t) \qquad (3.19)$$

Step 5: Accurate maternal and foetal ECG estimation

Since at this stage a rough multi-channel fECG estimate is available, it can be further exploited for an accurate estimation of so_p parameter, to be exploited in the optimal shrinkage technique. As such, Step 3 and 4 were repeated by simply considering a more reliable and robust estimation of the parameter so_p, associated to the characteristics of the corresponding rough fECG and its noise level. Specifically, on the *p*-th pre-processed abdominal channel, so_p was defined as a scaled value of the sample standard deviation of the corresponding *p*-th rough fECG (σ_p), as:

$$so_p = k \, \sigma_p \qquad (3.20)$$

with

$$\sigma_p = \sqrt{\frac{1}{N-1} \sum_{i=1}^{N} \left| \tilde{\boldsymbol{x}}_{fECG,p}(i) - \bar{x}_{fECG,p} \right|^2} \qquad (3.21)$$

where $\bar{x}_{fECG,p}$ identifies the mean value for the *p*-th rough fECG channel and k is a tuneable parameter, typically varying between 2 and 20, in case of real and synthetic signals respectively, according to preliminary fine-tuning based on visual inspection.

Finally, after the denoising process by optimal shrinkage and the nonlocal median was iterated on the pre-processed multi-channel abdominal recordings $\boldsymbol{x}(t)$, as shown in Figure 3.1, a more accurate multi-channel mECG was obtained ($\tilde{\tilde{\boldsymbol{x}}}_{mECG}(t)$), which can be further subtracted from $\boldsymbol{x}(t)$ to get an accurate estimate of the multi-channel fECG $\tilde{\tilde{\boldsymbol{x}}}_{fECG}(t)$, as:

$$\tilde{\tilde{\boldsymbol{x}}}_{fECG}(t) = \boldsymbol{x}(t) - \tilde{\tilde{\boldsymbol{x}}}_{mECG}(t) \qquad (3.22)$$

Step 6: Channel selection on accurate multi-channel fECG

Then, according to the foetal position and presentation, some channels in $\tilde{\tilde{\boldsymbol{x}}}_{fECG}(t)$ could not provide sufficient and useful information, while hampering a correct foetal R-peak detection. As such, in order to detect the best fECG channels among those included in the multi-channel set, a channel selection approach is introduced. In this regard, to select an appropriate number D of channels, with $D \leq P$, on each channel in $\tilde{\tilde{\boldsymbol{x}}}_{fECG}(t)$, i.e., $\tilde{\tilde{\boldsymbol{x}}}_{fECG,p}(t)$, two foetal R-peak detectors were applied. Specifically a Pan-Tompkins-based peak detector [110] and the combination of the beat tracking algorithm with the de-shape STFT [90], [93], [124] were used. Then, each $\tilde{\tilde{\boldsymbol{x}}}_{fECG,p}(t)$ was evaluated according to the R-peak annotation consistency provided by the two detectors. In this regard, R-peak detection consistency was assessed in terms of F1 score, by available tools [24], [25]. Specifically, all R-peak annotations identified by both detectors, exploiting a 20-ms tolerance window, were considered as true positives, whereas the extra beats identified only by the de-shape STFT-based detector [90], [93], [124] or only by the Pan-Tompkins-based peak detector [110] were assumed as false negatives and false positives, respectively. Then, all accurate fECG channels $\tilde{\tilde{\boldsymbol{x}}}_{fECG,p}(t)$ exhibiting an F1 score above a user-defined threshold (e.g., 0.85 or 0.9) were selected for the following steps. In case the adopted threshold was too selective, an a-priori defined number of fECG channels was selected anyway.

Step 7: Accurate foetal R-peak detection

On the selected fECG channels, an accurate foetal R-peak detection was then needed in order to further processed the traces. To this aim, the SVD decomposition was exploited along with two different signal quality indexes (SQIs) [158], according to the dataset nature (see Section 3.2.3).

On simulated signals, whose generation and characteristics are described in the following Section 3.2.3, the SVD decomposition was performed on the selected accurate fECG channels $\tilde{\tilde{\boldsymbol{x}}}_{fECG}(t)$ and the first $S \leq D$ components were reconstructed separately, where S can be selected by the user. However, as the number of SVD components must be necessarily lower than (or equal to) the number of selected fECG channels, the parameter S is automatically adjusted in case of improper setting, by reducing it accordingly.

From each of the S SVD components, a D-channel set of reconstructed signals $\boldsymbol{X}(t)_{SVD} \in R^{(S \cdot D) \times N}$ was obtained. Then, on each reconstructed signal $\boldsymbol{x}(t)_{SVD} \in R^{1 \times N}$, an SQI based on non-gaussianity was estimated. Specifically, non-gaussianity (SQI_{NG}) was measured in terms of negentropy, as [158]:

$$SQI_{NG} = \left| k_1 E_t\{\boldsymbol{x}(t)_{SVD}\, exp(-\frac{{\boldsymbol{x}(t)_{SVD}}^2}{2})\}^2 + k_2[E_t\{exp(-\frac{{\boldsymbol{x}(t)_{SVD}}^2}{2})\} - \frac{\sqrt{2}}{2}]^2 \right| \tag{3.23}$$

with $k_1 = 36/(8\sqrt{3} - 9)$ and $k_2 = 24/(16\sqrt{3} - 27)$. No centring or normalization by the variance was performed.

As such, since the foetal contribution is assumed to have a non-gaussian distribution because of its spiky R-peaks [158], the higher the non-gaussianity measure, the higher the foetal content in the reconstructed signal $\boldsymbol{x}(t)_{SVD}$. As such, the reconstructed synthetic signal showing the highest SQI_{NG} was selected for the subsequent foetal R-peak detection. Specifically, this signal was firstly filtered by the a bidirectional 10th-order IIR Butterworth high-pass filter with cut-off frequency of 10 Hz, for foetal QRS enhancement [110], [159], normalized according to its absolute maximum and then considered as input for foetal R-peak detection. On this trace, foetal R-peak detection was performed by de-shape STFT and beat tracking [90], [93], [124], along with a final R-peak annotation refinement by looking for a local maximum or minimum in a 10-ms window around each R peak location, according to the signal polarity and QRS balance, thus giving the final foetal R-peak locations $R_{f,def}$. If the annotation failed (i.e., a fHR below 120 bpm was detected), the parameter S was automatically increased of one unit and the process repeated once again.

On real signals, a similar approach was adopted, but exploiting a different SQI. After the SVD decomposition of the selected accurate fECG channels $\tilde{\tilde{\boldsymbol{x}}}_{fECG}(t)$, the first $S \leq D$ components were reconstructed separately. Each reconstructed signal $\boldsymbol{x}(t)_{SVD} \epsilon R^{1\times N}$ from the total set $\boldsymbol{X}(t)_{SVD} \epsilon R^{(S\cdot D)\times N}$ was then filtered by a bidirectional 10th-order IIR Butterworth high-pass filter with cut-off frequency of 10 Hz, in order to enhance foetal QRS, as in [110], [159]. Then, a modified version of the pseudo-periodicity measure proposed in [158] was exploited. Specifically, on each filtered signal $\boldsymbol{x}(t)_{SVD}$, i.e., $\overline{\boldsymbol{x}}(t)_{SVD}$, the foetal QRS detector based on de-shape STFT and beat tracking [90], [93], [124] was exploited. Then, on each signal $\overline{\boldsymbol{x}}(t)_{SVD}$, a window with duration equal to the mean RR interval ($\overline{RR}_f$) was extracted around each detected foetal R peak $R_f \in R^{nF\times 1}$, leading to the foetal beat matrix $\boldsymbol{B}_s \epsilon R^{nF\times \overline{RR}_f}$, defined as:

$$\boldsymbol{B}_s = [\overline{\boldsymbol{x}}(t)_{SVD}(R_f - 0.5\overline{RR}_f),\ldots,\overline{\boldsymbol{x}}(t)_{SVD}(R_f + 0.5\overline{RR}_f)] \quad (3.24)$$

From $\boldsymbol{B}_s$, a foetal beat template $\boldsymbol{b}_s \epsilon R^{1\times \overline{RR}_f}$ was then estimated by robust weighted average [158], [160]. On this basis, for each $\overline{\boldsymbol{x}}(t)_{SVD}$, the dissimilarity between each extracted foetal beat and the foetal beat template was estimated as pseudo-periodicity SQI (SQI_{PP}) by the sample-wise variance of their difference, as:

$$SQI_{PP} = \frac{1}{\overline{RR}_f}\sum_{j=1}^{\overline{RR}_f}\frac{1}{nF}\sum_{i=1}^{nF}(\boldsymbol{B}_s - \boldsymbol{b}_s)^2 \quad (3.25)$$

Then, since the higher the variance (i.e., the SQI_{PP}), the higher the dissimilarity, the SVD-based reconstructed signal showing the lowest SQI_{PP} was selected and its foetal R-peak locations were taken as final foetal QRS positions $R_{f,def}$. Then, similarly to the synthetic case, a final R-peak annotation refinement was performed by looking for a local maximum or minimum in a 10-ms window around each R peak location, according to the signal polarity and QRS balance. Finally, also in the real case, the parameter S was automatically adjusted in case of improper setting, by reducing it according to the number of selected fECG channels, or even in case of failed annotation (i.e., a detected fHR below 100 bpm). In this latter case, the parameter S was automatically increased of one and the SVD component selection and detection repeated once again.

Step 8: Optimal multi-channel fECG recovery by nonlocal median

Once the foetal R peaks were detected, as last step, the selected fECG channels were further denoised by the nonlocal median approach, in order to attenuate the noisy contributions due to acquiring instrumentation, maternal EMG activity related to uterine contractions, or eventually residual mECG.

Specifically, on each of the selected accurate fECG channels $\tilde{\tilde{\boldsymbol{x}}}_{fECG}(t) \epsilon R^{D\times N}$, all segments including the final foetal R-peak locations $R_{f,def}$. were extracted, by considering a window centred on each foetal R peak and with a duration equal to the median foetal RR interval ($\overline{RR}_{f,def}$) computed on $R_{f,def}$.

$$\tilde{\tilde{\mathbf{x}}}_{fECG}{}^{(j)} = [\tilde{\tilde{\mathbf{x}}}_{fECG}(R^{(j)}_{f,def} - 0.5\overline{RR}_{f,def}), \ldots, \tilde{\tilde{\mathbf{x}}}_{fECG}(R^{(j)}_{f,def} + 0.5\overline{RR}_{f,def})] \quad (3.26)$$

with $j = 1, \ldots, F$ and F representing the total number of detected foetal beats.

Then, similarly to the maternal ECG denoising by nonlocal median algorithm, uncorrelated residual noise was removed from the fECG by estimating a proper median template on the K_f nearest neighbours identified by the multi-channel squared Euclidean distance (see Equation 3.17). In this study, K_f was set equal to 80, for both real and synthetic data assessments, in order to consider a reasonable percentage of closest beats in each median template, according to the signal duration and the presumed fHR. Finally, the denoised fECG signals were reconstructed by introducing each median template in its proper location, tapering all foetal beat extremes by $w(n)$ as in Step 3 (see Equation 3.18 for its definition), and then performing an additional interpolation by a piecewise cubic Hermite interpolating polynomial function, only in those cases where foetal R peaks were more (or less) than $\overline{RR}_{f,def}$ apart.

3.2.3 Material

Two different datasets of abdominal recordings were used, to evaluate the performance of the proposed fECG extraction algorithm not only in terms of fHR estimation, but also for morphology analysis preservation. To this aim, results were evaluated on a physiologically-plausible synthetic dataset and a freely available real dataset [161].

The **synthetic dataset** includes 5-minute-long 32-channel abdominal recordings generated by an open-source non-invasive fECG signal simulator, *fecgsyn* [24], [25] at 2048 Hz. The maternal and foetal heart rates were assumed to be 90 and 150 bpm respectively, as in [162]. Specifically, despite the simulator offers 34 channels by default, for the evaluation of the proposed algorithm only abdominal channels were considered, whereas thoracic ones were ignored. The maternal heart coordinates were assumed equal to [2.0944, 0.2, 0.4], whereas foetal ones to [–0.412, 0.284, –0.300], as in [162]. The position of the simulated surface electrodes detecting the abdominal ECG are depicted in Figure 3.2.

Non-stationary realistic noises (i.e., muscular artifact, baseline wander and electrode motion) with different amplitudes were added, to challenge the fECG extraction algorithm and test its performance also in cases where typical blind source separation algorithms cannot perform accurately. As such, four different subsets of simulated data were obtained by considering a sinusoidal noise modulation, with the SNR of the mECG relative to noise ($\mathrm{SNR}_{\mathrm{mn}}$) equal to 3 dB, 6 dB, 9 dB and 12 dB, while keeping the same SNR of the fECG relative to the mECG ($\mathrm{SNR}_{\mathrm{fm}}$), imposed equal to -10 dB. This latter parameter was chosen equal to -10 dB as it produces a physiologically plausible foetal contribution in abdominal traces, resembling the characteristic of the analysed real dataset, which showed a mean $\mathrm{SNR}_{\mathrm{fm}}$ of about -10.8 dB, according to [161]. In each subset, ten different multi-channel recordings were included, simulating ten different pregnancies. Two examples of synthetic abdominal traces with different noise levels are shown in Figure 3.3.

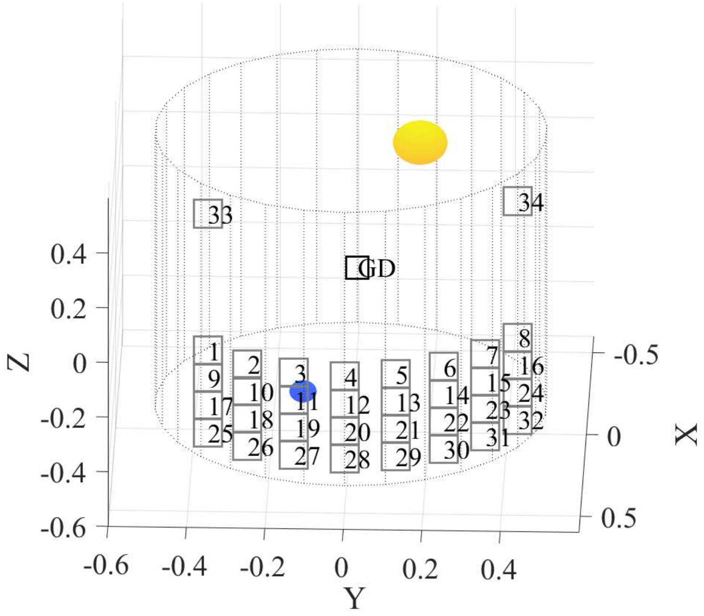

Figure 3.2. Maternal and foetal dipoles positions (yellow and blue sphere, respectively) along with the electrode locations (grey squares) both on the abdomen (from 1 to 32) and the thorax (33, 34). GD identifies the reference electrode position, on the maternal back.

Synthetic signals were introduced since a clean fECG signal for each abdominal channel is available, thus allowing for the quantitative and effective evaluation of the morphology preservation of the proposed fECG extraction algorithm. However, some characteristics of the synthetic signals do not frequently take place in real recordings, therefore for an analysis of the algorithm performance also a real dataset has been used. Specifically, the **real antenatal dataset** by Matonia *et al.* [161] has been selected for this investigation, since it provides 20-min long traces with the reference foetal R-peak annotations. Specifically, the real antenatal dataset includes four-channel abdominal recordings performed on ten pregnant women between the 32nd and the 42nd week of gestation. Signals were acquired by the KOMPOREL system at 500 Hz with 16-bit resolution, and preliminarily filtered to suppress powerline and low-frequency interferences [161]. Recordings were performed by four electrodes placed on the maternal abdomen near the navel, referenced to a common electrode on the pubic symphysis and with an active ground electrode on the left leg. Along with the abdominal recordings, also the foetal R-peak locations are provided after validation by clinical experts, with a flag denoting their annotation reliability. More details can be found in [161].

However, for the processing of the real dataset, a resampling at 1 kHz was performed in order to enable a more accurate foetal R-peak detection and evaluation.

3.3 Methods for the comparative analysis

The performance obtained by the novel fECG extraction algorithm has been quantitatively assessed in terms of foetal R-peak detection after the extraction (in the light of its potential adoption for fHR measurement applications), and recovered foetal beat morphology (for its potential adoption in clinical contexts where morphological analysis is relevant).

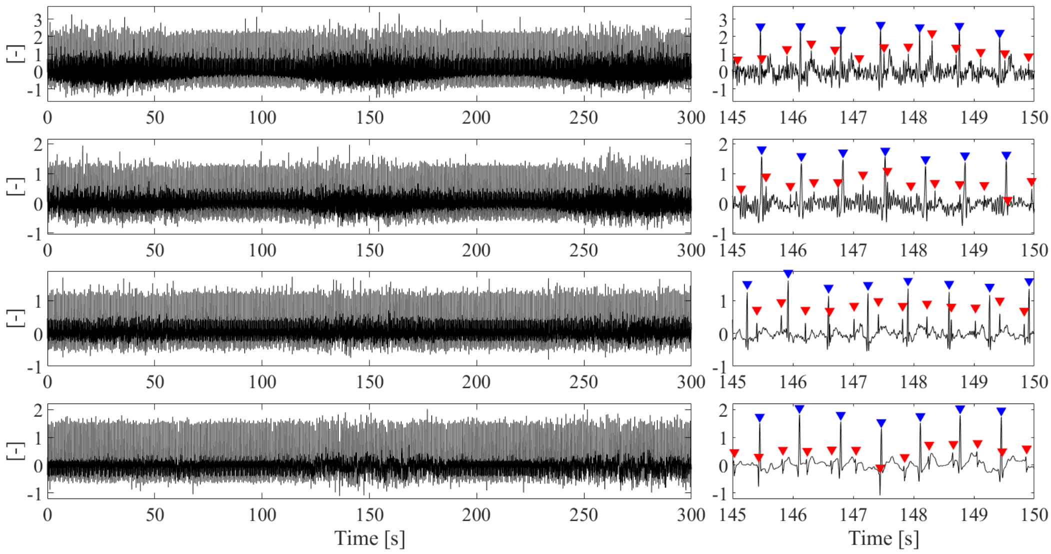

Figure 3.3. Examples of 5-min long abdominal ECG signals affected by physiologically plausible non-stationary noise included in the synthetic dataset. On the left, from top to bottom: a single-channel abdominal ECG signal with SNR_{mn} equal to 3 dB, 6 dB, 9 dB and 12 dB respectively. On the right, a 5-s zoom on corresponding left-side recordings with the foetal (red downward-pointing triangles) and maternal (blue downward-pointing triangles) QRS annotations. Amplitudes are dimensionless.

As regards the foetal R-peak detection performance, it was assessed on the extracted multichannel fECG signals of both real and synthetic datasets, by evaluating the foetal QRS complex detection Acc, TPR and PPV obtained by a de-shape STFT-based R-peak detection algorithm [90], [93], [124], as:

$$Acc = TP/(TP + FN + FP) \qquad (3.27)$$

$$TPR = TP/(TP + FN) \qquad (3.28)$$

$$PPV = TP/(FP + TP) \qquad (3.29)$$

where TP represents the correctly detected foetal beats, FN the undetected foetal R-peaks and FP the incorrectly detected ones. For this evaluation, a 20-ms tolerance window has been set.

Furthermore, the algorithm performance has been compared with other effective fECG extraction algorithms introduced in the scientific literature. As such, for an effective comparison, the same detection metrics were evaluated on the extracted fECG signals provided in the adopted real dataset [161], but also on the fECG signals extracted from the real abdominal recording by the algorithm proposed by Jamshidian-Tehrani and Sameni [158], which has been expressly developed for the fECG extraction from time-varying and low-rank abdominal mixtures. For its implementation, the OSET toolbox [163] and parameterization settings reported in [158] were exploited.

Conversely, the morphological preservation analysis was carried out only on synthetic signals, in which a noiseless ground truth is available, by estimating the RMSE, the r_s and ρ. Specifically, each metric was computed between each extracted fECG and the corresponding noiseless trace, beat-by-beat, and the median value for each extracted fECG channel was considered in the subsequent evaluations. Here, each noiseless fECG trace was pre-processed following Step 1 (see

Section 3.2.2), in order to prevent any signal morphology difference from being associated to the missing pre-processing stage. In this analysis, an interval of 300 ms around each foetal R peak was considered, by taking 120 ms before and 180 ms after the foetal QRS location [164].

All data processing was performed in MATLAB v2020a (MathWorks Inc., MA, USA).

3.4 Results and discussion

3.4.1 Algorithm performance on synthetic signals

All findings achieved on synthetic signals in terms of foetal R-peak detection effectiveness and morphology preservation are reported in Figure 3.4. As can be seen, foetal R peaks in the extracted fECG traces were accurately detected in all examined sets (median Acc values above 99.7%), with a high TPR and PPV (i.e., median values equal or above 99.7% and equal to 100%,

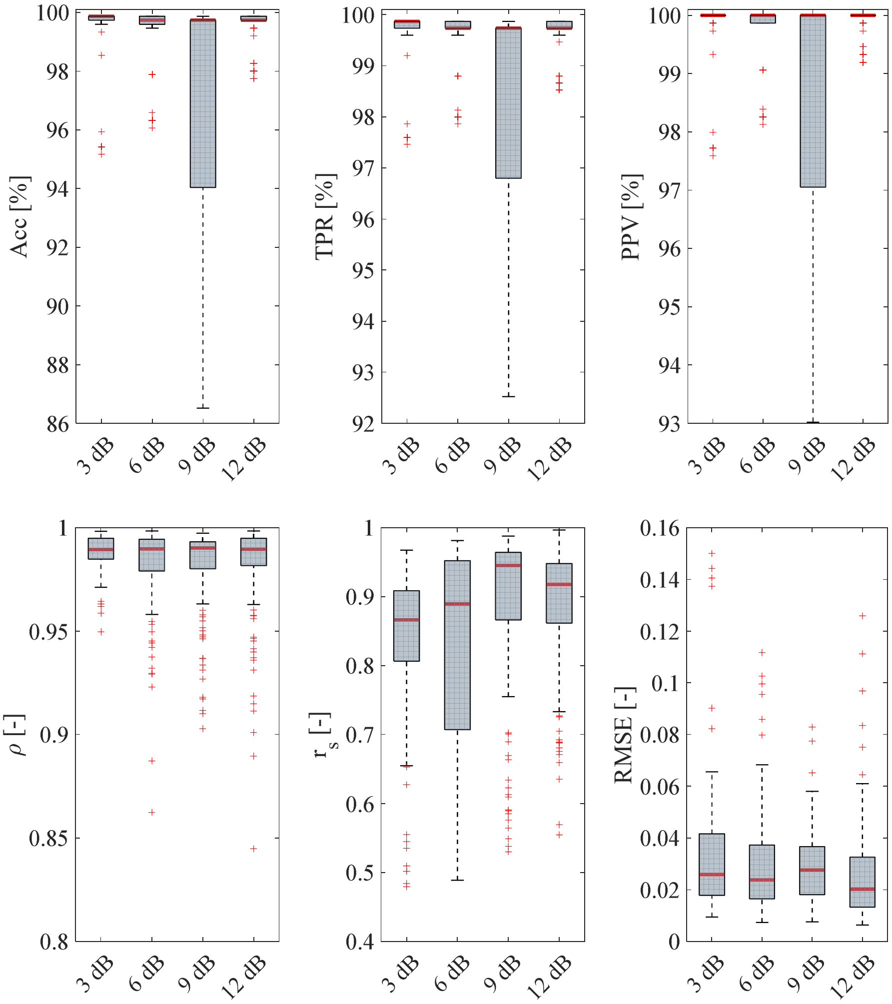

Figure 3.4. Results on the synthetic dataset. On top, foetal R-peak detection Acc, TPR and PPV values are reported for the four sets of simulated data affected by different non-stationary noise levels (i.e., SNR_{mn} equal to 3 dB, 6 dB, 9 dB and 12 dB respectively). Similarly, morphology-preservation metrics are represented for the same sets on bottom. For the RMSE, units are not reported since signal amplitudes are dimensionless. For the sake of clarity, five outliers for the 3-dB set and 14 outliers for the 9 dB were not depicted; specifically, for the 3-dB case, outliers were enclosed in the range 35-36% for Acc, 49-51% for TPR, 55-57% for PPV and 0.4-0.6 for ρ, whereas for 9-dB case they were included in 66-69% for Acc, 79-81% for TPR, 80-83% for PPV.

respectively), thus encouraging the use of the proposed algorithm for reliable fHR monitoring. In this regard, higher variability can be appreciated in the 9-dB subset distributions with respect to the other sets, even if performance proves to be good, with all 25th percentiles standing above 94%, 96.5% and 97% for Acc, TPR, and PPV, respectively.

Furthermore, when looking at morphology preservation metrics, some interesting insights can be provided. In fact, focusing on Figure 3.4, the fECG signals seemed to be faithfully recovered from a morphological perspective, with small distortions and residuals. In fact, median ρ and r_s values were found to be higher than 0.99 and 0.87 respectively, whereas median RMSE estimates were typically below 0.03, thus suggesting a very high consistency between the recovered foetal heartbeats and the corresponding noise-free cardiac cycles. This finding seemed to be stable and confirmed in all analysed synthetic subsets, regardless of the entity of the noise affecting the initial trans-abdominal recordings, thus guaranteeing good performances also in case of low SNR (see Figure 3.5), which is particularly important in the hypothesis of its exploitability in real applications. However, some rare exceptions occurred in the 9-dB subset, as shown in Figures 3.4 and 3.6. Remarkably, morphology-preservation findings are independent from the foetal R-peak detection ones, since only the foetal R peaks provided by *fecgsyn* were considered in their computations.

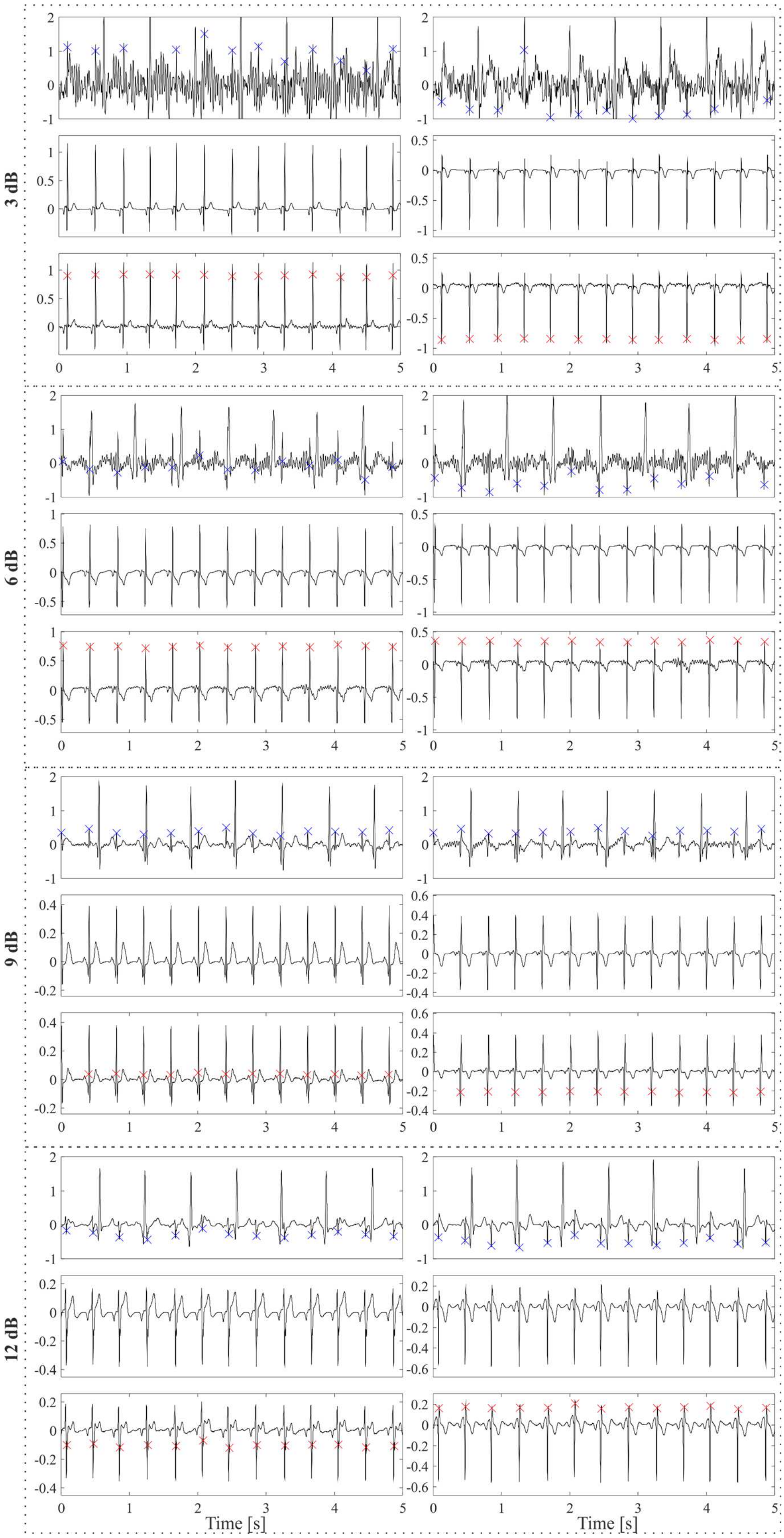

Figure 3.5. A 5-s zoom on two examples of synthetic signals for each subset (SNR$_{mn}$ of 3 dB, 6 dB, 9 dB, 12 dB). For each example, the pre-processed abdominal ECG (upper row) with reference foetal R-peak annotations (blue crosses), the pre-processed noiseless fECG (middle row) and the recovered fECG (bottom row) with the detected foetal R-peaks (red crosses) are reported.

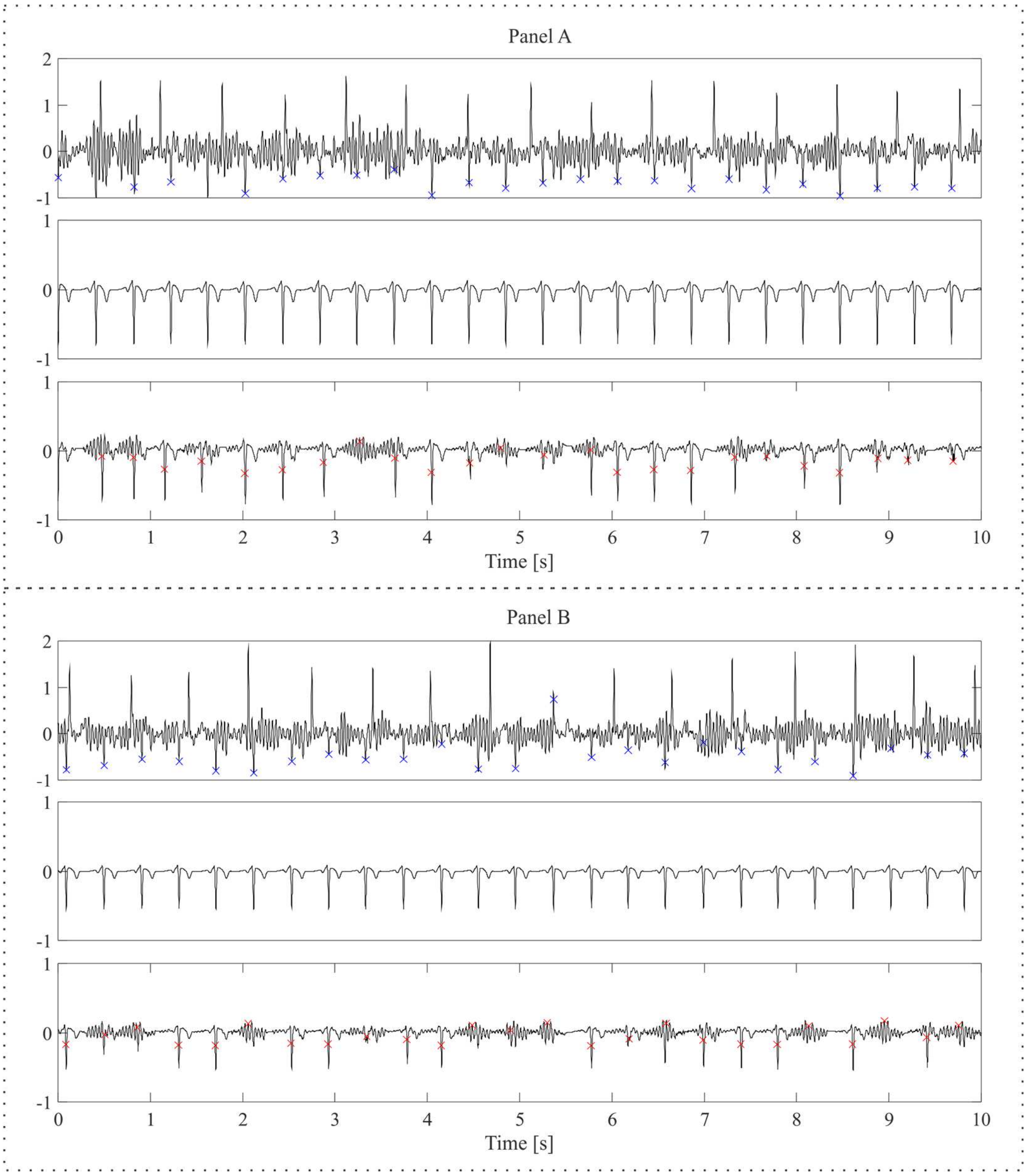

Figure 3.6. Two 10-s long examples of synthetic recordings from the simulated pregnancy #2 of the 9-dB subset (in Panel A and B, respectively). In each panel, the first row reports the pre-processed trans-abdominal ECG channel with the reference foetal R-peak annotations (blue crosses) provided by the fecgsyn simulator, the second row depicts the corresponding noiseless fECG after pre-processing, whereas the third row represents the optimal fECG signal extracted by the proposed algorithm along with the detected foetal R-peaks (red crosses). As can be seen, despite the adoption of the nonlocal median algorithm, some foetal beats are still completely buried by the residual noise, being their R-peak locations hardly recognized or missed by the proposed algorithm.

3.4.2 Algorithm performance on real signals

Results obtained on real dataset are reported in Figures 3.7 and 3.8 and Table 3.1. Specifically, Figure 3.7 reports the overall foetal R-peaks detection performance offered by the proposed approach, the Jamshidian-Tehrani and Sameni [158] algorithm, and those achieved on the NI-fECG signals extracted by Matonia *et al.* [161] across all the different channels and pregnancies.

As can be seen from this Figure and Table 3.1, the proposed algorithm offered very good performance in foetal R-peak detection, even when compared with effective state-of-the-art fECG extraction algorithms. Specifically, from Figure 3.7 it is evident that the overall accuracy is

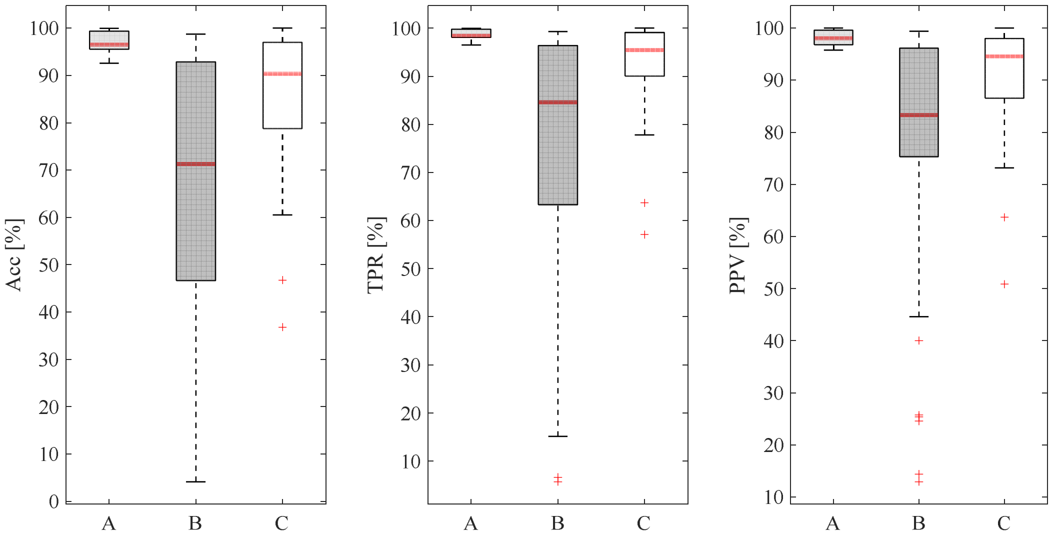

Figure 3.7. Results on the real dataset in terms of Acc, TPR and PPV achieved by the proposed approach (A, slight grey boxes), the Jamshidian-Tehrani and Sameni [158] algorithm (B, darker grey boxes), and those achieved on the extracted fECG signals by Matonia et al. [161] (C, white boxes) across all the different channels and pregnancies.

consistently above 90% (median Acc = 96.5%), a very high rate of positive predictions (median TPR = 98.4%) and high precision (i.e., median PPV = 98%), suggesting its potential effective exploitation in fHR monitoring devices. Same conclusions can be drawn from Figure 3.8, describing the fHR detection efficiency by the three examined approaches across the abdominal channels, by analysing the different pregnancies separately. In fact, it is clear that the proposed algorithm was able to guarantee stable values across the ten different analysed pregnancies, exhibiting mean Acc, TPR and PPV values above 92.5%, 96.5%, 95.7% respectively, in all examines cases (see Table 3.1). Furthermore, by looking at Figure 3.9, the capability of the proposed algorithm to recover high-quality morphology-preserved fECG signals can be visually appreciated, even when maternal and foetal cardiac cycles overlap.

3.4.3 Discussion

In this chapter, a novel multi-channel fECG extraction algorithm able to provide high quality signals for morphological analysis has been presented and assessed. Despite being less comfortable for the mother, a multi-channel NI-fECG monitoring would be an advantage with respect to single-channel or two-channels systems, allowing for a more accurate foetal cardiac assessment and providing many insights on the different cardiac projections. From our results on the synthetic dataset, it is evident that the proposed algorithm was able to recover high-quality, morphology-preserved fECG signals from non-invasive multi-channel abdominal recordings, even when the noise level was significantly high or maternal QRS complexes overlap with foetal ones. These findings are further confirmed when looking at Figure 3.5, in which the very high

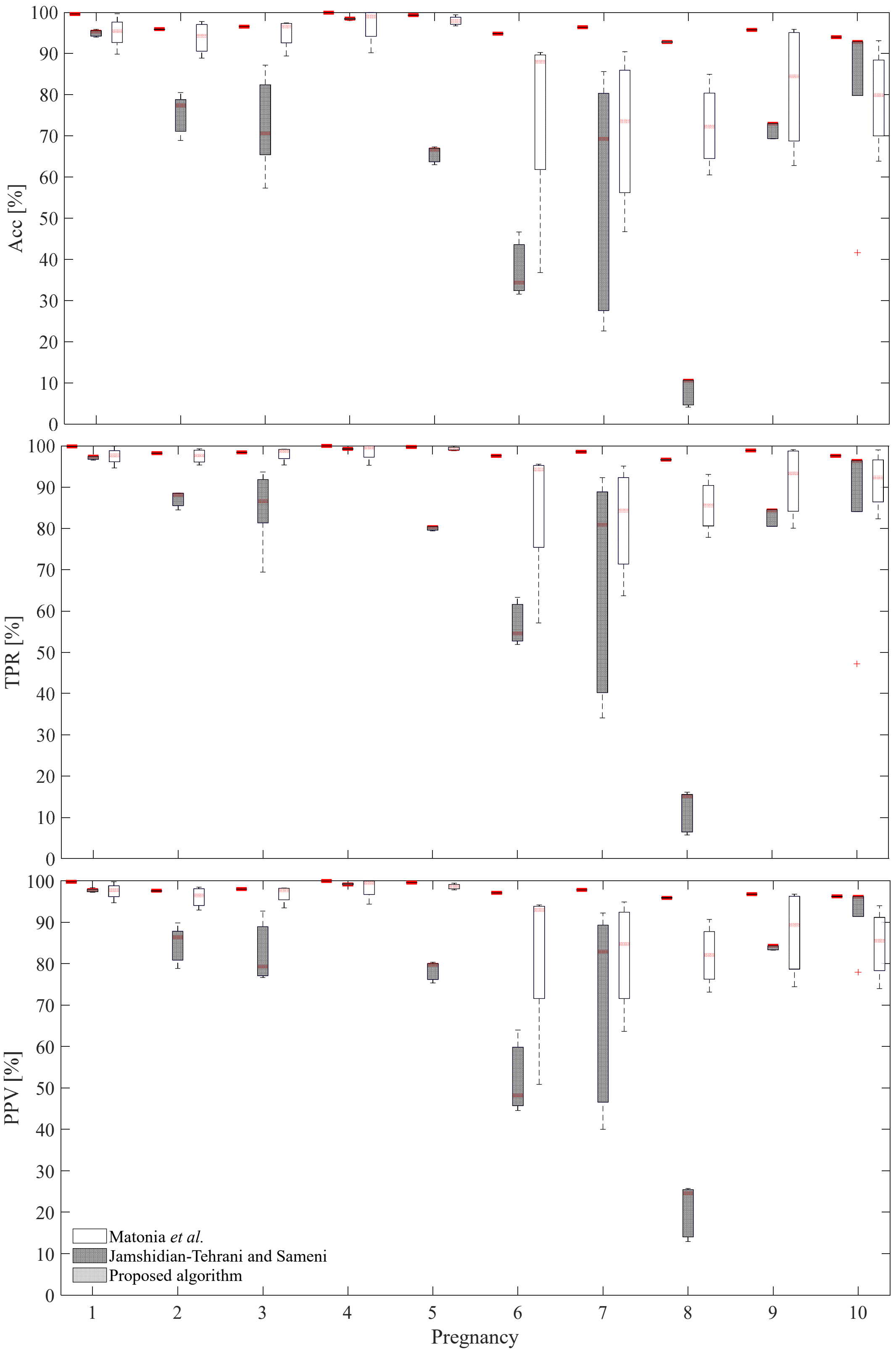

Figure 3.8. Results on the real dataset in terms of Acc (top), TPR (middle), and PPV (bottom), obtained by the novel proposed approach (light grey boxes), the Jamshidian-Tehrani and Sameni [158] algorithm (dark grey boxes), and those achieved on the extracted fECG signals by Matonia et al. [161] (white boxes) across the ten different analysed pregnancies.

Table 3.1. Results on the real dataset in terms of Acc, TPR, and PPV obtained by the proposed approach, the Jamshidian-Tehrani and Sameni [158] algorithm, and on the NI-fECG signals extracted by Matonia et al. [161], overall and across the ten different analysed pregnancies. Values are reported as mean ± standard deviation. For each case, highest values are presented in bold.

	Acc [%]										
	overall	*#1*	*#2*	*#3*	*#4*	*#5*	*#6*	*#7*	*#8*	*#9*	*#10*
Proposed algorithm	**96.7**	**99.6**	**95.9**	**96.5**	**99.9**	**99.3**	**94.8**	**96.4**	**92.8**	**95.7**	**94.0**
	±2.5	**±0.0**	**±0.1**	**±0.0**	**±0.0**	**±0.0**	**±0.0**	**±0.0**	**±0.2**	**±0.0**	**±0.0**
Jamshidian-Tehrani and Sameni [155]	66.4	95.0	75.4	72.8	98.4	65.6	37.6	57.1	8.2	71.5	82.5
	±28.3	±0.8	±4.8	±11.6	±0.2	±1.9	±6.7	±29.1	±3.4	±2.0	±22.9
Matonia *et al.* [158]	85.9	95.1	93.8	95.0	97.0	98.0	75.7	71.1	72.5	81.9	79.2
	±15.3	±4.0	±4.0	±3.8	±4.6	±1.1	±26.0	±19.2	±10.4	±16.0	±12.4
	TPR [%]										
	overall	*#1*	*#2*	*#3*	*#4*	*#5*	*#6*	*#7*	*#8*	*#9*	*#10*
Proposed algorithm	**98.6**	**99.8**	**98.2**	**98.4**	**100.0**	**99.7**	**97.6**	**98.5**	**96.6**	**98.9**	**97.6**
	±1.2	**±0.0**	**±0.0**	**±0.0**	**±0.0**	**±0.0**	**±0.0**	**±0.0**	**±0.1**	**±0.0**	**±0.0**
Jamshidian-Tehrani and Sameni [155]	75.4	97.1	87.1	85.2	99.2	80.1	56.7	67.5	11.8	82.9	86.6
	±26.8	±0.4	±1.8	±9.5	±0.1	±0.5	±5.1	±27.2	±5.1	±2.2	±22.0
Matonia *et al.* [158]	92.7	97.5	97.5	98.0	98.6	99.3	85.3	81.9	85.5	91.5	91.5
	±9.8	±2.2	±1.8	±1.8	±2.2	±0.5	±18.8	±13.8	±6.5	±9.1	±7.0
	PPV [%]										
	overall	*#1*	*#2*	*#3*	*#4*	*#5*	*#6*	*#7*	*#8*	*#9*	*#10*
Proposed algorithm	**98.0**	**99.7**	**97.6**	**98.0**	**100.0**	**99.6**	**97.1**	**97.8**	**95.9**	**96.8**	**96.2**
	±1.5	**±0.0**	**±0.1**	**±0.0**	**±0.0**	**±0.0**	**±0.0**	**±0.0**	**±0.1**	**±0.0**	**±0.0**
Jamshidian-Tehrani and Sameni [155]	76.2	97.7	84.7	82.7	99.2	78.4	52.3	70.4	20.6	83.9	92.5
	±24.3	±0.4	±4.5	±7.1	±0.2	±2.3	±8.5	±24.2	±6.4	±0.6	±8.1
Matonia *et al.* [158]	90.6	97.5	96.1	96.8	98.3	98.6	82.7	82.0	82.0	87.5	84.8
	±11.0	±2.1	±2.5	±2.2	±2.7	±0.7	±21.3	±13.8	±7.5	±10.7	±8.5

resemblance between the noiseless fECG and the recovered fECG is clearly evident, regardless of the noise level affecting the abdominal ECG trace.

Remarkably, the performance was evaluated by introducing realistic non-stationary noise with different amplitudes, which hampers a successful fECG extraction by typical processing methods as blind source separation algorithms. In this regard, as can be seen from Figure 3.4, a higher variability could be appreciated for the 9-dB synthetic subset. This aspect, despite unexpected, can be ascribed to the noise nature, which varies among the different simulated pregnancies despite same settings were imposed. Specifically, lowest values of Acc, TPR and PPV were found for the simulated pregnancy #2 belonging to the 9-dB subset, exhibiting much more correlated interferences which not only hamper the foetal R-peak detection of Step 7, but also impede an optimal fECG recovery, since they cannot be intrinsically suppressed by the nonlocal median

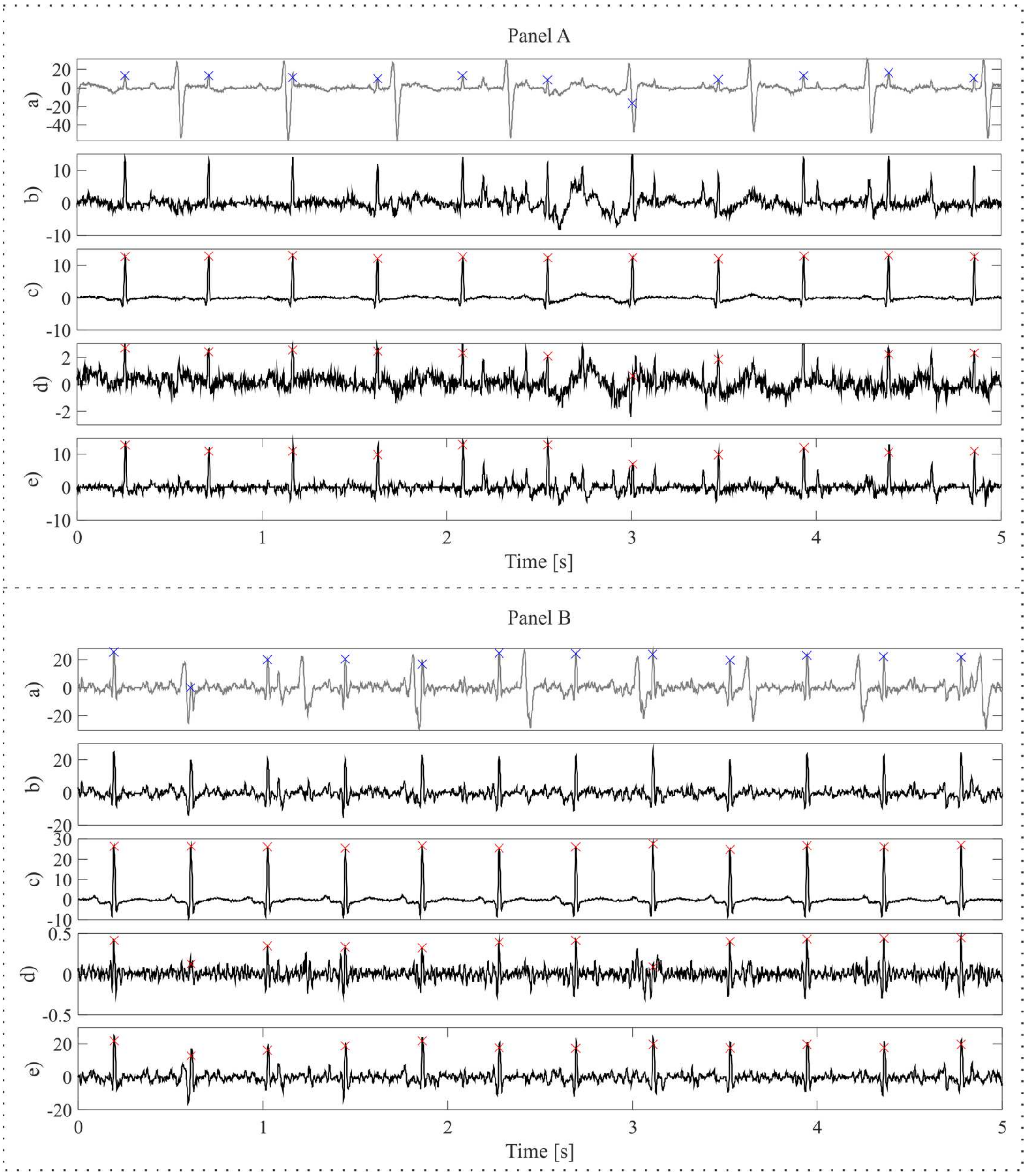

Figure 3.9. A 5-s zoom on two examples of real recordings acquired from two different pregnant women (in Panel A and B, respectively). Specifically, in each panel, the pre-processed trans-abdominal ECG signal (a), in grey) with the provided foetal R-peak annotations (a), blue crosses) are depicted, along with the corresponding accurate fECG extracted by the proposed method (b), in black) and the optimal fECG extracted by the proposed method (c), in black) obtained by the proposed algorithm, the fECG extracted according to Jamshidian-Tehrani and Sameni [158](d), in black) and provided by Matonia et al. [161] (e), in black). Red crosses identify the foetal R-peaks detected by the proposed approach. All amplitudes are reported in μV. However, different limits on amplitudes are offered, especially for (a) and (d), to allow a proper visual inspection of all the signals.

technique, since they cannot be completely considered as random noisy fluctuations with respect to the foetal cardiac cycle. As such, this correlated noises not only hamper the identification of a clean morphology, but also affect the SVD-based foetal R-peak identification, thus leading to uncorrected foetal beat template locations. In conclusion, this problem influences both results in terms of foetal R-peak detection and morphology preservation, deserving further investigations. For the sake of the completeness, two examples of fECG recovered from this subset are reported in Figure 3.6.

As regards the real dataset performance, although the recovered fECG morphologies can be qualitatively inspected, as in Figure 3.9, an effective and quantitative morphology-preservation assessment could not be enabled because of a missing ground truth on both waveforms and cardiac intervals. In this regard, many different algorithms have been proposed [25], [79], [80], [89]–[98], as already detailed in Section 1.4.1. However, a direct comparison with them is hampered by the adoption of different real datasets in their evaluation. Indeed, only in [165] the Matonia *et al.* antenatal NI-fECG dataset was exploited, but for a fHR detection algorithm assessment, thus diverging from the objective of this work. As such, two promising state-of-the-art fECG extraction algorithms were selected for the comparison. Remarkably, the proposed algorithm performance overcomes that offered by the Jamshidian-Tehrani and Sameni approach [158], and by Matonia *et al.* [161], not only in terms of Acc, but also in terms of PPV and TPR. Furthermore, from Table 3.1 and Figure 3.8, it is noteworthy that high-quality fECG signals were extracted by the proposed algorithm in different real scenarios, specifically even when the fECG level was much lower than noisy interferences, as for pregnancies #8 and #9 showing a mean foetal-to-noise SNR equal to -1.6 dB and -0.7 dB respectively, according to [161], and in those trans-abdominal recordings in which the mECG content was significantly higher than fECG one (i.e., for pregnancies #1 and #9 showing a mean maternal-to-foetal SNR equal to 11.1 dB and 17.7 dB respectively, from [161]), thus proving its potential usefulness also in inconvenient and troublesome long-term monitoring applications.

A few limitations on these results should be considered. First, the lack of a clinical validation of the recovered fECG morphologies. Second, despite the algorithm performance was examined on a real antenatal dataset, no assessment was performed in case of foetal arrhythmias or fECG morphology alterations, thus impeding the assessment of the proposed algorithm on unhealthy foetuses. Furthermore, due to the limited size of the analysed datasets, no statistical analysis was performed in this investigation, thus our results were not corroborated from a statistical perspective.

Chapter 4

Wavelet-based algorithms for non-invasive foetal ECG post-processing: materials and methods

4.1 Rationale

As discussed in Chapter 2, despite the high number of techniques developed in the literature for NI-fECG processing, the identification of a clean and undistorted fECG signal remains an open research issue [4]. Specifically, even after powerful fECG extraction algorithms, a post-processing step could be required to enhance the fECG content. In this context, WD has been adopted so far for the improvement of the SNR, to achieve a better fECG signal morphology [104], [136]–[141], [144]–[151]. However, this technique has been generally applied simply to reduce noisy interferences after fECG extraction algorithms, but fundamental evidence about the different wavelet implementation choices and parameterizations cannot be found in the scientific literature. In the scientific papers reporting on the application of specific algorithms, the datasets are of different type and quality, either real or simulated, whenever specified, which hampers the identification of an effective wavelet methodology for NI-fECG post-processing applications and the possibility to perform a comparative appraisal. Only in [104] and [105], an analysis of different WD algorithms and parameters was presented, albeit giving quantitative noise removal indications only on a limited set of simulated ECG signals affected by additive white gaussian noise in the former, while on a single fECG trace affected by muscular or powerline interference in the latter. Hence, a methodological study on the effect of WD on the post-processing of real and synthetic NI-fECG signals was missing. Therefore, this study aims to perform such an analysis, trying to answer relevant questions related to the optimal choices in terms of the granularity in the sub-band decomposition and of the thresholds able to combine an effective denoising with the preservation of the morphology of the fECG signal. To this aim, moving from our preliminary investigations on the topic [142], the adoption of stationary wavelet transform (SWT) and stationary wavelet packet transform (SWPT) was explored with different deepness of decomposition, chosen according to the fECG spectral characteristics [166]. In order to assess the importance of the dependency between the scaling factors used in the threshold computation and the decomposition level, we also compared three thresholds taken from the scientific literature, either conventional [167], [168] and unconventional [169], proposing and assessing some possible adaptations to SWPT for the latter. The analysis was performed on real and synthetic datasets of fECG signals extracted from non-invasive abdominal recordings. Since in the literature disparate dataset have been exploited for the NI-fECG WD post-processing assessment, the adopted dataset has been freely released by our group for research purposes and can be used as a benchmark for fECG post-processing techniques [162].

4.2 Materials and methods

WD is a signal processing technique based on the so-called time-scale representation, provided by the wavelet transform (WT) [170], [171]. Among the different non-linear denoising techniques, WD is widely used in biomedical signal processing because of its good localization in the time and frequency domains. This feature is particularly useful when dealing with non-stationary signals, such as the biomedical ones [172], [173]. Moreover, it allows for noise removal when noisy interferences share the same spectral band of the signal of interest.

4.2.1 Background on wavelet denoising

The most widely used form of WT for fECG filtering is the discrete wavelet transform (DWT), which is characterised by a small distortion of QRS complex extremes [105]. It is based on the dyadic decomposition of the signal in sub-bands of different width [170]. It can be implemented by filter banks, including high-pass and low-pass filters whose definition is strictly associated with the chosen mother wavelet [170]. Such filters equally split in two the signal band: the outputs of this filtering step are known as *detail* and *approximation* at the first level and are associated with the higher and lower half-bands, respectively. Then, the same process is iteratively repeated on the output of the low-pass filter of the previous filtering step until the lowest frequency components, i.e., the approximation of the last level, cover the range between 0 and $f_n/2^l$, where f_n denotes the folding frequency and l the chosen decomposition level. While only the approximation coefficients are given as input for the subsequent filtering steps in the WT, both detail and approximation are decomposed at each level in the wavelet packet transform (WPT) [170], generating a complete decomposition binary tree with consequent sub-bands of the same width, equal to $f_n/2^l$. As such, by WPT, a finer time-frequency analysis is obtained, as can be seen in Figure 4.1.

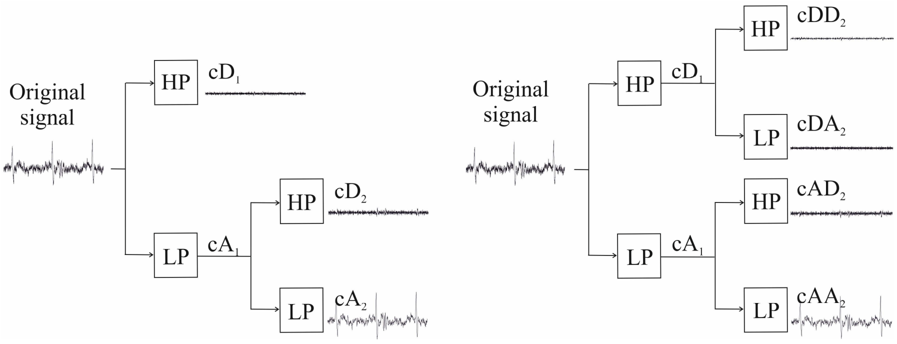

Figure 4.1. Example of 2-level decomposition of a real fECG signal (@2048 Hz) with WT (on the left) and WPT (on the right).

WD is essentially based on three main steps [170], [173]. In the first one (*analysis*), the signal is decomposed in a set of wavelet coefficients by WT; then, detail coefficients are compared to a threshold (*thresholding* phase), and those that exceed the threshold are used, along with the approximation, for time-domain reconstruction (*synthesis*). On the time-scale representation, the threshold is typically chosen to be proportional to the amount of noise, which, according to the noise affecting the signal of interest, can be estimated at each level by the robust median absolute deviation estimator, as [167], [168], [170], [174]:

$$\sigma_j = 1.4826 * median\left(\left|cD_j - \widehat{cD_j}\right|\right), \qquad (4.1)$$

where cD_j represents the detail coefficients at the j-th level while $\widehat{cD_j}$ represents their median value. Aside from σ_j, the threshold is defined by a scaling factor that may be fixed or level-dependent. For instance, the Universal and the Minimax thresholds [167], [168] reported in Equations 4.2 and 4.3 are largely adopted.

$$\theta_j = \sigma_j \sqrt{2ln(N)} \qquad (4.2)$$

$$\theta_j = \sigma_j(0.3936 + 0.1829\log_2(N)) \qquad (4.3)$$

Both thresholds depend on the signal length N. Once the threshold is computed at each detail level, different thresholding approaches can be implemented, but the most typical ones are the so-called hard thresholding and soft thresholding [167], [168], which are respectively defined as:

$$\overline{cD_{j,k}} = \begin{cases} cD_{j,k} & if \ |cD_{j,k}| \geq \theta_j \\ 0 & otherwise \end{cases} \qquad (4.4)$$

$$\overline{cD_{j,k}} = \begin{cases} sign(cD_{j,k})(|cD_{j,k}| - \theta_j) & if \ |cD_{j,k}| \geq \theta_j \\ 0 & otherwise \end{cases} \qquad (4.5)$$

where $cD_{j,k}$ is the k-th detail coefficient at level j, and θ_j is the threshold value calculated for the same level.

4.2.2 Wavelet denoising algorithms and parameterizations analysed

In WD algorithms, at each step, different implementation choices can influence the denoising result. In this study, some of these choices have been made basing on preliminary investigations, literature evidence or considerations associated with the specific problem of fECG denoising.

At first, the choice of the mother wavelet affects the WD output. During a preliminary investigation with different mother wavelets, as confirmed by other studies [175], the Haar mother wavelet achieved better results. Thus, it was selected for this work, also taking into account its smallest support, the simplicity of the coefficients of its filters and the associated advantages in any real-time implementation. Moreover, also hard-thresholding was selected to avoid the shrinkage effect associated with soft-thresholding, which reduces the amplitude of the denoised signal and negatively affects the quality indexes that could be adopted for the performance assessment. Finally, among the different implementations of the DWT, the SWT was chosen a priori because of its translation-invariance property [170], [176]–[178]. For the same reasons, the SWPT [179], [180] was used for the wavelet packet.

Conversely, different parameterizations algorithms have been compared and tested, whose impact on the denoising process was unpredictable and worth to be analysed, also deepening the motivations behind them. As regards the decomposition level, only two different parameterizations were tested: six and seven levels, on the basis of the frequency contributions of major interest for foetal QRS complexes (8–20 Hz) [78] and the sampling frequency of the adopted signals, which was equal to 2048 Hz. In 7-level decomposition, WD was performed from 1024 Hz down to 8 Hz (because details at level seven, cD_7, spread over the 8–16 Hz band); in 6-level decomposition, the lower limit for the details was 16 Hz (because the last detail, cD_6, spans over the 16–32 Hz band). As in every conventional WD algorithm, the approximation band was maintained without changes, so the low-frequency components associated with the other fECG waves are preserved by construction. In WD, the selection of the threshold is particularly relevant since it determines the aggressivity of the denoising [105] and, therefore, the output SNR but also the degree of morphological distortion. In this regard, the predominant presence of noise was assumed to be at high frequencies, whereas a more significant signal content was assumed at low frequencies. For these reasons, we decided to test a threshold proposed by Han *et al.* in [169] for chaotic time series, defined in Equation 4.6.

$$\theta_j = \begin{cases} \sigma_j\sqrt{2\ln(N)} & j = 1 \\ \sigma_j\sqrt{2\ln(N)}\,/\ln(j+1) & 1 < j < L \\ \sigma_j\sqrt{2\ln(N)}\,/\sqrt{j} & j = L \end{cases} \tag{4.6}$$

This unconventional threshold was conceived to perform a more aggressive denoising at higher frequencies while being more conservative at lower ones. The Han *et al.* threshold was compared to other conventional thresholds whose adoption is widespread in ECG signal processing, i.e. the Universal and the Minimax (reported in Equation 4.2 and 4.3, respectively) [167], [168]. Beyond the three thresholds and the two different levels of decomposition, a key aspect of this study was the assessment of SWT vs. SWPT. This is an interesting point, since the latter presents a finer granularity in the decomposition than the former, thus allowing for a more precise analysis of the signal, which is divided in equally sized sub-bands. Despite its use in different application fields and the aforementioned potentialities, SWPT, and more generally the WPT, was never used in fECG signal processing so far. A tentative approach was proposed only in [181] for powerline interference removal. However, to study its applicability to the fECG post-processing denoising, the adaptation of the Han *et al.* threshold was required, since this threshold was never used along with WPT and it is based on a level-dependent scaling factor of the estimated noise. Conversely, the transposition to the SWPT is direct for the Minimax and the Universal thresholds, by simply evaluating σ_j at each detail node. Therefore, three different adaptations of the Han *et al.* threshold for WPT, detailed in the following section, were compared and the best performing one was adopted for the comparisons with the SWT.

4.2.2.1 Proposed adaptation of the Han et al. threshold to WPT

The Han *et al.* threshold [169], which was originally conceived for DWT, uses a different scaling factor at the different levels (see Equation 4.6), which in turn implies a bind between the scaling factor of the threshold and the spectral band of the details. Therefore, it was required to assign a scaling factor to each of the sub-bands of the SWPT decompositions. Three approaches were conceived, with a growing aggressiveness in terms of denoising. For all of them, σ_j was evaluated at each detail node.

In the first approach, hereinafter referred to as SWPT-LI, a simple linear interpolation was adopted to properly identify a scaling value for each SWT node. Specifically, considering the scaling factor values defined for the SWT nodes (i.e., black circles in Figure 4.2), missing values for intermediate SWPT nodes were deduced by linear interpolation between consecutive SWT nodes enclosing them (as reported by black dotted line in Figure 4.2). To be more conservative, the original SWT scaling values were assigned to the SWPT node at the highest frequency in the range corresponding to that SWT detail sub-band. For example, by considering a 7-level decomposition as in Figure 4.2, SWT details at level three, cD_3, spread over the 32–64 Hz band, while in the SWPT case the same band is covered by node #4, #5, #6, #7. In order to identify the missing scaling values for the SWPT nodes, the scaling factor computed for SWT cD_3 was assigned to node #7, whereas the values for the remaining SWPT nodes were deduced by linear interpolation of the values assumed by node #3 and node #7. This is the most conservative threshold. In the second approach, hereinafter referred to as SWPT-CI, the missing threshold

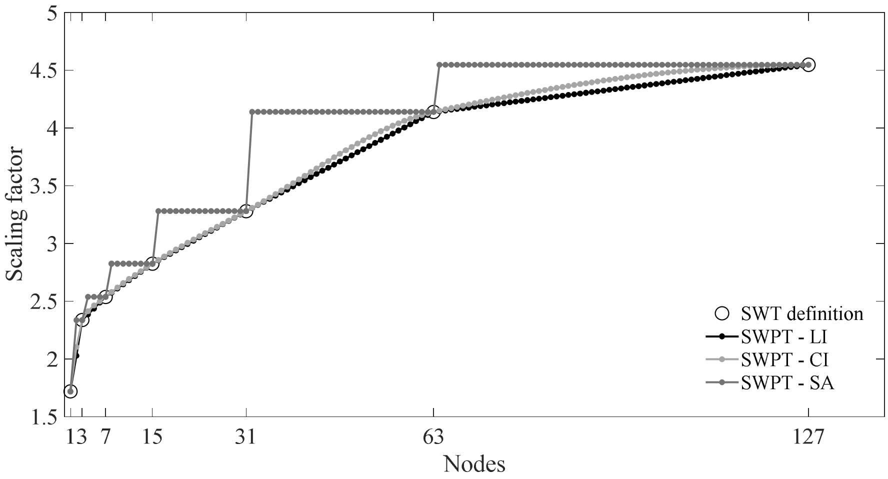

Figure 4.2. Comparison of the different scaling factors proposed to adapt the Han et al. threshold [169] to a 7-level decomposition with SWPT.

Black circles report the values for the SWT definition. The three SWPT adaptations, namely the linear interpolation (SWPT-LI, in black), the cubic interpolation (SWPT-CI, in light grey) and the spectral adaptation (SWPT-SA, in dark grey) are reported by putting in abscissa the SWPT nodes corresponding to specific spectral ranges: node 1 (8–16 Hz), node 3 (24–32 Hz), node 7 (56–64 Hz), node 15 (120–128 Hz), node 31 (248–256 Hz), node 63 (504–512 Hz) and node 127 (1016–1024 Hz).

values were interpolated by a piecewise cubic Hermite interpolating polynomial. Compared to the previous approach, the shape-preserving characteristic of this interpolation method allowed achieving a smoothly changing scaling factor across the different nodes of the SWPT decomposition. Finally, our approach introduced in [142] was evaluated, hereinafter referred to as SWPT-SA (for SWPT spectral adaptation). In this case, for each SWPT node, the definition of the scaling factor followed Equation 4.6 by considering as j the SWT detail level whose frequency band included that SWPT node. As can be seen in Figure 4.2, this approach is the most aggressive one.

4.2.3 Annotated real and synthetic datasets for non-invasive foetal electrocardiography post-processing benchmarking

A dataset composed of real and synthetic NI-fECG signals was created to perform the comparative assessment of the different WD methods and freely released [162]. The first subset of data was composed of physiologically plausible synthetic fECG signals uncorrupted by the maternal interference, whereas the second one was derived from real abdominal recordings after a fECG extraction processing based on an adaptive filtering. The two datasets allow studying different aspects of denoising. In fact, the signal distortion caused by WD can be evaluated only on the synthetic dataset, because a noise-free version of the fECG is available. However, such a dataset includes several ideal conditions that are not necessarily met at the output of a non-invasive fECG extraction method applied to real signals, motivating the adoption of a real dataset too. All real and synthetic data are meant to be used as a benchmark for fECG post-processing techniques, thus enabling the homogeneous analysis of different denoising algorithms, applied after the fECG extraction process, which was missing in the scientific literature. Moreover, these data can also be used as raw signals for the evaluation of different foetal QRS detection algorithms and fECG extraction methods, since both the corresponding real abdominal signals and the annotation of the foetal QRS complexes are provided.

The **synthetic dataset** included 40 fECG signals, generated with the *fecgsyn* open-source NI-fECG signal simulator [24], [25] at 2048 Hz, with a duration of 10 s each. By means of this tool, it is possible to generate several abdominal mixtures, selecting the beat-to-beat variability, heart rate baseline value and changes, $\mathrm{SNR}_{\mathrm{fm}}$, the $\mathrm{SNR}_{\mathrm{mn}}$, the position and orientation of the foetal and maternal hearts, foetal movements and uterine contractions. The toolbox calibrates the physiological and instrumental noise components with respect to the mECG signal by choosing the $\mathrm{SNR}_{\mathrm{fm}}$ and the $\mathrm{SNR}_{\mathrm{mn}}$. Specifically, this synthetic dataset was created by exploiting a new simulation with respect to the one introduced in Section 3.2.3, in order to obtain fECG signals affected by typical residual noises occurring after common fECG extraction algorithms as adaptive filters, and with similar duration with respect to the real case analysed in this chapter. Conversely, longer recordings and more channels were needed in the investigations performed in Chapter 3. As such, for the creation of the synthetic dataset adopted in this chapter, all parameters were selected in order to simulate physiologically plausible recordings and, wherever possible, in accordance with the real dataset acquisition setup. Specifically, the sampling frequency was set to 2048 Hz, as in the real dataset, and the signal duration to 10 s. The maternal and foetal heart rates were assumed to be fixed at respectively 90 and 150 bpm. The maternal heart coordinates were imposed equal to [2.0944, 0.2, 0.4] and those of the foetus to [–0.412, 0.284, –0.300], as in the previous chapter. The coordinates of the virtual surface electrodes detecting the abdominal ECGs were set to [-0.524, 0.500, -0.250] and [-0.785, 0.500, -0.250], which correspond to the schematic representation depicted in Figure 4.3. Virtual electrodes capture unipolar signals, referenced to a common GD electrode, so that a single differential lead was digitally created by subtracting the signal detected by the electrode 2 to the one detected by the electrode 1.

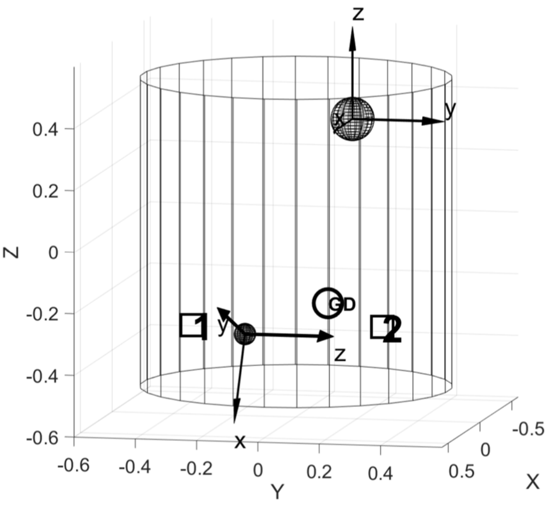

Figure 4.3. Graphical representation, provided by the fecgsyn tool, illustrating the virtual maternal torso, the location of the maternal heart (upper sphere) and the foetal heart (lower sphere). Squared boxes, located on the maternal abdomen, indicate electrode positions, and are numbered for the corresponding output channel. 1-2 represents the horizontal lead provided in this dataset, which simulates the horizontal lead adopted in the real dataset. The reference electrode is indicated by the GD circle, approximately placed on the back.

By construction, the differential horizontal abdominal lead was obtained completely free of the mECG components, as it would happen when the signal is produced by a perfect NI-fECG extraction stage. For the same reason, we avoided adding realistic noise sources mimicking muscular artefacts, baseline wander and electrode movements. Conversely, white and pink noises created by using the OSET toolbox [163] were added to the abdominal lead, with amplitudes chosen according to the desired SNR. Since the *fecgsyn* tool does not allow to set directly the

SNR of fECG relative to noise, we set the SNR_{fm} to −18 dB, whereas SNR_{mn} was linearly varied in the range between 3 dB and 15 dB, thus producing the 40 synthetic signals released in this dataset (see Table 4.1). Two examples of the abdominal lead for two virtual foetuses included in this dataset are shown in Figures 4.4 and 4.5.

Table 4.1. SNR_{mn} values for all the signals composing the synthetic dataset.

Signal	SNR_{mn} [dB]	Signal	SNR_{mn} [dB]
Synth_FECG_1	3.00	Synth_FECG_21	9.15
Synth_FECG_2	3.31	Synth_FECG_22	9.46
Synth_FECG_3	3.62	Synth_FECG_23	9.77
Synth_FECG_4	3.92	Synth_FECG_24	10.10
Synth_FECG_5	4.23	Synth_FECG_25	10.38
Synth_FECG_6	4.54	Synth_FECG_26	10.69
Synth_FECG_7	4.85	Synth_FECG_27	11.00
Synth_FECG_8	5.15	Synth_FECG_28	11.31
Synth_FECG_9	5.46	Synth_FECG_29	11.62
Synth_FECG_10	5.77	Synth_FECG_30	11.92
Synth_FECG_11	6.08	Synth_FECG_31	12.23
Synth_FECG_12	6.39	Synth_FECG_32	12.54
Synth_FECG_13	6.69	Synth_FECG_33	12.85
Synth_FECG_14	7.00	Synth_FECG_34	13.15
Synth_FECG_15	7.31	Synth_FECG_35	13.46
Synth_FECG_16	7.62	Synth_FECG_36	13.77
Synth_FECG_17	7.92	Synth_FECG_37	14.08
Synth_FECG_18	8.23	Synth_FECG_38	14.38
Synth_FECG_19	8.54	Synth_FECG_39	14.69
Synth_FECG_20	8.85	Synth_FECG_40	15.00

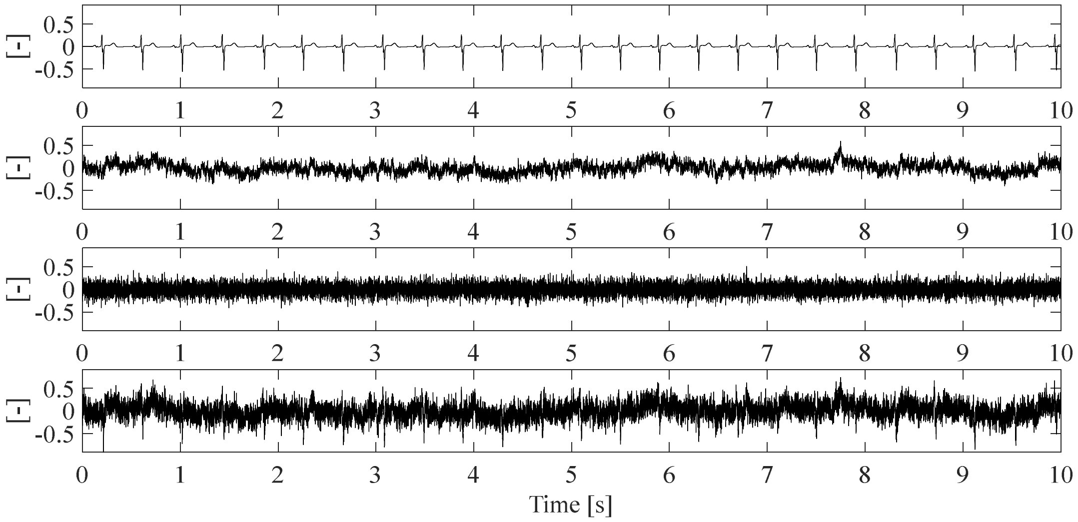

Figure 4.4. Example of the signals involved in the creation of a horizontal abdominal lead of the synthetic dataset, characterized by an SNR_{mn} of 3 dB. From top to bottom, the clean fECG signal, the pink noise, the white noise, and the noisy fECG signal obtained by their sum. Amplitudes are dimensionless.

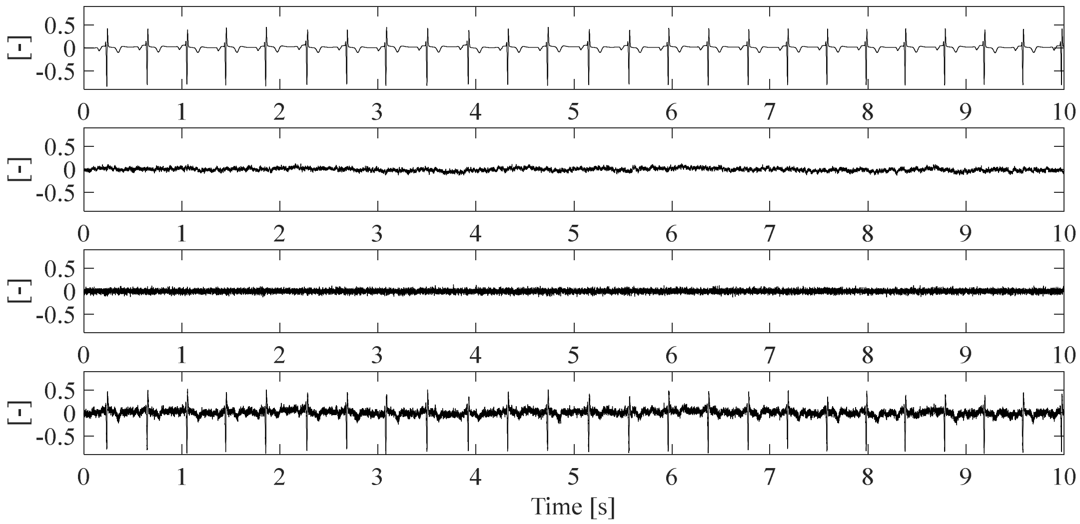

Figure 4.5. Example of a 15-dB horizontal abdominal lead of the synthetic dataset (lowest plot) along with the three components giving rise to it: the pure foetal ECG signal (upper plot), the pink noise (second row) and white noise (third row). Amplitudes are dimensionless.

Since this investigation was carried out before public availability of the dataset [161] adopted in Chapter 3, a different real dataset was used [162]. Such a **real dataset** included 42 fECG signals, that were extracted from non-invasive recordings from 17 pregnant women with healthy foetuses between the 21st and 27th weeks of gestation (see Table 4.2) and sampled at 2048 Hz, with a duration of 15 s each. The real dataset was acquired at the Division of Paediatric Cardiology, San Michele Hospital, Cagliari (Italy) by our group. The recording protocol was approved by the Independent Ethical Committee of the Cagliari University Hospital (AOU Cagliari) and performed following the principles outlined in the Helsinki Declaration of 1975, as revised in 2000. The volunteers provided their signed informed consent to the protocol. The recordings were carried out with the patient in a comfortable semi-sitting position. Before applying the electrodes, mild skin treatment was performed on the maternal abdomen by using an abrasive gel (NuPrep, Weaver and Company, USA) to reduce the skin contact impedance. The signals originated from 17 pregnant women satisfying the inclusion criteria during the dataset acquisition time frame, i.e. healthy foetuses between the 21st and 27th weeks of gestation. For each voluntary woman, only one recording session was performed, from which the good-quality abdominal signals' segments were extracted. The gestational epoch was selected to have the best morphological accuracy for the transabdominal signals. Specifically, the lower limit is due to the small size of the foetus heart, that cannot guarantee a good signal acquisition, whereas the upper limit allows reducing the influence of the vernix caseosa, completely covering the foetal skin between the 28th to the 32nd week of gestation [102]. In fact, as already discussed in Section 2.1, during this time frame, the fECG signal propagation towards the maternal abdomen is hampered, making the foetal signal hardly detectable with surface electrodes. After the 32nd week of gestation, this layer usually partially disappears but the morphology of the NI-fECG signal is questioned [103].

The biopotentials were recorded with the Porti7 portable physiological measurement system (TMSi, The Netherlands) with 22 bits of resolution (71.5 nV amplitude resolution) and choosing a sampling frequency set at 2048 Hz. The biopotential measurement system is characterized by an input bandwidth limited by a digital decimation filter to approximately 550 Hz (0.27x the sampling frequency). Moreover, it featured both differential and unipolar channels, and every unipolar channel is acquired with respect to the average of all the unipolar channels applied on the body so that the SNR of the raw signal is influenced by the number of used channels in the measurement. Three differential channels were used on the maternal thorax for the acquisition of

Table 4.2. Real dataset relevant anamnestic information (foetal presentation: L: left, R: right, O: occiput, S: sacrum, T: transverse, P: posterior A: anterior) along with the abdominal leads chosen for this study. Abdominal signals acquired from the same foetus are grouped together in the same row.

Real signal	Week of gestation	Foetus presentation	fECG channel 1	fECG channel 2
Real_FECG_1	24	breech, LST	horizontal	oblique
Real _FECG_2				
Real _FECG_3				
Real _FECG_4	21	breech, RSP	horizontal	vertical
Real _FECG_5				
Real _FECG_6	24	breech, RSP	horizontal	oblique
Real _FECG_7	26	vertex, ROP	vertical	oblique
Real _FECG_8	25	breech, RSP	horizontal	oblique
Real _FECG_9	25	vertex, ROP	horizontal	oblique
Real _FECG_10	24	vertex, LOP	horizontal	vertical
Real _FECG_11	21	breech, RSP	horizontal	oblique
Real _FECG_12	25	breech, RSP	horizontal	oblique
Real _FECG_13	24	breech, LSP	horizontal	vertical
Real _FECG_14	24	breech, LSP	horizontal	oblique
Real _FECG_15	21	vertex, OP	vertical	oblique
Real _FECG_16				
Real _FECG_17	22	breech, LSP	vertical	oblique
Real _FECG_18	24	vertex, LOP	vertical	oblique
Real _FECG_19	26	vertex, ROP	horizontal	oblique
Real _FECG_20	25	breech, LSP	vertical	oblique
Real _FECG_21	23	vertex, LOP	vertical	oblique

a reference mECG, whereas 24 unipolar channels were used on the abdomen, in order to have the highest possible SNR on the abdominal signals in terms of common-mode rejection. Among the unipolar channels, only three of them, clearly indicated in Figure 4.6, were selected to give rise to three abdominal differential leads digitally, such as 1–2 to obtain a horizontal lead, 2–3 to obtain a vertical lead and 1–3 to obtain an oblique lead.

Among the various methods available for the extraction of the fECG from non-invasive recordings, we chose to exploit a high-performance multireference QR-decomposition with back-substitution recursive least-squares (QRD-RLS) adaptive filter, available from the authors of [182], given its numerical stability and good performance [118]. Adaptive filters are not able to

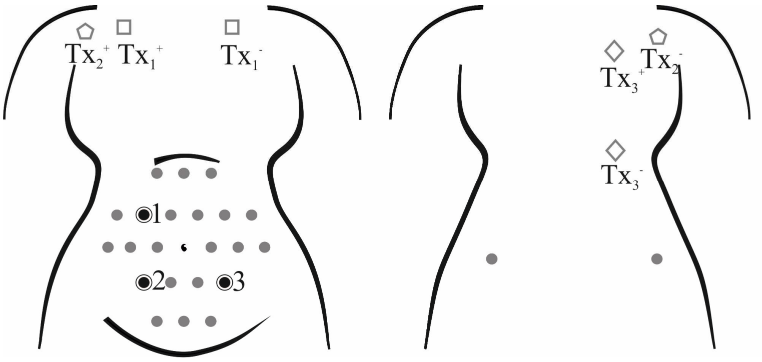

Figure 4.6. Electrode positioning for the real dataset acquisition. Circles indicate the electrodes utilized for unipolar recording while squares, pentagons, and rhombuses the electrodes for thoracic bipolar ones. Specifically, black circles represent the unipolar electrodes selected for the construction of the differential abdominal leads.

reject noise sources not in common with the reference channels and, as such, they demand a post-processing denoising stage more than other techniques. Compared to other approaches, such as blind source separation [183], [184], adaptive filters are real-time algorithms able to extract the fECG from a reduced number of abdominal electrodes, which can be useful for wearable systems [185] and real-time embedded platforms [184]. The three thoracic leads were used as reference signals in order to produce a good representation of the mECG on the abdomen. The forgetting factor λ was set to 0.999 while the number of filter coefficients was set to 20, in accordance with previous studies [159]. Considering that the recording device adopted for the raw data collection was DC-coupled, all the leads were pre-processed to reduce the baseline wandering artefact in order to facilitate the QRD-RLS adaptive filter processing. In fact, such an artefact appears in different forms in the various leads and cannot be reduced by the application of the adaptive filter. Pre-processing consisted of a high-pass linear-phase equiripple FIR filter with a cut-off frequency of 1 Hz. Compared with the current guidelines that would impose a 0.67 Hz limit for the cut-off frequency of ECG signals [186], some studies on non-invasive fECG proved that a higher cut-off frequency of the high-pass filter allows achieving better results, still preserving the low-frequency components of the ECG, mainly related to P and T and to the ST segments [159]. Remarkably, the frequency range affected by this pre-processing stage does not interfere with the assessment of the WD approaches but only with the fECG extraction process, since the removed frequencies would lie in the approximation band which is not affected by the denoising. For the sake of completeness, the whole processing chain used to extract the fECG is presented in Figure 4.7.

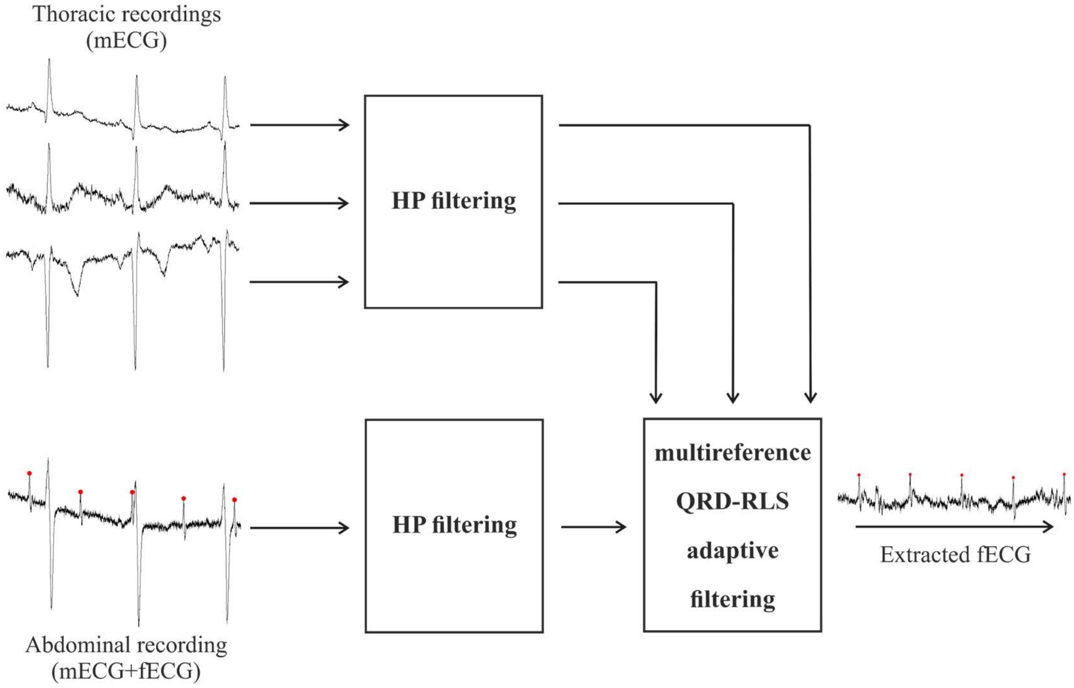

Figure 4.7. Schematic representation of the whole processing chain for fECG extraction. Three thoracic leads along with each abdominal trace are pre-processed with a high-pass (HP) filter with a cut-off frequency of 1 Hz and passed to the QRD-RLS adaptive filter for fECG extraction. Red dots mark the foetal QRS complexes.

The annotation of the real foetal QRS complexes was performed manually and validated by an expert paediatric cardiologist with the help of a simultaneous cardiac foetal pulsed-wave Doppler signal recorded during the procedure, thus providing a mechanical reference for the electrophysiological signal. Despite the low SNR of some real traces, the presence of three different simultaneous abdominal leads (horizontal, vertical, and oblique) helps the R-peaks annotation, enabling the identification of clear foetal R peaks at least in one good-quality trace. The annotation procedure was verified before and after the fECG extraction process to provide the most accurate indication of the foetal QRS complexes. Some examples of the extracted fECG are shown in Figure 4.8. From this inspection, it emerged that some extracted fECG channels were unreadable, from a clinical perspective. In order to use the same number of leads for each recording, the best two fECG traces per recording were selected to be released and exploited in the NI-fECG post-processing study (see Table 4.2).

For the computation of the WD threshold according to the different methods presented in Section 4.2, for synthetic signals the noise level σ_j was evaluated on a segment presenting only noise, i.e. approximately each interval between two foetal beats, since the mECG was not present. On the real dataset, the noise level σ_j in the different sub-bands was hampered by the possible presence of mECG residuals after the fECG extraction. In this case, a part of the signal representative only of the noise could be identified on the fECG leads between the time instants comprised between the end of a maternal T wave and the beginning of the maternal P wave of the next beat (delineated in a thoracic lead, where only the mECG is visible, by using the algorithm presented in [187]). This avoided considering maternal components in noise estimation. However, such signal segments were excluded in the presence of a foetal QRS complex in that interval.

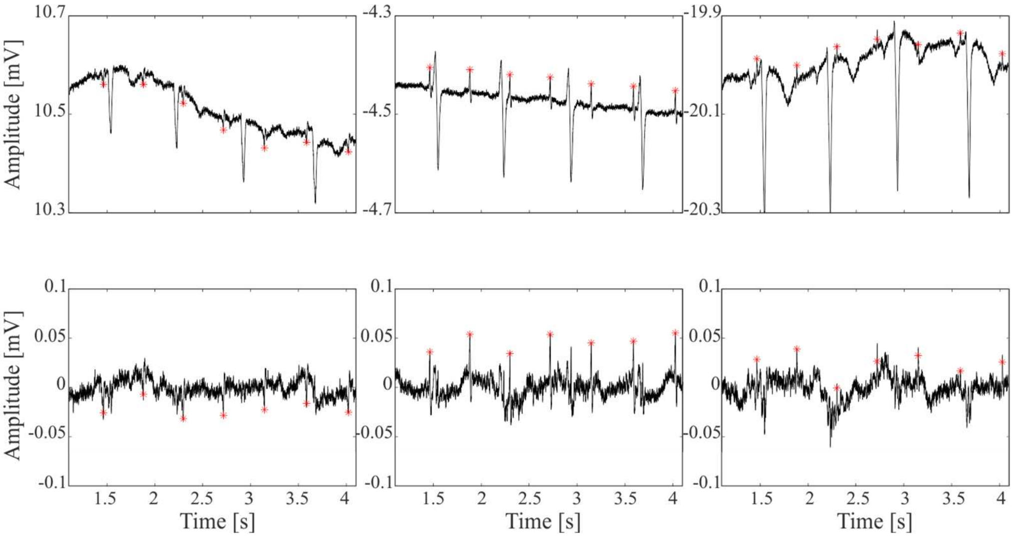

Figure 4.8. Example of raw abdominal traces (upper plots) and the corresponding extracted foetal ECG signals (lower plots). From the left to the right: horizontal, vertical, and oblique leads. Red markers indicate the manually annotated foetal R peaks.

4.3 Methods for the comparative analysis

The different parameterizations of the WD methods assessed in this NI-fECG post-processing study are summarised in Figure 4.9. In this regard, the performance of the different WD approaches and parameterizations were systematically analysed by exploiting several indexes: the SNR, the foetal QRS detection Acc, and the foetal QRS detection TPR, or Sensitivity. On the synthetic dataset, the following indexes were also evaluated: the RMSE, the ρ and the r_s.

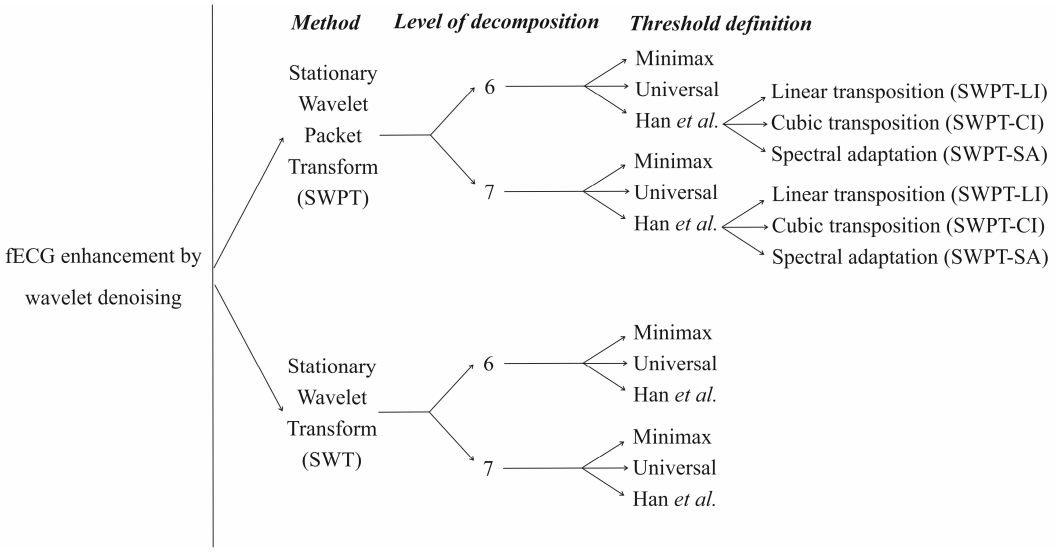

Figure 4.9. All the wavelet parameterizations investigated in this study. Two translation-invariant wavelet transforms (SWT and SWPT) along with two different decomposition levels (six and seven) and three thresholds (Minimax, Universal, Han et al. [169]) were assessed and compared. Specifically, due to its level-dependent scaling factor, three different SWPT transpositions were proposed and evaluated for the Han et al. threshold (SWPT-LI, SWPT-SA, SWPT-CI).

The SNR is widely used to evaluate the quality of the trace in terms of power in the signal of interest and the noise sources. It was computed as:

$$SNR_{dB} = 20log_{10}(App_f/4\sigma) \qquad (4.7)$$

where App_f is the peak-to-peak amplitude of the fECG and σ is the standard deviation of the noise. For the sake of the SNR calculation only, the estimation of the standard deviation of the noise was conceived as the median of the standard deviations computed on each interval between two foetal beats. This approach considers the presence of both the noise and potential residual mECG (the latter only in the real dataset). Moreover, before the WD, we computed the App_f of a given signal on its average QRS complex, obtained by synchronized averaging, to reduce the inter-beat amplitude variability and the noise effect. On the simulated dataset, all foetal peaks were considered in the averaging since the signals were free from the mECG interference. In the real dataset, where mECG residuals could be present after the fECG extraction algorithm, the QRS averaging involved only those complexes exhibiting a Pearson's correlation coefficient ρ above a given threshold, empirically chosen to be 0.6. If the number of correlated beats was lower than four, the signal was treated as non-deterministic, then substituting App_f by the computation of four times the median standard deviation of such beats. To evaluate the SNR after the WD, we computed App_f as the median value of the peak-to-peak amplitudes of highly correlated beats or of all beats for real and simulated signals, respectively. In every case, the time support of the foetal QRS complex was considered equal to 40 ms, centred around the R peak. Taking into account that the measurement on the QRS complex is limited to its peak-to-peak-amplitude, the chosen size allowed including only the relevant parts of the complex, according to the literature [164]. Moreover, the adoption of a larger time frame would not change the results unless for the possible inclusion of noise spikes. Since the denoising should in principle help a foetal QRS detection algorithm, another performance index considered in this work was the Acc and the TPR of a state-of-the-art peak detector [110], computed as in Equations 3.27 and 3.28, respectively. All these performance indexes are important on real recordings because the actual fECG waveform morphology is unknown, and it is impossible to assess the distortion introduced by the different post-processing methods. Conversely, this is possible on the simulated signals. To this aim, the RMSE, ρ and Spearman's rank correlation coefficient r_s were evaluated between each WD-processed simulated signal and the corresponding noiseless fECG signal. For each signal, considering an interval of 300 ms around each foetal R wave, 120 ms before and 180 ms after [164], the three indexes were computed for each beat and their median values were used as measures of signal morphology preservation, as in Chapter 3.

As regards the different comparisons between the WD methods along with the associated statistical analysis methodology, in order to reduce the number of comparisons, an assessment was preliminarily performed to identify the best adaptation of the Han *et al.* threshold to SWPT to be used for the subsequent analyses. To this aim, we compared all the available performance indexes computed on both datasets for each tested decomposition level. Then, we selected the best adaptation Han *et al*. threshold to SWPT for the subsequent analyses. At this point, we could consider three thresholds (Minimax, Universal and Han *et al.*) for each of the two WD methods (SWT and SWPT). On them, a statistical analysis was performed to investigate the following aspects:

(i) *WD effectiveness* in terms of SNR, Acc and TPR. The comparisons were performed by considering denoised signals vs. raw signals, on both datasets, separately for six and seven decomposition levels

(ii) *superiority of SWT or SWPT* in terms of SNR, Acc and TPR for both datasets and ρ, r_s and RMSE for the synthetic one only, for each decomposition level and threshold

(iii) *the best decomposition level* for a given method, i.e., by considering the comparison among SWPT or SWT approaches grouped by decomposition level. The analysis was performed on the same metrics as in (ii)

(iv) *the best WD approach* for each of the two decomposition levels by comparing the performance of a given method (SWT and SWPT) and threshold against all the other approaches available at that decomposition level. The analysis was performed on the same metrics as in (ii).

The schematic representation of the comparative assessments discussed above is depicted in Figure 4.10.

For the statistical analysis, the normality of the distributions was preliminarily investigated by using the Lilliefors test. If a result did not satisfy the assumption of a normal distribution, a non-parametric statistical test was adopted. In specific, we used the Kruskal–Wallis test when comparing more than two distributions whereas the Wilcoxon test when comparing two distributions only. When the results of the Lilliefors test did not reject the assumption of a non-normal distribution, we adopted the one-way ANOVA instead of the Kruskal–Wallis test and the Student's t-test instead of the Wilcoxon test. Bonferroni correction was applied only when the goal of the analysis was the identification of the best solution, i.e. for the analysis (iv). In all the statistical tests, we considered $p < 0.05$ for statistical significance. All data processing was performed in MATLAB v2018b (MathWorks Inc., MA, USA).

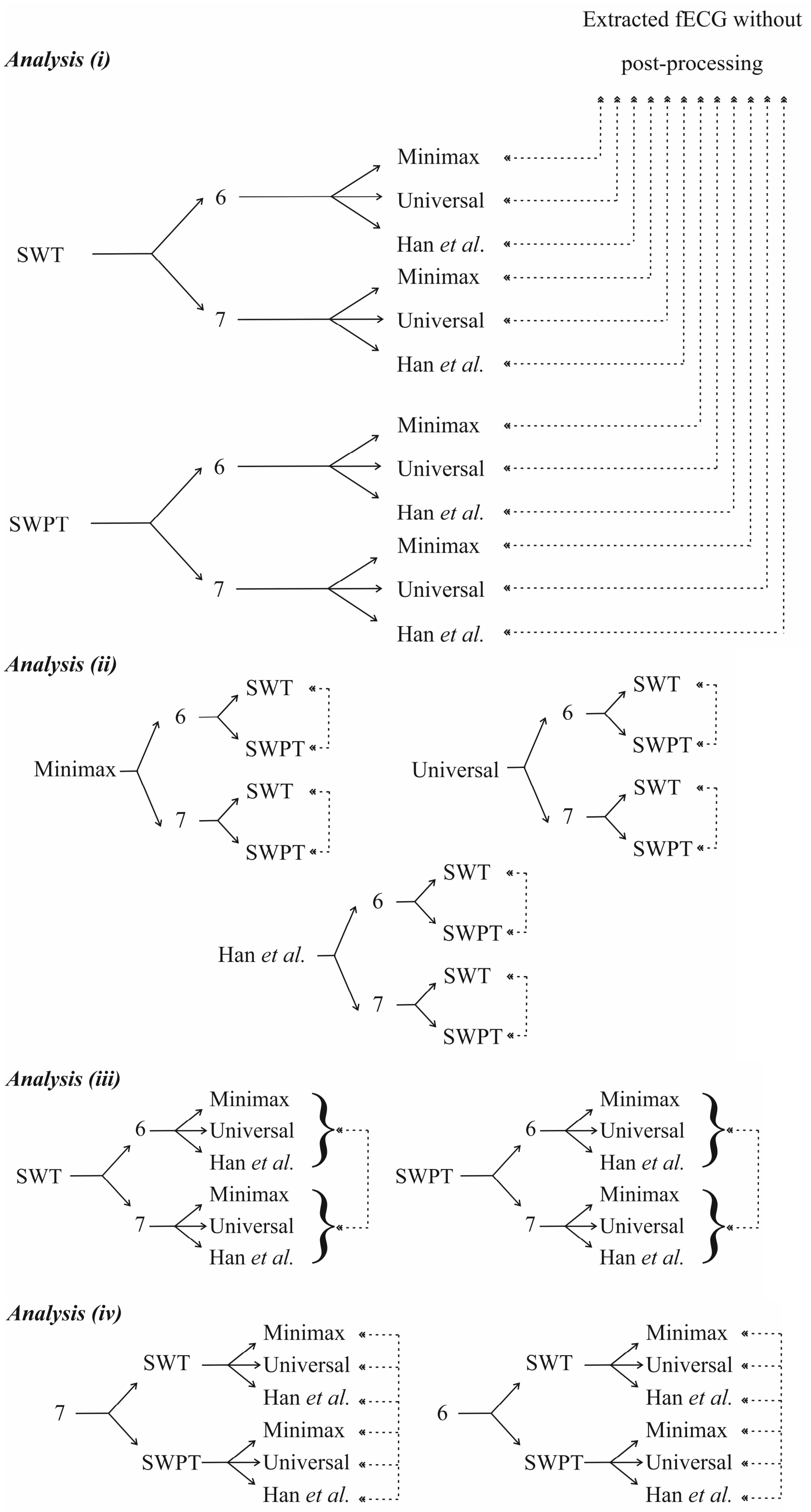

Figure 4.10. General scheme of all the comparative analyses performed in this work. Dashed arrows represent the different comparisons carried out whereas solid arrows the wavelet parametrizations involved in each analysis. Two wavelet transforms (SWT and SWPT), along with the chosen levels of decomposition (6 and 7) and three thresholds (Minimax, Universal, Han et al.) were included in the comparative analyses. For the Han et al. threshold, the best SWPT adaptation identified in this work is reported.

4.4 Results and discussion

4.4.1 Best adaptation of the Han *et al.* threshold to SWPT

The analysis aiming at identifying the best adaptation of the Han *et al.* threshold to SWPT did not reveal any statistically significant difference among the three proposed approaches on both datasets. However, all methods improved the quality of the signals in terms of SNR ($p < 0.05$ for the real dataset, $p < 0.0001$ for the synthetic one) and TPR for real signals ($p < 0.0004$) compared to the raw noisy signal, as can be seen in Figure 4.11, but not in terms of Acc in the QRS detection (data not shown). Despite the non-significant statistical difference, the SWPT-LI was selected for the subsequent analyses because it is simpler than SWPT-CI and exhibits qualitatively better performance than SWPT-SA in terms of SNR on real signals, as can be seen by looking at the SNR median values in Figure 4.11.

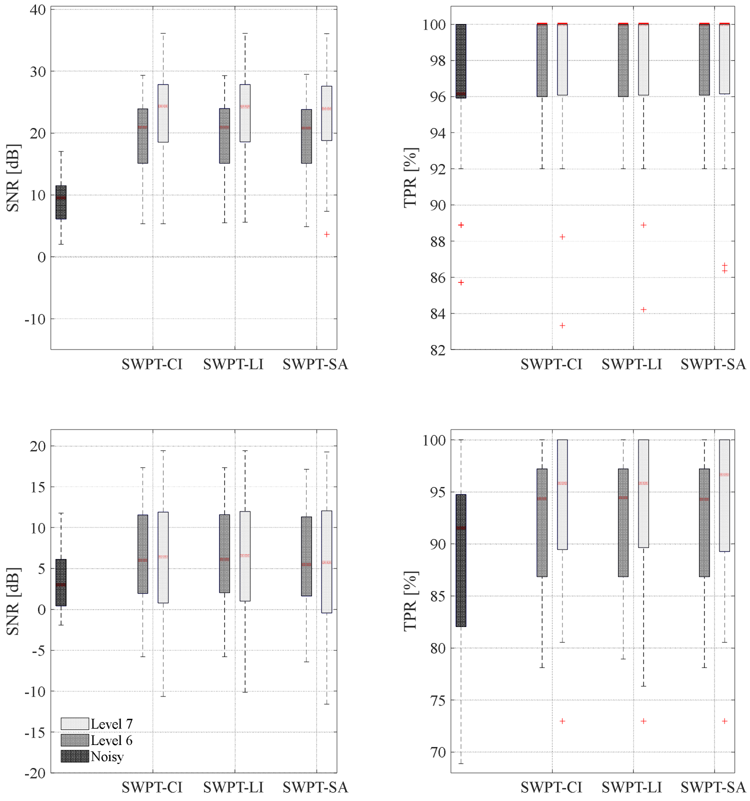

Figure 4.11. SNR and TPR performance indexes for SWPT-CI, SWPT-LI and SWPT-SA denoised fECG signals with 6-level or 7-level decompositions and for raw noisy fECG signals. Top: results on the synthetic dataset. Bottom: results on the real dataset.

4.4.2 WD effectiveness

As can be seen in Figure 4.12, the behaviour of WD algorithms with their various parameterizations was different for the synthetic and real dataset. On the former, the SNR was always significantly improved ($p < 0.0001$ and $p < 0.0004$, respectively for six and seven decomposition levels) whereas on the latter only the Han *et al.* threshold produced a significant improvement in terms of SNR ($p < 0.01$) with all the parameterizations. However, Minimax produced a significant SNR enhancement only with SWT ($p < 0.004$) whereas Universal generally produced a significant reduction of the SNR ($p < 0.04$, for all but the SWT with seven decomposition levels). Focusing on the accuracy in the QRS detection, although with 6-level

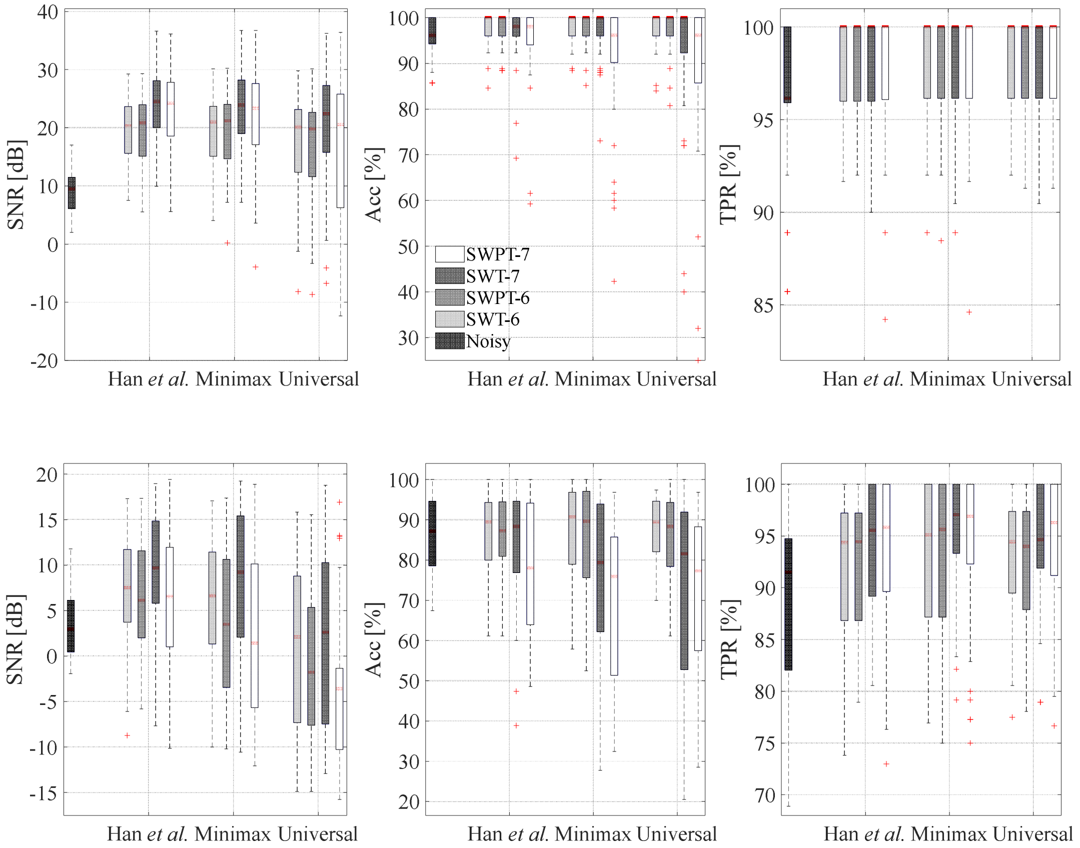

Figure 4.12. WD effectiveness in terms of SNR, Acc and TPR on the synthetic dataset (top) and the real one (bottom).

decompositions the median values of Acc for all the approaches exceeded those achievable on the noisy raw signals, no statistical significance was reached except for the SWT with Minimax on synthetic signals ($p = 0.04$). Moreover, with 7-level decompositions, WD significantly degraded the Acc with SWPT Universal and Minimax ($p < 0.04$), on the synthetic dataset, and with all the methods ($p < 0.02$) but the SWT Han *et al.* on the real one. Differently, TPR analysis showed that WD generally improved the QRS detector sensitivity with respect to the raw signals. On the real dataset, this was significant for all the algorithms ($p < 0.001$), whereas on the synthetic dataset statistical significance was achieved only by Minimax ($p < 0.03$ for both levels, SWT and SWPT) and Universal ($p = 0.02$, with 7-level SWT, and $p = 0.03$, with 6-level SWPT).

4.4.3 Superiority of SWT or SWPT

By exploiting the synthetic dataset, the results of this assessment in terms of the morphology preservation quality indexes are presented in Figure 4.13. Even though the results appear to be quite similar, the statistical analysis revealed significantly better morphology preservation by SWT with respect to SWPT in terms of ρ, RMSE and r_s ($p < 0.04$ for all thresholds and levels, except for the RMSE with Minimax at level six where no statistically significant difference was observed). Moreover, by considering the performance indexes reported in Figure 4.12, SWT was always superior in terms of SNR ($p < 0.0008$) on real signals, whereas on the synthetic ones this superiority was statistically significant ($p < 0.0003$) for Universal (both levels) and for Han *et al.* and Minimax (only for level seven). The same holds also for the Acc in all 7-level approaches on real signals, with a noteworthy improvement with Minimax ($p = 0.004$) and Han *et al.* ($p =$

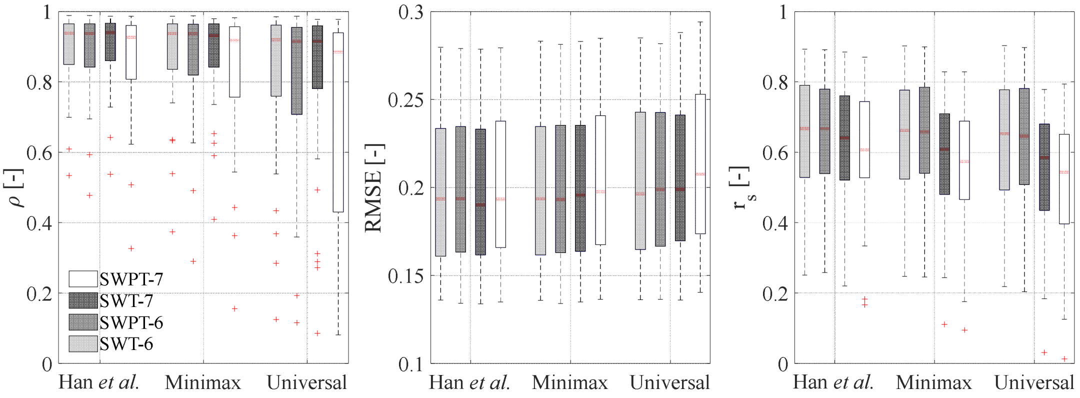

Figure 4.13. Results obtained with the three selected thresholds on the simulated dataset for both decomposition levels (six and seven) and WD methods (SWT and SWPT) in terms of morphology preservation. Specifically: Pearson's correlation coefficient (ρ), RMSE and Spearman's rank correlation coefficient (r_s) distributions are reported in the different analysed cases.

0.0009), and on synthetic signals for Minimax ($p = 0.0003$, level seven). No statistical difference was found in terms of TPR.

4.4.4 Best decomposition level

Figure 4.14 shows that six decomposition levels allowed reaching significantly higher r_s values on both SWT and SWPT ($p < 0.01$) on the synthetic signals. No other morphological performance indexes were revealing a statistically significant difference between the two methods. By looking at the other indexes, six decomposition levels were significantly better in terms of Acc for the SWPT only ($p = 0.003$) on the synthetic dataset and for SWT and SWPT on the real one ($p = 0.0006$ and $p < 0.0001$, respectively). Conversely, seven decomposition levels revealed significantly better results in terms of SNR for both SWT and SWPT ($p < 0.02$) on the synthetic dataset and only for SWT on the real one ($p < 0.05$). TPR followed a similar trend only on the real dataset ($p = 0.04$ and $p = 0.03$ for SWT and SWPT respectively).

4.4.5 Best WD approach

For the last analysis, every parameterization was compared with all the others, by keeping separate the different levels. On the synthetic dataset, the SWT with Han *et al*. threshold stood out as the best choice in 7-level decomposition in terms of ρ only ($p < 0.0001$ for all possible paired comparisons). On the real dataset, again SWT with Han *et al.* threshold outperformed all the other methods, this time in terms of SNR enhancement ($p < 0.003$) with both levels (Figures 4.12 and 4.13).

4.4.4 Discussion

The adoption of translation-invariant wavelet decomposition for noise reduction was already proven to be effective in fECG morphology preservation, both using complex wavelets [147] and comparing the same processing with the decimated WT [150] . However, focusing the attention on real WT only, no quantitative comparison can be found in the scientific literature for the fECG problem, since in [150] only simulated signals with unspecified characteristics and extracted by an adaptive neuro-fuzzy interference system (ANFIS) have been exploited. Moreover, even

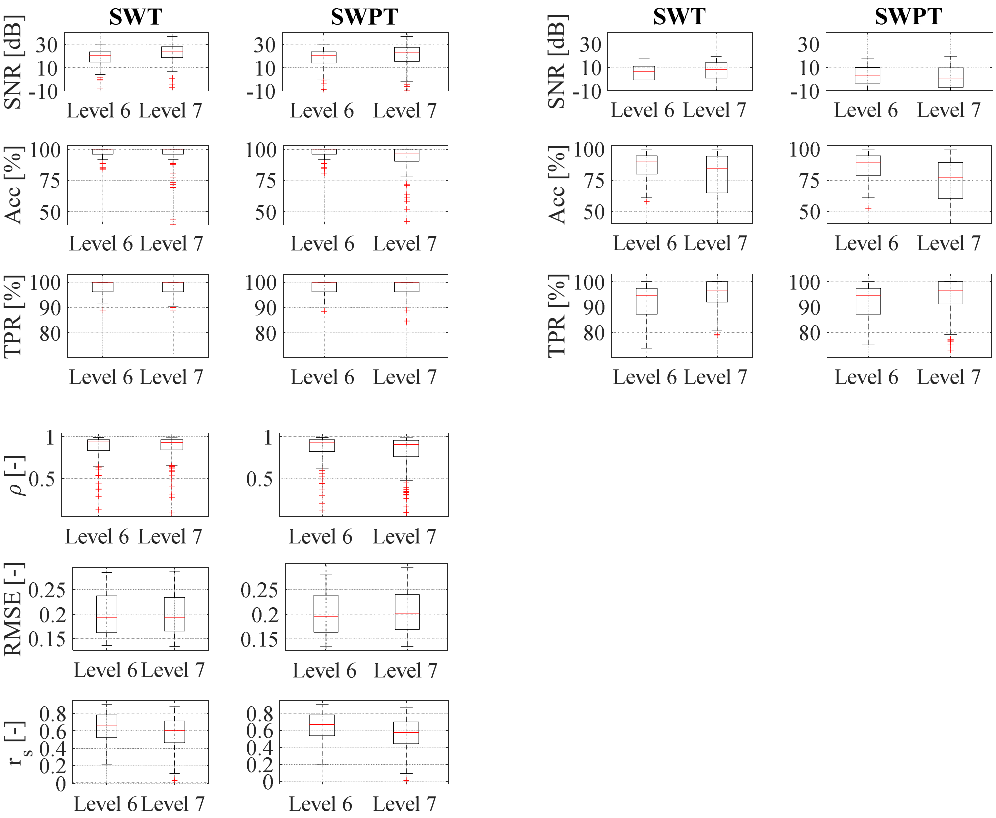

Figure 4.14. Results obtained on the simulated dataset (first two columns) and on the real one (last two columns) for 6-level (Level 6) and 7-level (Level 7) decompositions, grouping all approaches by SWT and SWPT. The considerable number of outliers is due to the heterogeneity of the grouped distributions.

though the SWPT was identified as a tool for powerline interference suppression on simulated fECG signals, albeit in an unconventional denoising approach [181], no previous work focused on its use on wide-band noise removal in fECG signals. Therefore, to the best of our knowledge, this study assessed in detail for the first time this kind of wavelet decomposition for fECG post-processing. Since one of the selected thresholds, the Han *et al.* one, was conceived for DWT and not for SWPT, three different adaptations to the SWPT were proposed and evaluated, which revealed a substantial equivalence from a statistical perspective. These findings confirmed the importance of WD as fECG post- processing tool. This result is in line with previous works, although in those cases WD was performed in different ways and after different fECG extraction algorithms [139], [144], [148], [151].

Moreover, the datasets that have been exploited in the related works [104], [136]–[141], [144]–[146], [148], [149], [151], both real and synthetic, were heterogeneous, so that a quantitative comparison with these results was not possible. Furthermore, a quantitative analysis of the post-processing results is frequently missing in the related works [140], [141], [148], [151] or a complete definition of the selected implementation choices is not clearly stated [136], [138], [145], [146], [148], [149]. Nevertheless, in [144] the effectiveness of WD as a post-processing tool for fECG signals was claimed, revealing how this technique could offer better performance in terms of fECG enhancement than its use as pre- processing or as both pre- and post-processing steps. However, the extraction process was carried out by a polynomial network and quantitative analysis was performed only on synthetic data in terms of SNR, whose improvement cannot be clearly quantified. A similar assessment was proposed in [139], where ANFIS was adopted as a separation algorithm. However, in this case, the adoption of WD is totally different from the typical use, retaining only the approximation coefficients and thus producing only a low-pass filtering behaviour. WD introduced an SNR improvement also in [145], where the extraction of foetal components was not performed due to the different recording system, and in [105], in which the WD noise removal was assessed on a single simulated trace affected by muscular or powerline interference. In the light of this scenario, our findings quantitatively revealed the performance of WD as fECG post-processing tool and, thanks to the open data availability [162], can provide a benchmark for other fECG post-processing algorithms. Moreover, our results can be generalised to different fECG recordings and projections, since our real dataset included different foetal heartbeat morphologies, as can be seen in Figure 4.15.

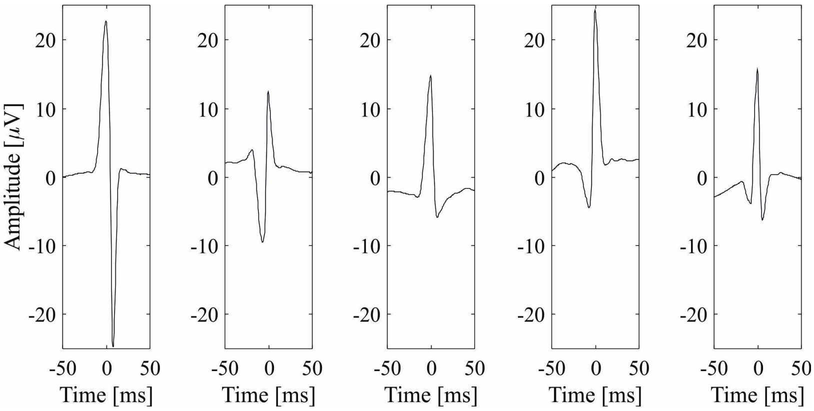

Figure 4.15. Main different foetal heartbeat morphologies from the real dataset obtained by synchronized averaging of the highly correlated beats (ρ > 0.6) after WD post-processing exploiting SWT with 7-level decomposition and Han et al. threshold [169].

From our results, it was clear that WD was generally unsuccessful in improving the accuracy of the foetal QRS detection, at least with the foetal QRS detector chosen in this work [110]. In fact, by focusing at first on the real signals, WD algorithms generally improved the accuracy of the foetal detection with 6-level decompositions, but not significantly, probably because of the high Acc values already achieved on the raw signals. On the other hand, forcing the denoising effect until 8 Hz (i.e. with 7-level decompositions), the accuracy performance was generally worse except for Han *et al.* threshold in SWT implementations. Nevertheless, the TPR analysis revealed that WD significantly enhanced the sensitivity of the foetal QRS detector on both datasets. By looking at Equations 3.27 and 3.28, the Acc and TPR behaviours can be related to the increase in FP number when using WD, probably due to the aggressive denoising that emphasized the residual artefacts compared with the background noise, challenging the QRS detector.

Despite the results obtained on the QRS detection, the SNR was generally improved by WD, as expected [144]. On the synthetic signals, this finding was statistically demonstrated for all the methods, thresholds, and levels, whereas SNR results showed less homogeneity on the real signals. Excluding Han *et al.* threshold, which presented a significantly higher SNR regardless of the WD method and the decomposition level, Minimax achieved significant improvement only when used in combination with the SWT. On the other hand, Universal generally failed in improving the SNR of the signal. This evidence is consistent with [104], [138], where the superiority of Minimax with respect to Universal was proven considering hard thresholding, despite their quantitative analyses were carried out only on simulated data. However, this difference in SNR performance among thresholds is probably due to the shrinkage effect due to the threshold amplitudes. In fact, the Universal threshold presented the higher scaling factor of σ_j

with respect to the other thresholds, whereas Han *et al.* threshold achieved higher values than Minimax up to level 3, i.e. at higher frequencies, being more conservative below 128 Hz.

As regards the WD methods, SWT-based approaches outperform the more complex SWPT-based ones in fECG post-processing. Our analysis showed that SNR and the QRS detection Acc were significantly higher in the SWT-based algorithms with respect to SWPT-based ones, despite these findings were not always statistically significant. Moreover, on synthetic signals, the SWT methods demonstrated a significantly superior capability to preserve the fECG signal morphology. Overall, the SWT outperformed the SWPT, and the adoption of seven levels for the decomposition of the signal provided more relevant improvement in the performance of the former method compared with the latter. By comparing all possible WD methods involved in this study, the Han *et al.* threshold with SWT decomposition significantly outperformed all the other approaches in terms of ρ (on the synthetic dataset) and SNR (on the real dataset), despite statistical significance was rarely achieved. This result further confirmed the superiority of the SWT over the SWPT.

Finally, by focusing on the level of decomposition, 6-level decomposition preserved the most the morphology of the underlying fECG signal, because the r_s (on the synthetic dataset) and the Acc (on both datasets) were significantly higher at this level for all the WD methods. These findings suggested a less aggressive denoising with six levels of decomposition with respect to seven levels, as confirmed by the higher SNR values of the latter on both datasets, at least for the SWT. This result is coherent with the fact that 7-level decompositions introduce thresholding in a part of the signal band that is preserved in the 6-level case. However, Figure 4.16 visually shows how the SWT reached a better performance in terms of waveform distortion than the SWPT (which in turn reduces the amplitude of the foetal R peaks). Figure 4.16 also suggests that, regardless the chosen WD method, the different thresholds can produce substantial differences in the morphology of the fECG trace, particularly emphasized by the Universal threshold that often leads to complete cancellation of the foetal beats.

Qualitative and quantitative analyses confirmed that the Han *et al.* threshold with SWT is the best approach for the denoising of fECG signals after signal separation, even though the Minimax threshold also achieved good denoising performance. Finally, even though WD is typically suitable for real-time processing, some points must be analysed. Remarkably, after setting the signal length and the level of decomposition to be exploited, the computational complexity associated to the three thresholds compared in this work can be considered equal, since all the scaling factors can be pre-computed off-line. Nonetheless, in this context, the computational complexity of the fECG post-processing is not considerably affected by the chosen WD algorithm but rather by the other algorithms involved in the evaluation of the σ_j, i.e. the fECG extraction method, the mECG delineator and the foetal QRS detector, whose computational load depends on the selected algorithms and its estimation is beyond the scope of this study.

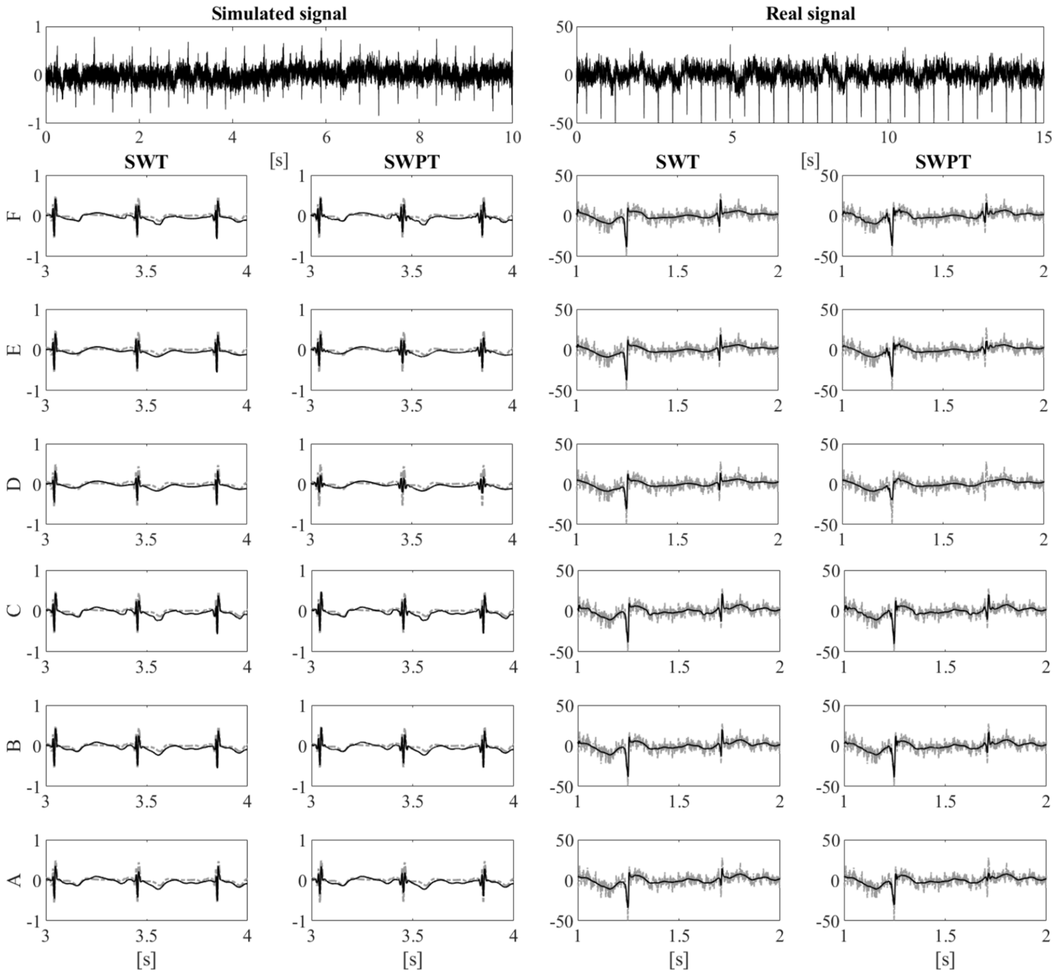

Figure 4.16. Example of SWT and SWPT denoising results with both levels and decompositions with Universal (A, D for level six and seven respectively), Minimax (B, E for level six and seven respectively) and Han et al. threshold [169] (C, F for levels six and seven, respectively). On the right, results obtained on a real extracted fECG signal from an abdominal recording were reported in μV; on the left, results obtained on a synthetic signal were represented. Zoom on one-second of each denoised fECG signal is reported to appreciate foetal beats morphology after wavelet denoising, with the original foetal beats in case of synthetic data and with the noisy traces in case of real ones (in grey).

Chapter 5

Wavelet-based algorithms for non-invasive foetal ECG post-processing: a methodology review

5.1 Rationale

As already detailed in Chapter 4, different scientific works exploited WD for NI-fECG enhancement. However, WD has been generally applied to reduce noisy interferences after fECG extraction algorithms, without providing evidence about the different wavelet implementation choices, parameterizations nor the dataset characteristics. As such, on the basis of the previous methodological study on the effect of WD on the post-processing of NI-fECG signals [142], [166], in order to potentially identify the best performing approach for the fECG post-processing, a systematic and quantitative comparative review of the different WD algorithms introduced for NI-fECG post-processing was performed. To this purpose, WD algorithms proposed in the scientific literature were accurately implemented in MATLAB or applied by exploiting ad-hoc software tools provided by the authors. However, when WD parameterizations were not always clearly stated, the most frequently adopted WD parameters and those referred to as the best options in our previous study [166] (see Chapter 4) were exploited, along with the decimated DWT. Performances were evaluated by providing quantitative evidence of WD effectiveness in noise reduction and morphological preservation on the same synthetic NI-fECG dataset described in Chapter 4, which was freely released by our group for the benchmarking of NI-fECG post-processing algorithms [162]. Results were analysed in terms of SNR, Acc and TPR of a foetal QRS detector [110], RMSE, Pearson's correlation coefficient ρ and Spearman's rank correlation coefficient r_s. Specifically, in order to summarize all these figures of merit and consider all of them simultaneously, a single performance index (*PI*) was conceived by exploiting PCA. After the best parameterization settings were identified for those algorithms in which different choices were possible, all WD approaches were statistically compared to identify a possible optimal solution for NI-fECG enhancement.

5.2 Materials and methods

In the light of the WD basic principles illustrated in Chapter 4, the parameterizations for a WD algorithm are mainly identified in the WT adopted for the decomposition, the mother wavelet, the decomposition level, the threshold definition, and the thresholding approach. In the scientific literature, different WD algorithms have been proposed for NI-fECG post-processing [104], [105], [136]–[151], [166], [181]. However, some of them [136], [188] did not provide sufficient information for their effective implementation, i.e. did not explicit most of the aforementioned parameterizations, thus preventing an effective comparison. Moreover, another work [181] analysed a SWPT-based methodology on fECG signals but for powerline interference suppression only, without taking into account any broad-band noise as in typical applications, and as such it was not included in this study. Overall, the methodological analysis was carried out on 17 WD methods, which are better explored in the following section. Wherever the authors did not specify any of the parameterizations needed for the algorithm implementation, the most frequently adopted WD parameters and/or those identified as the best options in Chapter 4 were exploited, along with the decimated DWT, which is most often employed for this purpose. Remarkably, as already detailed in Chapter 4, the decomposition level identifies the frequency sub-bands on which the denoising is performed, according to the adopted sampling frequency. Therefore, in order to implement each WD algorithm as closely as possible to its original definition, in this study the decomposition level was adapted by based on the limits of details and approximation sub-bands when taking into account the sampling frequency of the exploited synthetic dataset [162], i.e. 2048 Hz.

5.2.1 Non-invasive fECG WD-based post-processing algorithms included in the study

The quantitative analysis was performed on 17 WD algorithms, detailed hereinafter and summarized in Table 5.1. Each algorithm was characterized by a single set or multiple sets of parameters, in terms of wavelet decomposition, mother wavelet, threshold definition, thresholding approach and level of decomposition. Furthermore, in case of missing settings, parameterizations were implemented as detailed in the next Section 5.2.2.

The first algorithm included in this study was proposed by Ahmadi *et al.* [144]. They adopted the Daubechies8 (db8), the Symlet8 (sym8) and the Coiflet4 (coif4) as mother wavelets and the Universal threshold (see Equation 4.2). Following [144] and considering the different nature of the noisy interferences affecting the adopted synthetic dataset, the amount of noise was estimated as:

$$\sigma_j = 1.4826 * median(cD_j) \qquad (5.1)$$

where cD_j represents the detail coefficients at the j-th level, computed on the full-length fECG signal.

In the work by Castillo *et al.* [104] different WD parameterizations were tested and compared. Finally, the authors identified the db6, a 3-level decomposition, the Minimax threshold and the soft thresholding (see Equations 4.3 and 4.5, respectively) as best solutions for the NI-fECG denoising. Nonetheless, since our simulated signals are not affected by baseline wandering artifact, its suppression by zeroing the approximation, as suggested in [104], was not implemented. Moreover, the authors imposed the same DWT decomposition level for different NI-fECG datasets, i.e., the DaIsy dataset [189], the Non-Invasive Fetal ECG Database [190] and the Abdominal and Direct Fetal ECG Database [81], which however are characterized by different sampling rates, thus preventing an accurate WD adaptation to the signal frequency band. Conversely, the mathematical formulation for the σ_j followed the estimation expressed in Equation 4.1.

A WD algorithm was introduced by Jamaluddin *et al.* [145], in which the DWT was exploited along with the Biorthogonal 1.5 (bior1.5) mother wavelet, hard thresholding (see Equation 4.4), five levels of decomposition and a custom threshold. However, since the decomposition level was assumed by the authors for a sampling frequency of 8000 Hz, it was fixed to five in order to be employed on our signals, which are sampled at 2048 Hz. Moreover, since the threshold was not analytically described in [145], it was deduced by the inspection of Figure 6 in [145] and adapted according to the signal amplitude in order to resemble the most the original WD approach in [145].

Another work by Ivanushkina *et al.* [148] adopted WD after fECG extraction. In their study, ad-hoc synthetic NI-fECG signals and real recordings from the Abdominal and Direct Fetal ECG Database [81], [190] were denoised by using a 6th-order symmetric mother wavelet, a 5-level decomposition and a custom thresholding, which zeroes all detail coefficients at the first and second levels while adopting soft thresholding on the third one. As such, by adapting the decomposition level to six according to the characteristics of our synthetic dataset, also the thresholding approach was revised by zeroing the same sub-bands (i.e., all detail coefficients of the first three levels) while considering the soft thresholding in the fourth detail level, ranging from 64 Hz to 128 Hz in our case. Furthermore, since the mother wavelet was not clearly identified, all the 6th-order wavelets meeting the requirements of symmetry, i.e. the sym6 and the bior2.6, were included and tested in following analyses.

In [149], Jadhav and Dhang employed the coif5 wavelet and a 5-level decomposition for the post-processing of two available real NI-fECG datasets [81], [190] sampled at 1000 Hz. As such, in order to faithfully reproduce their approach, a 6-level decomposition was considered on our simulated dataset.

Conversely, in [138] Shayesteh and Fallahian investigated the role of WD in combination with BSS approaches. They adopted different parameter settings, concluding that several mother wavelets (i.e., db3, db4, db5, db6 and from the biorthogonal family) in combination with the Rigrsure threshold and hard thresholding [167], [168] allowed for getting best results. As detailed in Table 5.1, the authors considered two different decomposition levels (i.e., six and seven) without specifying any information about their data sampling rate. As such, following the approach adopted in the previous Chapter 4, both 6-level and 7-level decompositions were examined in this comparative analysis.

Moreover, Swarnalatha and Prasad [139] considered a custom WD denoising, in which only the approximation was preserved. In their algorithm, a 5-level decomposition based on DWT was employed on several datasets digitalized at different sampling rates, thus inhibiting a proper adaptation according to the signal band in this study. Moreover, since the authors declared that the coiflet mother wavelets were used for the decomposition without identifying the order, all coiflets available in MATLAB were tested and compared in this investigation.

In their work [140], Vigneron *et al.* used the biorthogonal wavelet family along with the Rigrsure threshold and 6-level decomposition for the WD post-processing of NI-fECG signals sampled at 1000 Hz. Therefore, in this case, a proper adaptation of the decomposition level according to the sampling rate of our dataset was used, by considering seven levels of decomposition.

In Wang *et al.* [141], a WD stage based on a 5th-order symmetric biorthogonal wavelet and 4-level decomposition was tested on the DaIsy dataset [189], which is sampled at 250 Hz. As such, in its implementation, a 7-level decomposition was considered, whereas for the missing parameters the choices will be explained in the next section.

Also Jaros *et al.* [143] integrated a WD post-processing stage in their hybrid NI-FECG extraction system. In their work, the authors adopted a WD post-processing stage on the Abdominal and Direct Fetal ECG Database [81] and the set A of the PhysioNet/Computing in Cardiology Challenge 2013 Dataset [190], [191] by considering a window-dependent threshold, defined as:

$$th_{j,k} = K\ \sigma_{j,k} \qquad (5.2)$$

where K is a constant value equal to 2.5 and $\sigma_{j,k}$ identifies the standard deviation computed for the k-th detail level on each j-th window composed of 500 samples. Moreover, in their algorithm, Jaros *et al.* considered the db4 mother wavelet, a soft thresholding approach and a 6-level decomposition on NI-fECG signals sampled at 1000 Hz, which was adjusted as 7-level decomposition for our dataset.

Similarly, Martinek *et al.* [105] investigated the use of WD as NI-fECG processing tool for the removal of powerline and muscular interferences. Focusing on muscular artifacts, the authors achieved better denoising results when considering the sym4 mother wavelet, hard thresholding, and the adaptive threshold, which was defined as in Equation 5.2. However, in this work [105], K was set equal to 2.8 and $\sigma_{j,k}$ was computed on 1000-sample windows, following Equation 5.1.

In [151], Mochimaru *et al.* used the Wavelet Analysis and Spectrum Analysis MEM software [192] for the WD post-processing. In this context, they used the coif24 as mother wavelet and a 12-level decomposition on data sampled at 5000 Hz or 2048 Hz, along with a custom threshold. The latter was conceived by weighting the standard deviation of the wavelet coefficients by level-dependent factors, which were defined by minimizing the information cost-function while maximizing the determination coefficient [151], [193]. However, in a previous study [194] the same authors not only exploited a similar approach on data sampled at different sampling rates, but they also specified the weighting factors. Therefore, this latter work [194] was taken into account in order to faithfully reproduce the threshold proposed in their algorithm, avoiding any adjustment for the level of decomposition.

In [146], Ionescu proposed a WD approach for NI-fECG post-processing by considering the Abdominal and Direct Fetal ECG Database [81], [190]. In this work, WD was performed by using the LabVIEW Wavelet Denoised Express VI tool and exploiting an undecimated WT (i.e., the SWT), the bior4.4 mother wavelet and an 8-level decomposition. Since no additional information was clarified regarding the threshold and the thresholding method, all possible parameterizations offered by the tool were considered in MATLAB (i.e., hard and soft methods for thresholding, and Minimax, Universal, Rigrsure and Heursure for the threshold definition). Moreover, due to the different sampling frequency adopted in [146], the decomposition level was set to nine.

In [150], Jothi *et al.* proposed the combined use of the undecimated WT, Rigrsure threshold and soft thresholding with different mother wavelets belonging to the Daubechies, Symlets, Coiflets, Biorthogonal and Reverse Biorthogonal families. Unlike some other works, the choice of the mother wavelet was not found to be crucial by Jothi *et al.* in this context, thus all wavelets from those families that were available in MATLAB were considered and compared (see Table 5.1). Moreover, Jothi *et al.* considered a 4-level decomposition on data sampled at 4000 Hz, thus this parameter was set to three in order to be properly applied to our synthetic dataset.

Similarly, in their work [137], Rivet *et al.* employed the SWT with the Rigrsure threshold and hard thresholding. The authors tested different levels of decomposition and found that six levels of decompositions offered higher SNRs than five, despite inducing a more aggressive denoising. However, they did not give any detail about the sampling rate of the adopted dataset nor the chosen mother wavelet. As such, the level of decomposition was considered equal to six without any adaptation, as also in accordance with our previous investigation [166], while the mother wavelet was selected according to Section 5.2.2.

Ishikawa *et al.* [147] proposed a NI-fECG denoising based on the perfect-translation-invariant (PTI) complex DWT, which was found to be promising for the diagnosis of foetal arrhythmia. Specifically, by exploiting the WavePti software developed by the author H. Toda, it was possible to accurately reproduce their WD algorithm by choosing a Universal threshold and a soft thresholding, as revised in [147]. As regards the decomposition level, Ishikawa *et al.* performed WD by using a 7-level decomposition for NI-fECG signals sampled at 5000 Hz, while considering five levels of decomposition when signals were digitalized at 1250 Hz. As such, in the light of the adopted sampling rate for our dataset (i.e., 2048 Hz), in this quantitative review a 6-level decomposition was imposed.

Finally, a WD algorithm based on the best parameterizations among those examined in our previous investigations [166] (see Chapter 4) was included in the comparative analysis. This approach, referred to as Baldazzi *et al.* algorithm hereinafter, involves the SWT, the Haar mother wavelet, a 6-level decomposition, the threshold proposed by Han *et al.* [169] and computed following [166] (see Chapter 4) and hard thresholding.

Table 5.1. WD algorithms and their parameterizations as included in the review. Missing settings were considered as reported in bold italics, and decomposition levels eventually adapted are detailed in brackets. Remarkably, coifX, dbX, symX, bioX.X, rbiorX.X represent all wavelets belonging to the Coiflet, Daubechies, Symlet, Biorthogonal and Reverse Biorthogonal families respectively, and available in MATLAB. In this analysis, DWT expressly indicates the decimated WT decomposition, SWT the undecimated one, whereas PTI identifies a perfect-translation-invariant complex DWT decomposition.

	Wavelet transform	Mother wavelet	Decomposition level	Threshold	Thresholding
Ahmadi *et al.* [144]	DWT	coif4, sym8, db8	***6***	Universal	***hard, soft***
Castillo *et al.* [104]	DWT	db6	3	Minimax	soft
Jamaluddin *et al.* [145]	DWT	bior1.5	5 (3)	custom	hard
Ivanushkina *et al.* [148]	DWT	***sym6, bior2.6***	5 (6)	***Rigrsure, Han et al.*** [166]	custom
Jadhav and Dhang [149]	DWT	coif5	5 (6)	***Rigrsure, Han et al.*** [169]	***hard, soft***
Shayesteh and Fallahian [138]	DWT	db3, db4, db5, db6, bior1.1	6, 7	Rigrsure	hard
Swarnalatha and Prasad [139]	DWT	***coifX***	5	none	custom
Vigneron *et al.* [140]	DWT	***biorX.X***	6 (7)	Rigrsure	***hard, soft***
Wang *et al.* [141]	DWT	***bior5.5***	4 (7)	***Rigrsure, Han et al.*** [169]	***hard, soft***
Jaros *et al.* [143]	DWT	db4	6 (7)	Adaptive	soft
Martinek *et al.* [105]	DWT	sym4	***6***	Adaptive	hard
Mochimaru *et al.* [151]	DWT	coif24	12	custom	***hard, soft***
Ionescu [146]	SWT	bior4.4	8 (9)	***Universal, Minimax, Rigrsure, Heursure***	***hard, soft***
Jothi and Prabha [150]	SWT	***coifX, dbX, symX, bioX.X, rbiorX.X***	4 (3)	Rigrsure	soft
Rivet *et al.* [137]	SWT	***Haar, biorX.X***	6	Rigrsure	hard
Ishikawa *et al.* [147]	PTI complex DWT	PTI complex wavelet	7, 5 (6)	Universal	soft
Baldazzi *et al.* [166]	SWT	Haar	6	Han et al. [169]	hard

5.2.2 Chosen parameterizations in case of missing information

Despite lot of scientific effort has been put in WD as post-processing stage for NI-fECG enhancement, as described in the previous section, in several works some information for an accurate and reliable implementation of the WD algorithm was missing. As such, in those cases where parameterizations were not reported, the most frequently adopted WD parameters and those referred to as the best options in our previous investigations [166] (see Chapter 4) were assumed. Specifically, unless otherwise noted, the decomposition was performed by the decimated DWT. As regards the mother wavelet, the most widely adopted family (i.e., the Biorthogonal wavelets) and the Haar wavelet proposed in our study [166] were considered, whereas a 6-level decomposition was taken into account in case of missing information. Moreover, when the threshold definition was not clearly stated, the most common threshold (i.e., the Rigrsure) and the one proposed by Han *et al.* [169], that was found as best solution in our previous analyses [166], were investigated. In each case, unless otherwise specified, σ_j was quantified on the full-length NI-fECG trace following Equation 4.1. Finally, when the thresholding method was not declared, both soft and hard thresholding were tested and evaluated.

5.3 Methods for the comparative analysis

The different WD algorithms and their parameterizations were quantitatively assessed and systematically compared by exploiting 40 synthetic fECG signals (see Section 4.2.3) affected by different levels of noise (i.e., with 40 $\mathrm{SNR}_{\mathrm{mn}}$ between 3 dB and 15 dB, obtained by additive pink and white noise). The comparative analysis was carried out in terms of different figures of merit: SNR, Acc and TPR of a foetal QRS detector [88], RMSE, ρ and $\mathrm{r_s}$. Specifically, SNR, Acc and TPR allow for the noise removal quantification, whereas the RMSE, ρ and $\mathrm{r_s}$ allow assessing the capability to preserve the signal morphology after denoising offered by each WD algorithm as in both Chapters 3 and 4 and in our previous assessment [166]. Specifically, the SNR was computed as in Equation 4.7, by considering App_f as the peak-to-peak amplitude of the beat template obtained by synchronized averaging of all foetal beats, and σ as the median value of the standard deviations evaluated on each interval comprised between two consecutive foetal beats. Besides, the Acc and TPR were computed as reported in Equations 3.20 and 3.21, whereas the RMSE, ρ and $\mathrm{r_s}$ were estimated between each beat in the WD-processed simulated signal and the corresponding one in the noiseless fECG signal. The three indexes were computed considering a window of 120 ms before and 180 ms after each beat [164].

However, as can be seen in Table 5.1, most of the algorithms (i.e., those by Ahmadi *et al.*, Ivanushkina *et al.*, Jadhav and Dhang, Shayesteh and Fallahian, Swarnalatha and Prasad, Mochimaru *et al.*, Ionescu, Vigneron *et al.*, Wang *et al.*, Ionescu, Jothi and Prabha, Rivet *et al.*) were developed considering several alternative parameterizations. As such, a preliminary analysis was required in order to identify, for each approach, which set of parameters achieved better performance. After this initial investigation, each WD algorithm was associated to its best-performing parameterization. Then, all the 17 WD algorithms were statistically compared in order to identify a possible optimal WD approach for the NI-fECG post-processing problem in terms of both noise removal effectiveness and signal morphology preservation. To be able to consider all the chosen figures of merit simultaneously, a single performance index PI was deduced by PCA. In this context, PCA was used to perform dimensionality reduction by exploiting the first two PCs, which retained the 94.1±3.4 % of the total variance across the different analyses. Specifically, the projection of each WD algorithm in the plane identified by the first two PCs, also known as $score$, was obtained according to its figures of merit. Then, the PI was estimated as the pairwise distance between the point representing each WD approach, i.e. $score_i$, and an ideally defined optimal result score, $score_{optimal}$, as:

$$PI = \sqrt{(score_i - score_{optimal})(score_i - score_{optimal})^T} \quad (5.3)$$

Obviously, the smaller the distance from the optimal score, the higher the performance of the WD algorithm. The $score_{optimal}$ valuewas defined by assuming as ideal conditions Acc, TPR, ρ and r_s equal to 1, RMSE equal to 0 and the SNR as the highest estimate achievable among those computed on the noiseless fECG signals (i.e., 49.6 dB), normalized to 1. In fact, as the SNR assumes higher values than all the other figures of merit, each computed SNR was normalized by the aforementioned highest value before PCA.

Specifically, for each WD algorithm, the six figures of merit were computed on the 40 synthetic signals after denoising and then the PCA was performed on these values. In this regard, at first PCA analysis and *PI* estimation were adopted to identify the best parameterization for WD algorithms involving different options. Then, PCA was used on all the 17 WD algorithms with a single/best parameterization, and the identification of the best NI-fECG post-processing was based on the *PI* metrics. This final analysis was also carried out in two steps. At first, the optimal WD algorithm was identified considering all the indexes simultaneously, thus giving an overall performance overview. The contribution of each figure of merit to the first two PCs is reported in Figure 5.1. In a second step, since the WD may be applied not only for fHR estimation, but also for morphological analyses, the analysis was focused specifically on noise removal and signal morphology preservation separately, by applying the PCA only on SNR, TPR and Acc on the one hand, and on RMSE, ρ and r_s on the other hand. Figure 5.2 schematically reports the steps adopted in all performed investigations.

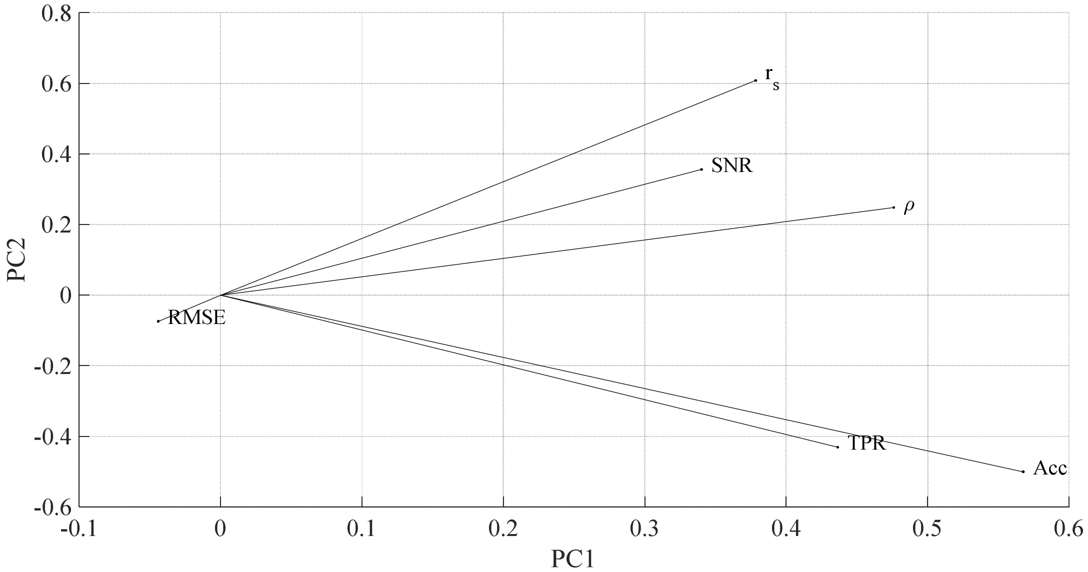

Figure 5.1. Graphical representation of PCA loadings for the first two PCs. For each figure of merit, the module and the direction of its vector suggest the metric contribution to the PCs: the larger the loading, the higher the contribution of the figure of merit for the specific PC. Conversely, the direction, i.e., the sign of the loading, indicates if the analysed figure and the PC are positively or negatively correlated.

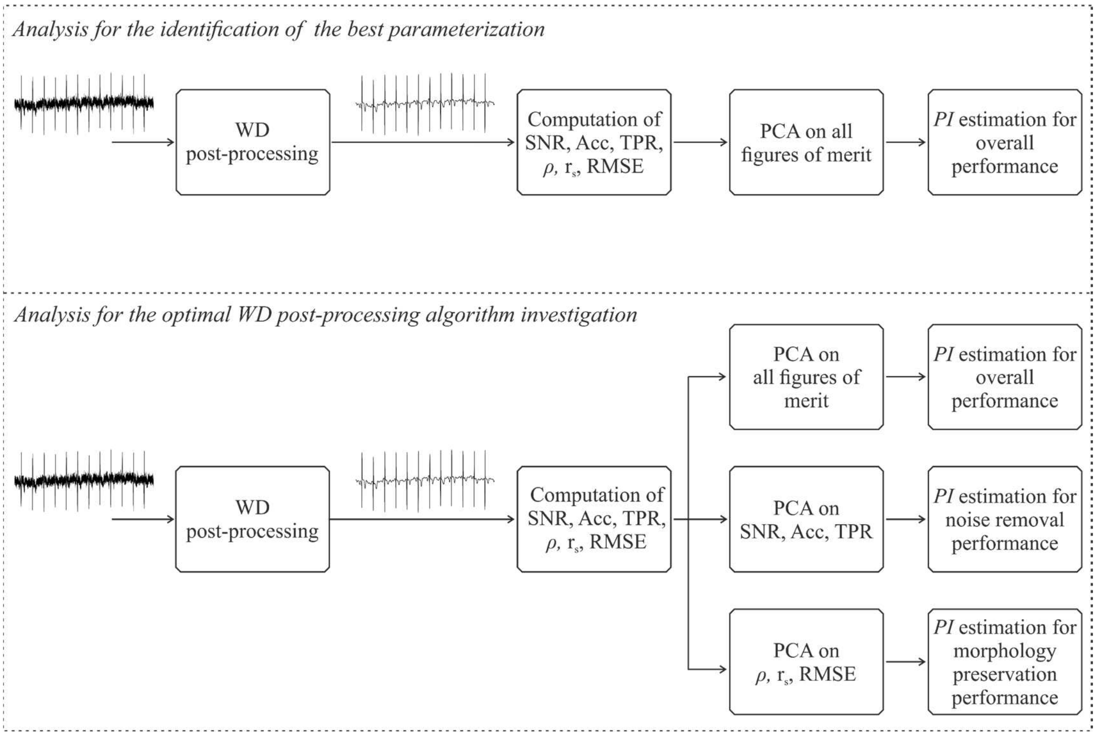

Figure 5.2. Schematic representation of the analysis performed for the identification of the best parameterization for WD algorithms involving different options (top) and the analysis carried out for the optimal WD post-processing investigation (bottom).

For the statistical analysis, the normality of the *PI* distributions was preliminarily investigated by using the Lilliefors test. However, since in most cases the assumption of a normal distribution was not satisfied, a non-parametric statistical approach was chosen. Specifically, the Kruskal–Wallis test was adopted for multiple comparisons, whereas the Wilcoxon signed rank test was selected for pairwise comparisons. Bonferroni correction was applied in each comparative analysis. In all the statistical tests, $p < 0.05$ was considered for statistical significance. All data processing was performed in MATLAB v2020a (MathWorks Inc., MA, USA).

5.4 Results and discussion

5.4.1 Best parameterization

Results for the first analysis concerning the identification of the best parameterization for the algorithms exposing multiple options are reported in Table 5.2 in terms of best parameter combinations. Moreover, *PI* distributions for each WD algorithm and parameterization are reported in Figures 5A.1-11 in Appendix A.

In this regard, for the Ahmadi *et al*. algorithm [144], six different parameterizations were assessed and compared (see Table 5.1) and, among them, a statistically significant difference was found ($p = 0.0004$). Specifically, the parameterization including sym8 mother wavelet and hard thresholding statistically outperformed all the others ($p < 0.0001$) except for the one involving coif4 mother wavelet and hard thresholding ($p > 0.05$). However, the latter showed an higher median distance from the optimal score, thus we selected the first one, i.e. the sym8 mother wavelet.

As regards the Ivanushkina *et al.* algorithm [148], no statistically significant difference was achieved among the four available parameter combinations ($p > 0.05$). Nonetheless, in order to represent each WD algorithm by a single parameterization in the next analysis, the parameter setting offering the highest median performance (i.e., the lowest median distance from the optimal score) was selected, i.e. the sym6 wavelet and the Rigrsure threshold.

For the Jadhav and Dhang algorithm [149] four different parameterizations were assessed. However, in this case, a statistically significant difference was found in the group ($p = 0.0004$), and, among the possible choices, the parameterization characterized by the Han *et al.* threshold and the hard thresholding achieved the best performance ($p < 0.0001$).

Conversely, for the Shayesteh and Fallahian algorithm [138] no significant difference was found among the ten different parameterizations ($p > 0.05$), thus the one exhibiting the highest performance (i.e., db6 wavelet and 6-level decomposition) was chosen for the next assessment. The same findings were obtained for the multiple comparisons in the Swarnalatha and Prasad algorithm [139], the Jothi and Prabha algorithm [150] and the Rivet *et al.* algorithm [137]. As such, they were represented by the coif1, rbior2.2 and bior2.4 mother wavelets respectively.

Besides, between the two possible parameter settings available for the Mochimaru *et al.* algorithm [151], the one involving the hard thresholding achieved statistically significant higher performance ($p < 0.0001$).

Conversely, for the Vigneron *et al.* algorithm [140], a statistically significance different was found in the multiple comparison test ($p < 0.0001$). However, the best performing parameterization (i.e., the one showing the lowest distance from the optimal score) was not statistically identifiable. In fact, the parameter combination exhibiting the lowest median distance from the optimal score (i.e., bior6.8 and soft thresholding), despite being chosen for the next analyses, was not significantly different from the other parameterizations showing similar good performances but with different mother wavelets (i.e., bior1.1, bior1.3, bior2.2, bior2.4, bior2.6, bior2.8, bior3.9, bior4.4 and bior5.5).

As regards the Wang *et al.* algorithm [141], after a statistically significant difference was found among the four possible parameterizations ($p = 0.0016$), the pairwise comparisons revealed that the best performance was achieved when considering the Han *et al.* threshold with hard thresholding ($p < 0.0023$).

Finally, for the Ionescu algorithm [146], a statistically significant difference was found among the eight possible parameter combinations ($p < 0.0001$). Moreover, pairwise comparisons allowed choosing the parameterization combining Minimax threshold and hard thresholding, since it presented the lowest distance from the optimal score ($p < 0.0018$).

Table 5.2. Best WD parameterizations identified for those algorithms where multiple parameter combinations were originally presented. Decomposition levels after adaption to the sampling rate of the testing dataset are reported in brackets.

	Wavelet transform	Mother wavelet	Decomposition level	Threshold	Thresholding
Ahmadi *et al.* [144]	DWT	sym8	6	Universal	hard
Ivanushkina *et al.* [148]	DWT	sym6	5 (6)	Rigrsure	custom
Jadhav and Dhang [149]	DWT	coif5	5 (6)	Han et al. [169]	hard
Shayesteh and Fallahian [138]	DWT	db6	6	Rigrsure	hard
Swarnalatha and Prasad [139]	DWT	coif1	5	none	custom
Vigneron *et al.* [140]	DWT	bior6.8	6 (7)	Rigrsure	soft
Wang *et al.* [141]	DWT	bior5.5	4 (7)	Han et al. [169]	hard
Mochimaru *et al.* [151]	DWT	coif24	12	custom	hard
Ionescu [146]	SWT	bior4.4	8 (9)	Minimax	hard
Jothi and Prabha [150]	SWT	rbior2.2	4 (3)	Rigrsure	soft
Rivet *et al.* [137]	SWT	bior2.4	6	Rigrsure	hard

5.4.2 Optimal WD post-processing for non-invasive fECG enhancement

Once the best parameterization settings were selected for those algorithms presenting multiple options, all the 17 WD algorithms were statistically compared to identify a possible optimal solution for NI-fECG enhancement. The assessment was initially performed by considering all figures of merit simultaneously, and then by evaluating noise removal performance only (i.e., SNR, Acc, TPR) and morphology preservation performance only (i.e., RMSE, ρ and r_s).

PI distributions for the overall performance analysis are reported in Figures 5.3. Besides, Table 5.3 summarizes statistical results of the pairwise comparisons.

As can be seen, Baldazzi *et al.* algorithm [166] (A17 in Figure 5.3 and Table 5.3) significantly outperformed all the other WD approaches ($p = 0.0006$ in the comparison with Ionescu algorithm [146], i.e., A13, $p < 0.0001$ in all the other assessments).

Good performance was exhibited also by the WD algorithms by Jadhav and Dhang [149] and Martinek *et al.* [105], despite not reaching statistical significance in several comparisons, especially with Ionescu *et al.* [146] (see Table 5.3). The worst performance was marked by the Swarnalatha and Prasad algorithm [139]. However, such performance was not significantly different with respect to the results obtained by the Shayesteh and Fallahian [138] and the Jaros *et al.* [143] WD approaches.

Table 5.3. Statistical results for the quantitative comparison, in terms of overall performance, of the 17 WD algorithms included in this study: A1) Ahmadi et al. [144], A2) Castillo et al. [104], A3) Jamaluddin et al. [145], A4) Ivanushkina et al. [148], A5) Jadhav and Dhang [149], A6) Shayesteh and Fallahian [138], A7) Swarnalatha and Prasad [139], A8) Vigneron et al. [140], A9) Wang et al. [141], A10) Jaros et al. [143], A11) Martinek et al. [105], A12) Mochimaru et al. [151], A13) Ionescu [146], A14) Jothi and Prabha [150], A15) Rivet et al. [137], A16) Ishikawa et al. [147], A17) Baldazzi et al. [166].
Specifically, $p < 0.05$, $p < 0.005$ *and* $p < 0.0001$ *are represented by *, ** and ***, respectively, whereas – indicates no statistically significant difference.*

	A2	A3	A4	A5	A6	A7	A8	A9	A10	A11	A12	A13	A14	A15	A16	A17
A1	–	–	**	***	*	**	–	–	***	***	–	–	–	–	**	***
A2		***	***	***	***	***	***	_	***	**	_	_	***	***	_	***
A3			***	***	***	***	_	_	***	***	**	_	*	***	_	***
A4				**	***	***	***	*	***	_	_	_	***	***	***	***
A5					***	***	***	***	***	_	**	_	***	***	***	***
A6						_	***	***	*	***	***	***	***	***	_	***
A7							***	***	_	***	***	***	***	**	*	***
A8								_	***	***	**	_	**	***	_	***
A9									***	***	_	_	_	**	_	***
A10										***	***	***	***	**	***	***
A11											*	_	***	***	***	***
A12												_	_	***	_	***
A13													_	**	_	**
A14														***	_	***
A15															_	***
A16																***

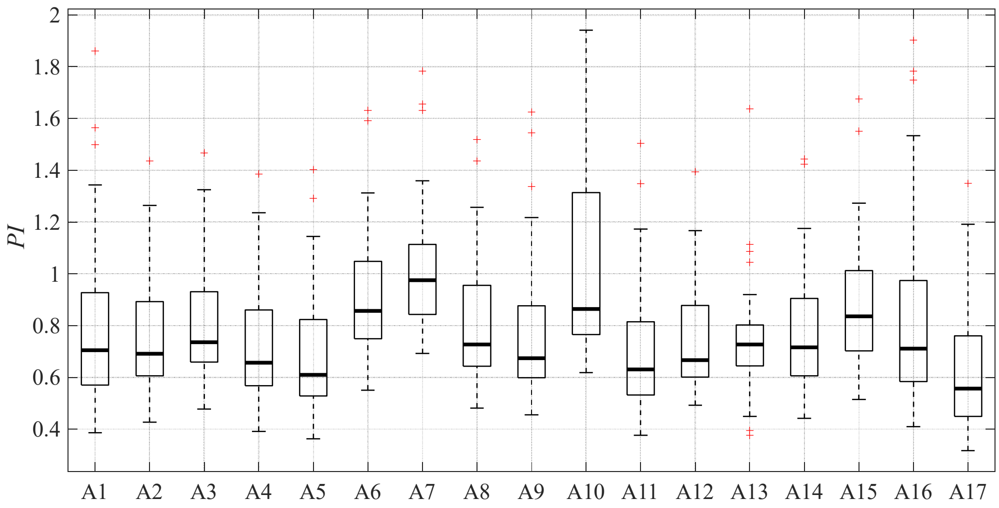

Figure 5.3. PI distributions obtained when considering all the figures of merit for the different WD algorithm examined in this study (the lower the better): A1) Ahmadi et al. [144], A2) Castillo et al. [104], A3) Jamaluddin et al. [145], A4) Ivanushkina et al. [148], A5) Jadhav and Dhang [149], A6) Shayesteh and Fallahian [138], A7) Swarnalatha and Prasad [139], A8) Vigneron et al. [140], A9) Wang et al. [141], A10) Jaros et al. [143], A11) Martinek et al. [105], A12) Mochimaru et al. [151], A13) Ionescu [146], A14) Jothi and Prabha [150], A15) Rivet et al. [137], A16) Ishikawa et al. [147], A17) Baldazzi et al. [166].

Moreover, Figure 5.4 provides the *PI* values obtained at the different noise levels affecting the noisy synthetic NI-fECG signals. As expected, *PI* values decreased (higher performance) for increasing values of the SNR, as expected, due to the higher quality of the signals before WD, whereas the *PI values* increased (worse performance) when the initial SNR was lower (i.e., in signals of lower quality). In fact, when the original NI-fECG signal was only limitedly affected by noise from the beginning, the WD algorithm might perform generally better, getting closer to the ideal condition (i.e., higher SNR, ACC, TPR, ρ and r_s and lower RMSE values).

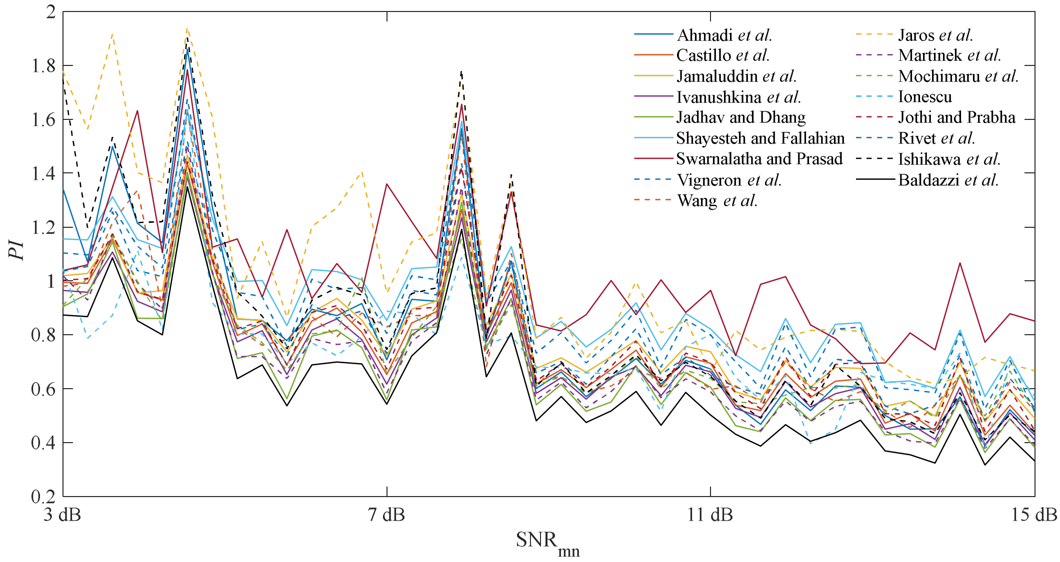

Figure 5.4. PI distributions obtained in the overall performance evaluation when varying the noise level affecting the synthetic NI-fECG recordings (i.e., before any WD was performed).

As regards the performance only in terms of noise removal, Tables 5.4 and Figure 5.5 report the results in terms of statistical significance obtained in the pairwise comparisons and *PI* distributions for each WD algorithm, respectively.

*Table 5.4. Statistical results for noise removal performance evaluated for the 17 WD algorithms included in this study: A1) Ahmadi et al. [144], A2) Castillo et al. [104], A3) Jamaluddin et al. [145], A4) Ivanushkina et al. [148], A5) Jadhav and Dhang [149], A6) Shayesteh and Fallahian [138], A7) Swarnalatha and Prasad [139], A8) Vigneron et al. [140], A9) Wang et al. [141], A10) Jaros et al. [143], A11) Martinek et al. [105], A12) Mochimaru et al. [151], A13) Ionescu [146], A14) Jothi and Prabha [150], A15) Rivet et al. [137], A16) Ishikawa et al. [147], A17) Baldazzi et al. [166]. Specifically, $p < 0.05$, $p < 0.005$ and $p < 0.0001$ are represented by *, ** and ***, respectively, whereas – indicates no statistically significant difference.*

	A2	A3	A4	A5	A6	A7	A8	A9	A10	A11	A12	A13	A14	A15	A16	A17
A1	–	–	–	***	–	**	–	*	***	***	***	***	–	–	***	***
A2		**	***	***	***	***	–	–	–	***	***	***	–	***	–	***
A3			***	***	***	***	–	*	–	***	***	***	–	***	–	***
A4				***	***	***	–	–	*	**	**	***	***	***	***	***
A5					***	***	***	–	***	–	–	***	***	***	***	**
A6						–	***	**	–	***	***	***	***	**	–	***
A7							***	***	–	***	***	***	***	**	–	***
A8								–	**	***	***	***	*	***	**	***
A9									***	–	–	***	–	**	***	-
A10										***	***	***	–	–	–	***
A11											–	***	***	***	***	***
A12												***	***	***	***	–
A13													***	***	***	***
A14														***	–	***
A15															–	***
A16																***

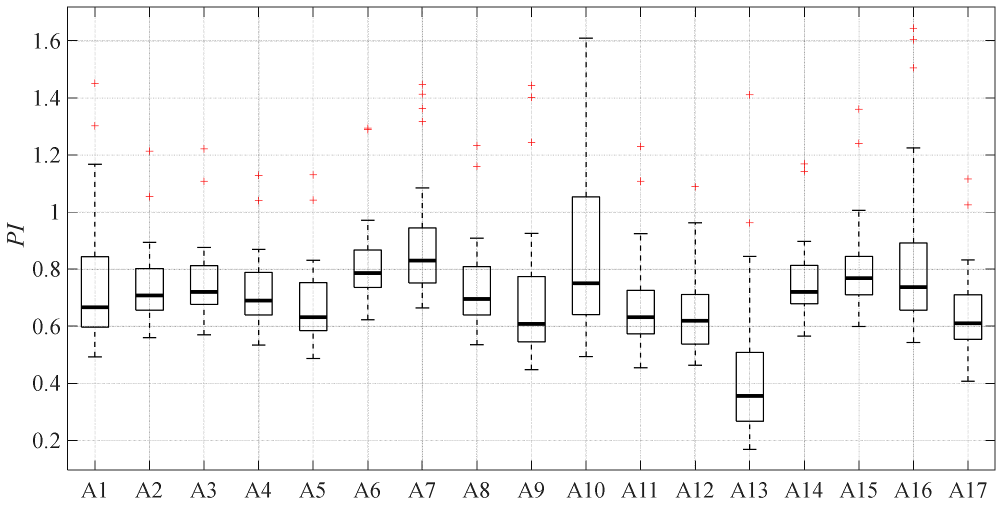

Figure 5.5. PI distributions obtained in the noise removal performance assessment: A1) Ahmadi et al. [144], A2) Castillo et al. [104], A3) Jamaluddin et al. [145], A4) Ivanushkina et al. [148], A5) Jadhav and Dhang [149], A6) Shayesteh and Fallahian [138], A7) Swarnalatha and Prasad [139], A8) Vigneron et al. [140], A9) Wang et al. [141], A10) Jaros et al. [143], A11) Martinek et al. [105], A12) Mochimaru et al. [151], A13) Ionescu [146], A14) Jothi and Prabha [150], A15) Rivet et al. [137], A16) Ishikawa et al. [147], A17) Baldazzi et al. [166].
As can be seen, the lowest distance from the optimal score is obtained by the Ionescu algorithm, thus guaranteeing the highest performance in terms of noise reduction.

As can be noticed, when only SNR, TPR and Acc indexes were taken into account, the best performance was marked by the Ionescu algorithm [146], which outperformed all the other WD approaches significantly ($p < 0.0001$). Conversely, although without statistically significant differences in the comparison with several WD approaches, the highest median distance from the optimal score was marked by the Swarnalatha and Prasad algorithm [139], followed by the WD proposed by Shayesteh and Fallahian [138], and Rivet *et al.* [137].

Furthermore, depending on the noise level affecting the synthetic NI-fECG (see Figure 5.6), the *PI* obtained considering the noise removal figures of merit only followed the same trend found in

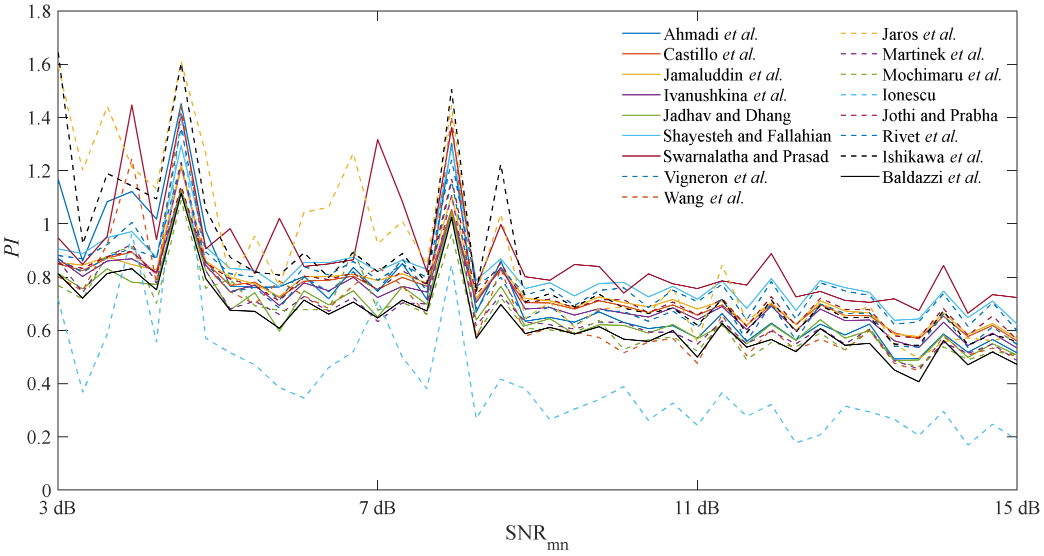

Figure 5.6. PI values in the noise reduction performance evaluation when varying the noise entity affecting the synthetic NI-fECG signals before WD post-processing.

the overall performance assessment, as expected. However, the *PI* trend exhibited by the Ionescu algorithm [146] was substantially different from all the others.

Finally, as regards the morphological performance investigation, results are reported in Figures 5.7 and 5.8, and in Table 5.5. Like the overall performance case, the best performance in terms of signal morphology preservation (i.e., higher ρ and r_s and lower RMSE) was achieved by the Baldazzi *et al.* algorithm [166] ($p < 0.0001$), followed by the Jadhav and Dhang [149] and Martinek *et al.*[105] approaches, whereas the Ionescu algorithm [146] seemed to be far from the

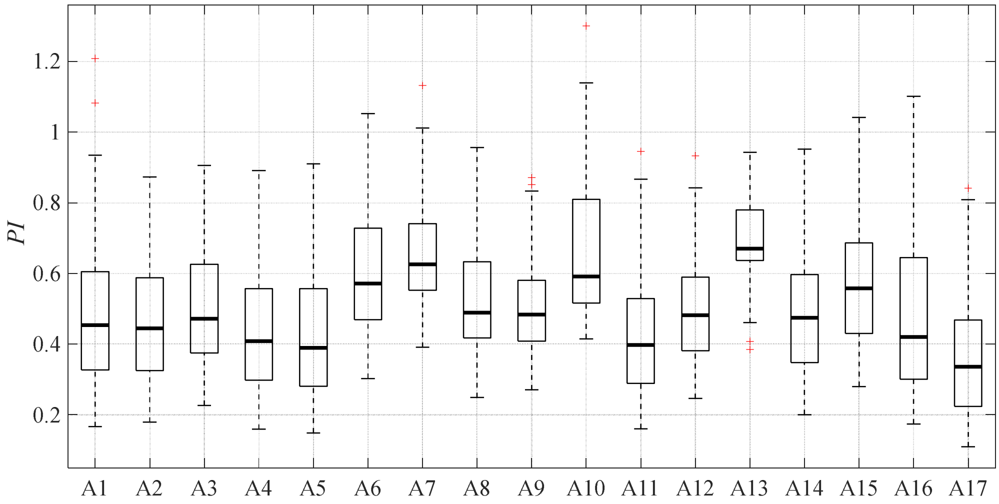

Figure 5.7. PI distributions obtained in the morphological performance investigation: A1) Ahmadi et al. [144], A2) Castillo et al. [104], A3) Jamaluddin et al. [145], A4) Ivanushkina et al. [148], A5) Jadhav and Dhang [149], A6) Shayesteh and Fallahian [138], A7) Swarnalatha and Prasad [139], A8) Vigneron et al. [140], A9) Wang et al. [141], A10) Jaros et al. [143], A11) Martinek et al. [105], A12) Mochimaru et al. [151], A13) Ionescu [146], A14) Jothi and Prabha [150], A15) Rivet et al. [137], A16) Ishikawa et al. [147], A17) Baldazzi et al. [166].
In this case, the highest performance (i.e., lowest PI) is achieved by the Baldazzi et al. algorithm, as such providing the highest performance in terms of morphology preservation.

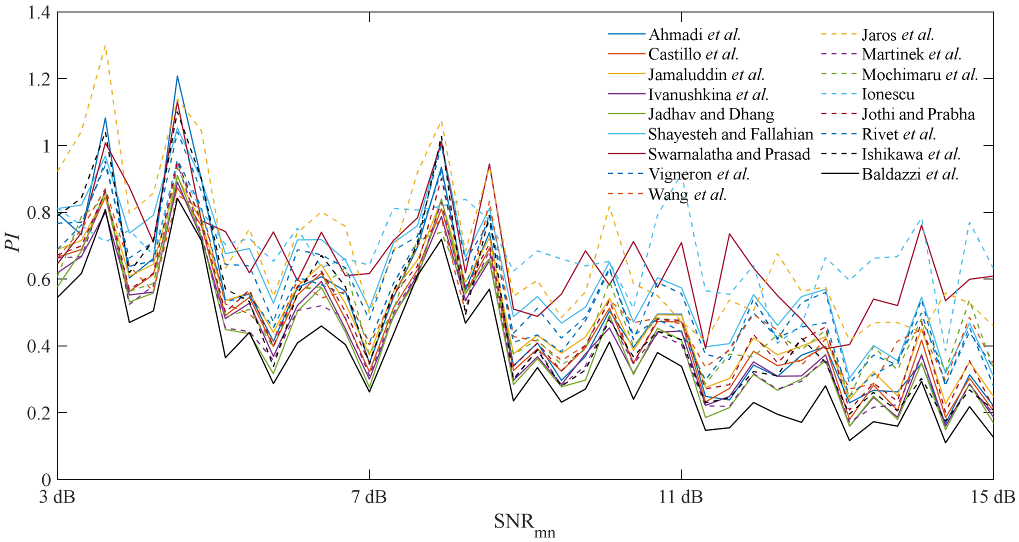

Figure 5.8. PI values obtained in the morphological performance investigation when considering the different noise entities affecting the synthetic NI-fECG signals before WD post-processing.

Table 5.5. Statistical results for the quantitative analysis on morphological preservation performance, computed on the 17 WD algorithms included in this study: A1) Ahmadi et al. [144], A2) Castillo et al. [104], A3) Jamaluddin et al. [145], A4) Ivanushkina et al. [148], A5) Jadhav and Dhang [149], A6) Shayesteh and Fallahian [138], A7) Swarnalatha and Prasad [139], A8) Vigneron et al. [140], A9) Wang et al. [141], A10) Jaros et al. [143], A11) Martinek et al. [105], A12) Mochimaru et al. [151], A13) Ionescu [146], A14) Jothi and Prabha [150], A15) Rivet et al. [137], A16) Ishikawa et al. [147], A17) Baldazzi et al. [166].
*Specifically, $p < 0.05$, $p < 0.005$ and $p < 0.0001$ are represented by *, ** and ***, respectively, whereas – indicates no statistically significant difference.*

	A2	A3	A4	A5	A6	A7	A8	A9	A10	A11	A12	A13	A14	A15	A16	A17
A1	–	–	***	***	**	**	–	–	***	***	–	**	–	**	–	***
A2		***	***	***	***	***	***	*	***	**	–	***	***	***	–	***
A3			***	***	***	***	**	–	***	***	–	***	–	***	–	***
A4				–	***	***	***	***	***	–	***	***	***	***	–	***
A5					***	***	***	***	***	–	***	***	***	***	**	***
A6						–	***	***	**	***	***	–	***	***	***	***
A7							***	***	–	***	***	–	***	–	**	***
A8								–	***	***	–	**	***	**	–	***
A9									***	**	–	***	–	**	–	***
A10										***	***	–	***	**	***	***
A11											**	***	***	***	*	***
A12												***	–	**	–	***
A13													***	*	**	***
A14														***	–	***
A15															**	***
A16																***

optimal score, showing higher *PI* values, even though without statistically significant differences compared to the closer Swarnalatha and Prasad [139], Jaros *et al.* [143] and Shayesteh and Fallahian [138] WD algorithms. For the sake of the completeness, Figure 5.8 represents the *PI* values obtained for each analysed WD algorithm at different initial SNRs. As can be seen, the Baldazzi *et al.* [166] algorithm exhibited the lowest *PI* values for all noise levels.

5.4.3 Discussion

In this study, different WD post-processing algorithms and parameterizations have been explored and statistically compared for the identification of a possible optimal NI-fECG enhancement approach in terms of noise reduction and morphological preservation effectiveness. At first, a preliminary analysis for the identification of best parameterization was carried out, in order to represent each WD algorithm by a singular and best parameter combination, as reported in Table 5.2. However, by comparing at Tables 5.1 and 5.2, some further interesting aspects emerged. Firstly, hard thresholding seemed to overcome the soft one, on average. It was underlined for the WD algorithms proposed by Ahmadi *et al.* [144], Jadhav and Dhang [149], Wang *et al.* [141], Mochimaru *et al.* [151], and Ionescu [146], but not for Vigneron *et al.* algorithm [140], in which soft thresholding offered significantly better *PI* values (see Figure 5A.6 in Appendix A). These findings, despite in contrast with those achieved in [104], are coherent with the results obtained in [105], [138]. In fact, although hard thresholding may introduce discontinuities [104], it did not shrink the signal amplitude [105], thus guaranteeing a higher SNR and less morphology distortion, as can be seen in Figure 5.9. Conversely, for the Vigneron *et al.* algorithm, the trend was opposite since the WD did not effectively reduce the noise whereas the soft one did, as can be seen in Figure 5.9.

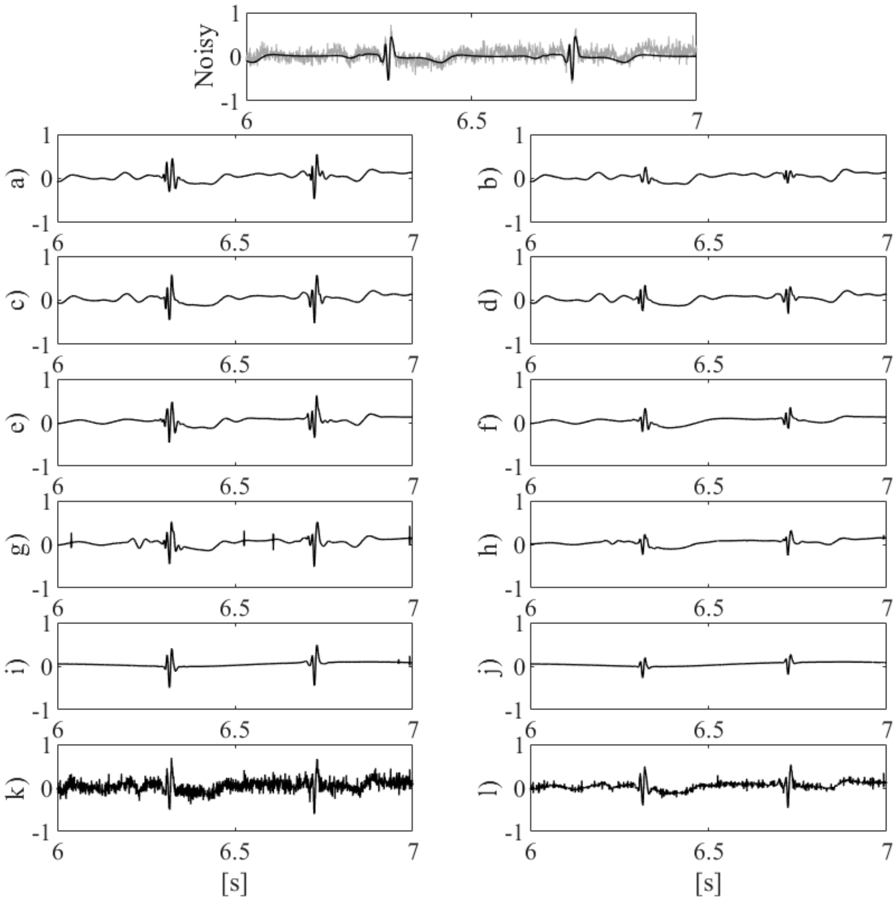

Figure 5.9. Effect of hard and soft thresholding in WD. In the upper row, the noisy fECG signal (SNR_{mn} originally equal to 7 dB) is represented in grey while the noiseless fECG component is depicted in black. Then, the same signal is displayed after WD by Ahmadi et al. algorithm [144] with hard (a) and soft (b) thresholding, Jadhav and Dhang algorithm [149] with hard (c) and soft (d) thresholding, Wang et al. algorithm [141] with hard (e) and soft (f) thresholding, Mochimaru et al. algorithm [151] with hard (g) and soft (h) thresholding, Ionescu algorithm [146] with hard (i) and soft (j) thresholding, and Vigneron et al. algorithm [140] with hard (k) and soft (l) thresholding. For all the other WD settings, default or best parametrizations were considered. Amplitudes are dimensionless.

Moreover, when looking at the parameter setting comparison for the Ionescu algorithm [146], it was evident that, among the most typical thresholds (i.e., Universal, Minimax, Rigrsure and Heursure), the Minimax threshold got better results than others, although in this case a single mother wavelet and decomposition level were considered. Moreover, despite in [138] the Rigrsure threshold was identified as optimal, our results are in accordance with other previous studies [104], [166] and are further confirmed by visual inspection of WD signals (see Figure 5.10).

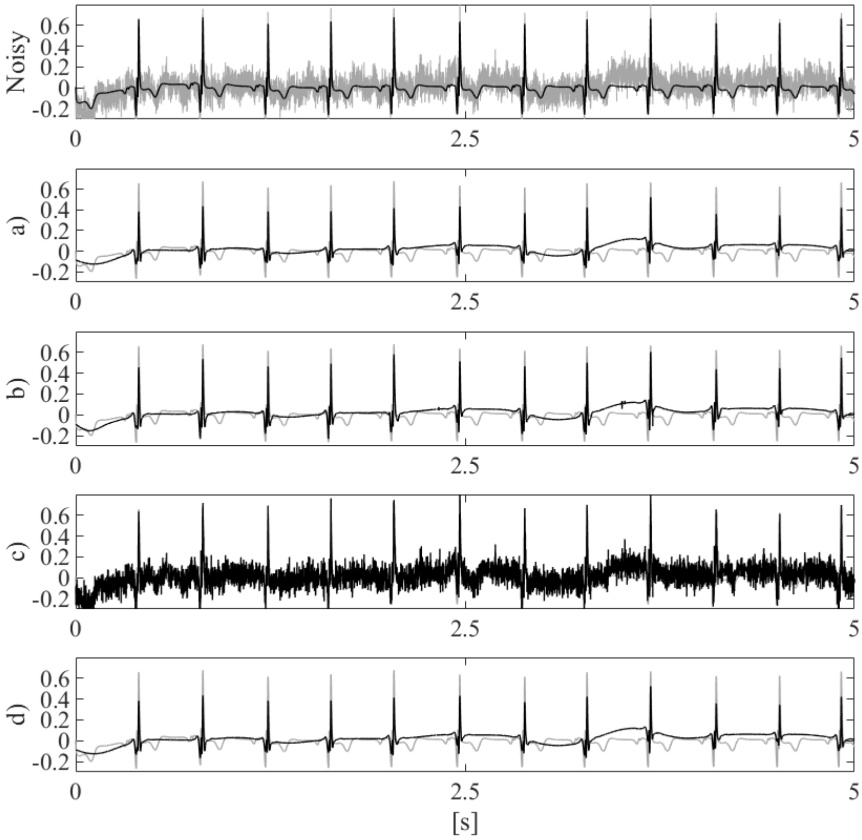

Figure 5.10. Effect of classical WD threshold on NI-fECG signal. In the upper row, the NI-fECG signal with and without noise (in grey and black, respectively) before WD is depicted, with SNR_{mn} at 9.2 dB. The same signal after WD by Ionescu et al. algorithm [146] is represented in the other rows, by exploiting bior4.4 mother wavelet, 9-level decomposition, hard thresholding and Universal (a), Minimax (b), Rigrsure (c), Heursure (d) thresholds. In row (a)-(d), the corresponding noiseless trace is depicted in grey.

Focusing on the last investigation, our results suggested that, when comparing all the 17 WD approaches in terms of overall performance, the Baldazzi *et al.* algorithm [166] showed significantly higher denoising effectiveness than all the others. This finding, which is based on the proposed *PI* formulation, is also evident when referring to Figure 5.11. In fact, as can be seen, the Baldazzi *et al.* algorithm [166] scores are the closest to the optimal one.

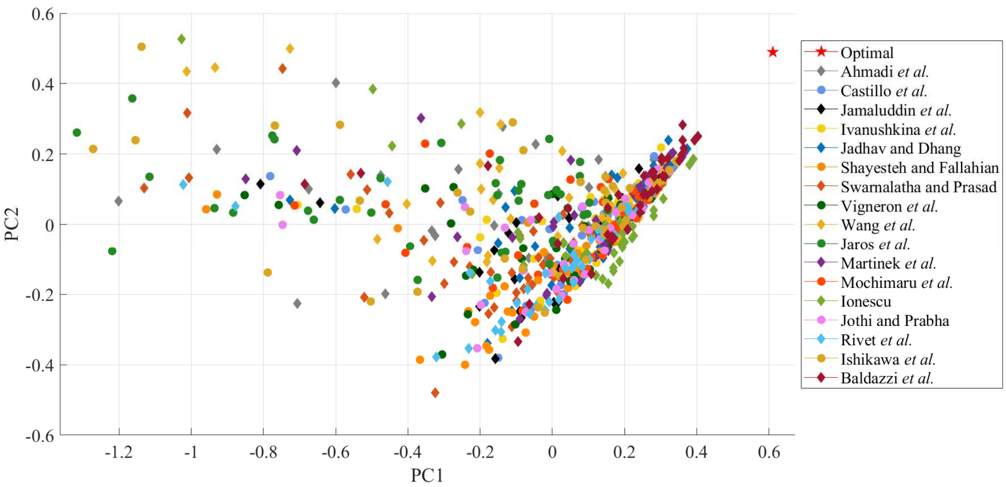

Figure 5.11. Scores of the different WD algorithms in the plane identified by the first two PCs in the overall performance assessment.

However, by looking at Figure 5.3, also WD algorithms by Jadhav and Dhang [149] and Martinek *et al.* [105] showed high performance when considering noise removal and morphological distortion together (see Figure 5.12), although without reaching statistical significance in some comparisons (see Table 5.3). The same trend was found when looking at the signal morphology preservation performance only, thus highlighting that the weight assigned to ρ and r_s was significantly higher than that assigned to the SNR in the overall performance investigation, as can be also appreciated in Figure 5.1. This latter aspect is further confirmed in Figure 5.12. Conversely, in this context, the WD approach by the Swarnalatha and Prasad [139] exhibited the highest median distance from the optimal score, followed by Jaros *et al.* [143], and Shayesteh and Fallahian [138] algorithms.

Since NI-fECG recordings may be useful for fHR estimation applications only, in which morphology is not assessed, in this study the noise removal efficiency exhibited by the different WD algorithms was investigated separately. In this analysis, the Ionescu algorithm [146] seems to be the best option. This finding, which has a marked statistical significance ($p < 0.0001$), is also confirmed by visual inspection in time-domain (see Figure 5.12) and in the PC plane (see Figure 5.13). Besides the Ionescu algorithm [146], also Wang *et al.* [141] and Baldazzi *et al.* [166] offered good noise reduction results.

Conversely, in order to give a deeper insight for an optimal fECG enhancement in applications requiring fECG morphological analyses, only ρ, r_s and RMSE were considered too. In this latter investigation, the Baldazzi *et al.* algorithm [166] stood out as best approach, as can be seen also in Figures 5.12 and 5.14, allowing for a less aggressive denoising with respect to the Ionescu algorithm [146] which, on the other hand, allowed for a better noise reduction. In this framework, valuable results were also achieved by Jadhav and Dhang [149] and Martinek *et al.* [105] algorithms.

In conclusion, the results of this comparative review highlighted how the adoption of different WD settings can significantly affect the denoising effectiveness, both in terms of noise reduction and signal morphology distortion. Moreover, the outcomes of our study suggest that parameter settings and denoising algorithms should be chosen according to the specific application. In fact, a higher noise reduction can determine a loss of significant signal content, which hampers any morphological analysis, but could be useful for the detection of foetal arrhythmias [70], [73]. On the other hand, WD algorithms introducing lower signal morphology distortions could reduce the effectiveness of fHR estimation algorithms, as the denoising is less aggressive.

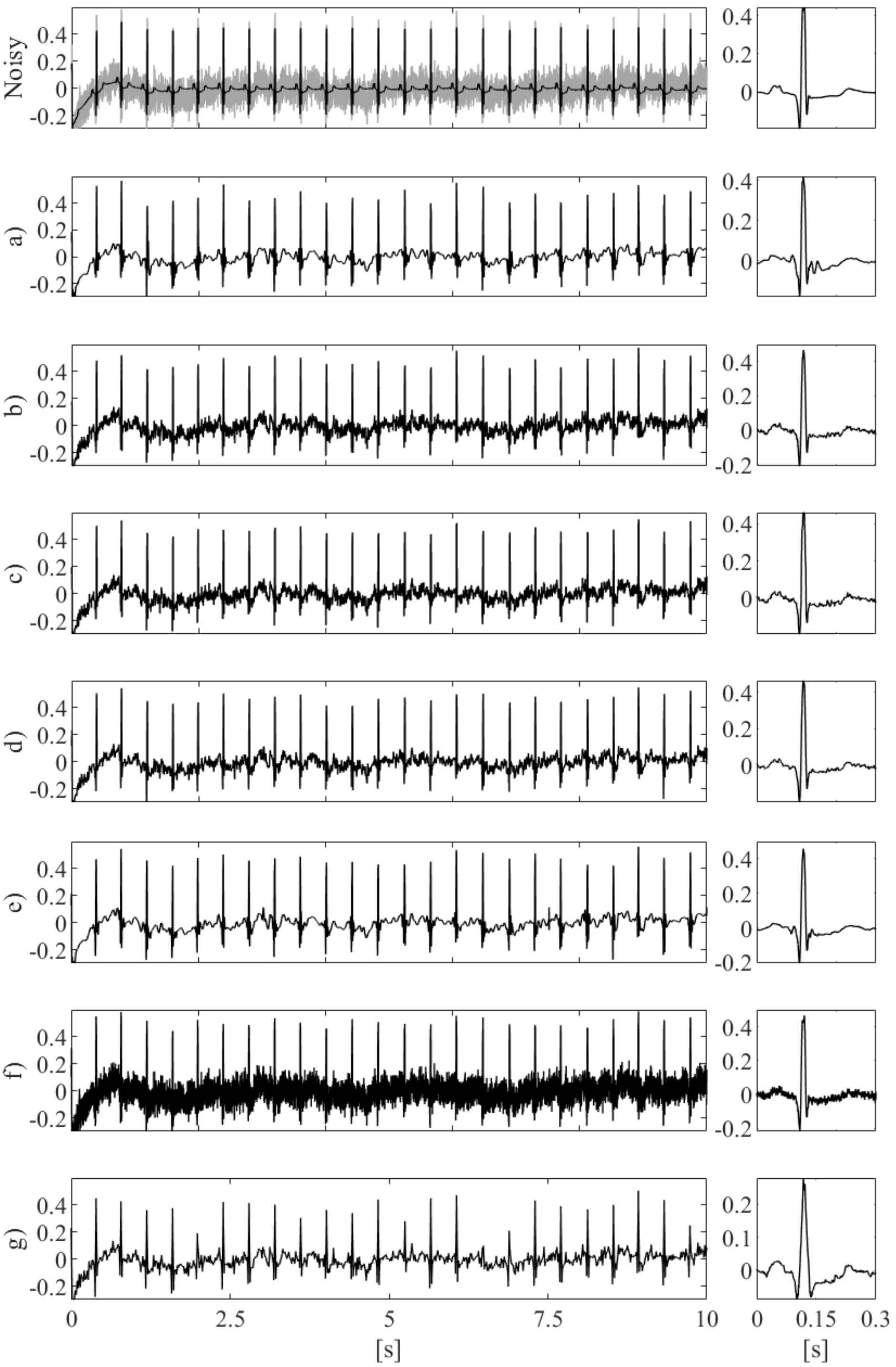

Figure 5.12. Effect of WD algorithms on NI-fECG signals. On the bottom left, a synthetic NI-fECG signal before WD (in grey, with initial SNRmn of 12.5 dB) and its noiseless counterpart (in black) are depicted, whereas on the right side its noiseless median template obtained by synchronized averaging is represented. In the next leftward rows, the same signal is represented after WD performed through the algorithm by a) Ahmadi et al. [144], b) Castillo et al. [104], c) Jamaluddin et al. [145], d) Ivanushkina et al. [148], e) Jadhav and Dhang [149], f) Shayesteh and Fallahian [138], g) Swarnalatha and Prasad [139], h) Vigneron et al. [140], i) Wang et al. [141], j) Jaros et al. [143], k) Martinek et al. [105], l) Mochimaru et al. [151], m) Ionescu [146], n) Jothi and Prabha [150], o) Rivet et al. [137], p) Ishikawa et al. [147], q) Baldazzi et al. [166]. In the corresponding rightward rows, the median templates obtained by synchronized averaging are shown. Figure is divided on two pages for better visualization.

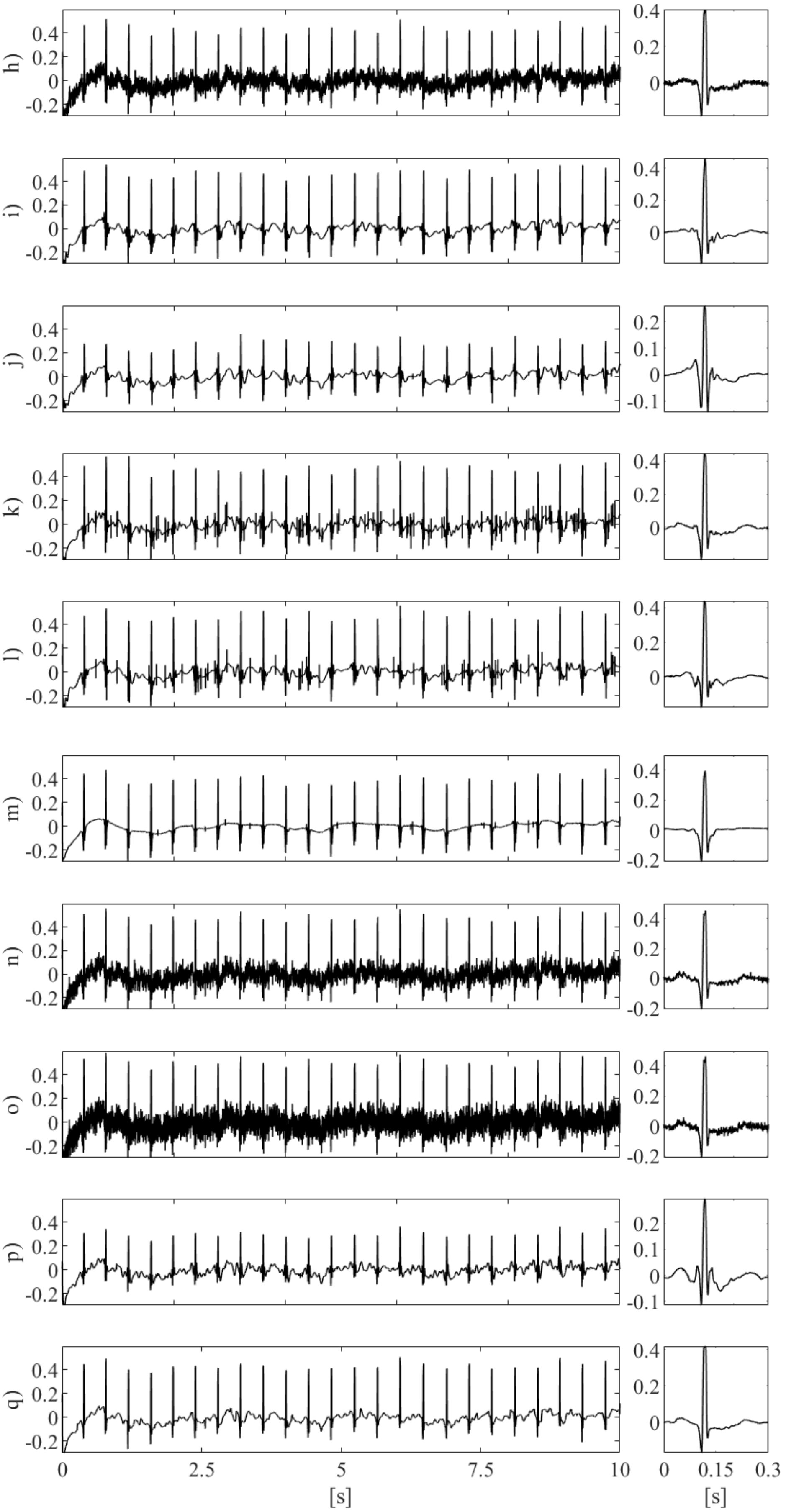

Figure 5.12. (Continued)

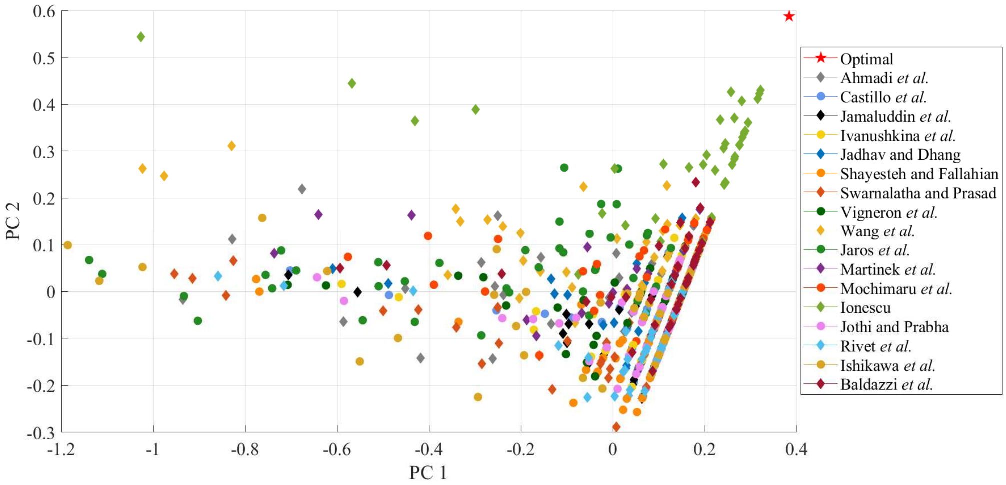

Figure 5.13. Scores of the different WD algorithms in the plane identified by the first two PCs in the noise reduction assessment.

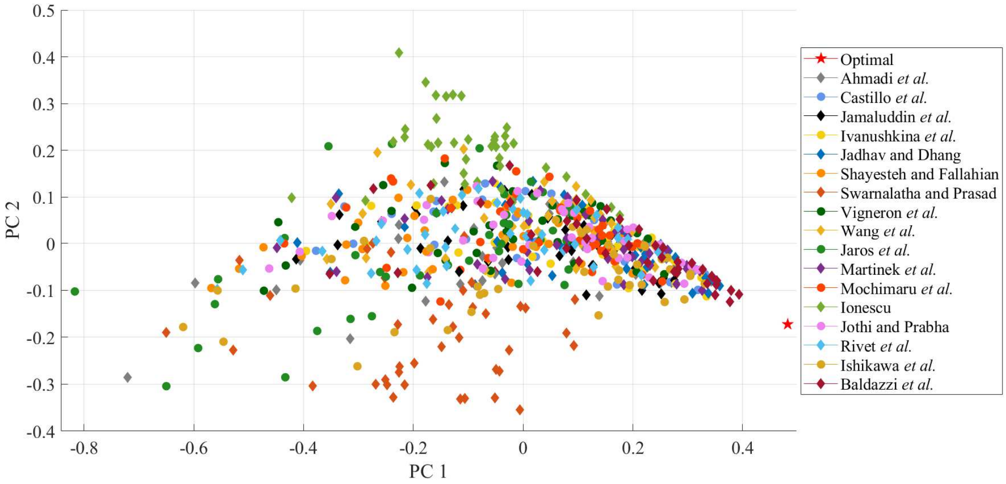

Figure 5.14. Scores of the different WD algorithms in the plane identified by the first two PCs in the morphology preservation assessment.

All these aspects should be carefully taken into account when performing the denoising of NI-fECG signals for their effective enhancement. Finally, another interesting aspect of this work concerns the innovative approach proposed for the assessment of post-processing algorithms. In fact, our evaluation methodology was robustly founded on the PCA and, remarkably, allowed the assessment of the different WD algorithms from different perspectives while avoiding the introduction of any biased weight to be assigned to the different figures of merit, in order to obtain a reliable *PI* definition.

Chapter 6

Conclusions on Part I

As discussed from the beginning of the Part I of this PhD thesis, the acquisition of high-quality fECG signal from non-invasive trans-abdominal biopotential recordings is severely hampered by different issues, mainly related to the NI-fECG signals low SNR and amplitude [3], [4], [17], [78], thus inhibiting the adoption of this technique for foetal cardiac wellbeing assessment in the conventional clinical practice [27]. This part of my PhD work came up in this context, studying and developing advanced signal processing tools aiming at providing morphologically preserved NI-fECG recovery. Specifically, both the NI-fECG extraction and the fECG post-processing stages have been deeply examined.

As regards the NI-fECG extraction algorithm, a novel approach was proposed in collaboration with Prof. Hau-Tieng Wu (Department of Mathematics and Statistical Science, Duke University, Durham, NC, USA). The proposed methodology showed promising results, not only in terms of foetal R-peak detection, but also in terms of signal morphology preservation capabilities, thus paving the way for its possible application in fHR monitoring devices and for clinically useful morphological analyses. Remarkably, further important advancements of the proposed techniques were not reported in this thesis, as their validation is still in progress, but will hopefully be presented in the scientific literature soon.

As regards the NI-fECG post-processing investigations, despite the widespread application of WD on different biomedical signals, in this context WD has been generally applied to remove noise interference without paying particular attention to its possible implementation setting. Conversely, this part of my PhD thesis underlined that this powerful tool must be used with special care in this particular application because of its possible negative impact on the signal morphology or even on further signal processing steps applied downstream, such as the foetal QRS detection. The results revealed how the adoption of a level-dependent scaling factor in the definition of the threshold significantly improves the denoising effectiveness, compared with conventional approaches proposed in the literature. Specifically, the best WD algorithm settings delineated in Chapter 4 emerged as the best option for the NI-fECG post-processing purpose when compare with all the approaches proposed in the scientific literature until now, to the best of my knowledge, especially in terms of signal morphology preservation. However, a different strategy derived from the work by Ionescu [146] was better when noise reduction can be achieved without special attention to the signal morphology, such as for fHR extraction. All the underlined aspects could be valuably considered when approaching the denoising of fECG signals for enhancement, thus contributing to the exploitation of the NI-fECG for effective antenatal cardiological assessment.

Part II

Intracardiac electrophysiology

Chapter 7

Overview of cardiac arrhythmias: basic classifications, electrophysiological substrates and studies

7.1 Cardiac arrhythmias

The electrophysiological principles of the conduction system in a healthy human heart have been already described in Section 1.2. However, some abnormal alterations of the normal sinus rhythm can occur, giving birth to the so-called *arrhythmias*. According to the heart rate observed, we can mainly distinguish between *tachycardias* (also named as tachyarrhythmias), in which the heart rhythm is accelerated (>100 beats per minute or bpm, at rest), and *bradycardias* or bradyarrhythmias, in presence of which the rhythm is slowed down (<60 bpm)[14], [19]. Focusing on tachycardias, according to their site of origin we can identify supraventricular and ventricular tachycardias.

Supraventricular tachycardias originate above the ventricular conduction system, i.e. in the atria, in the sinoatrial node and in the atrioventricular junction. Depending on the terminology, they may include sinus tachycardia and paroxysmal supraventricular tachycardias (i.e. mainly atrial tachycardias, atrioventricular nodal re-entrant and atrioventricular re-entrant tachycardias) showing a nearly organized rhythm, but also atrial flutter and atrial fibrillation, with higher atrial rates and characteristic waves in ECG leads [19].

Ventricular arrhythmias are due to ectopic depolarizations occurring in the ventricles and comprise premature ventricular beats or contractions (PVCs), ventricular tachycardias (VTs) and ventricular fibrillation (VF). Given the topic of this PhD thesis, ventricular arrhythmias are deeply explored in the following paragraph, with a special focus on VTs.

7.1.1 Ventricular arrhythmias and tachycardias

Among ventricular arrhythmias, **PVCs** are abnormal ectopic beats typically arising before an expected normal beat, i.e. a sinus P wave. They can appear as a single beat or as subsequent depolarizations, frequently with regular rates with respect to normal cardiac activations, as such giving rise to characteristic ECG recordings as in the case of ventricular bigeminy and trigeminy [19]. PVCs may have unifocal or multifocal origins, and their site of origin determines the morphologies by which they appear in the different ECG leads. PVCs mainly reflect the automatic activity of extra ventricular pacemakers and may affect healthy subjects and patients suffering from heart diseases, both symptomatically (i.e., palpitations) or not.

VTs are identified by abnormal ventricular depolarizations resulting in a heart rate of at least 100 bpm at rest. VTs can be classified according to their duration and morphology [19], [195], [196]. Depending on the tachycardia duration, VTs can be identified as sustained or non-sustained. Specifically, non-sustained VTs have a duration of 30 s or less and terminate spontaneously without hemodynamic compromise, whereas sustained VTs typically last more than 30 s and/or require prompt termination because of hemodynamic vulnerability [19], [195]–[197]. Nonetheless, the appearance-based classification distinguishes between monomorphic and polymorphic VTs. Monomorphic VTs exhibit a singular, repetitive, and stable QRS morphology. Among the most common symptoms due to this form of VT, palpitations, shortness of breath, and light-headedness could be mentioned [19]. Conversely, polymorphic VTs are characterized by multiple and variable QRS morphologies, which reflect multiple origins and variable activation patterns [195], [197]. Torsades de Pointes is an example of polymorphic VT pathology with QT interval prolongation. Except for idiopathic forms, VTs can be caused by structural heart disease, both related to previous ischaemic events and non-ischaemic cardiomyopathies as congenital heart disease, but also by genetic conditions and metabolic alterations [197]. VT patients are frequently exposed to a major risk of sudden cardiac death, and their treatment may vary from pharmacological antiarrhythmic therapy, electrical shock therapy by implantable cardioverter-defibrillators (ICDs) and catheter ablation, mainly according to the underlying heart disease and clinical presentation [198], [199]. The prognosis is also difference, according to the originating condition. In this regard, while polymorphic VTs are mainly due to myocardial ischemia or inherited disorders, monomorphic VTs commonly originate from re-entrant mechanisms occurring in myocardial scars [197], and will be better explored in Sections 7.2 and 8.1.

VF is a rapid (> 300 bpm, usually) and completely irregular ventricular activation with variable QRS morphologies and timings, due to very disorganized depolarization pathways [195], [196]. It is frequently associated with pre-existing monomorphic or polymorphic VTs conditions [19]. VF is the most risky among all the cardiac arrhythmias since it determines a totally uncoordinated ventricular contraction that, if not promptly interrupted by electrical defibrillation, leads to unconsciousness, cardiac arrest and death [14].

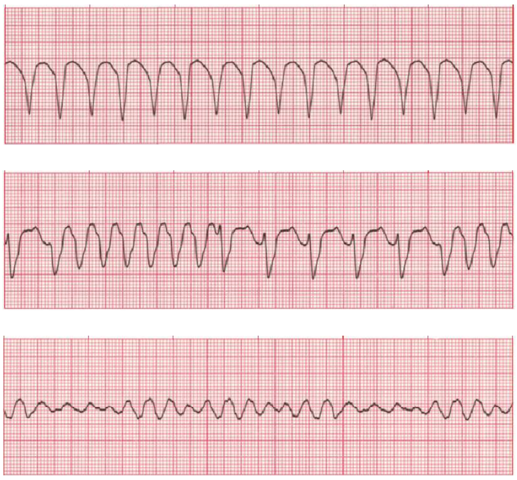

Figure 7.1. Examples of surface ECG recordings in presence of monomorphic VT (top), polymorphic VT (middle) and VF (bottom).

7.2 Electrophysiological mechanisms underlying cardiac arrhythmias

The electrophysiological mechanisms leading to the development of cardiac arrhythmias may be associated with alterations in the cardiac impulse formation, including automaticity and triggered activity, or disorders in its propagation, i.e. re-entry [195], [198], [200]–[202].

Automaticity is defined as the ability of cardiac cells to autonomously generate action potentials [200]. As already explained in Section 1.2, it reflects a physiological condition occurring in healthy heart, and specifically in the pacemaker cells of the sinoatrial node. In normal conditions, sinoatrial pacemaker cells exhibit the highest depolarization rate and, as such, they act as primary drivers of cardiac electrical depolarization. However, in case of sinoatrial node dysfunctions or alterations in the impulse propagation, other cardiac structures in atria or ventricles, also including the so-called latent or subsidiary pacemaker cells, may develop spontaneous depolarizations. Overall, disorders of impulse formations can be ascribed to altered normal automaticity, i.e. suppression or enhancement of pacemaker activity in specialized heart cells as those in sinoatrial node, atrioventricular node and Purkinje system, or to abnormal automaticity arising in non-pacemaker myocardial cells in atria and ventricles [202]. In general, arrhythmias can be caused by inappropriate discharge of the sinoatrial node, resulting from improper activity of the autonomous nervous system or other factors, but also by the action of the latent pacemakers, or both, leading to a shift of the impulse origin in ectopic sites [195], [200]. Indeed, when the rate of the sinus node decreases, it may happen that sinoatrial node does not overdrive subsidiary pacemakers of ectopic sites anymore, as such allowing them to start firing at their intrinsic rate. On the other hand, latent pacemakers can be subject to an enhanced automaticity, thus resulting in overdriving the normal sinoatrial discharge and leading to accelerated automatic rhythms. Nonetheless, automaticity may include also parasystole, in which the latent pacemaker, also known as parasystolic focus, is protected from the sinoatrial impulse propagation, thus generating ectopic activations with different intrinsic rates simultaneously [200]. Normal or abnormal automaticity often contribute to cardiac arrhythmias which, in principle, are due to nonautomatic mechanisms. This is the case of premature beats generated by automaticity that, however, can pave the way for re-entrant mechanisms [195].

Triggered activity is associated with impulse generation caused by depolarizing oscillations in the membrane potential, also called afterdepolarizations [200], [202]. In this case, the activity is not self-generating but triggered by the afterdepolarization. Afterdepolarizations can generate focal arrhythmias by inducing a depolarization exceeding the activation threshold, but also re-entrant arrhythmias, which cause a prolongation in action potential, which consequently may determine the development of a refractoriness-related unidirectional block [201]. Afterdepolarizations may occur during the repolarization phase of a preceding action potential (early afterdepolarizations, EADs), or later (delayed afterdepolarizations, DADs). Specifically, DADs occur after repolarization phase is fully completed, and their possibility to induce triggered activity strongly depends on their amplitude and on the actual membrane potential. Conversely, the EADs are depolarizations developed in membrane potential that may appear during the plateau level (phase 2 EADs) or during the repolarization phase (phase 3 EADs) (see Figure 7.2), and as such they are able to alter the repolarization upstroke of cardiac myocytes by sudden depolarizing shifts of the membrane voltage [195].

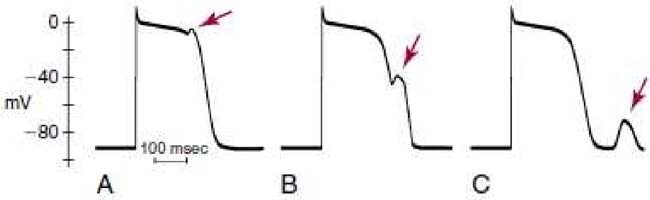

Figure 7.2. Schematic representation of afterdepolarizations occurring with a Purkinje cell action potential. A) EAD occurring during plateau phase, B) EAD developed during repolarization phase and C) DAD [195].

Re-entry mechanism is based on the persistence of a propagating impulse that excites the cardiac tissue repetitively and continuously [201]. In this condition, an excitatory wavefront does not vanish after activation as in normal conductive pathways, but propagates in a circular path and activates the same surrounding cardiac tissue cyclically, taking advantage of the periodical out-of-refractoriness periods. Remarkably, re-entrant mechanisms are responsible of most clinical tachyarrhythmias [195], [202], as such they deserve a deeper explanation in the following.

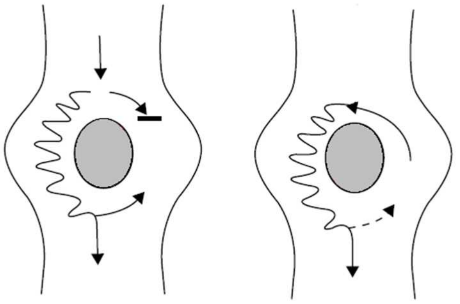

Figure 7.3. Schematic representation of a re-entry. Adapted from [202].

For the re-entry to be initiated and sustained, different prerequisites have to be accomplished [195], [201], [202]. As regards the substrate, the myocardial tissue constituting the circuit has to present heterogeneous properties, from the electrophysiological, conductive and refractoriness perspectives. Moreover, in order to induce the excitatory wavefront to travel along the circular path, a central area of anatomical and/or functional block composed of unexcitable tissue is needed. Another essential element is the unidirectional conduction block, which can be temporary or not, since in case of its absence, the impulse would travel along both sides of the central block, flow down and extinguish itself (see Figure 7.3). Moreover, its role is fundamental to guarantee the initial excitability of half-side of the re-entry. Furthermore, since the wave of excitation might flow only in excitable cardiac tissue, the already excited tissue should have completed its refractory period for the circular pathway to completely pass through again. As such, the wavefront must be sufficiently delayed in its propagation in order to encounter, at each time, out-of-refractoriness myocardial cells. This aspect is typically ensured by slow-conduction areas in re-entrant pathways, which exhibit a decreased conduction velocity [195], [200], [202]. Finally, the re-entrant mechanism may need an initiating trigger to be established, as a premature depolarization, but also a critical mass of tissue to be sustained.

When the re-entry is due to anatomical structures, it is referred to as anatomical re-entry. In this case, the central area of block is given by an anatomical obstacle, around which the re-entry is maintained. In this regard, two essential aspects have to be introduced: the *wavelength* and the *excitatory gap* [195], [202]. The former is defined as the product of conduction velocity and refractory period, and mainly concerns the possibility for the re-entry to be sustained in all those cases in which the wavelength is shorter than the length of the circular path. Conversely, the excitatory gap embodies any possible excitable tissue arising between the head of the re-entrant excitatory wavefront and the tail of the preceding one, and it is important not only for the re-entry perpetuation but also for its possible termination by external electrical stimulation. Another type of re-entrant mechanism is the functional re-entry, which is due to the heterogeneous electrophysiological properties of the involved myocardium. Among functionally defined re-entries, several types can be mentioned according to the different paths and principles [195], [200], [202]. The first one is the leading circle re-entry, in which the excitatory waveform travels on partially refractory pathways and around a core that, conversely, is totally non-conducting because exposed to continuous excitations. Furthermore, a different re-entrant type is due to the different conduction and repolarization properties affecting the myocardium in specific circumstances, which may cause the so-called anisotropic re-entry. A singular example is given by the figure-of-eight re-entry, which is derived by the combination of two excitatory wavefronts that, despite travelling in opposite sense, may converge into the same common isthmus. A different form is represented by the reflection mechanism, in which the wavefront may propagate in both directions on the same path thanks to the presence of a slow-conduction tissue that guarantees the extinction of the refractory period. Finally, the last functional re-entry types are characterized by a spiral rotating propagation pattern that, on one hand, ensures that the core remains inactive, whereas on the other allows for slow conduction of the impulse. Most of the functional re-entrant mechanisms are schematically reported in Figure 7.4.

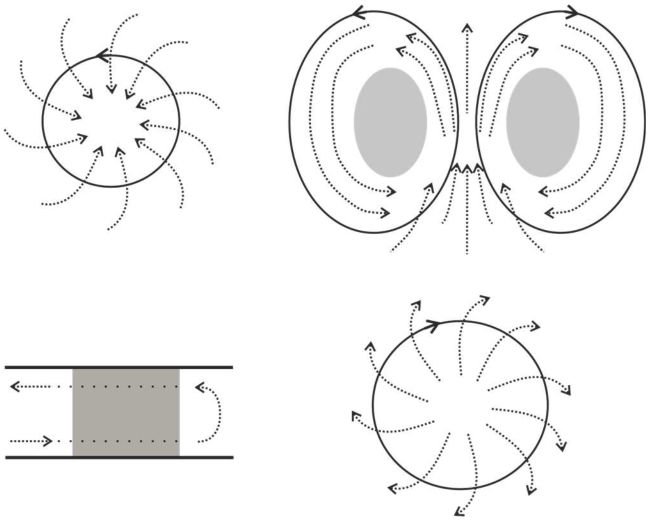

Figure 7.4. Schematic representation of different functional re-entry types: leading circle (on the top left), figure-of-eight (on the top right), reflection (on the bottom left) and a spiral wave (on the bottom right). Adapted from [195,202]. Arrows represent excitatory wavefronts, whereas solid lines the resulting re-entry. In the figure-of-eight re-entry, central block areas are depicted in light grey, whereas slow-conduction areas of reflection mechanism are reported in dark grey.

7.3 Electrophysiological study of cardiac arrhythmias

Electrophysiological studies are often indicated in patients affected by cardiac arrhythmias [203]. During these invasive diagnostic examinations, the cardiac electrical activity is examined locally, in order to reach a deeper understanding of the nature and source of the involved arrhythmia, but also to identify the best-suited intervention for its treatment. The electrophysiological study is performed by slightly invasive clinical procedures, in which a variable number of thin multielectrode catheters are inserted percutaneously and are guided directly into the cardiac chambers, sometimes using fluoroscopy [201]. As such, the electrical activity can be acquired from the cardiac chamber in which the catheter is positioned, leading to intracardiac recordings called *electrograms* (EGMs) [195], [204]. However, intracardiac catheters may have different properties and forms in order to perform recording, but also pacing and ablation, in different sites and with different modalities.

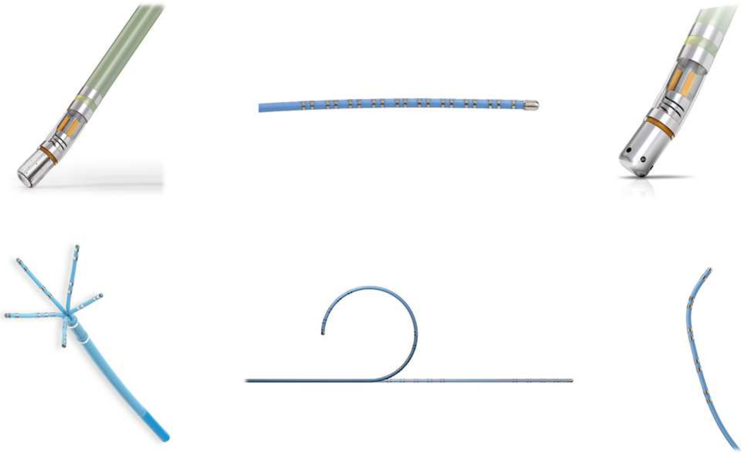

Figure 7.5. Examples of multi-electrode catheter for mapping and ablation.
On top row, ThermoCool SmartTouch SF (left), CristaCath (middle), ThermoCool SmartTouch catheters are represented. On bottom row, the PentaRay (left), the Duo-Decapolar catheter (middle) and Decapolar catheters are depicted (Biosense Webster, Inc., Diamond Bar, CA, USA).

7.3.1 Intracardiac electrograms

Unlike the surface ECG, that allows the recording of the whole cardiac electrical activity, intracardiac EGMs represent the electrical activity of the local cardiac tissue close to the catheter electrodes [195]. Specifically, near-field potentials related to the local electrical activity near the recording electrodes of the catheter, and far-field potentials from remote cardiac activations are present in intracardiac EGMs [201]. Important information can be deduced by EGM amplitude, morphology, duration and its relationship with other recorded intracardiac signals, as the local activation time, the direction of wavefront propagation and the activation complexity of the myocardial tissue surrounding the recording electrode [195], [201]. Similarly to the ECG acquisition, extracellular potentials may be modelled as multiple electric dipoles, whereas the wavefront can be seen as their vectorial sum [204].

EGMs may be acquired in bipolar or unipolar recording modes, leading to signals with different morphologies and characteristics, mainly in terms of field of view, directionality, spatial and temporal resolution [204]. However, many aspects should be taken into account when analysing the EGM morphologies, as the adopted filtering, the sampling frequency, the electrode size, the contact force and the catheter position [205].

Unipolar EGMs are acquired as the potential difference between the voltage of the recording (exploring) electrode, which is placed in contact with the cardiac chamber, and the reference voltage offered by either an indifferent electrode located at a distance from the heart or the Wilson’s central terminal [195], [204]–[206]. Therefore, their field of view encloses all activations occurring between the recording and the reference electrodes. In general, a positive deflection will be displayed on the unipolar EGM when the activation wavefront is approaching the exploring electrode, whereas a negative deflection will appear when it travels away from it (see Figure 7.6). On these premises, this recording modality may provide information about the direction of wavefront propagation. Nonetheless, the amplitude of the unipolar EGM is inversely proportional with respect to the distance between the source and the recording electrode. In this regard, one main disadvantage of the unipolar EGMs is that they are strongly and inevitably affected by considerable far-field signals, of limited amplitude the farther they are coming from [204], [206]. However, unipolar recordings allow to record signals with good resolution in both time and spatial domains, which are not affected by the propagation direction.

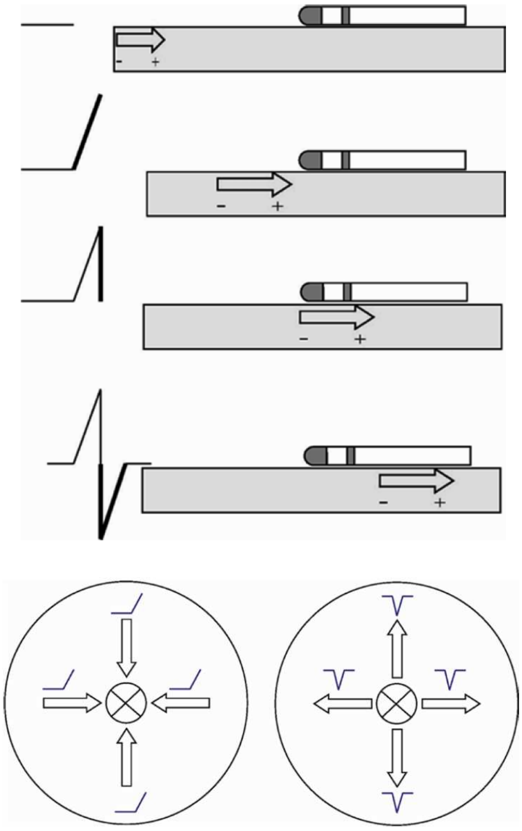

Figure 7.6. Representation of the unipolar electrogram recording. When the excitatory waveform (arrows) is approaching the recording electrode, a positive deflection in displayed. Conversely, when it flows away, the recorded signal becomes negative. As such, even if the wavefront is moving towards from different directions, it would not be reflected by the electrogram morphology [204].

Bipolar EGMs are given by the potential difference obtained between two exploring electrodes placed both in contact with the myocardium, or, equivalently, by the mathematical difference between two unipolar recordings [204], [206], [207]. Bipolar EGMs show higher SNR and better represent high-frequency components with respect to unipolar recordings [195], [205], being less affected by the far-field and common noise contributions. As such, bipolar EGMs are preferentially adopted to record local activity deflections, as in the case of depolarizations arising from impaired myocardial tissue, which are frequently associated to arrhythmogenicity [147]. The amplitude and duration (or width) of bipolar EGMs are strongly influenced by several factors, including the distance between the source and the electrodes, the inter-electrode distance, the direction of propagation and the conduction velocity [195], [204]. In this regard, myocardial areas of slower conduction result in wider deflections in bipolar EGMs. However, bipolar EGMs cannot provide proper information about the propagation direction. As such, despite the bipolar EGMs are those typically adopted in electrophysiological and mapping studies, simultaneous unipolar recording may help in some conditions, as for propagation direction and local activation time assessment [195], [201]. Given the different drawbacks of both recording modalities, different solutions have been proposed in recent years, as the omnipolar recording and the Laplacian technique [205].

In the light of the objective of the second part of this PhD thesis, it should be highlighted that the EGM morphology, amplitude, and timings play a key role in the clinical electrophysiological procedures. Firstly, the EGM amplitudes are important from the clinical perspective, especially in mapping and ablation procedures, since they are used for the distinction of healthy myocardial tissues from damaged ones [206]. In fact, an amplitude reduction may be due to structural changes or zones of activation blocks, inducing a reduced number of cells to be activated [205]. Specifically, in ventricular bipolar EGMs, peak-to-peak amplitudes below 0.5 mV have been associated to dense scar tissue[2], whereas voltages above 1.5 mV to normal myocardium [208]. Moreover, in case of alteration in the cell-to-cell electrical coupling or, more in general, because of anisotropic properties of the substrate, the propagation patterns of myocardial cells may be affected. Particularly, these situations may lead to a disordered and asynchronous conduction sequence, which results in fractionated EGMs, as represented in Figure 7.7. This condition is frequently associated with the presence of local fibrosis, which may occur in normal cardiac tissues, but mainly in myocardial tissues damaged by ischemia [195], [204]. As such, these features in intracardiac EGMs may provide a lot of information regarding many underlying electrophysiological problems.

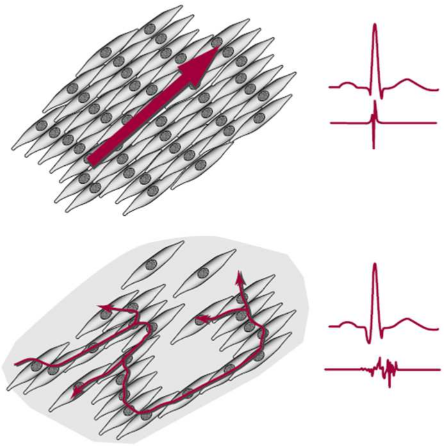

Figure 7.7. Electrograms obtained by healthy myocardial tissue (top) and by myocardial scar (bottom). As can be seen, in the top figure, the electrogram recorded is sharper, because many cells are activated rapidly and synchronously. Conversely, in presence of a scar (bottom), the conduction is highly irregular and displaced, thus the resulting electrogram is significantly fragmented and attenuated [195].

7.3.2 Cardiac mapping: tools and techniques

Heart rhythms and arrhythmias are frequently analysed through specific electrophysiological procedures, in which their electrical potentials are characterised from different perspectives and their sources are spatially localised in 3D in the cardiac chamber. These processes are generally referred to as cardiac mapping, in which different recording modalities and systems can be exploited [195], [201], [207]. Specifically, signal acquisition for the cardiac mapping can be performed by catheters in direct contact with the endocardium (endocardial mapping) or the epicardium (epicardial mapping), by intracardiac non-contact electrodes (non-contact mapping) or by body surface electrodes (body surface potential mapping or ECG imaging) [195], [204], [206]. In this regard, many different intracardiac catheters are available, with a single electrode allowing point-by-point acquisitions, or multiple electrodes for several simultaneous recordings.

---

[2] Here, scar is associated to ventricular myocardial tissue in which fibrotic tissue developed after an injury, thus hampering the normal impulse propagation. Ventricular scars are mainly due to ischaemic events, and specifically to myocardial infarction, but also to nonischaemic cardiomyopathies or to cardiac surgical treatments [214].

Cardiac mapping may include very different techniques, as activation mapping, pace mapping, entrainment mapping, and voltage or substrate mapping.

Activation mapping analyses the cardiac activation sequences and patterns based on EGM local activation time. Therefore, it provides this temporal activation information visually, by representing the local activation time as colour-coded filling of the reconstructed three-dimensional cardiac chamber, which can be useful in focal and macro re-entrant arrhythmias [195], [206], [207]. As such, after a reasonable number of points in the chamber of interest have been recorded, a continuous progression of colours, spanning from the earliest to the latest local activation in the mapped chamber can be appreciated.

Pace mapping aims to identify the tachycardia source by pacing at different endocardial sites, in order to induce the same ECG morphology, i.e. P wave and QRS complexes similar to those observed during tachycardia [195], [206], [207], [209]. In fact, by pacing at specific cycle lengths in proximity of the tachycardia focus, it is possible to induce the same activation sequence, thus resulting in similar ECG waveforms recorded. The catheter is considered to be as close to the tachycardia site as higher the accordance of the ECG waveforms recorded during pacing and tachycardia. Therefore, in this sense, the analysis of the surface ECG and its correlation with tachycardia ECG recording allows estimating the pacing site location of the tachycardic focus.

Entrainment mapping allows detecting the presence and location of a re-entry circuit by exploiting pacing manoeuvres and their interaction with the tachycardia [195], [206], [207], [210]. Entrainment is mainly based on the presence of an excitable gap in the re-entry, whose excitable myocardial tissue can be captured by a premature pacing stimulus. In this condition, the external stimulus may propagate in antidromic (retrograde) direction, colliding with the previous wavefront of activation, but also in orthodromic (anterograde) direction in the same re-entrant path, therefore resetting the tachycardia.

Substrate (or voltage) mapping provides the spatial distribution of the EGM peak-to-peak maximum amplitude, by adopting colour scales and the superposition of acquired voltage values to the anatomical cardiac chamber geometry [195], [206], [207]. It is important since, as already explained in the previous section, amplitude reduction can be ascribed to structural or functional alterations [205]. Local EGM amplitude can be acquired in sinus rhythm or during pacing, and allows for the identification of low-voltage areas (such as scars) from normal voltage areas (such as healthy tissues), but also border-zones regions associated to damaged but still significantly conductive myocardium [204], [205]. As such, voltage mapping allows the delineation of re-entrant circuits and localization of arrhythmia, frequently guiding substrate ablation in ventricular tachycardia [201], [206]. However, in this regard, many novel mapping strategies have been proposed [211].

Several new mapping systems have been proposed in the last decades, providing novel insights into arrhythmias generation and maintenance, but also for their ablative therapy [207], [212]. Specifically, many **electroanatomic mapping (EAM) systems** have been proposed to overcome the limitations imposed by conventional contact mapping systems based on fluoroscopy, allowing to obtain both electrophysiological and anatomical data of the cardiac chamber with high resolution, high efficacy in arrhythmia mapping and reduced fluoroscopic time and exposure [207], [213]. These systems are particularly useful when arrhythmic scar-related mechanisms involve complex anatomy or arrhythmia substrates close to important cardiac structures, as in those cases the functional heart structures can be marked and avoided by ablative therapies while focusing specifically on the arrhythmia origin [213]. The most widely adopted three-dimensional EAM mapping systems in the clinical procedures are the CARTO®3 system (Biosense Webster, Inc., Diamond Bar, CA, USA), the EnSite NavX system (St. Jude Medical, Inc., St. Paul, MN, USA) and the Rhythmia system (Boston Scientific, Inc., Marlborough, MA, USA) [206]. Three-dimensional EAM systems allow the study of the cardiac chamber by performing intracardiac recordings and 3D representation of different cardiac activation properties though colour-coded strategies. Specifically, many features as activation timing and amplitude voltages are extracted from the intracardiac EGMs, which are acquired at different sites in the cardiac chamber. Remarkably, in these systems, the mapping-ablation catheter is precisely located in the three-dimensional space of the heart by the mapping system using magnetic-based and/or impedance-based technology [206]. Moreover, the outer positions assumed by the mapping electrode catheter are exploited to generate the surface geometry of the EA map. As such, thanks to the accurate three-dimensional location of the different EGM acquisition sites, these extracted data can be exploited to generate a three-dimensional reconstructed map of the cardiac chamber with colour coding, thus allowing electrophysiologists to pinpoint arrhythmogenic re-entry or the focus of origin of the arrhythmia to target for ablation. Many technological advances are permeating in the field, leading to the integration of different technologies as contact force sensors and blending of images acquired by computer tomography, magnetic resonance or synchronous intracardiac ultrasound catheters [206], [207].

Nonetheless, EAM is typically aimed at the identification of target sites for consequent catheter ablation. Catheter ablation is mostly based on radiofrequency (RF) energy, which is delivered on the myocardial tissue to induce thermal lesions and inhibit the conductive functioning in arrhythmogenic sites [195], [201]. The RF catheter ablation is found to be the dominant modality of arrhythmia ablation, despite new technologies have been introduced, as ultrasound, laser, microwave, and cryoablation [206].

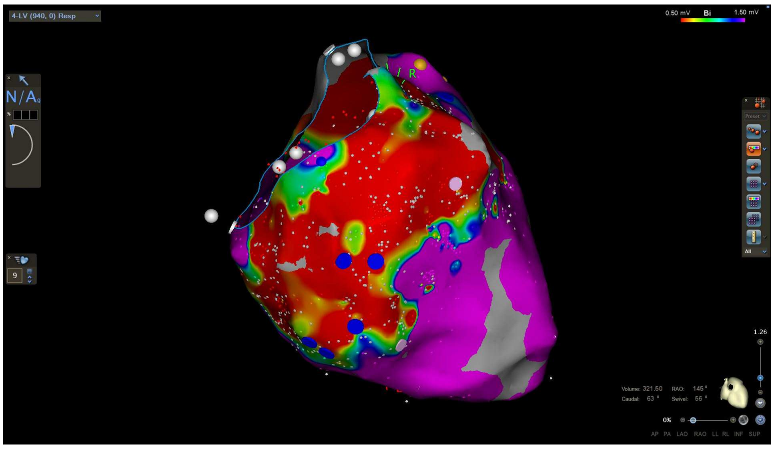

Figure 7.8. Example of a voltage map obtained from the EAM of a left ventricle in a post-ischaemic patient by using the CARTO®3v6 system (Biosense Webster, Inc., Diamond Bar, CA, USA). Bipolar voltage values below 0.5 mV are displayed in red, above 1.5 mV in purple, whereas intermediate amplitudes are coloured accordingly. Along with bipolar voltages, some tags introduced during the clinical procedure are also reported.

Chapter 8

Background on post-ischaemic ventricular tachycardia: arrhythmogenic substrate and targeting strategies for ablation

8.1 Role of scar in VT arrhythmogenesis

VTs are mainly induced by ventricular scars in several forms of heart disease [214]. Ventricular scars are typically caused by myocardial infarction, but also by nonischaemic cardiomyopathies and events involving fibrogenesis. Indeed, within scars, surviving myocyte bundles may coexist with dense fibrotic tissues, which together may lead to slow conduction, disordered propagation and conduction blocks, thus creating the conditions for re-entrant mechanisms [214]–[217]. Therefore, scar-related re-entry is found to be the primary arrhythmogenic mechanism for VT in structural heart disease [218]–[221]. VT circuits are typically characterized by complex morphologies with multiple entrances and exits [222], [223]. In this regard, structural heterogeneity of these areas may lead to multiple and variable re-entry morphologies involving epicardial, endocardial and/or midmyocardial tissues. However, some patterns of VT circuits as single-loop, double-loop and multiple-loop re-entries have been described [218], [224], [225].

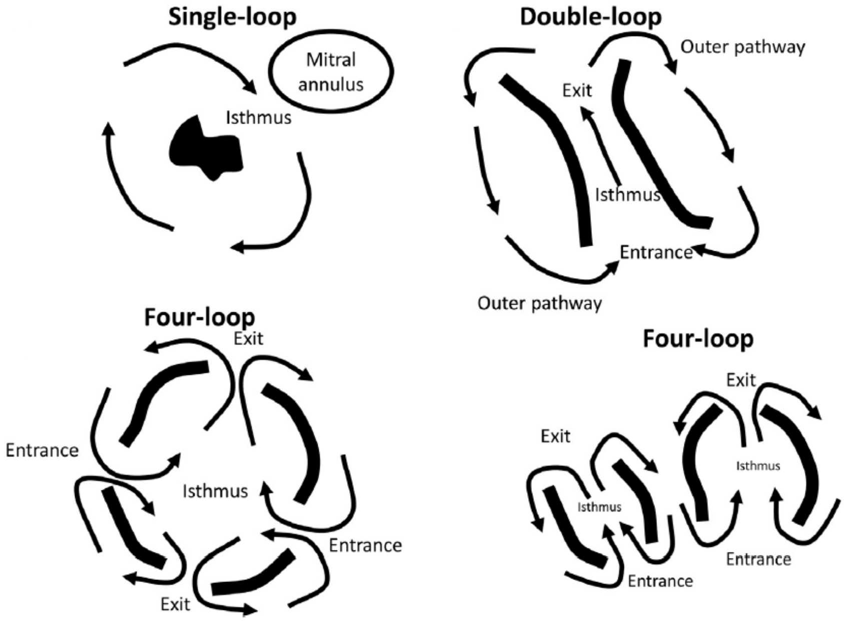

Figure 8.1. Examples of VT re-entry circuits [218].

These slow-conduction scar-related myocardial areas are characterized by low-amplitude voltages [222] and have been frequently associated to characteristic morphologies in the recorded EGMs, identified as fractionation [215], [226]–[228], isolated [229] and late potentials (LPs) [230]–[232], and local abnormal ventricular activity (LAVA) [233], [234]. However, despite variously defined, both LAVA and LPs have been proven to be associated to fundamental components of VT re-entry [235].

All these EGM features and properties have been exploited for targeting arrhythmogenic sites during substrate-guided mapping for their subsequent ablation, to make these areas unexcitable from an electrical point of view.

8.2 Substrate-guided mapping and catheter ablation in scar-related VTs

Catheter ablation represents an effective therapeutic option for different forms of VT [199], [236]–[240], and as such often indicated for VT management [241]. In this context, it is exploited to suppress arrhythmogenic areas and, as such, enable the control of VT [242]. Nowadays, catheter ablation can be guided mainly by activation, substrate, pace and entrainment mapping, and is normally based on RF energy delivery, but many promising alternatives have been proposed [211], [243]. Recent research has demonstrated that substrate-guided mapping and catheter ablation during sinus rhythm may be a reasonable strategy to decrease arrhythmia recurrence [244], [245] and prevent implantable cardioverter-defibrillator (ICD) shocks [246]. Substrate-guided mapping is based on the identification of low-voltage slow-conducting areas in sinus rhythm, which become targets for catheter ablation in order to inhibit electrical conduction in arrhythmogenic tissue [247]. Despite voltage mapping may be hampered by several factors [206], [248], EGM characteristics in addition to peak-to-peak voltage amplitudes are frequently exploited for the identification of the arrhythmogenic substrate [249], [250]. In this regards, many different substrate-based strategies have been proposed, mainly including [206], [243], [250]–[254]:

- **LPs abolition,** aimed at performing catheter ablation in scar-related myocardial areas whose EGMs are affected by LPs, which have been found to effectively mark slow-conduction re-entrant isthmuses [232], [247], [255]–[260];
- **LAVA ablation**, based on the elimination of low-voltage, abnormal, high-frequency potentials associated with scar-related pathological tissue [247], [261], [262];
- **Scar dechannelling,** focusing on the identification of entrances of slow conductive channels in VT circuits through their EGM characteristics, in order to perform a selective and targeted ablation only on these regions [263];
- **Core isolation**, ablating the VT re-entry circuit around the scar, thus inhibiting possible electrical conduction by its entrances, isthmuses and exits [264];
- **Scar homogenization**, aimed at performing the ablation on the entire scar, guided by the presence of local abnormal conduction [265].

In this regard, Figure 8.2 schematically represents different substrate-guided catheter ablation strategies performed in scar-related VT substrates.

8.2.1 Ventricular abnormal potentials as high-frequency deflections in intracardiac electrograms

To summarize, despite many different strategies and tools have been proposed in the literature [206], [211], [221], [250]–[253], [266], [267], substrate-guided mapping and ablation procedures generally aim at targeting slow-conduction pathways, which are mainly identified by EGMs affected by so-called abnormal ventricular potentials (AVPs), with the final aim of silencing them, i.e. making these myocardial areas electrically inactive. Many authors have proposed different definitions of AVPs according to their temporal and morphological characteristics [206], [232], [244], [255]–[257], [259], [261], [262], [268], [269], which, nevertheless, have been proven to be frequently influenced by the infarct age in post-infarction VT [270]. AVPs are often qualitatively referred to as high-frequency deflections in intracardiac EGMs [206], [211], [261], [262], and different automated recognition algorithms are based on this assumption [271]–[273]. However,

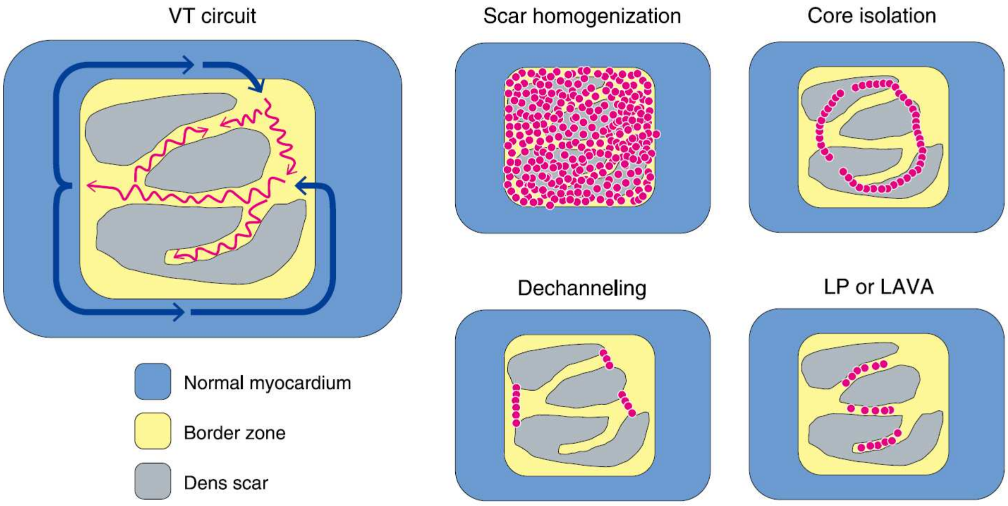

Figure 8.2. Schematic representation of different substrate-guided catheter ablation strategies performed in scar-related VT substrates [254].

no spectral characterisation of AVPs and post-ischaemic physiological potentials from intracardiac bipolar recordings has been performed so far. In fact, spectral analysis and time-frequency analysis techniques have been previously exploited on ventricular EGMs only with the goal of identifying short-term frequency content variations induced by myocardial ischaemia [274], distinguishing monomorphic and polymorphic VTs [275], local and distant electrical activities [276] and VT EGMs from normal sinus rhythm ones [277], [278], or targeting arrhythmogenic sites [271]–[273], but not to identify peculiar signatures of AVPs in the frequency domain. A study [279] investigating the effect of post-myocardial infarct on the frequency characteristics of ovine unipolar recordings acquired by multi-electrode plunge needles determined the relationship between high-frequency spectral characteristics and arrhythmogenic substrates. However, whilst the latter analysed peculiar histological and electrophysiological aspects, no evidence on AVPs was provided, nor their spectral contents were compared with post-ischaemic physiological EGM spectra. Moreover, as previously described, despite the unipolar recording mode being independent of the direction of the depolarisation wavefront, bipolar EGMs are less affected by other distant electrical activities. Indeed, because they allow the detection of high-frequency components and obtain higher SNRs [204], bipolar recordings are clinically preferred when targeting fractionated potentials and LPs [205].

8.2.2 Background on developed tools supporting VT arrhythmogenic substrate identification to guide catheter ablation

As previously detailed, VT ablation outcomes strongly depend on the identification of AVPs, and different 3D EAM mapping systems are adopted by electrophysiologists in order to recognize AVPs during substrate-guided mapping and ablation procedures. Generally, nowadays AVPs are visually identified by the cardiologist during electrophysiological studies and manually tagged on the electroanatomic maps in order to perform ablation subsequently. On this basis, electrophysiological procedures and their outcomes strongly depend on the cardiologist's expertise, who is asked to visually inspect a huge number of signals in real-time when spatially targeting ablation sites, thus making the clinical procedure time-expensive and operator-dependent. Due to the relevance of an accurate detection of the VT arrhythmogenic substrate, several supporting mapping tools have been proposed, such as the CARTO®3 ripple mapping [280], the Rhythmia HDx mapping and the Ensite Precision automatic mapping [267], the Ensite

Precision fractionation mapping algorithm [281], the Rhythmia Lumipoint algorithm [282], as long as identification algorithms including the mapping strategy based on voltage, fragmentation and duration criteria [283], the simultaneous amplitude frequency EGM transformation (SAFE-T) mapping [272], the fragmentation map [271], the combination of voltage limit adjustment with the Fast Fourier Transform [273], the automated fractionation detection algorithm [284], [285], the re-entry vulnerability index (RVI) [286], [287] and the recent algorithm for 3D visualization of EGM duration [288], but also many alternative targeting strategies, as the decrement evoked potential (DEEP) mapping [289]–[291], the high-density mapping based on deceleration zones [292] and the hidden slow conduction (HSC) analysis [293], [294]. However, despite the variety of novel identification and mapping algorithms proposed for targeting VT arrhythmogenic sites during intracardiac procedures, none of the developed approaches currently exploited artificial intelligence tools for the automatic detection of VT substrate.

8.3 Conclusion

Among cardiac arrhythmias, VT has drawn the attention of many researchers due to its incidence and impact on the patient's life. As previously detailed, scar-related VTs are frequently treated by substrate-guided mapping and RF catheter ablation, in order to make arrhythmogenic sites electrically inactive but, despite the clinical and scientific effort, the VT recurrence is still high [206], [295]. This unsuccess could be related to the fact that mechanisms underlying the VT origin and maintenance have been studied but still not completely understood [296], as long as to the need of a deeper understanding of the dynamic changes in tissues inducing re-entrant mechanisms, that would be useful in order to optimize these clinical approaches [297]. Moreover, the need of improving catheter ablation outcome runs in parallel to the need of focusing the ablation only on decisive and essential target points [298]. In light of all these premises, the second part of this PhD thesis aims to report the development of an effective artificial intelligence tool able to support the cardiologists in the recognition of the ablation targets during electrophysiological procedures, in the perspective of reducing clinical procedure times while improving their efficiency, the arrhythmogenic substrate delineation and, possibly, the clinical outcome. Simultaneously, another goal is to give support in reaching a deeper understanding of the mechanisms underlying the generation of abnormal signals, through the characterization of EGMs in the frequency domain. As such, in the next Chapter 9, the power contributions of post-ischaemic physiological potentials and AVPs are explored in the frequency domain, along with some spectral features, to highlight specific spectral signatures for these signals, while in the Chapter 10 a novel computer-assisted algorithm for targeting arrhythmogenic sites is presented.

Chapter 9

Novel insights on post-ischaemic VT arrhythmogenic substrate: spectral characterisation of ventricular intracardiac potentials in human post-ischaemic bipolar electrograms

9.1 Rationale

On the premises of the previous Chapter 8, a detailed spectral characterisation of AVPs and post-ischaemic physiological potentials in bipolar recordings was performed to provide deeper insights on these signals and move towards a comprehensive understanding of the arrhythmogenic substrate. Specifically, this chapter aimed at the identification of the spectral components exhibiting the highest informative and peculiar contribution for both AVPs and physiological potentials, as long as some peculiar features of the morphology of their spectra, in order to provide robust and hitherto unavailable characterization of these signals. Beyond providing novel insights on these signals, such a complete spectral characterization has been exploited as the basis for further studies aimed at their targeted automatic recognition, as detailed in the next Chapter 10.

As such, in this study, the power contributions of post-ischaemic physiological potentials and AVPs in bipolar intracardiac EGMs have been investigated, focusing on their spectral analysis after sub-band division. Here, bipolar recordings were selected as they ease the detection of high-frequency components with good signal-to-noise ratio [204], [205]. As better detailed in the following sections, 450 real bipolar EGM segments acquired in sinus rhythm from seven patients affected by post-ischaemic VT have been retrospectively analysed for this purpose. Because of the high variability of their morphology, AVPs of three different types and post-ischaemic physiological potentials of two types were considered. On these signals, we investigated the power contributions by exploiting conventional spectral analysis methods combined with a sub-band partitioning. In particular, the periodogram power spectrum and power spectral density estimate (PSD) were selected as the most suitable tools to provide an easily understandable spectral characterization. Along with the absolute powers, the relative power contents on each sub-band and different spectral features were appraised to provide a complete overview. Compared to other published works, the significant novelty of our study is the detailed assessment of bipolar signals, which are typically inspected by the electrophysiologists during the ablation procedures, to identify the spectral signatures of AVPs and physiological potentials, along with their distinctive spectral characteristics, providing new insights also on their PSD morphology.

9.2 Materials and Methods

This retrospective study was based on a dataset consisting of 450 bipolar EGM segments acquired from seven patients (86% male; mean age, 64 ± 9 years) affected by post-ischaemic VT at the San Francesco Hospital (Nuoro, Italy) between 2017 and 2018. This study on anonymised patient data was approved by the Independent ATS Ethical Committee (Azienda Tutela Salute, Sardegna) and performed following the principles outlined in the 1975 Helsinki Declaration, as revised in 2000. All patients provided their informed consent. Recordings were performed in sinus rhythm during left ventricular EAM by using the CARTO®3v6 system (Biosense Webster, Inc., Diamond Bar, CA, USA) at a sampling frequency of 1 kHz. After the EAM was completed, catheter RF ablation followed the usual clinical protocols. Bipolar intracardiac EGMs were recorded using PentaRay™ (Biosense Webster, Inc.) 2-6-2 mm, by exploiting only the 2-mm spaced electrode pairs, ThermoCool SmartTouch® and ThermoCool SmartTouch® SF (Biosense Webster, Inc.) catheters and band-pass filtered between 16 and 500 Hz by the CARTO®3v6 system. Whilst the duration of each exported CARTO®3v6 recording was 2.5 s, only the biopotential around the reference annotation[3] was guaranteed to be acquired by the multielectrode catheter in effective contact with the endocardium. Therefore, a window of 200 ms before and 300 ms after the reference point was identified as the portion of interest for all subsequent analyses. According to the sampling frequency adopted in the CARTO®3v6 system (i.e., 1000 Hz) and the chosen duration of the analysis window for each EGM (500 ms), the available frequency resolution for the discrete-time frequency analyses was 2 Hz.

All intracardiac EGMs were manually labelled by an experienced cardiologist using an ad hoc MATLAB graphical user interface (GUI) expressly developed for this purpose (see Figure 9.1). Specifically, by exploiting the corresponding simultaneous surface ECG leads, all abnormal potentials occurring after or during the corresponding QRS complexes were considered, as in other works [259], and all physiological potentials from post-ischaemic damaged substrates were also included in the study, as detailed hereinafter. Conversely, all noisy or doubtful traces were discarded.

Abnormal potentials, i.e. AVPs, were divided into three types [259], to take into account the high variability of the morphologies of all the bipolar intracardiac EGMs:

- LP1: endocardial bipolar abnormal deflections spreading after the end of the corresponding surface QRS depolarisation,
- LP2: endocardial bipolar depolarisations starting during the corresponding surface QRS depolarisation but vanishing after its end, and
- EP: endocardial early EGM deflections completely falling within the corresponding surface QRS depolarisation boundaries.

Physiological biopotentials (i.e., those without any abnormal deflection) originating from damaged myocardial substrates were also considered, dividing them into border-zone and scar-related types. Only these physiological potentials were categorised according to their peak-to-peak amplitudes (A_{pp}) recorded in the bipolar EGMs. Conventionally [208], endocardial border-zone potentials satisfied the constraint $0.5 \text{ mV} < A_{pp} < 1.5 \text{ mV}$, whereas scar-related ones were characterised by $A_{pp} < 0.5 \text{ mV}$. Amplitude categorisation was not applied to AVPs signals. All noisy or doubtful traces were discarded.

Over all the procedures, equal numbers of examples were randomly selected for each type of potential, (90 per type) to provide an effective and balanced comparative assessment. Figure 9.2 reports some typical examples of each EGM type.

The power contents for all bipolar EGMs were evaluated in the frequency domain. This analysis was carried out by adopting PSD and multiple spectral features to characterise the signals and their spectra better, as detailed in the following section.

---

[3] The reference annotation is a temporal reference point which all other signals are aligned to by the CARTO®3 system. It corresponds to the timing in which a predefined event (e.g. the R peak) is observed in the reference surface ECG, for each cardiac cycle. However, different events may be considered according to the chosen identification criterion adopted during the procedure.

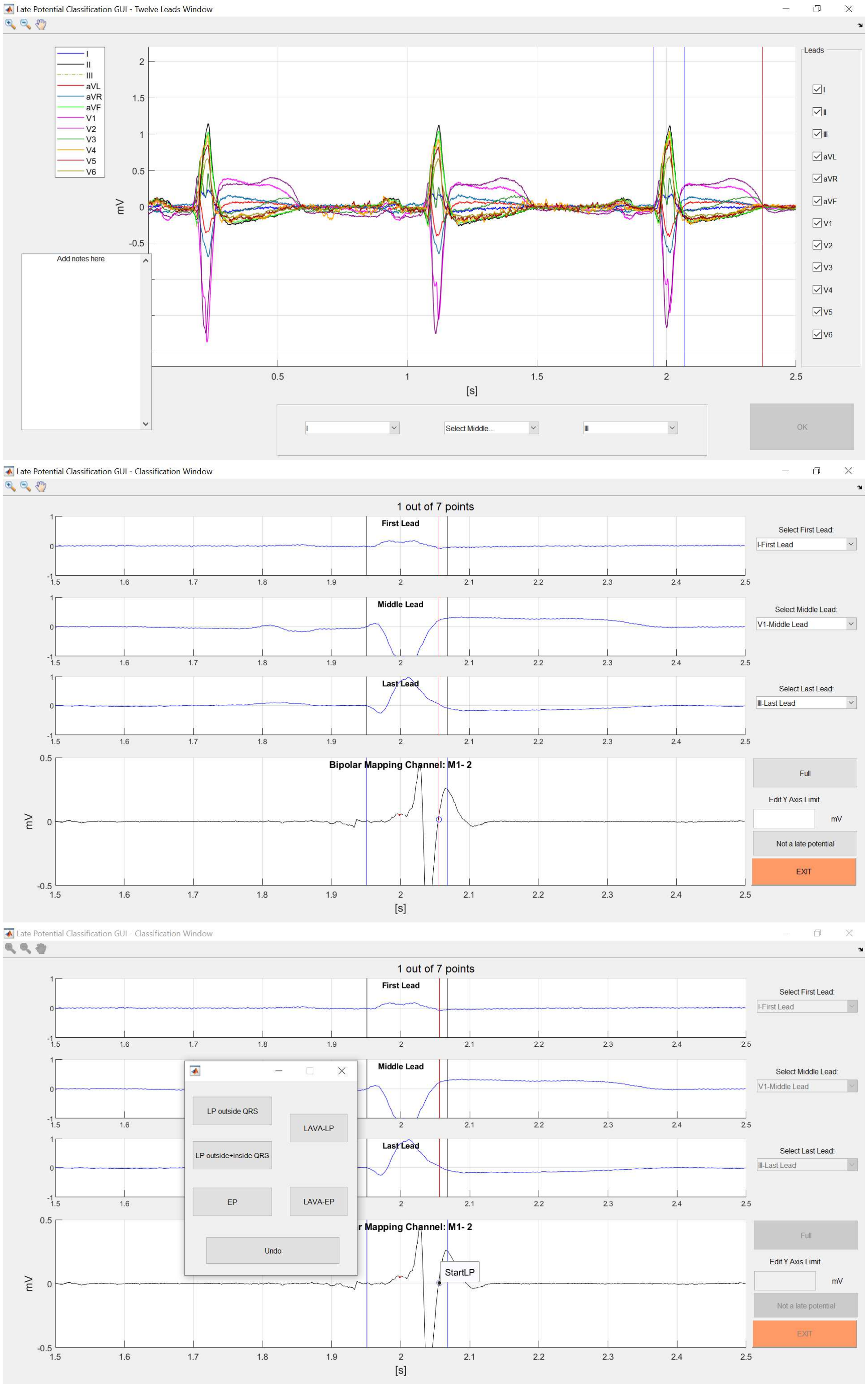

Figure 9.1. GUI developed for the EGMs labelling. Upper plot: first window for the ECG leads selection is represented: there, the electrophysiologist is asked to select the ECG leads in which the QRS occurs with earlier, intermediate and later latency. Blue bars identify the onset and the end of the QRS in all the twelve leads by an ad-hoc developed algorithm, while the moving red bar helps the clinician in its identification. Middle plot: after the selection, the GUI reports the three selected surface ECG leads and the analysed EGM. Red bar with a blue point allows the expert to mark the onset of any AVP. Bottom plot: by a simple click, different labels can be assigned both for AVPs, and for the other EGMs (i.e., choosing between physiological or garbage potentials by the "Not a late potential" button). In the process, different zooms and lead choices are allowed according to the visualisation requirements.

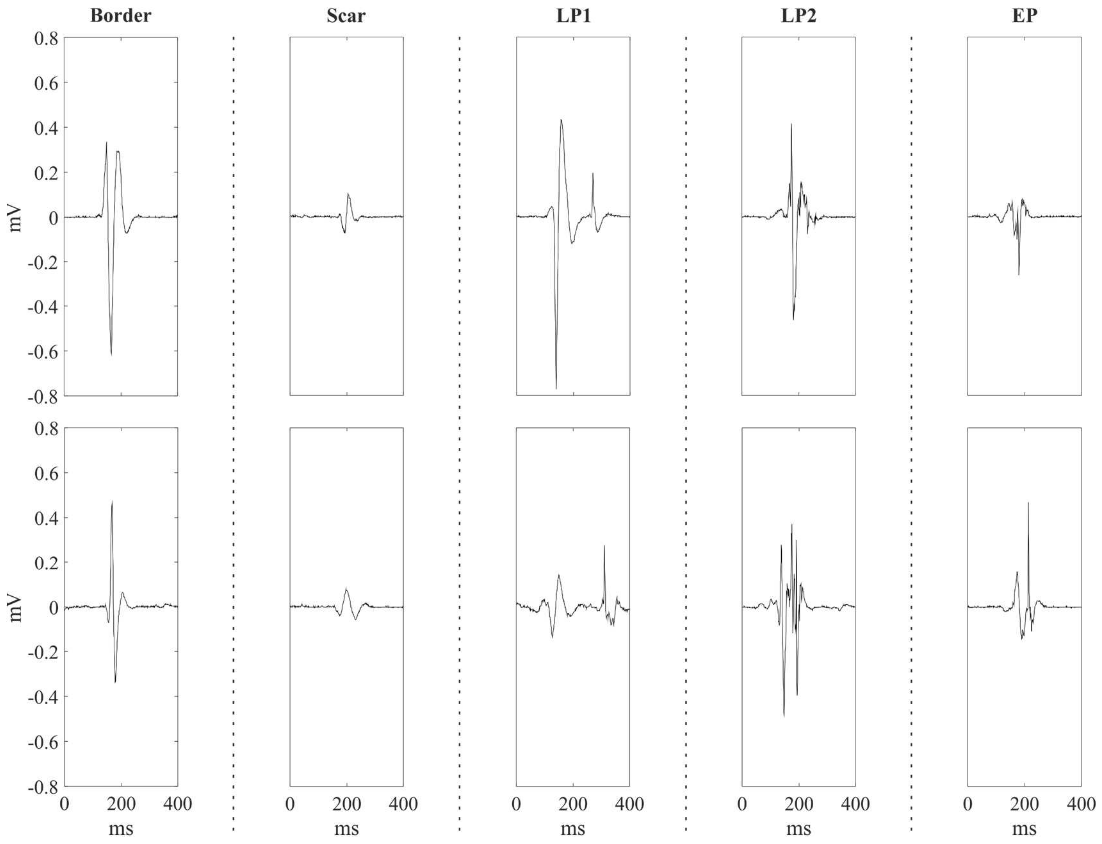

Figure 9.2. Prototypical examples for each EGM type. Two examples are represented on top and bottom rows for each EGM type. Specifically, from left to right, border-zone potentials, scar potentials, LP1 EGMs, LP2 EGMs and EP EGMs are depicted.

9.2.1 Spectral analysis methods

The spectral analysis included several steps. Firstly, the main frequency range of interest for these signals was identified, as described hereinafter, to reduce the dimensionality of the problem by focusing on the spectral range that contains the largest part of the signal power. Then, the power contributions in different sub-bands were assessed and compared, to perform a fine-grained analysis of the EGM spectral content. Sub-band partitioning with a bandwidth of 20 Hz was performed, as also described in a previous study [279], on the basis of the frequency resolution imposed by the chosen window length. This choice allowed reducing the impact of both noise and intrinsic limitations of the signal analysis methods adopted, by trading off robustness and accuracy of the characterisation.

The PSD method was exploited for spectral power estimation; here, the results were studied over sub-band partitions of the main frequency range of interest. Furthermore, the absolute and relative power contents of the potentials in the different sub-bands were computed because relative power analysis allows the elimination of signal amplitude influence, mainly due to the far field component, which clearly affects the power estimated from the spectral analysis. Finally, different spectral features were evaluated to characterise the different PSD morphologies and contents of the EGM types.

At first, a preliminary identification of the main frequency range of interest was performed in order to focus the signal frequency analysis on the components that provide the largest part of information, leading to a more effective and understandable sub-band analysis of ventricular endocardial potentials. This approach allowed to restrict the number of sub-bands whilst still guaranteeing fine granularity during spectrum partitioning. for each EGM, we computed the PSD and estimated its total power as the area under the PSD curve over the entire frequency band limited by the Nyquist frequency. Then, we identified the frequency f_H corresponding to the value for which the 95% of the total PSD power was retrieved (see Figure 9.3). Finally, considering the f_H values for each of the five EGM types, the 95th percentiles (ξ_{95}) were computed separately for each EGM type and the lowest sub-band including the maximum ξ_{95} was identified. The frequency range of interest was defined as the band between zero and the upper boundary of that sub-band.

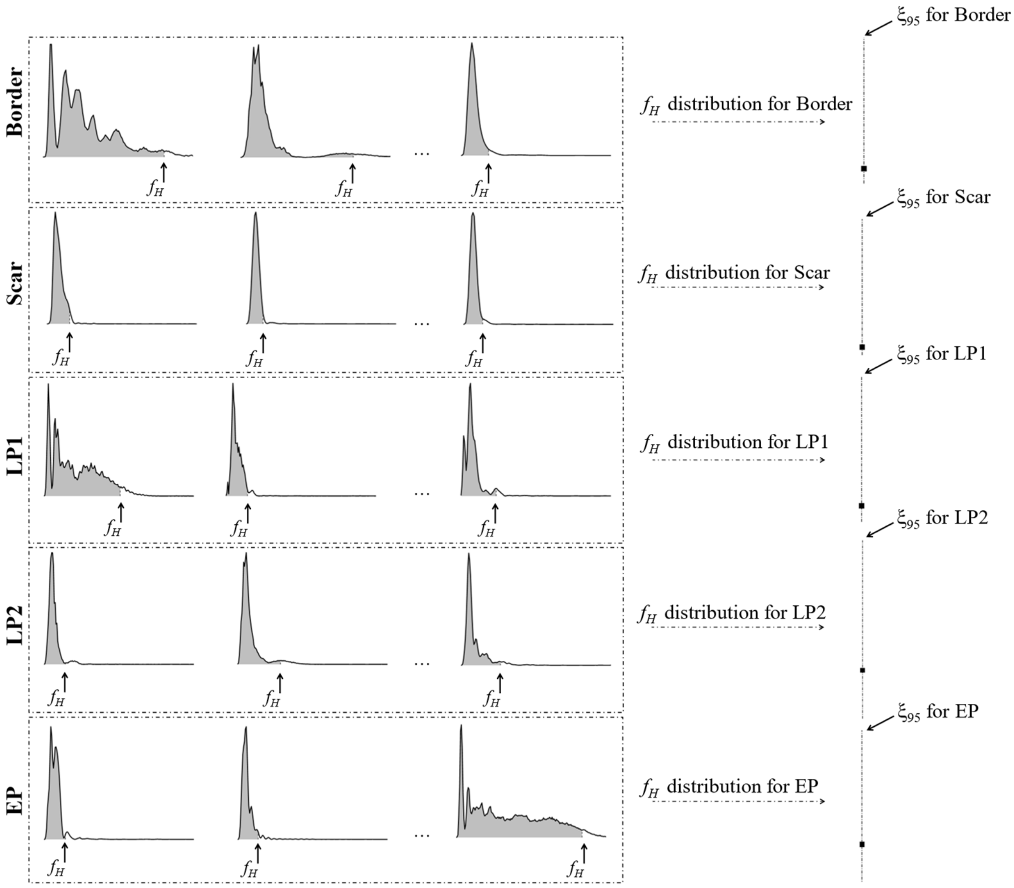

Figure 9.3. Schematic representation of the identification procedure for the frequency values f_H, in order to determine the upper boundary for the subsequent sub-band spectral analysis. For each potential and EGM type, the frequency f_H corresponding to the value for which the 95% of the total PSD power (grey area) was retrieved was firstly determined. Then, for each EGM type separately, the distribution of the f_H values was deduced in terms of median (black squares on the right) and 5th and 95th percentiles (ξ_{95}), identified by the extremes of the dotted lines, on the right). As such, the lowest 20-Hz sub-band enclosing the maximum ξ_{95} across the five EGM type was selected as upper boundary for subsequent spectral analysis.

As regards the spectral analysis, it was performed by PSD and power spectrum. The power spectrum of the discrete-time signal represents its power as a function of the frequency bin ω_k, which is the normalized frequency, defined as $\pi f/(f_s/2)$, where f_s represents the adopted sampling frequency. When the discrete Fourier transform (DFT) is used, ω_k assumes the discrete values $2\pi k/N$. In fact, in its simplest non-parametric estimate, the power spectrum can be computed from the DFT of the windowed signal of interest ($\boldsymbol{x}[n]$) consisting of N samples, by normalising its squared magnitude as follows [299]:

$$\boldsymbol{PS}[\omega_k] = \frac{|\boldsymbol{DFT}\{\boldsymbol{x}[n]\}|^2}{(\sum_{n=0}^{N-1} w[n]\,)^2} \qquad (9.1)$$

where

$$\boldsymbol{DFT}\{\boldsymbol{x}[n]\} = \sum_{n=0}^{N-1} x[n]\, e^{-j2\pi kn/N} \qquad (9.2)$$

and where $\boldsymbol{w}[n]$ identifies the chosen window, while n and k span between 0 and $N-1$, being N the signal length. Specifically, in this study, the fast Fourier transform was adopted along with a rectangular window function. The latter was chosen to avoid attenuation of the signal at its borders, as border effects are still limited by the high-pass pre-processing stage of the recording system. In this application, the choice of the DFT and windowing was imposed by the short duration of the EGM, thus providing a single epoch for each intracardiac potential.

The spectral power was estimated as the area under the PSD curve. PSD can be computed by dividing the power spectrum by the effective noise equivalent bandwidth [299]. According to this assumption, PSD can be mathematically expressed as:

$$\boldsymbol{PSD}[\omega_k] = \frac{|\boldsymbol{DFT}\{\boldsymbol{x}[n]\}|^2}{f_s \sum_{n=0}^{N-1} w[n]^2} \qquad (9.3)$$

Here, absolute power analysis was carried out by computing the area under the PSD curves in each sub-band.

The relative powers were also computed to avoid any influence in the analysis due to the amplitude of the signals, which is mainly ascribable to the far field component. These powers were estimated as the percentage ratio between the absolute power values of each sub-band and the area under the whole PSD curve in the main frequency range, similarly to a previous work [274].

Moreover, a deeper characterization of the different PSD morphologies was obtained by exploiting some frequency-domain features [300]. Specifically, for each EGM, the following features were considered:

- the mean frequency (MF), which is computed as the weighted sum of the power spectrum contents PS_j and the corresponding frequencies f_j with respect to the total power estimated in the main frequency range of interest (P):

  $$MF = \frac{\sum_j (f_j\, PS_j)}{P} \qquad (9.4)$$

  where $P = \sum_j PS_j$; on this basis, MF explains if the power spectrum contents are mostly localized at the higher or lower frequencies;
- the mean spectral power (MP), which is defined as the mean power in the main frequency range of interest and, as such, expresses how much power, on average, is contained under each PSD in that range;
- the maximum or peak frequency (PKF), which corresponds to the frequency in which the maximum of the power spectrum occurs, and
- the power spectrum ratio (PSR), which is estimated as the ratio between the spectral power included near the PKF and the total power estimated in the main frequency range of interest (P):

  $$PSR\,[\%] = 100 \cdot \frac{P_0}{P} \qquad (9.5)$$

  where $P_0 = \sum_{j=PKF-\delta}^{PKF+\delta} P_j$. Specifically, δ was set to be equal to 4 Hz. As such, the estimation was performed on a spectral interval equal to 8 Hz centred around the PKF to give an overview of how much power is concentrated around the PKF, highlighting how sharp the PSD morphology is around its maximum.

All computations were performed with MATLAB v2019b (MathWorks Inc., MA, USA).

9.3 Methods for the comparative analysis

The normality of all data distributions was preliminary assessed by Shapiro–Wilk's test, and the homogeneity of variances was evaluated with Levene's test. Data deviating from normality were presented as median values, and differences between groups were compared by the Kruskal–Wallis test. When the p-value from Kruskal–Wallis test was statistically significant, a post hoc Conover's non-parametric multiple comparison test [301], [302] was used to determine which group differed from the others. Several statistical inferences were simultaneously applied for all multiple comparisons, and the Bonferroni procedure for family-wise error rates was applied to control type-I errors by multiplying the uncorrected p-value with the total number of pairwise tests; the adjusted p-value for all computations was reported. Following Bonferroni adjustment, $p < 0.025$ was accepted as significant.

All statistical analyses have been performed using STATA 16 (StataCorp LP, College Station, TX, USA).

9.4 Results and discussion

9.4.1 Identification of the main frequency range of interest

The distributions of the f_H values for the five different EGM types are presented in Figure 9.4 as median and 5th and 95th percentile values. Visual inspection indicates that the spectral power analysis can be effectively carried out on all contents below approximately 320 Hz, which includes all of the most extreme f_H values.

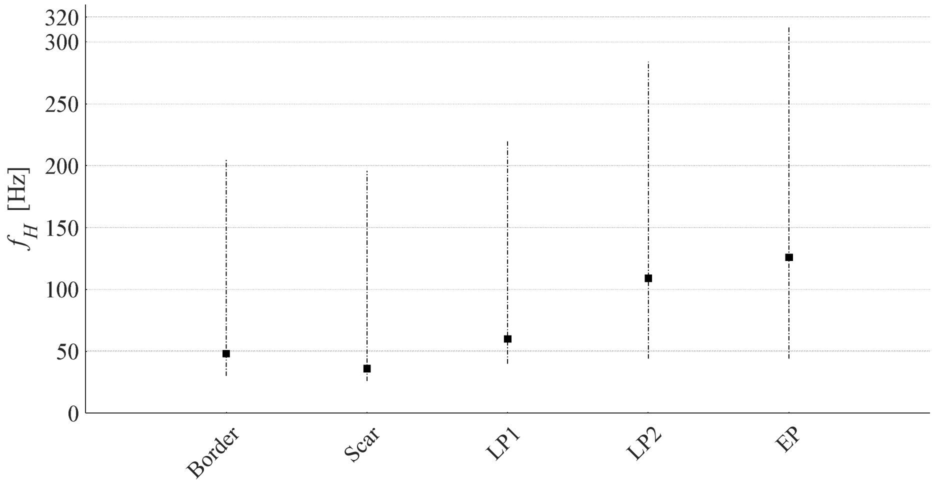

Figure 9.4. Distribution of the frequency values f_H including 95% of the total PSD power for each EGM type. Distributions of frequency limits f_H are reported as medians (squares) and 5th and 95th percentiles.

9.4.2 Spectral investigations

In this section, all spectral power estimations are reported as pair-wise comparisons amongst the different EGMs types. The results are organised into three groups, according to the nature of the EGMs included in the comparison. In the first group, all post-ischaemic physiological potentials (i.e., border and scar) were studied. In the second group, all AVPs (i.e., LP1, LP2, and EP) were examined; in the third group, physiological potentials were compared with AVPs. Table 9.1 summarises the spectral power results of pairwise comparisons for different spectral ranges. In the table, the different groups are identified by vertical dashed lines. Tables 9B.1 and 9B.2 in Appendix B report the absolute and relative power contents obtained for each EGM type in the different spectral ranges. Figure 9.5 presents the results of the relative power analysis in terms of median values graphically, and Figure 9.6 describes the results in terms of spectral features, as medians and 5th and 95th percentiles.

Table 9.1. Statistically significant differences ($p < 0.025$) amongst the different pairwise comparisons obtained via PSD analysis considering absolute (●) and relative (♦) power contents in the different spectral sub-bands by the post hoc Conover's non-parametric multiple comparison statistical test. Wherever statistically significant differences could not be found, no symbol was reported.
The colour of each symbol (black or grey) is associated with the EGM type, indicated in the heading line of that column with the same colour, exhibiting the highest median power content in that specific comparison (e.g., in the first column, which is related to the comparison between Border and Scar, black symbols are reported whenever an higher contribution of the border EGMs was detected, whereas grey symbols are present in case of significantly greater contribution of scar EGMs).

Frequency range (Hz)	Border vs. Scar	LP1 vs. LP2	LP1 vs. EP	LP2 vs. EP	Border vs. LP1	Border vs. LP2	Border vs. EP	Scar vs. LP1	Scar vs. LP2	Scar vs. EP
0 – 20	● ◇	●	●		●	● ♦	● ♦	○ ♦	♦	♦
20 – 40	● ♦	● ♦	● ♦		●	●	● ♦	○ ◇	○	○
40 – 60	● ♦	◇				● ◇	● ◇	○ ◇	○ ◇	○ ◇
60 – 80	●	◇	◇		◇	◇	◇	○ ◇	○ ◇	○ ◇
80 – 100	● ♦	◇	◇		◇	◇	◇	○ ◇	○ ◇	○ ◇
100 – 120	● ♦	◇	◇			◇	◇	○ ◇	○ ◇	○ ◇
120 – 140	● ♦	◇	○ ◇			◇	◇	○ ◇	○ ◇	○ ◇
140 – 160	● ♦	◇	◇			◇	◇	○ ◇	○ ◇	○ ◇
160 – 180	●	◇	◇			◇	◇	○ ◇	○ ◇	○ ◇
180 – 200	●	◇	◇		◇	◇	◇	○ ◇	○ ◇	○ ◇
200 – 220	●		◇	○ ◇	◇	◇	◇	○ ◇	○ ◇	○ ◇
220 – 240	●	◇	◇	○	◇	◇	◇	○ ◇	○ ◇	○ ◇
240 – 260	●	◇	◇	○	◇	◇	○ ◇	○	○ ◇	○ ◇
260 – 280	●	◇	◇	○	◇	◇	○ ◇	○	○ ◇	○ ◇
280 – 300	●	◇	◇	○	○ ◇	◇	○ ◇	○	○ ◇	○ ◇
300 – 320	●	◇	◇	○	◇	◇	○ ◇	○	○ ◇	○ ◇

9.4.2.1 Post-ischaemic physiological potentials

Conversely from absolute power and MP results, which were driven by the signal amplitude and confirmed that border power contents were significantly higher than scar ones in all examined ranges ($p < 0.0001$). relative power analyses revealed how scar power values were significantly higher than border ones at the lowest frequencies, i.e. 0–20 Hz ($p < 0.0001$). However, border relative powers were again higher than scar ones only up to 160 Hz, specifically in 20–60 Hz ($p < 0.0001$) and 80–160 Hz ($p < 0.0074$), although statistical significance was nearly achieved in the 60–80 Hz range ($p = 0.0391$). Scar MF and PKF values were significantly lower ($p < 0.0001$ for both cases) whereas scar PSR estimations were significantly higher ($p < 0.0001$) than border ones, thus confirming that this EGM type demonstrates its main contribution at lower frequencies than border cases.

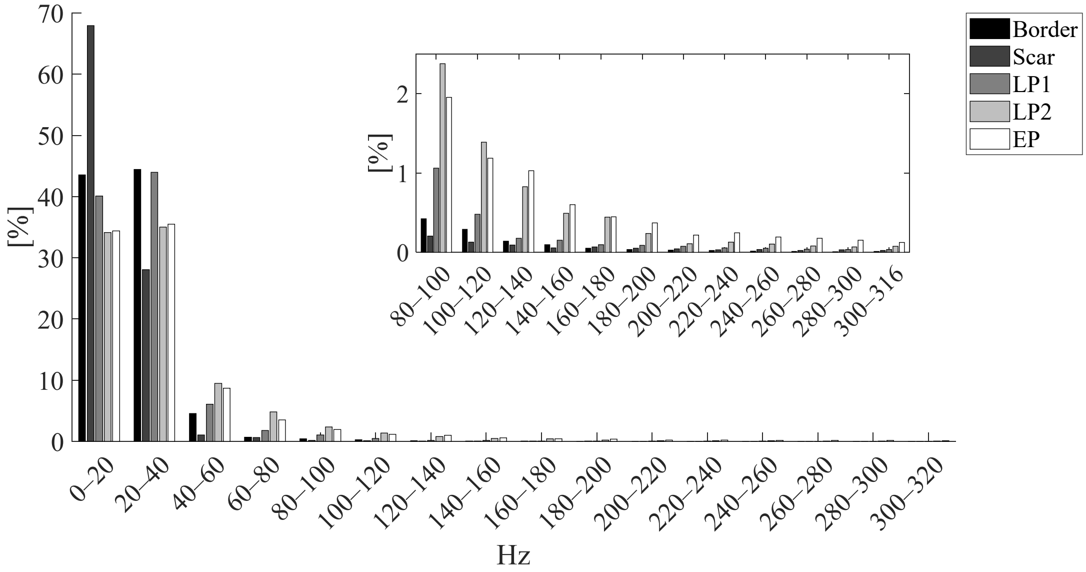

Figure 9.5. Median relative power contents in the different sub-bands for each EGM type. Median values of relative power contents obtained in the different spectral ranges are reported for Border (black bars), Scar (darker grey bars), LP1 (middle grey bars), LP2 (lighter grey bars) and EP (white bars) EGMs. A zoom on the upper sub-bands (i.e., from 80 Hz to 320 Hz) is also provided to allow for a better visualization of the relative power contributions at the higher frequencies. The legend graphically details the association between colours and the different EGM types.

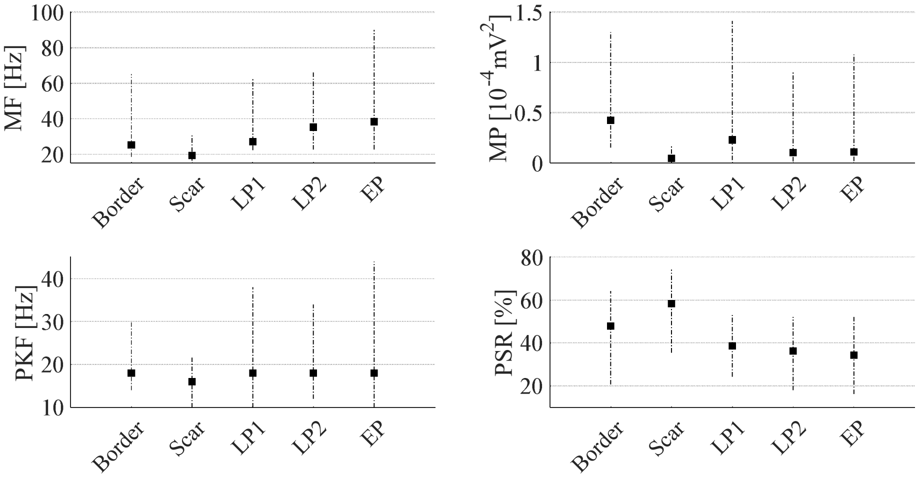

Figure 9.6. Spectral features estimated for all EGM types. Spectral feature results are reported as medians (black squares) and 5th and 95th percentiles. Specifically, in a) the distributions of mean frequency (MF) values are represented for all EGM types, whereas in b), c), and d) those referred to the mean spectral power (MP), the maximum or peak frequency (PKF) and the power spectrum ratio (PSR), respectively.

9.4.2.2 Post-ischaemic abnormal potentials

LP1 and LP2 potentials. In terms of MP, our experiments revealed significantly higher values of LP1 than LP2 ($p < 0.0001$). Although absolute power analyses showed statistically significant differences only in the 0–40 Hz range, in which LP1 values were significantly higher than LP2 ones ($p < 0.0001$), relative power analysis revealed a different scenario. In this case, LP1 contents exceeded LP2 ones at low-frequencies, in particular in the 20–40 Hz range ($p = 0.0007$), whereas LP2 showed significantly higher contributions at all the higher frequencies ($p < 0.0120$), except in the 200–220 Hz sub-band, in which no statistical significance was achieved. This finding was confirmed by the MF analysis, in which LP1 showed lower mean frequencies than LP2 ($p = 0.0001$). No statistical evidence was found between PKF and PSR.

LP1 and EP potentials. This comparison is similar to the previous one. MP values were significantly higher for LP1 than EP ($p < 0.0001$). Although absolute power analysis showed statistically significant significances mainly in the 0–40 Hz range, in which LP1 contributions were considerably higher than EP ones ($p < 0.0001$), relative power analysis demonstrated several statistically significant differences between 20 and 320 Hz. Specifically, although LP1 showed higher median contents at low frequencies, i.e. 20–40 Hz ($p = 0.0002$), EP values consistently exceeded those of LP1 between 60 and 320 Hz ($p < 0.0249$). Significant lower-frequency contributions for LP1 with respect to EP were also found when MF values were assessed ($p < 0.0001$).

LP2 and EP potentials. In general, no significant difference was found between the LP2 and EP classes below 200 Hz. For higher frequencies, EP demonstrated significantly higher values in the 200–320 Hz range ($p < 0.0233$) during absolute power analysis but only in the 200–220 Hz range in the corresponding relative power analysis ($p = 0.0187$).

9.4.2.3 Physiological versus abnormal potentials

Border and LP1 potentials. The MPs of border EGMs were significantly higher than those of LP1 EGMs ($p = 0.0002$). Statistical differences were rarely observed between these EGM types when absolute powers were analysed, i.e. essentially in the 0–40 Hz ($p < 0.0217$) range, in which border powers exceeded LP1 ones. However, when relative powers were analysed, LP1 spectral contents exceeded border ones in the range of 60–100 Hz ($p < 0.0091$) and above 180 Hz ($p < 0.0156$). Furthermore, border PSR values were significantly higher than LP1 ones ($p = 0.0017$), thus suggesting a lower dispersion of power contributions around the maximum frequency in border EGMs.

Border and LP2 potentials. Border EGMs showed statistically higher MP values than LP2 ($p < 0.0001$). During absolute spectral analysis, statistically significant differences were noted only at frequencies below 60 Hz, where border power contents exceeded LP2 ones ($p < 0.0070$). However, LP2 and border EGMs significantly differed in terms of relative power in all the sub-bands except in the 20–40 Hz one. Table 9.1 reveals that LP2 showed higher power contents in higher frequency ranges, i.e. between 40 and 320 Hz ($p < 0.0001$); the opposite behaviour was observed at the lowest frequencies, i.e. 0–20 Hz ($p = 0.0048$), where border EGMs exhibited higher power contributions. The main low-frequency contributions of border EGMs are also reflected by the MF results, in which border contributions were significantly lower than LP2 ones ($p < 0.0001$). PSR values suggested a major power gathering around the frequency peak for border EGMs ($p < 0.0001$).

Border and EP potentials. The MP values of border EGMs were significantly higher than those of EP EGMs ($p < 0.0001$). Conversely, EP MF values significantly exceeded border ones ($p < 0.0001$) with lower PSR contents ($p < 0.0001$).Absolute power analysis revealed statistically significant differences below 60 Hz, in which border power contents exceeded EP ones ($p < 0.0156$), and above 240 Hz, where the opposite trend was noted ($p < 0.0063$). In terms of relative power, border and EP EGMs significantly differed in all the sub-bands, with border potentials showing higher contributions at lower frequencies (i.e. 0–40 Hz, $p < 0.0197$) and EP above 40 Hz ($p < 0.0001$).

Scar and LP1 potentials. Scar EGMs consistently showed significantly lower contributions than LP1 when absolute powers, MP, MF and PKF were examined ($p < 0.0001$). However, scar relative power values exceeded LP1 one in the lowest sub-band, i.e. 0–20 Hz ($p < 0.0001$, see Table 9.1). LP1 power contents were significantly higher than scar ones at higher frequencies, i.e. 20–240 Hz ($p < 0.0119$). Furthermore, scar PSRs exceeded LP1 ones ($p < 0.0001$). These results clearly indicate that scar EGMs exhibited lower powers in absolute terms, but higher relative low-frequency contents (see Figure 9.5) with a considerable amount of spectral power around their PKFs, which are typically observed below 25 Hz, as can be seen in Figure 9.6.

Scar and LP2 potentials. Scar EGMs showed significantly lower power contributions than LP2 in terms of MP ($p < 0.0001$) and in the absolute power analysis at frequencies above 20 Hz ($p < 0.0001$). However, similarly to the previous case, the relative power contributions of these potentials demonstrated some interesting characteristics. Specifically, scar EGMs showed higher relative power contents at the lowest frequencies, i.e. below 20 Hz ($p < 0.0001$), but lower contents at higher frequencies, i.e. above 40 Hz ($p < 0.0001$). As in the previous case, this finding was confirmed by the trends of MF and PKF, in which scar contents were significantly lower than LP2 ones ($p < 0.0001$), and PSR values, in which scar EGMs exceeded LP2 ones ($p < 0.0001$).

Scar and EP potentials. Scar EGMs showed significantly lower powers than EP EGMs in terms of MP ($p < 0.0001$). The comparison in terms of absolute and relative power analysis led to the same results obtained in the previous case. The MF and PKF distributions confirmed the previous findings, thus suggesting higher scar contributions than EP ones ($p < 0.0001$ and $p = 0.0002$, respectively) at low frequencies, with major gathering around PKF in terms of PSR rather than EP ($p < 0.0001$).

9.4.3 Discussion

In this chapter, different spectral power analyses were performed to characterise abnormal and physiological post-ischaemic bipolar potentials and provide an accurate and quantitative comparative assessment amongst the different EGM types analysed. The results were grouped in terms of comparisons between physiological potentials, abnormal potentials and physiological versus abnormal potentials, i.e. AVPs.

Although the absolute power analysis is influenced by the amplitude of the signals, which is mainly driven by the far field component, its results are quite interesting when compared to the relative power analysis and the insights synthetically provided by the identified spectral features. According to the absolute power analysis results (see Table 9.1), scar EGMs consistently demonstrated lower power values than all other types of potentials, regardless of the frequency range analysed. However, the spectral feature analysis results (see Figure 9.6) clearly show that scar MF and PKF are typically below 30 Hz, around which substantial power contributions are concentrated, as indicated by their higher PSRs. These findings suggest that scar power spectra are quite condensed around their maximum and may confirm the association between the lowest-frequency contributions and the scar areas, as further demonstrated by the relative power analysis results. While PKF allowed to statistically emphasize scar potentials, PSR contents allowed to discriminate physiological potentials from AVPs, since both border and scar EGMs showed major power contributions around PKF (i.e., higher PSR in Figure 9.6) MF analysis seemed to delineate three clusters, namely, border and LP1, LP2 and EP, and scar.

However, the absolute power results in Table 9.1 suggest that, below 40 Hz, border EGMs show higher contribution than all AVPs and that, amongst AVPs, LP1 EGMs involve greater slow components. The same finding could be confirmed by looking at the lower MF values in Figure 9.6 for LP1 and border EGMs. Conversely, EPs showed higher contributions than border EGMs above 240 Hz, revealing significant high-frequency components, which also emerged in the comparison with LP2 above 200 Hz. This finding was supported by the MF evaluation, in which the values of EP were found to be generally higher than those of all other EGM types.

Although absolute power analysis results are interesting for the spectral characterization of physiological potentials and AVPs, the relative power analysis (see Table 9.1) provides several novel insights into the characterisation of these signals. Overall, our results indicate that physiological EGMs have greater contributions at lower frequencies (i.e. mainly below 20 Hz) than pathological ones, as conceivable according to the fragmented nature of AVPs. In particular, scar-related EGMs consistently indicated higher contributions at lower frequencies (i.e. 0–20 Hz) than all the other physiological and pathological types, which, however, gradually decreased when moving towards higher sub-bands. These findings are at least partially in accordance with previous scientific studies on post-ischaemic epicardial EGMs [274], [275]. In fact, Mor-Avi and Akselrod [274] demonstrated that myocardial ischaemia is responsible for a shift of the major frequency contents below 40 Hz whilst attenuating high-frequency spectral components. Sierra *et al.* [275] concluded that most of the signal energy is concentrated below 30 Hz in monomorphic and polymorphic VT recordings.

Relative powers of LP2 and EP exhibited significantly greater values from 40 Hz than post-ischaemic physiological potentials, even though statistical significance was not achieved on some spectral ranges (see Table 9.1). Conversely, whilst LP1 EGMs showed significantly higher power contents than scar potentials in the 20–240 Hz range, they generally did not assume significantly higher values than border potentials until 180 Hz. As such, AVPs presented greater relative powers at higher frequencies with respect to physiological potentials, with some differences in spectral ranges depending on the AVP type. Moreover, as regards the significances amongst AVPs, while LP1 showed lower power contributions than LP2 and EP mainly above 60 Hz, LP2 and EP EGMs statistically differed in 200–220 Hz sub-band.

In summary, AVPs demonstrated higher relative power contributions at higher frequencies (i.e. mainly above 40 Hz) when compared with physiological potentials, as can be also deduced from Figure 9.7. These findings are quite consistent with the a priori assumptions described in [271], in which spectral contents above 80 Hz were identified as a marker of highly fragmented EGMs, and another study [272], which identified the range of 70–180 Hz to be the useful spectral range for the arrhythmogenic potentials identification. Moreover, our results partially agree with another study [273], which indicated the 40–100 Hz range to be of interest for fractionated EGM recognition, and an earlier analysis [279], in which arrhythmogenic scar potentials showed significantly higher root mean square powers than non-arrhythmogenic ones from approximately 40 Hz, at least in dense scar tissue. However, in all these previous studies, no justification behind the choice of the specific spectral range was provided. Indeed, differently to the previous works, our study characterises the spectral signatures of human endocardial post-ischaemic EGMs, both normal and abnormal, quantitatively by analysing their power contents in different sub-bands and looking at their spectral morphologies. Our analysis not only focuses on scar-related and arrhythmogenic substrates but also describes, in detail, the different AVP and physiological EGM types, thus providing additional important information for their characterisation.

Whilst the rigorous assessment described above allows for studies on statistical differences, the generalisability of the presented results is affected by some limitations of this study. Specifically, the analysis was carried out on a limited set of bipolar EGMs acquired from seven post-ischaemic VT patients. Thus, larger datasets are necessary to reinforce the results or reduce the strength of our findings. Moreover, all recordings were annotated by a single cardiologist, whose experience may have biased the subsequent analyses. Furthermore, the labelling process and the subsequent analyses were carried out simply based on the signals as they were recorded by the CARTO®3 system and as exploited during the clinical procedures, without taking into account any dependence from wavefront directionality and electrode parameters, which however affect the substrate-guided mapping techniques inherently [248], [303]–[305]. Other studies are in progress to address the far-field effect on AVP power estimations to provide a deeper characterisation of these potentials after the influence of global ventricular depolarisation is removed.

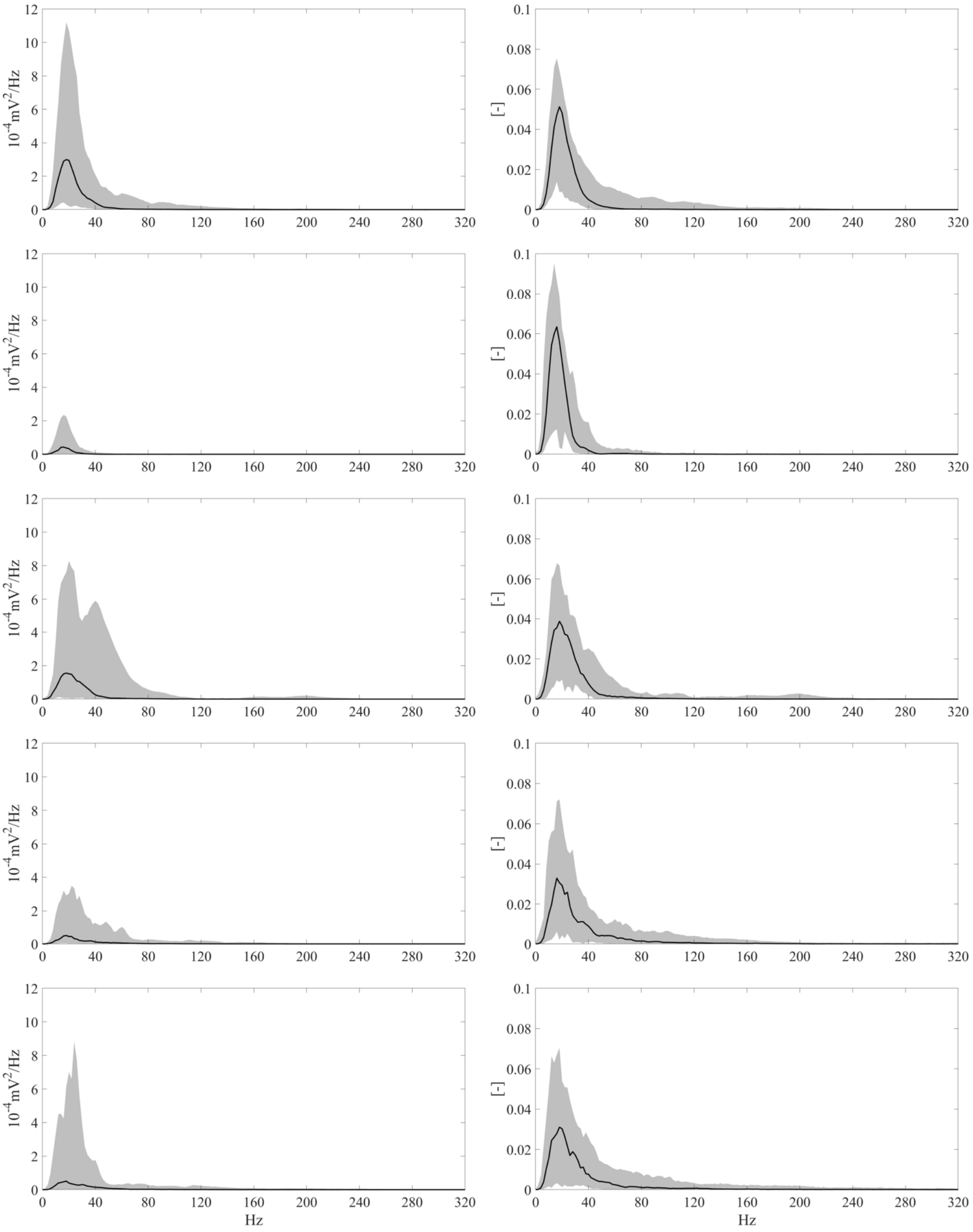

Figure 9.7. Absolute and normalised PSDs for all EGM types. Representative PSDs for both physiological and pathological signals in terms of medians (black solid line) and 5th and 95th percentiles (grey zones). From top to bottom: PSDs for border, scar, LP1, LP2 and EP EGMs. The left column illustrates standard PSD curves, whilst the right column depicts the same PSD curves after normalisation so that the area under each curve is unitary, thus allowing for a comparative overview of both absolute and relative power contents for all EGM types in different sub-bands.

Chapter 10

Computer-assisted arrhythmogenic sites detection

10.1 Rationale

As explained in Section 8.2, catheter ablation is performed to inhibit the electrical conduction in arrhythmogenic substrate causing or sustaining the VT. According to the adopted mapping strategy, the identification of arrhythmogenic sites may be guided by the presence of AVPs. However, the procedure is entirely manual and time consuming, strongly relying on clinicians' expertise in the visual inspection of the EGMs and their detection ability. Furthermore, as detailed in Section 8.2.2, many tools supporting the VT arrhythmogenic substrate identification have been introduced in the literature, but none of them addressed the challenge by exploiting artificial intelligence systems. On these premises, the adoption of machine learning methods for the computer-aided recognition of AVPs would be a relevant advancement, reducing the operator-dependence and the procedure mapping times, but also supporting the clinicians in a more accurate targeting of arrhythmogenic sites, thus possibly improving clinical outcomes and VT recurrence. In fact, artificial intelligence tools have proven to achieve very high performance, both for biomedical signal analysis and biomedical imaging [306]. Therefore, in this chapter, the use of machine learning tools for the automatic recognition of AVPs in substrate mapping procedures has been explored.

10.2 Materials and Methods

In this retrospective study, a dataset consisting of 2603 bipolar EGM segments acquired from nine patients with post-ischaemic VT at the San Francesco Hospital (Nuoro, Italy) between 2017 and 2018 was adopted. All signals were collected in sinus rhythm during the EAM procedure in left ventricle by the CARTO®3v6 system (Biosense Webster, Inc., Diamond Bar, California) and then exported in digital format for further processing. As for the previous investigation, bipolar EGM segments were recorded by PentaRay (Biosense Webster, Inc.) 2-6-2 mm, ThermoCool SmartTouch and ThermoCool SmartTouch SF catheters (Biosense Webster, Inc.) in left ventricle (LV) at a sampling frequency of 1 kHz and band-pass filtered between 16 and 500 Hz. After the EAM, RF catheter ablation was performed according to standard clinical protocols. The study on the anonymised data was approved by the Independent ATS Ethical Committee (Azienda Tutela Salute, Sardegna) and performed following the principles outlined in the 1975 Helsinki Declaration, as revised in 2000. All patients provided their informed consent.

As previously explained in Chapter 9, the intracardiac catheter can be considered in effective contact with the endocardium in correspondence of the reference annotation, therefore only the EGM segment around the reference annotation timing was considered for the following analyses. Nevertheless, some exported EGMs were spatially projected onto empty areas of the reconstructed cardiac map, in which EAM was found to be irrelevant by clinicians for VT ablation and as such discarded during the clinical procedures. As a result, these intracardiac EGMs were removed, resulting in a final dataset of 2561 EGMs. For the sake of clarity, in Figure 10.1 an example of a LV map constructed during fast anatomical mapping (FAM, i.e., before any electrical information was acquired) with discarded portions is reported.

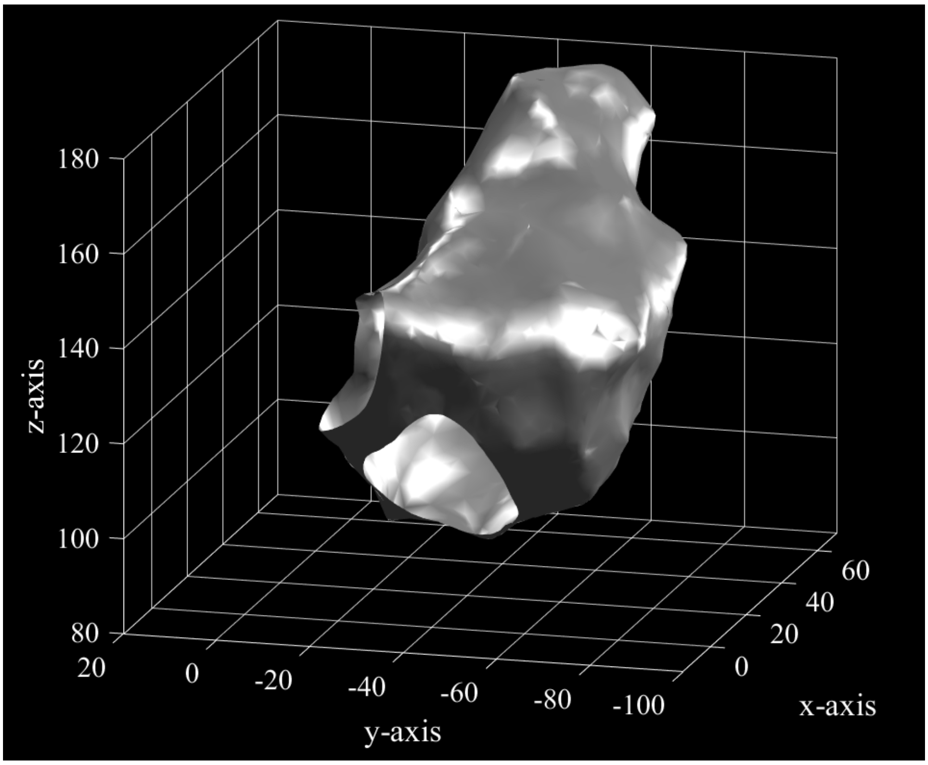

Figure 10.1. Example of a FAM map in which some LV portions were discarded during the mapping procedure, thus resulting in an empty area.

As for the previous Chapter 9, all EGMs were manually annotated by an experienced cardiologist using an ad-hoc MATLAB graphical user interface implemented for this specific purpose (see Figure 9.1), as in our previous investigation [307]. In this assessment, in order to perform the recognition between normal and abnormal potentials, all AVP types (see Section 9.2) and all physiological EGMs regardless of their A_{pp} were considered, while all noisy or doubtful traces were excluded from the analysis. Some examples of EGMs included in the dataset adopted for the development of the automatic recognition tool are reported in Figure 10.2. However, since the post-ischaemic arrhythmogenic VT substrates are spatially restricted with respect to the healthy myocardial tissue, the number of recorded AVPs was typically limited in the exported procedures, thus resulting in two significantly imbalanced classes (namely, AVPs and Physio), as can be seen in Figure 10.3. Therefore, in this study, the Physio class was randomly down-sampled in order to provide a balanced and unbiased number of normal and abnormal observations for the machine learning tools. This procedure was performed when using a 10-time 10-fold cross-validation approach, as better detailed in Section 10.3.

10.2.1 Feature extraction and classification tools

During my PhD, several investigations have been performed in terms of automatic recognition of AVPs. Specifically, at first only the features from the time domain and the time-scale domain detailed below were analysed on a reduced set of the actual available dataset, providing good results [308]. However, by exploiting the time-series representing the EGM as input for an ANN, we questioned the usefulness of these feature-based models [307], as such other features were needed. Therefore, after the spectral characterisation of AVPs (see Chapter 9) was performed, several other features were included from the frequency domain, as also some features from the related EA maps, in order to improve the classification performance. As such, in this chapter the latest investigation only was reported, in which four types of features were extracted, both from

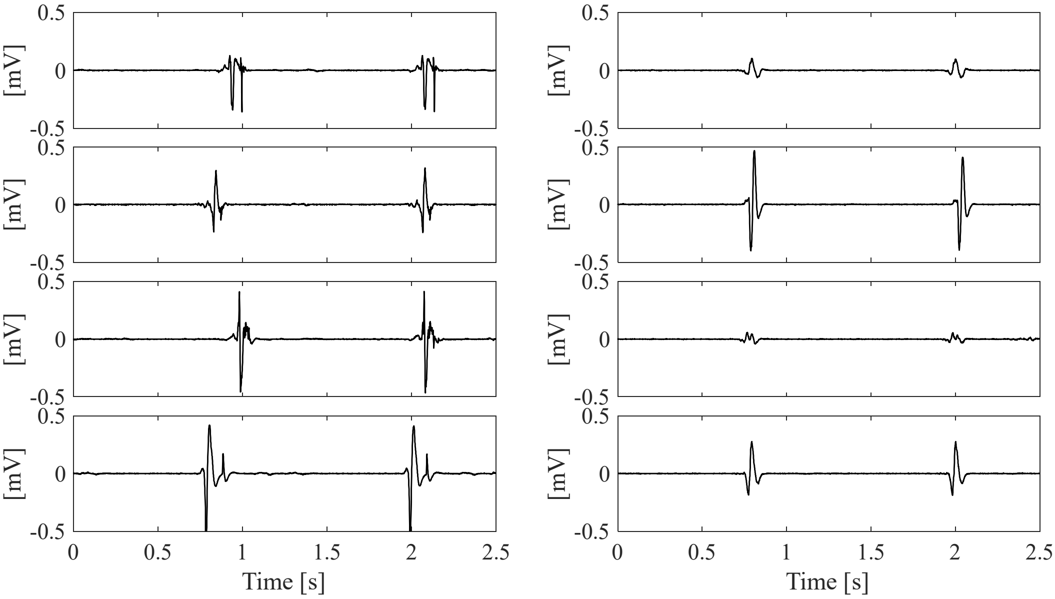

Figure 10.2. Some examples of raw EGMs (i.e., before windowing and any processing stage) included in the classification dataset. In the left column, observations from the AVPs class are reported, whereas on the right one EGMs belonging to physiological potentials class are depicted.

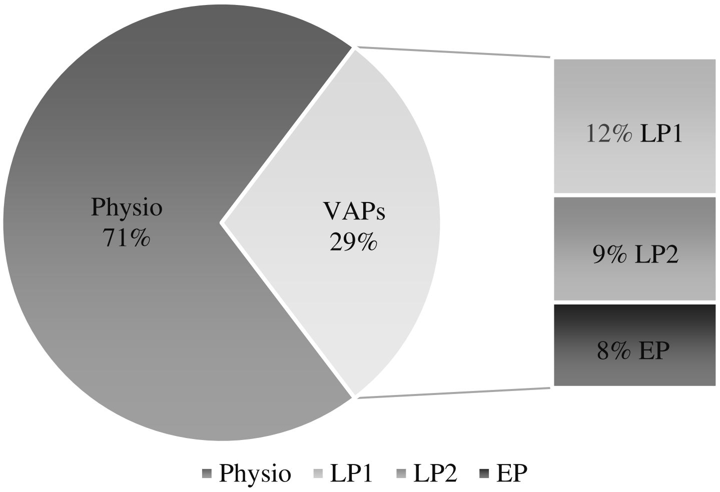

Figure 10.3. Composition of the available dataset. Numerically, 752 EGMs were classified as AVPs whereas 1809 as physiological potentials (Physio). Thus, more than 70% of EGMs were labelled as physiological ones, so that, in the 10-time 10-fold cross-validation, a balancing strategy was adopted.

direct processing of the EGMs in the time, frequency and time-scale domains, but also from their spatial localization in the EA map.

Features from the time domain. In the time domain, two features were extracted: the A_{pp} and a fragmentation measure. The A_{pp} of each bipolar EGM was evaluated in a 350ms window around the reference annotation, considering 50ms before and 300ms after the annotation timing. As already detailed in Sections 7.3.1 and 9.2, this aspect has been largely exploited in the scientific literature [208], [251], [256], [309], it was introduced in order to help discriminating between high voltage EGMs, which are typically associated with normal myocardium, and those originating from border-zone and scar- related areas.

The fragmentation measure was extracted in order to highlight fragmented EGMs, that are typically associated with slow and disordered conduction areas [195], [215], [226]–[228], [271]. In this study, the fragmentation was computed as the total number of peaks in the 350ms-long signal, the latter being windowed by a rectangular window. Specifically, in order to provide a quantitative measure to the classifier, the windowed signal was rectified by taking its absolute value, and all peaks exceeding the 75% of its mean absolute deviation value were counted. An example for the fragmentation measure computation is provided in Figure 10.4.

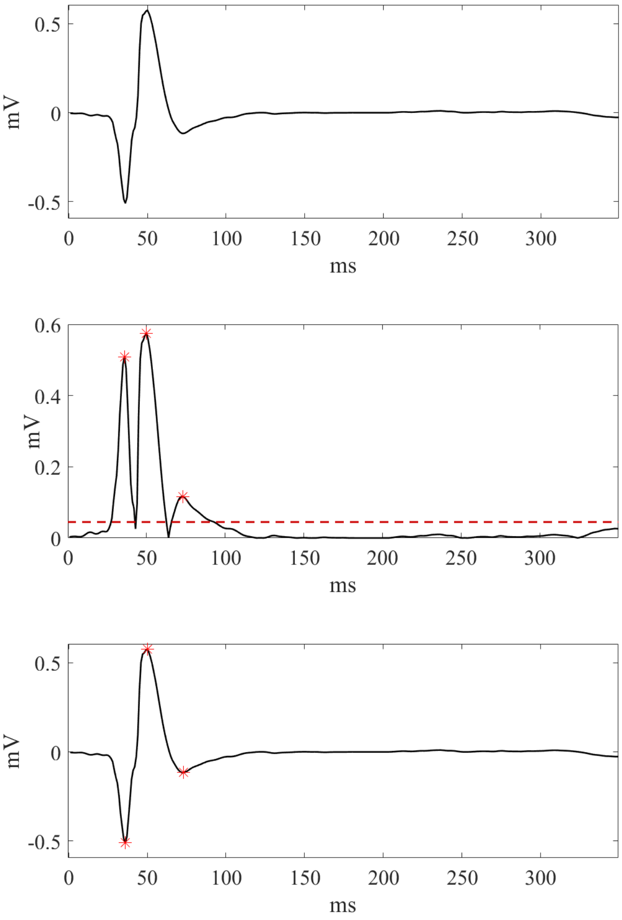

Figure 10.4. Example of fragmentation measure captured by the proposed approach. In the upper plot, the windowed signal (i.e. 50ms before and 300ms after the reference annotation timing) is reported. In the middle, the rectified signal is depicted in black, whereas the threshold based on the 75% of its mean absolute deviation as a red dashed line. As can be seen, three peaks exceeding the proposed threshold can be identified (in red), corresponding to three potential deflections found in the time-domain representation (lower plot).

Features from the time-scale domain. Two features were also extracted from the time-scale domain, based on the continuous WT (CWT). CWT relies on a time-scale representation of the signal $f(t)$ through a set of coefficients, which are obtained as [170], [171], [173]:

$$WT_f\,(a,\tau) \;=\; \frac{1}{\sqrt{a}} \int_R f(t)\,\psi^*\left(\frac{t-\tau}{a}\right) dt \qquad (10.1)$$

where $a \in R^{+}$ and $\tau \in R$ represent the scale and time-shift parameters, respectively, whereas $\frac{1}{\sqrt{a}}\psi\left(\frac{t-\tau}{a}\right)$ represents a time-shifted and scaled version of the function ψ, which embodies the mother wavelet. In other words, for every translation in time, each wavelet coefficient represents a similarity index between of the signal and the scaled version of ψ. Specifically, the scale factor regulates the degree of stretching of the mother wavelet and, as such, it is inversely proportional to the frequency: small scales generate a compressed ψ, for which higher frequency components of the signal are examined; conversely, larger scales are associated to a more stretched ψ, and so to lower frequency contributions are accounted for. This approach leads to a variable support of the wavelets in close relationship with the explored frequency band, which is not possible with the Fourier analysis. As such, unlike Fourier analysis, WT guarantees a good resolution both in time and in frequency domain, which can be exploited to identify AVPs. While in the DWT the scale parameter is varied discretely by powers of two, in the CWT there is not such a constraint. However, in the computer implementation of the technique, the scale parameter is also discretized but finely, e.g. as fractional powers of two.

For the extraction of the features in the time-scale domain, the signal was firstly pre-processed by a WD stage [307], [308]. A translation-invariant *à trous* (undecimated) algorithm was adopted, using a Daubechies2 mother wavelet, the Universal threshold, the soft-thresholding and a decomposition level equal to 2, in order to implement the denoising only on the upper part of the signal band, i.e. from the folding frequency down to about 125 Hz. In this way, under-threshold small fluctuations of the signal that could represent confounding factors for the subsequent analysis were removed. Then, on the WD windowed signal, the CWT decomposition was computed by exploiting the Daubechies2 mother wavelet and all the scales from 2 to 35, in order to analyse the spectral components between about 16 Hz and 500 Hz. Then, the average power on each scale a was evaluated according to the following equation:

$$\check{P}(a) = \frac{1}{N} \sum_{\tau=1}^{N} WT_f\,(a,\tau)^2 \qquad (10.2)$$

where N is the total number of wavelet coefficients at that scale. For each windowed EGM, the five scales with the highest $\check{P}(a)$ were selected. Then, the standard deviation of such $\check{P}(a)$ and their sum were computed and considered as features in the time-scale domain.

Features from the frequency domain. Based on the results obtained in Section 9.4, different features were considered in the frequency domain. Specifically, due to the statistically significant differences observed between the different AVPs and physiological EGMs, all the spectral features (i.e. MNF, PKF, MNP, PSR introduced in Section 9.2.1) along with the relative power contents in 0–20 Hz and in each 20-Hz sub-band between 40 and 320 Hz were extracted for each EGM to train and test the machine learning tools.

Features from the spatial domain. In order to go one step forward with respect to the features derived only from the EGM itself, different features were also deduced from the EA voltage and local activation time (LAT) maps. In fact, despite EGM trends may contain many distinctive and relevant characteristics, their spatial localisation is essential in the EAM procedure. Therefore, different spatial features were also introduced. Remarkably, despite the proposed method is thought for retrospective investigations in which the whole EA map is available, it could be exploited also in a live context, by gradually obtaining the information needed and updating the spatial information accordingly while the mapping is being performed.

As regards the voltage map, for each EGM, the spatial location on the map was reconstructed by a custom MATLAB software starting from the data exported from the CARTO®3v6 procedure. Then, for each spatial point P, a circular area of radius ϵ and centred on the EGM location of interest was identified. Specifically, different values of ϵ were tested (i.e., from 2 mm up to 7 mm), in order to evaluate its impact on the classification performance. However, since best performance were achieved when setting the parameter ϵ equal to 6 mm, this value was chosen for all the subsequent analyses. Then, in order to assess the electrical properties of all EGMs localised in close proximity of *P*, all the EAM neighbours falling within this area were considered for the feature extraction. A schematic representation of the circular 6-mm neighbourhood exploited for the extraction of the spatial features is reported in Figure 10.5. Once the neighbour points were identified, for each point *P* the following features were extracted:

- the mean bipolar voltage, which was defined as the mean value of the A_{pp} exhibited by the bipolar EGMs falling into the neighbourhood;
- the weighted mean bipolar voltage, in which the mean value of A_{pp} was computed by weighting the contribution of each EGM according to the inverse of its squared Euclidean distance to the point *P*; in case of multiple EGMs sharing the same virtual coordinates of the point P onto the voltage map, their weight was forced to be equal to one;
- the standard deviation of the A_{pp} exhibited by the bipolar EGMs acquired into the neighbourhood;
- the number of neighbours exhibiting $A_{pp} < 0.5$ mV, 0.5 mV < $A_{pp} < 1.5$ mV and $A_{pp} >$ 1.5 mV; in this case, all values were normalized with respect to the total neighbours identified for *P,* in order to provide the classifiers with a feature set getting rid of the density of the points acquired during the EAM procedure.

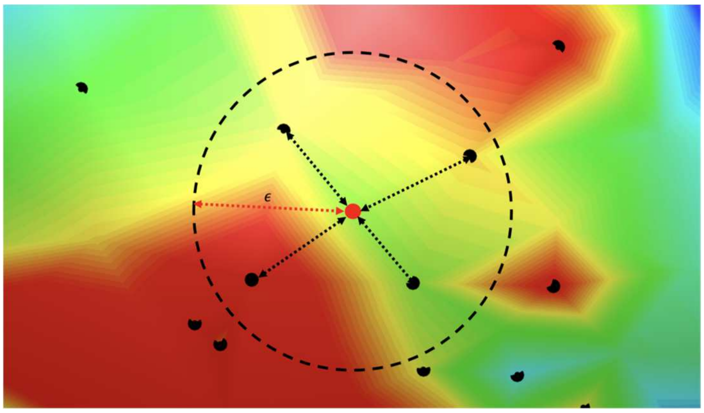

Figure 10.5. Schematic representation of the 6-mm circular area determining the neighbours of the point P (in red) into the voltage map. As can be seen, the neighbourhood is centred on the location of the EGM of interest (P) and spans for a radius equal to ϵ = 6 mm. Black arrows represent the distances between each neighbour point and P. All EGM points falling within the selected area are exploited for the computation of the spatial features of P.

As regards the LAT map, which relies on a temporal estimate of the local activation, it was exploited for the definition of three additional spatial features: the LAT value, the conduction velocity (CV) and the coherence of directions (CD). The LAT value identified the local activation time for each EGM. In this study, it was derived from the CARTO®3v6 exported files or, if absent, by interpolation of map neighbours, and expressed in ms. In fact, in those cases in which LAT values were missing, it was decided to associate a LAT value equal to the corresponding one in the EA map in which the EGM point was localized, typically generated by the interpolation performed by the CARTO®3 system itself. It is important to note that this is an approximation taken in order to avoid being forced to eliminate further points from the dataset.

On the other hand, the CV was adopted since it provides important information on the wavefront speed and the direction of its propagation, thus being intrinsically related to electrophysiological properties of the myocardial substrate, even in case of arrhythmogenic mechanisms [310]. Following [311], [312], it was possible to derive not only the intrinsic CV value, but also the direction of wavefront conduction as CV vectors. Indeed, starting from the discrete LAT values [311], [312], the activation map can be reconstructed using Cubic Radial Basis Function interpolation. Once interpolation is performed, a LAT value is obtained for each position of the EA map. However, since the LAT is a temporal measure associated in each point to a spatial position X = [x, y, z], a continuous and differentiable interpolation function t = t(x, y, z) can be obtained at this phase, describing the variation of the activation time as a function of the position [311]. As such, through the derivation of the function t, the components of the CV vector can be computed for each point. An example of LAT map with CV vectors is reported in Figure 10.6.

On this basis, in order to measure how much chaotic and turbulent the conduction was, the coherence of the directions of the different velocity vectors was estimated. Specifically, to this aim, the neighbours in the 6-mm circular area were identified, and the angle between the CV vectors belonging to the point *P* and to each neighbour was estimated. Therefore, in order to measure the coherence of the propagation direction, the standard deviation of the angles was extracted as CD feature for each EGM map point. Specifically, the higher the conduction disorganization and chaoticity, the higher the CD value. In Figure 10.7 a conceptual representation of the CD computation is provided.

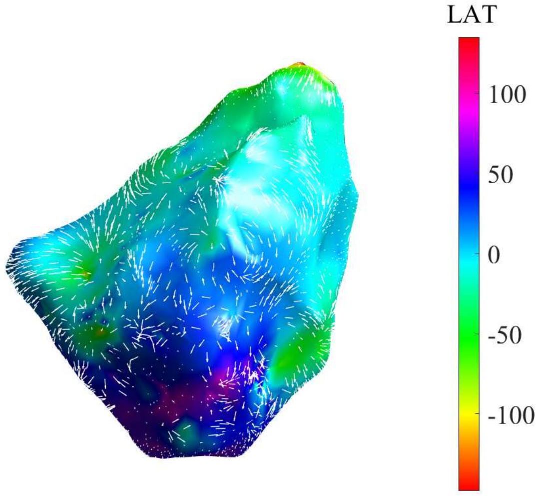

Figure 10.6. Example of LAT map with CV vectors (white arrows).

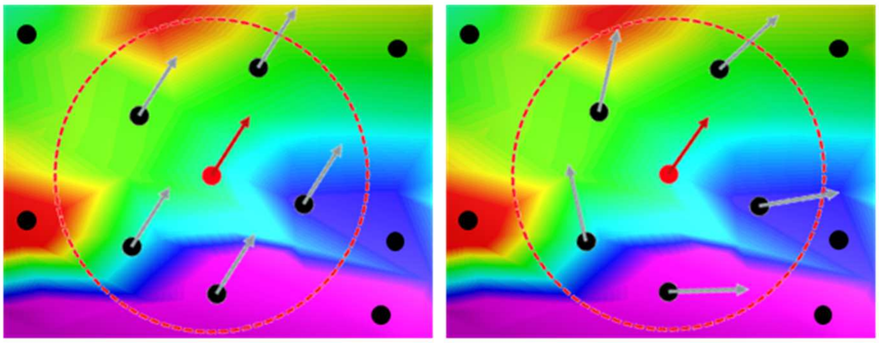

Figure 10.7. Schematic representation of CD feature computation. Once the 6-mm neighbourhood (dashed line in red) around the point P (red point) is identified, the CV vector of each neighbour (grey arrow) is evaluated as long as its orientation with respect to the CV vector of P (red arrow). If the wavefront propagation is not disorganized (on the left), the CD will be low, being computed as the standard deviation of the angles between the red arrow and grey arrows. Conversely, in case of disordered propagation (on the right), the CV vectors in the neighbourhood will point towards different directions, thus resulting in higher CD values.

Finally, all features were standardized with mean zero and unit variance and used to train two machine learning models.

Specifically, in order to evaluate the features effectiveness in AVPs and physiological EGMs recognition, a binary support vector machine (SVM) classifier with a 3rd order polynomial kernel was chosen. On the other hand, due to the variety of characteristics and morphologies affecting the AVPs class, another binary classifier based on a multi-class weighted k-nearest neighbour (KNN) classification model was also introduced to recognise the LP1, LP2, EP and physiological EGMs. In the latter, a number of neighbours equal to ten were imposed, whereas the distance weighting function was set equal to the inverse of the squared distance. The parameters mentioned above were chosen according to a preliminary investigation performed with MATLAB Classification Learner toolbox (data not shown). For all the other parameters, the default values were used, as the dataset size is intrinsically limited and an hyperparameter optimization could lead to overfitting. Thus, any future fine-tuning of any classifier parameter on larger dataset could help in reaching better performance, which however was not the primary objective of this PhD thesis.

While the SVM classifier was asked to binary recognize between AVPs and Physio signals, the weighted KNN was forced to perform a multi-classification between the different types of AVPs and the Physio class, in order to improve their identification while enabling a deeper analysis on the pathological signals, thus allowing for a higher-level recognition among the different morphologies and characteristics. Nonetheless, the main objective of the developed machine learning tool is the identification of AVPs as target point for VT substrate-guided ablation, regardless of their type, in order to support the clinicians in their detection during the EAM and ablation procedures. As such, even if the weighted KNN is trained using four labelling types, during the test phase the annotations were converted into binary neglecting the type of AVP signal recognized, i.e. all EGMs classified as LP1, LP2 and EP were simply considered as AVPs.

Moreover, since in our previous investigation [307] the benefit of the feature extraction was questioned, an artificial neural network (ANN) trained and tested on time-domain segments of the same intracardiac potentials was included in this study. Specifically, a feedforward, fully-connected neural network with rectified linear unit (ReLU) activation function, with a size of fully connected layer equal to 100, and strength of the regularization term set to 0, was adopted to recognize between AVPs and Physio classes. For this purpose, the same time-window of 350 ms around the reference annotation was adopted and the time-domain course of each raw EGM was considered as input for an ANN model, after standardization with mean zero and unit variance.

10.3 Methods for the comparative analysis

In order to provide an objective and quantitative evaluation of the proposed classification approaches, all classification methods were trained and tested through a 10-time 10-fold cross-validation scheme and a leave-one-subject-out cross-validation scheme. The first validation strategy was adopted in order to obtain an objective and robust assessment of the performance by exploiting stratified partitions, whereas the second one allows, on one side, for an accurate performance evaluation on observations never seen by the classifier during training, thus resembling the most a real application scenario, and, on the other hand, for the evaluation of the impact due to eventual patient-specific characteristics of this kind of signal.

As detailed in previous Section 10.2, the overall dataset was significantly imbalanced (i.e., more than 70% of EGMs belonged to the Physio class, as shown in Figure 10.3). Therefore, a random downsampling of physiological EGMs was performed in order to achieve an equal number of Physio and AVPs observation (i.e., 752 EGMs for each class), thus balancing the dataset composition. This strategy was adopted in the 10-time 10-fold cross-validation approach, in each time and fold sub-division, but not in the leave-one-subject-out case, in order to avoid reducing even more the dataset composition according to the very small number of AVPs for each patient. Finally, to perform an effective comparative analysis of the performance obtained by the different machine learning approaches, all models were trained and tested using the same AVPs and Physio sets, in each possible sub-division of the main dataset, thus exploiting the same folds among the models in each considered iteration.

To evaluate the performance of the classifiers, five indices were estimated, i.e., the accuracy (Acc_{cl}), the true positive rate (TPR_{cl}) or Sensitivity, the true negative rate (TNR_{cl}) or Specificity, the false positive rate (FPR_{cl}), i.e. the false AVPs alarm rate, and the F1-score$_{\mathrm{cl}}$, as:

$$Acc_{cl} = \frac{TP_{cl} + TN_{cl}}{P_{cl} + N_{cl}} \tag{10.3}$$

$$TPR_{cl} = \frac{TP_{cl}}{P_{cl}} \tag{10.4}$$

$$TNR_{cl} = \frac{TN_{cl}}{N_{cl}} \tag{10.5}$$

$$FPR_{cl} = \frac{FP_{cl}}{N_{cl}} \tag{10.6}$$

$$F1 - score_{cl} = 2\,\frac{PPV_{cl} \cdot TPR_{cl}}{PPV_{cl} + TPR_{cl}} \tag{10.7}$$

where P_{cl} and N_{cl} represent the total number of AVPs and Physio EGMs, TP_{cl} and TN_{cl} the number of AVPs and Physio potentials correctly identified, respectively, FP_{cl} the normal EGMs classified as AVPs and PPV_{cl} the positive predictive value or precision, defined as:

$$PPV_{cl} = \frac{TP_{cl}}{TP_{cl} + FP_{cl}} \qquad (10.8)$$

Specifically, in the 10-time 10-fold cross-validation scheme, the performance indexes were evaluated on the total number of $TP_{cl}, TN_{cl}, FP_{cl}, P_{cl}$ and N_{cl} obtained by summation over the different folds at each time. Therefore, all indexes were computed for each group of ten folds, and results were reported as mean and standard deviation of the values obtained across the ten iterations, thus yielding to cumulative indexes better representing the behaviour of the models over the whole dataset. Conversely, confusion matrices were assessed cumulatively, by summing up not only the predictions in the different fold, but also the predictions of all the experiments repeated ten times. Similarly, in the leave-one-subject-out case, summation was exploited over the different patient-related subsets, thus obtaining a single value per performance index in the end. Nonetheless, this choice was mandatory for the leave-one-subject-out case because of the imbalanced dataset, in order to avoid getting results strongly biased by the number of AVPs included in each partition.

Furthermore, two additional investigations were added, in order to evaluate the impact of the feature selection and the projection distance on the automatic recognition results.

As regards feature selection, after the Pearson's correlation coefficient ρ on each pair of features was appraised (see Figure 10.8), the minimum redundancy maximum relevance (mRMR) feature selection method was adopted to minimize the redundancy and maximize the relevance of the feature set with respect to the response variable [313], [314], thus trying to identify the features with most useful information content. The feature selection was initially carried out on the training set obtained in each fold and time, for the 10-time 10-fold cross-validation scheme, and for each patient-related iteration in the leave-one-subject-out case, leading to 100 feature selections for the 10-time 10-fold cross-validation, whereas to nine feature selections in the leave-one-subject-out case. Then, a common set of features for the entire assessment was derived as follows. Based on the importance score provided by the mRMR algorithm for each feature, a score vector was generated at each iteration and then normalized between 0 and 1. Subsequently, the sum of the scores was considered for each specific feature, and a single score vector (V) with a relevance value for each feature was obtained. Then, V was sorted in descending order and the contribution of each feature, from the most important to the less important one, was cumulatively summed until the 80% of the total information content was reached. At this point, the first M features contributing to the 80% of the total information content were considered as selected features for the investigation on the entire set. The 80% threshold was imposed on the information content empirically, according to preliminary investigations in which the imposed value was found to be adequate for feature reduction (data not shown). All features selected for each cross-validation scheme are reported in Table 10.1.

As regards the impact of the projection distance, it was assessed in order to evaluate if any discrepancy in the results could be observed when including in the dataset only those EGMs with an accurate projection on the EA map, i.e. those exhibiting a mismatch or distance lower than a specific threshold. This investigation has been introduced additionally, in order to check if the classification results obtained on the complete dataset could be confirmed or even enhanced by eliminating those points with less accurate and reliable spatial location, but not as a primary analysis since it causes a decrease of the total number of EGMs included in the analysis, thus affecting even more the limited size of the adopted dataset. As such, classification results were

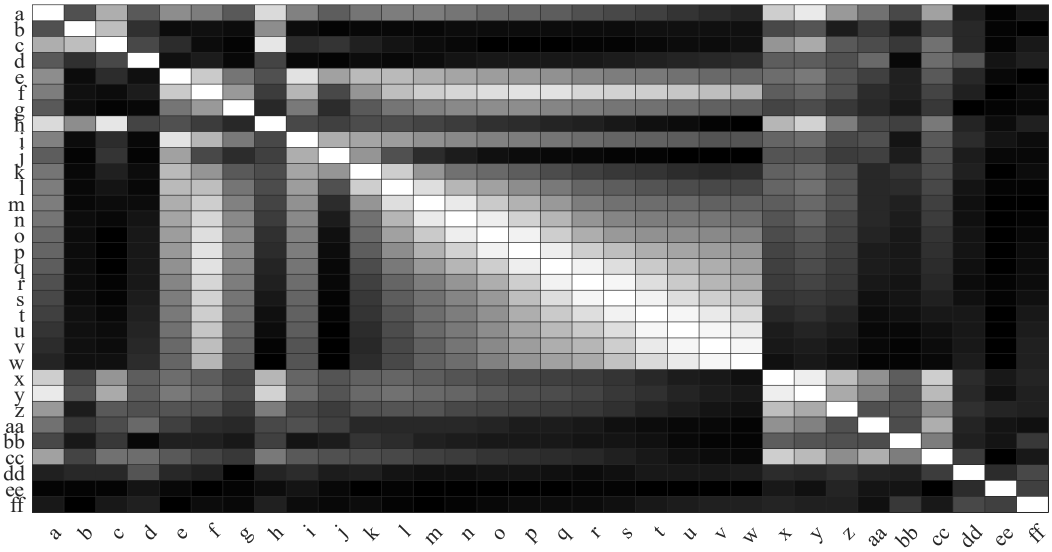

Figure 10.8. Schematic representation of the Pearson's correlation coefficient ρ computed on each pair of features. Black colour represents higher correlation (i.e., one in absolute terms), while white colour reflects lower correlation (i.e., zero). Abbreviations stand for: a) bipolar A_{pp}, b) standard deviation of the five highest CWT powers, c) sum of the five highest CWT powers, d) fragmentation measure, e) PSR, f) MNF, g) PKF, h) MNP, i) relative PSD power in 0 – 20 Hz, j) in 40 – 60 Hz, k) in 60 – 80 Hz, l) in 80 – 100 Hz, m) in 100 – 120 Hz, n) in 120 – 140 Hz, o) in 140 – 160 Hz, p) in 160 – 180 Hz, q) in 180 – 200 Hz, r) in 200 – 220 Hz, s) in 220 – 240 Hz, t) in 240 – 260 Hz, u) in 260 – 280 Hz, v) in 280 – 300 Hz, w) in 300 – 320 Hz, x) mean bipolar A_{pp} in the neighbourhood, y) weighted mean bipolar A_{pp} in the neighbourhood, z) standard deviation of the A_{pp} in the neighbourhood, aa) neighbours with $A_{pp} < 0.5$ mV, bb) neighbours with 0.5 mV $< A_{pp} < 1.5$ mV, cc) neighbours with $A_{pp} > 1.5$ mV, dd) LAT, ee) CV, ff) CD.

computed also after the dataset was cleaned up by removing 1422 EGMs (i.e., 1156 EGMs from Physio and 266 from AVPs) exhibiting a projection distance on the map greater than 6 mm. Table 10.2 details the number of EGM recordings that were removed for each class and patient in this latter evaluation. Interestingly, in the two different cross-validation scenario, similar features are selected.

All computations were performed with MATLAB v2021a (MathWorks Inc., MA, USA).

Table 10.1. Feature selected by the mRMR approach in the two cross-validation schemes. Specifically, features included for each validation approach are identified by ■. As can be seen, most of them are shared between the two cross-validation methods.

Feature	10-time 10-fold cross-validation	leave-one-subject-out cross-validation	Feature	10-time 10-fold cross-validation	leave-one-subject-out cross-validation
Bipolar A_{pp}	■	■	Relative PSD power in 180 – 200 Hz	■	■
Standard deviation of the five highest CWT powers	■	■	Relative PSD power in 200 – 220 Hz	■	■
Sum of the five highest CWT powers	■	■	Relative PSD power in 220 – 240 Hz	■	■
Fragmentation measure	■	■	Relative PSD power in 240 – 260 Hz		■
PSR			Relative PSD power in 260 – 280 Hz		
MNF			Relative PSD power in 280 – 300 Hz		
PKF			Relative PSD power in 300 – 320 Hz	■	■
MNP	■	■	Mean bipolar A_{pp} in the neighbourhood	■	■
Relative PSD power in 0 – 20 Hz			Weighted mean bipolar A_{pp} in the neighbourhood	■	■
Relative PSD power in 40 – 60 Hz		■	Standard deviation of the A_{pp} in the neighbourhood	■	■
Relative PSD power in 60 – 80 Hz			Neighbours with A_{pp} < 0.5 mV		■
Relative PSD power in 80 – 100 Hz	■		Neighbours with 0.5 mV < A_{pp} < 1.5 mV		
Relative PSD power in 100 – 120 Hz	■	■	Neighbours with A_{pp} > 1.5 mV	■	■
Relative PSD power in 120 – 140 Hz			LAT	■	■
Relative PSD power in 140 – 160 Hz	■	■	CV		
Relative PSD power in 160 – 180 Hz	■	■	CD	■	

Table 10.2. Number of EGM recordings that were removed for each class and patient by limiting the projection distance to 6 mm. As can be seen, a total of 1422 EGMs were discarded, of which 266 among AVPs.

	Patient #1	Patient #2	Patient #3	Patient #4	Patient #5	Patient #6	Patient #7	Patient #8	Patient #9
Physio	235	31	24	450	56	152	55	130	23
LP1	23	1	3	42	2	29	3	1	9
LP2	14	24	5	2	0	31	3	0	1
EP	9	0	4	0	6	41	12	1	0

10.4 Results and discussion

10.4.1 Results by proposed automatic recognition approaches

Performance results obtained by the SVM and KNN approaches are shown in Tables 10.3 and 10.4 for the 10-time 10-fold and the leave-one-subject-out cross-validation schemes respectively, along with those achieved by the ANN-based strategy. Remarkably, for the leave-one-subject-out cross-validation, a single value for ACC_{cl}, TPR_{cl}, FPR_{cl}, TNR_{cl}, and F1-$score_{cl}$ is provided since the performance indexes were evaluated on the total number of TP_{cl}, TN_{cl}, FP_{cl}, P_{cl} and N_{cl} obtained by summation over the different patients at each iteration (see Section 10.3).

Table 10.3. Results achieved by the SVM and KNN models by the 10-time 10-fold cross-validation scheme. Cumulative values are reported as mean and standard deviation computed across the ten times. For the sake of a complete comparison, also the results of the ANN-based model have been reported.

	SVM model	KNN model	ANN model
ACC_{cl} [%]	90.2 ± 0.8	92.4 ± 0.7	83.7 ± 0.9
TPR_{cl} [%]	91.0 ± 0.7	90.7 ± 0.8	82.0 ± 1.2
TNR_{cl} [%]	89.4 ± 1.1	94.1 ± 1.0	85.3 ± 1.2
FPR_{cl} [%]	10.6 ± 1.1	5.9 ± 1.0	14.7 ± 1.2
F1-$score_{cl}$	0.90 ± 0.01	0.92 ± 0.01	0.83 ± 0.01

As can be seen, classification performances were quite high, similar, and stable for both proposed methods, whereas in case of ANN model they worsened considerably. Nonetheless, F1-$scores_{cl}$ underlined that both feature-based approaches exhibited high precision and TPR. However, a deterioration in all performance indexes could be perceived when jumping from the 10-time 10-fold to the leave-one-subject-out case, as expected. Furthermore, some differences could be appreciated when focusing on TPR_{cl}, TNR_{cl} and FPR_{cl}, since these values became slightly different in SVM and KNN models. In fact, while the recognition of AVPs and Physio classes seemed to be well balanced in the SVM model, it was not true for the KNN one, especially when considering

Table 10.4. Performance indexes achieved by the SVM and KNN models through the leave-one-subject-out cross-validation strategy. Also in this case, the results of the ANN-based model have been reported.

	SVM model	KNN model	ANN model
ACC_{cl} [%]	81.6	85.4	70.3
TPR_{cl} [%]	77.8	68.8	57.0
TNR_{cl} [%]	83.2	92.3	75.8
FPR_{cl} [%]	16.8	7.7	24.2
F1-$score_{cl}$	0.71	0.73	0.53

the leave-one-subject-out case. Specifically, looking at first at 10-time 10-fold cross-validation results, both AVPs and Physio EGMs were correctly recognized by the SVM in approximately 90% of cases, whereas in the KNN model the ability of Physio recognition reached higher values (i.e., about 94%) than AVPs. These results implicitly led to higher FPR_{cl}, i.e. more frequently false AVPs alarms, in the SVM model than in the KNN one (10.6% vs. 5.9%, respectively). Conversely, bigger differences in TPR_{cl}, FPR_{cl} and TNR_{cl} values were found in the leave-one-subject-out case. In fact, in this scenario, the SVM model seemed to better recognise Physio EGMs than AVPs (i.e., 83.2% vs. 77.8%, see Table 10.4) with an higher false AVPs alarm rate, and the same trend was visible for the KNN approach, in which the gap between TPR_{cl} and TNR_{cl} was more emphasized (i.e., 92.3% vs 68.8%, see Table 10.4). However, considering that the aim of the developed tool should be supporting clinicians in the recognition of arrhythmogenic substrates, which are identified by AVPs, the performance of the SVM classifier seemed to move closer to the purpose, even if drawing attention to an higher number of false AVPs. Cumulative confusion matrices are reported in Figures 10.9 and 10.10.

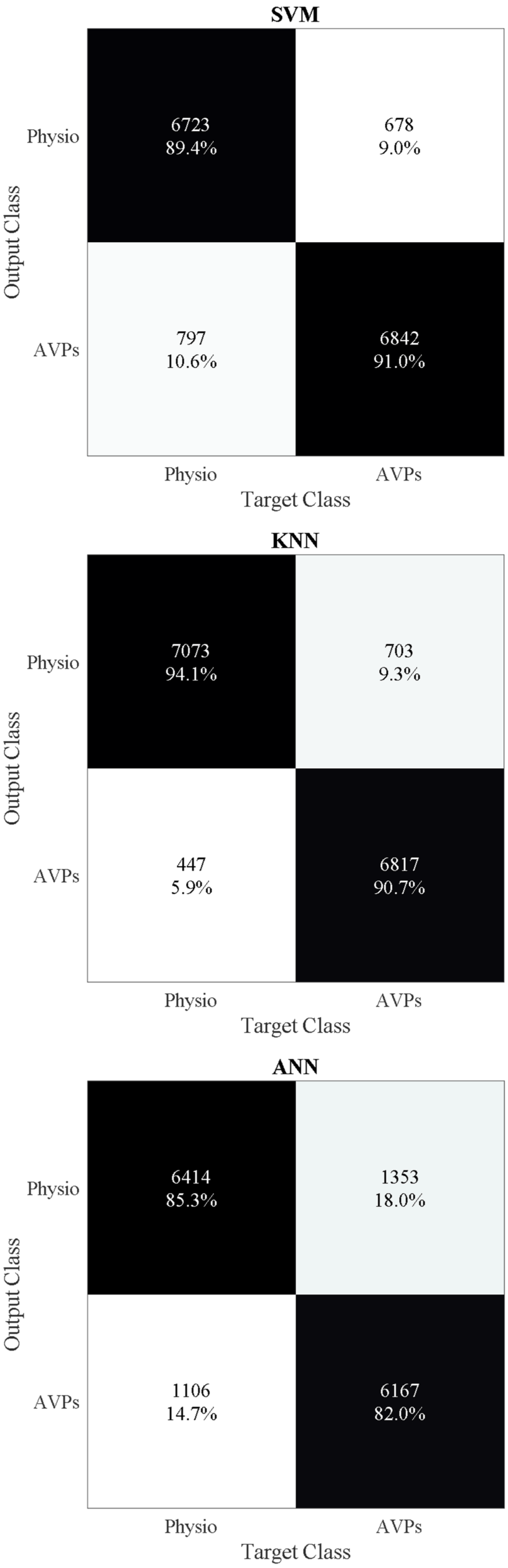

SVM

Output Class \ Target Class	Physio	AVPs
Physio	6723 89.4%	678 9.0%
AVPs	797 10.6%	6842 91.0%

KNN

Output Class \ Target Class	Physio	AVPs
Physio	7073 94.1%	703 9.3%
AVPs	447 5.9%	6817 90.7%

ANN

Output Class \ Target Class	Physio	AVPs
Physio	6414 85.3%	1353 18.0%
AVPs	1106 14.7%	6167 82.0%

Figure 10.9. Confusion matrices for the three classification models obtained in the 10-time 10-fold cross-validation scheme.

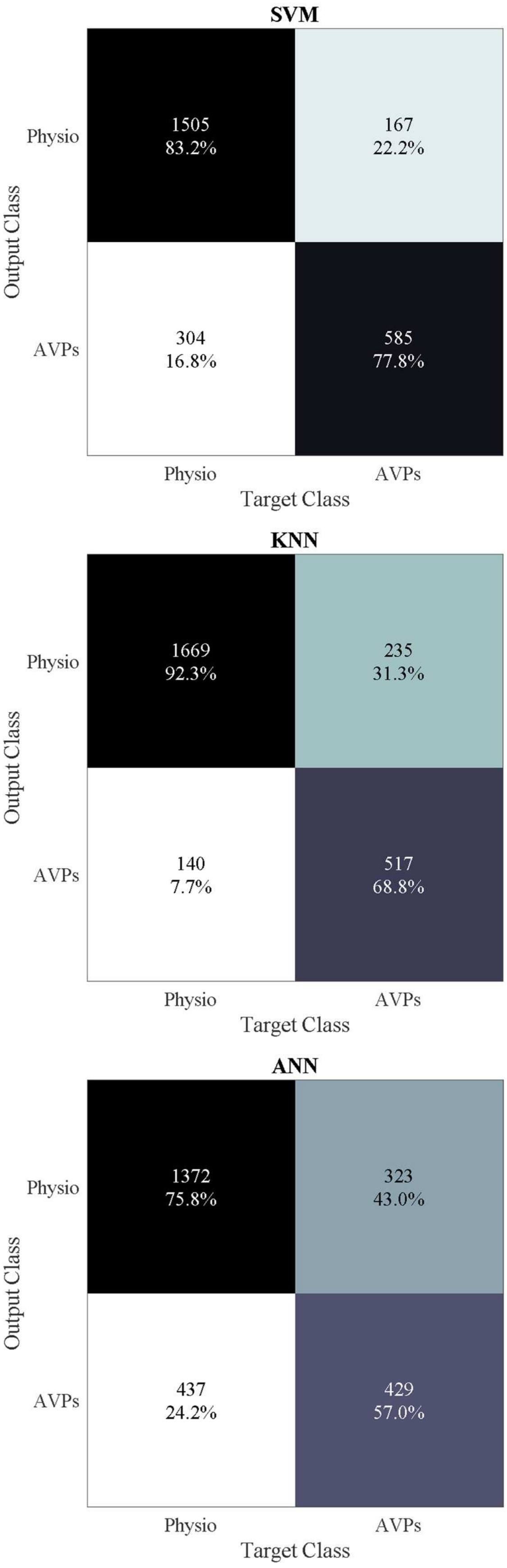

SVM

Output Class \ Target Class	Physio	AVPs
Physio	1505 83.2%	167 22.2%
AVPs	304 16.8%	585 77.8%

KNN

Output Class \ Target Class	Physio	AVPs
Physio	1669 92.3%	235 31.3%
AVPs	140 7.7%	517 68.8%

ANN

Output Class \ Target Class	Physio	AVPs
Physio	1372 75.8%	323 43.0%
AVPs	437 24.2%	429 57.0%

Figure 10.10. Confusion matrices for the three classification models obtained in the leave-one-subject-out cross-validation scheme.

10.4.2 Results of feature selection and projection distance

Results obtained by **feature selection** are reported in Tables 10.5 and 10.6 for the 10-time 10-fold and the leave-one-subject-out cross-validation schemes respectively. By looking at those values, it is evident that the performance remained stable when only some features were taken into account, in terms of all the performance indexes and for both classification models. Thus, reducing the number of involved features could lead to high and accurate performance as well as using all the features, with same disparities in TPR_{cl}, FPR_{cl} and TNR_{cl} values. Similarly, also the cumulative results obtained in the confusion matrices (see Figure 10.11) showed no improvements nor substantial modifications (i.e., below 2.5%) with respect to the results achieved by considering the complete feature set.

Table 10.5. Mean and standard deviation of the different performance indexes obtained by the SVM and KNN models by the 10-time 10-fold cross-validation scheme when feature selection was adopted.

	SVM model	KNN model
ACC_{cl} [%]	88.9 ± 0.7	91.7 ± 0.4
TPR_{cl} [%]	90.6 ± 0.8	89.6 ± 0.8
TNR_{cl} [%]	87.3 ± 1.1	93.8 ± 0.7
FPR_{cl} [%]	12.7 ± 1.1	6.2 ± 0.7
F1-$score_{cl}$	0.89 ± 0.01	0.92 ± 0.00

Table 10.6. Performance indexes achieved by the SVM and KNN models through the leave-one-subject-out cross-validation strategy when feature selection was performed.

	SVM model	KNN model
ACC_{cl} [%]	83.1	84.3
TPR_{cl} [%]	77.8	68.5
TNR_{cl} [%]	85.4	90.8
FPR_{cl} [%]	14.6	9.2
F1-$score_{cl}$	0.73	0.72

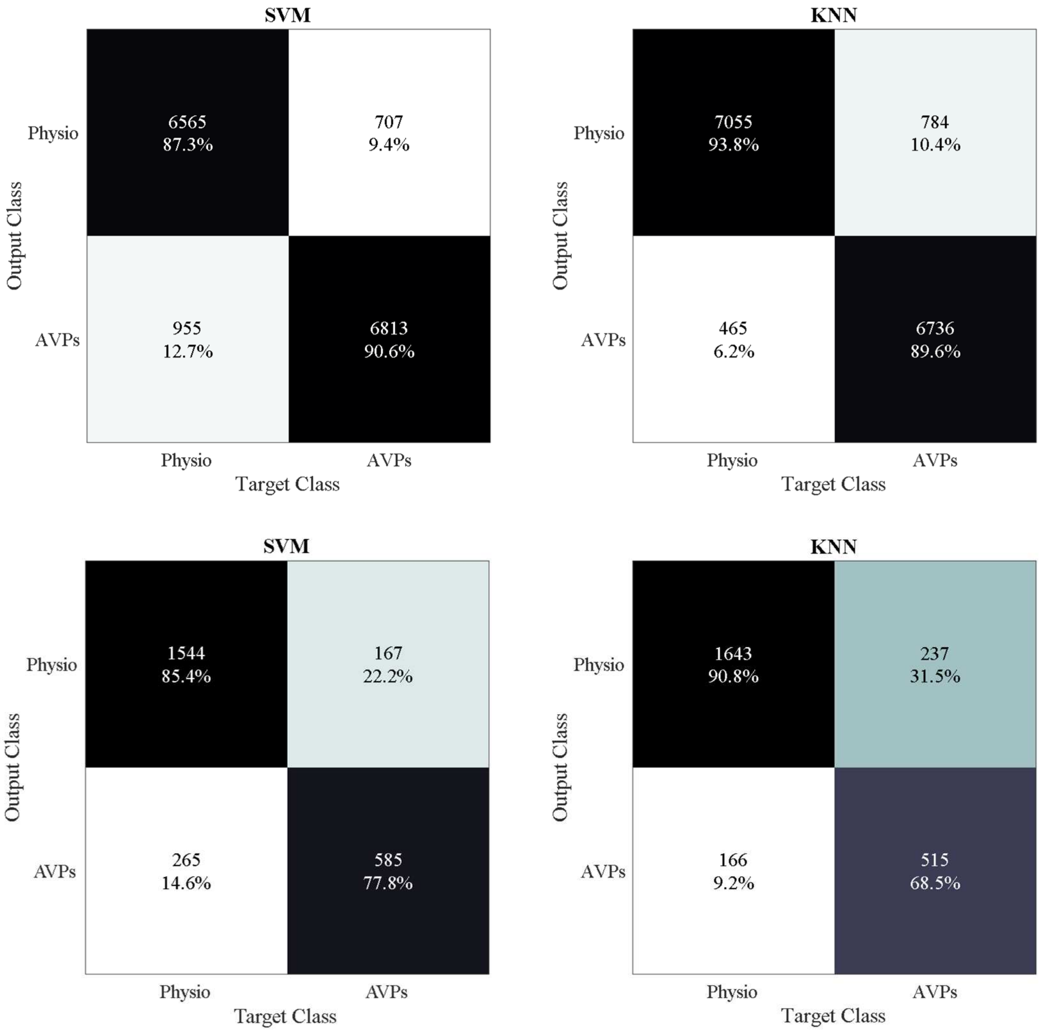

Figure 10.11. Cumulative confusion matrices for the SVM-based and KNN-based classification approaches obtained in the 10-time 10-fold cross-validation scheme (top) and in the leave-one-subject-out cross-validation strategy (bottom) when feature selection was adopted.

Finally, Table 10.7 and 10.8 along with Figure 10.12 report the results achieved by limiting the **projection distance**. As can be seen, by comparing the results obtained in the 10-time 10-fold cross-validation (see Tables 10.7 and 10.3), no significant differences were visible, whereas the same imbalance in AVPs and Physio recognition by the KNN-based model could be still appreciated. Conversely, when considering the leave-one-subject-out validation (see Tables 10.8 and 10.4), some slight changes can be appreciated, especially when looking at TNR$_{cl}$ and FPR$_{cl}$ values in SVM and KNN models. In fact, on the one hand, both classification approaches showed a consistent decrease in the Physio detection accuracy, equal to 5.7% for SVM and 8.5% for KNN, thus resulting in lower accuracies, despite TPR$_{cl}$ values were well preserved. On the other, FPR$_{cl}$ values consistently increased for both SVM (+5.7%) and KNN (+8.5%) approaches, thus suggesting a greater presence of false positive alarms in both methods. Interestingly, when considering only EGMs with accurate and reliable spatial location, the findings obtained by the ANN model seemed to be improved in terms of TPR$_{cl}$ (i.e., 57.0% vs. 69.5%, see Tables 10.4 and 10.8) but not in terms of TNR$_{cl}$ (75.8% vs. 67.8%), nonetheless leading, on the one hand, to very high FPR$_{cl}$ (32.2%), and on the other to low accuracy (ACC$_{cl}$ = 68.6%) and precision (F1-score$_{cl}$ = 0.66) in the recognition of both classes also in this case.

Table 10.7. Performance indexes in terms of mean and standard deviation obtained by the SVM, KNN and ANN models through the 10-time 10-fold cross-validation scheme when projection distance was limited to 6 mm.

	SVM model	KNN model	ANN model
ACC_{cl} [%]	91.3 ± 0.7	92.8 ± 0.7	85.8 ± 1.4
TPR_{cl} [%]	91.6 ± 0.9	91.2 ± 1.0	83.6 ± 2.1
TNR_{cl} [%]	91.0 ± 1.0	94.4 ± 1.1	88.0 ± 1.1
FPR_{cl} [%]	9.0 ± 1.0	5.6 ± 1.1	12.0 ± 1.1
F1-$score_{cl}$	0.91 ± 0.01	0.93 ± 0.01	0.86 ± 0.02

Table 10.8. Performance indexes achieved by the SVM, KNN and ANN models through the leave-one-subject-out cross-validation strategy when projection distance was limited to 6 mm.

	SVM model	KNN model	ANN model
ACC_{cl} [%]	78.3	77.6	68.6
TPR_{cl} [%]	79.4	69.3	69.5
TNR_{cl} [%]	77.5	83.8	67.8
FPR_{cl} [%]	22.5	16.2	32.2
F1-$score_{cl}$	0.76	0.73	0.66

10.4.3 Discussion

In this chapter, different feature-based classification models were proposed to support cardiologists in the recognition of abnormal and physiological potentials in order to reduce the operator-dependence and the EAM procedure times, but also to enable a more accurate targeting of arrhythmogenic sites, thus possibly improving clinical outcomes and VT recurrence. Results reported in Section 10.4.1 showed that the adoption of machine learning methods for the computer-aided recognition of AVPs would be very useful, allowing for a reliable and accurate recognition of abnormal potentials in more than 90% of cases when considering the 10-time 10-fold cross-validation (i.e., 90.2% and 92.4% for SVM and KNN models, respectively; see Table 10.3). Accuracies decreased when the leave-one-subject-out validation was adopted (i.e., 81.6% vs. 90.2% for the SVM model, and 85.4% vs. 92.4% for the KNN-based one, respectively; see Table 10.4), and some discrepancies emerged between AVPs and Physio recognition, especially in the KNN-based approach, and in terms of false AVPs alarm rate between the SVM and KNN. This finding suggests, on the one hand, that the high imbalance between the AVPs and Physio (in the composition of the overall dataset, and as such in every patient-related subset considered in each iteration of the leave-one-subject-out validation) could significantly affect the performance of the classifier. On the other hand, this ambiguity could underline also the presence of patient-specific characteristics among post-ischaemic EGM features in the used dataset. However, despite

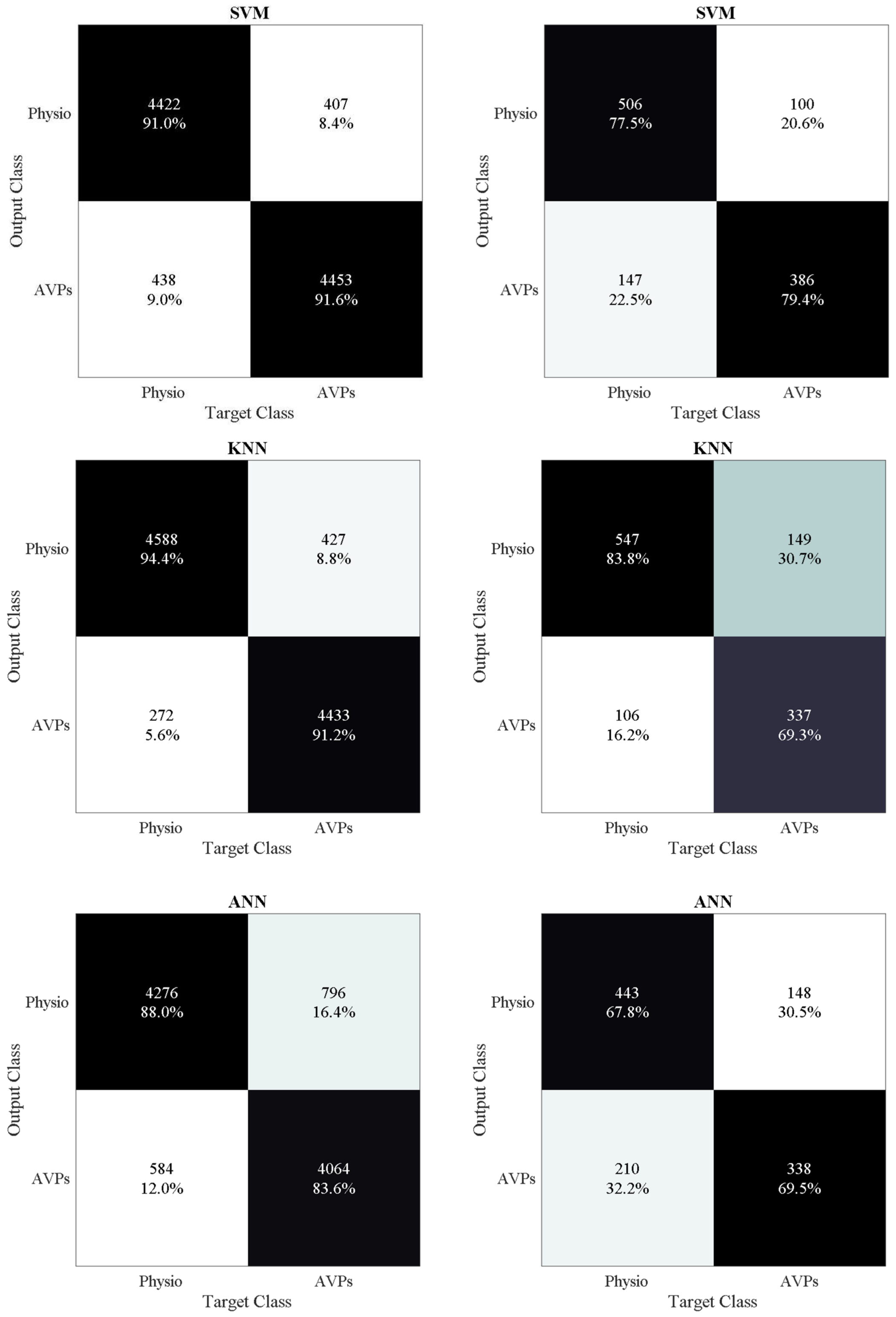

Figure 10.12. Cumulative confusion matrices for the 10-time 10-fold cross-validation scheme (left side) and in the leave-one-subject-out cross-validation strategy (right side) when projection distance was limited to 6 mm.

our previous investigations questioned the usefulness of feature-based models [307], from this analysis it is clear that the only adoption of the time-series representing the EGM is not sufficient to guarantee an accurate and reliable identification of AVPs (i.e., 83.7% and 70.3 % in the 10-time 10-fold and leave-one-subject-out cross-validation schemes, respectively; see Tables 10.3 and 10.4), even when considering only EGMs with a rigorous spatial projection on the EA map (i.e., 85.8% and 68.6% in the 10-time 10-fold and leave-one-subject-out cross-validation schemes, respectively; see Tables 10.7 and 10.8), leading to high false AVPs detection rate, especially when the leave-one-subject-out case is considered.

Moreover, when introducing a feature selection (see Section 10.4.2), classification performance remained stable and high, which is important for real-time application scenarios.

Conversely, the inclusion of only those EGMs with an accurate projection on the EA map overall confirmed the previous results, but in the leave-one-subject-out validation results, some difference arose. Specifically, TNR_{cl} values decreased significantly in both SVM-based and KNN-based models, whereas TPR_{cl} findings remained quite stable (see Tables 10.4 and 10.8). This fact could be due to the considerable reduction in Physio observations when the projection distance was limited. In fact, among the 1422 removed EGMs, 1156 were from Physio and 266 from AVPs, thus generally affecting even more the size of the adopted dataset, especially in terms of physiological potentials. Furthermore, as shown in Table 10.2, an abundance of discarded physiological EGMs occurred mostly in two patients (i.e., patients #1 and #4), which could have determined a consistent bias, especially in our leave-one-subject-out results, since several EGMs for these patients were not considered in this latter analysis. As such, the results of this investigation would benefit from the adoption of a larger database that we are currently contributing to create.

Chapter 11

Conclusions on Part II

As already detailed in Chapter 8, despite the clinical and scientific effort put in the treatment of VTs, their recurrence is still high [206], [295]. Some aspects related to the mechanisms underlying the VT origin and maintenance are still an open issue [296], [297], as long as the need of performing ablation only on decisive and essential target points [298].

In light of all these premises, the first aim of this part of my PhD thesis was the characterization of EGMs in the frequency domain. In this regard, despite the widespread association of AVPs with high-frequency spectral contents in post-ischaemic intracardiac bipolar EGMs, a rigorous spectral analysis of these signals was missing in the scientific literature. In this thesis, this gap was addressed, and the investigation revealed that the main frequency contributions of physiological and pathological post-ischaemic EGMs are found below 320 Hz. Moreover, when amplitude influences are eliminated, physiological potentials show greater contributions at lower frequencies whereas AVPs demonstrate higher spectral contributions at frequencies above ~40 Hz. Conversely, when looking at AVPs only, LP1 showed lower power contributions than LP2 and EP mainly above 60 Hz, whereas LP2 and EP EGMs statistically differed in 200–220 Hz sub-band. In the light of the above-mentioned spectral signatures of AVPs and physiological potentials, these findings may be valuable not only because they represent a spectral characterisation of these potentials, moving a step forward in the direction of a deeper understanding of arrhythmogenic substrate mechanisms, but also to support the development of automatic tools for the efficient and targeted distinction of different physiological and abnormal EGM types.

The second aim of this part was the development of a novel and effective computer-assisted algorithm for targeting arrhythmogenic sites in VT trans-catheter ablation procedures. The main goal concerned the conception of the artificial intelligence tools to support cardiologists in the recognition of the ablation targets during post-ischaemic VT electrophysiological procedures, thus possibly reducing the procedure time while improving their effectiveness in the arrhythmogenic substrate identification and, possibly, the clinical outcome. As such, different classification methods for the automatic identification of AVPs in intracardiac bipolar EGMs were presented and compared. The first two approaches were based on a SVM classifier and a weighted KNN model, trained and tested on different features extracted from the time, the time-scale, the frequency and the spatial domains, while another one was based on an ANN trained on the time-series of the samples forming the bipolar EGM. The latter was introduced in order to assess the actual need of exploiting features in the automatic AVPs recognition, already questioned in our preliminary investigations [307]. Classification results showed high accuracy for both feature-based methods, with some differences in terms of false positive and negative rates according to the chosen identification approach. These findings are promising, also when exploiting feature selection, and are even confirmed when including in the dataset only those EGMs exhibiting a reliable spatial location in the EA map, suggesting the efficacy of proposed methods and, as such, the possibility of AVPs automatic recognition with the suggested features. Even though the results are encouraging and confirm the possibility for the technological development of computer-aided systems to be successfully applied in interventional electrophysiology, their generalizability should be carefully considered because of the limited size of the dataset. Moreover, signal annotation was performed by a single expert cardiologist, which could have led to a biased response. Deeper analyses on larger datasets could overcome these limitations and assess the actual exploitability of the proposed approach in clinical procedures.

Chapter 12

Final conclusions

According to the high incidence and mortality of cardiovascular diseases [1], [2], a huge amount of scientific effort and research attempt have been recently put in investigating and developing innovative strategies and devices aiming to improve not only the diagnosis and treatment, but also monitoring and prevention. This PhD thesis was developed in the path of this trend, aiming to study and conceive novel approaches supporting the diagnosis and treatment of cardiac diseases, by exploiting advanced signal processing and machine learning tools. Specifically, the focus of this research was pointed on two main topics: NI-fECG and intracardiac electrophysiology, mainly related to post-ischaemic VT substrate-guided mapping and radiofrequency ablation.

As regards the NI-fECG investigation, different advanced signal processing tools were introduced and assessed with the aim of recovering morphologically preserved NI-fECG signals. Specifically, a novel NI-fECG extraction algorithm has been developed, in collaboration with Prof. Hau-Tieng Wu (Department of Mathematics and Statistical Science, Duke University, Durham, NC, USA). The proposed algorithm exhibited high performance, not only when evaluated in terms of fHR detection, but also when a morphological analysis is pursued. Furthermore, different WD post-processing algorithms have been investigated in order to provide an accurate and efficient NI-fECG enhancement, and statistically compared in a quantitative review. Remarkably, the WD algorithm settings underlined in our initial investigation proved to be the best-performing solution for the NI-fECG post-processing with respect to other approaches proposed in the scientific literature, especially in terms of signal morphology preservation, whereas a different strategy derived from the work by Ionescu [146] appeared as the best methodology when the noise reduction is mainly required, as in fHR monitoring devices.

Both NI-fECG extraction and post-processing investigations are of great relevance, since they could allow for a better recovery of fECG signals, thus paving the way for its adoption in clinical practice for antenatal screening and diagnosis, but also for their integration in foetal cardiac monitoring devices, as the one proposed in the PRIN ICT4MOMS project, in which I'm currently involved. In this sense, other different datasets could be exploited for an effective evaluation of these methods on unhealthy foetuses, but also on twin pregnancies, especially for the NI-fECG extraction purpose. Furthermore, future research could be focused on accurate channel selection to be applied before NI-fECG extraction step, in order to develop a smart wearable NI-fECG monitoring system able to adapt to the foetal positions and gestational age. All these future steps are actually work-in-progress, along with further improvements to the fECG algorithms based on geometrical information.

As regards the intracardiac electrophysiology, different signal processing and artificial intelligence tools have been introduced with a twofold purpose: giving new spectral insights of both AVPs and post-ischaemic physiological EGMs, thus moving a step forward in the direction of a deeper understanding of the VT arrhythmogenic mechanisms, on the one hand, and supporting clinicians in the recognition of the ablation targets during electrophysiological procedures, thus possibly reducing procedure times while improving their effectiveness in the arrhythmogenic substrate delineation and, eventually, the clinical outcome, on the other one. As such, in the light of the first objective, a deeper spectral characterization of both physiological and abnormal potentials has been carried out. The study revealed that the main frequency contributions of physiological and abnormal post-ischaemic EGMs are found below 320 Hz.

Furthermore, when amplitude influences were disregarded, physiological potentials showed greater contributions at lower frequencies, i.e., manly below 20 Hz, whereas AVPs demonstrated higher spectral contributions at frequencies above approximately 40 Hz, but several finer differences may be observed between the different AVP types. These achievements may be valuable not only to achieve a basic characterisation of these potentials and a deeper understanding of arrhythmogenic substrate mechanisms, but also when developing automatic approaches for their recognition. In fact, in order to address the second scientific objective, different artificial intelligence tools have been introduced and assessed for the automatic identification of AVPs in intracardiac bipolar EGMs. Supervised automatic recognition results showed high accuracy, with some differences in terms of false positive and negative rates according to the chosen classification approach. These findings are promising in different scenarios, suggesting the efficacy of proposed features and recognition methods and, as such, the possibility of AVPs automatic identification in clinical context.

Also in this case, both investigations are valuable since consistently contribute to a deep characterization of the arrhythmogenic substrates and their related signals, while introducing possible computer-aided systems to support clinicians in their recognition during substrate-guided mapping procedures. Despite the need of a more substantial dataset and annotations by multiple experts, this PhD thesis opens to the technological development of artificial intelligence systems to be integrated in off-the-shelf EAM devices and successfully applied in post-ischaemic VT substrate mapping and ablation procedures, thus improving the clinical strategy and outcome. However, in this sense, many interesting aspects are still to be inspected, as the use of other advanced signal processing and machine learning methods, such as complexity analysis and deep learning, but also filtering strategies in order to enhance only the pathological signatures. Remarkably, all this aspects are currently being studied and a patent is being deposited.

References

[1] S. S. Virani *et al.*, "Heart Disease and Stroke Statistics - 2020 Update: A Report From the American Heart Association," *Circulation*, vol. 141, no. 9, pp. e139-596, 2020.

[2] S. S. Virani *et al.*, "Heart Disease and Stroke Statistics - 2021 Update: A Report From the American Heart Association," *Circulation*, vol. 143, no. 8, pp. e254–e743, 2021.

[3] M. T. Donofrio *et al.*, "Diagnosis and Treatment of Fetal Cardiac Disease," *Circulation*, vol. 129, no. 21, pp. 2183–2242, May 2014.

[4] R. Sameni and G. D. Clifford, "A Review of Fetal ECG Signal Processing; Issues and Promising Directions," *Open Pacing. Electrophysiol. Ther. J.*, vol. 3, pp. 4–20, Jan. 2010.

[5] A. Darma *et al.*, "Predictors of long-term mortality after catheter ablation of ventricular tachycardia in a contemporary cohort of patients with structural heart disease.," *Eur. Eur. pacing, arrhythmias, Card. Electrophysiol. J. Work. groups Card. pacing, arrhythmias, Card. Cell. Electrophysiol. Eur. Soc. Cardiol.*, vol. 22, no. 11, pp. 1672–1679, Nov. 2020.

[6] I. Bulatovic, A. Månsson-Broberg, C. Sylvén, and K.-H. Grinnemo, "Human fetal cardiac progenitors: the role of stem cells and progenitors in the fetal and adult heart," *Best Pract. Res. Clin. Obstet. Gynaecol.*, vol. 31, pp. 58–68, 2016.

[7] M. Buckingham, S. Meilhac, and S. Zaffran, "Building the mammalian heart from two sources of myocardial cells," *Nat. Rev. Genet.*, vol. 6, no. 11, pp. 826–835, 2005.

[8] A. Finnemore and A. Groves, "Physiology of the fetal and transitional circulation," in *Seminars in fetal and neonatal medicine*, 2015, vol. 20, no. 4, pp. 210–216.

[9] R. H. Anderson *et al.*, "Normal and Abnormal Development of the Heart BT - Pediatric and Congenital Cardiology, Cardiac Surgery and Intensive Care," E. M. Da Cruz, D. Ivy, and J. Jaggers, Eds. London: Springer London, 2014, pp. 151–177.

[10] C. M. J. Tan and A. J. Lewandowski, "The transitional heart: from early embryonic and fetal development to neonatal life," *Fetal Diagn. Ther.*, vol. 47, no. 5, pp. 373–386, 2020.

[11] S. U. Morton and D. Brodsky, "Fetal physiology and the transition to extrauterine life," *Clin. Perinatol.*, vol. 43, no. 3, pp. 395–407, 2016.

[12] B. Cuneo, "Transition from Fetal to Neonatal Circulation BT - Pediatric and Congenital Cardiology, Cardiac Surgery and Intensive Care," E. M. Da Cruz, D. Ivy, and J. Jaggers, Eds. London: Springer London, 2014, pp. 179–199.

[13] R. N. Pittman, "The Circulatory System and Oxygen Transport," in *Regulation of Tissue Oxygenation*, San Rafael (CA): Morgan & Claypool Life Sciences, 2011.

[14] J. E. Hall and M. E. Hall, *Guyton and Hall Textbook of Medical Physiology*, 12th ed. Philadelphia, PA 19103-2899: Saunders Elsevier Health Sciences, 2011.

[15] D. Bers, *Excitation-contraction coupling and cardiac contractile force*, vol. 237. Springer Science & Business Media, 2001.

[16] J. M. Nerbonne and R. S. Kass, "Molecular Physiology of Cardiac Repolarization," *Physiol. Rev.*, vol. 85, no. 4, pp. 1205–1253, Oct. 2005.

[17] A. Agostinelli *et al.*, "Noninvasive fetal electrocardiography: an overview of the signal electrophysiological meaning, recording procedures, and processing techniques.," *Ann. noninvasive Electrocardiol. Off. J. Int. Soc. Holter Noninvasive Electrocardiology, Inc*, vol. 20, no. 4, pp. 303–313, Jul. 2015.

[18] S. Meek and F. Morris, "ABC of clinical electrocardiography — Introduction. II—Basic

terminology," *Bmj*, vol. 324, no. 7335, pp. 470–473, 2002.

[19] A. L. Goldberger, Z. D. Goldberger, and A. Shvilkin, *Goldberger's Clinical Electrocardiography: A Simplified Approach*, 8th ed. Elsevier, 2013.

[20] J. Malmivuo and R. Plonsey, *Bioelectromagnetism: principles and applications of bioelectric and biomagnetic fields*. Oxford University Press, USA, 1995.

[21] R. Vullings, "Non-invasive fetal electrocardiogram : analysis and interpretation," Technische Universiteit Eindhoven, Eindhoven, 2010.

[22] P. E. McSharry, G. D. Clifford, L. Tarassenko, and L. A. Smith, "A dynamical model for generating synthetic electrocardiogram signals," *IEEE Trans. Biomed. Eng.*, vol. 50, no. 3, pp. 289–294, 2003.

[23] R. Sameni, G. D. Clifford, C. Jutten, and M. B. Shamsollahi, "Multichannel ECG and noise modeling: Application to maternal and fetal ECG signals," *EURASIP J. Adv. Signal Process.*, vol. 2007, pp. 1–14, 2007.

[24] J. Behar, F. Andreotti, S. Zaunseder, Q. Li, J. Oster, and G. D. Clifford, "An ECG simulator for generating maternal-foetal activity mixtures on abdominal ECG recordings," *Physiol. Meas.*, vol. 35, pp. 1537–1550, Jul. 2014.

[25] F. Andreotti, J. Behar, S. Zaunseder, J. Oster, and G. D. Clifford, "An open-source framework for stress-testing non-invasive foetal ECG extraction algorithms," *Physiol. Meas.*, vol. 37, no. 5, p. 627, 2016.

[26] E. Keenan, C. K. Karmakar, and M. Palaniswami, "The effects of asymmetric volume conductor modeling on non-invasive fetal ECG extraction," *Physiol. Meas.*, vol. 39, no. 10, p. 105013, 2018.

[27] M. Peters *et al.*, "Monitoring the fetal heart non-invasively: a review of methods.," *J. Perinat. Med.*, vol. 29, no. 5, pp. 408–416, 2001.

[28] C. E. Valderrama, N. Ketabi, F. Marzbanrad, P. Rohloff, and G. D. Clifford, "A review of fetal cardiac monitoring, with a focus on low- and middle-income countries.," *Physiol. Meas.*, vol. 41, no. 11, p. 11TR01, Dec. 2020.

[29] S. L. Bloom *et al.*, "Fetal Pulse Oximetry and Cesarean Delivery," *N. Engl. J. Med.*, vol. 355, no. 21, pp. 2195–2202, Nov. 2006.

[30] M. Rooijakkers, "Innovative Devices and Techniques for Multimodal Fetal Health Monitoring," in *Innovative Technologies and Signal Processing in Perinatal Medicine, Volume 1*, 1st ed., Springer, Ed. 2020, pp. 147–168.

[31] E. W. Abdulhay, R. J. Oweis, A. M. Alhaddad, F. N. Sublaban, M. A. Radwan, and H. M. Almasaeed, "Review Article: Non-Invasive Fetal Heart Rate Monitoring Techniques," *Biomed. Sci. Eng.*, vol. 2, no. 3, pp. 53–67, Oct. 2014.

[32] S. E. Nicklin, I. A.-A. Hassan, Y. A. Wickramasinghe, and S. A. Spencer, "The light still shines, but not that brightly? The current status of perinatal near infrared spectroscopy," *Arch. Dis. Child. - Fetal Neonatal Ed.*, vol. 88, no. 4, pp. F263--F268, 2003.

[33] Mozurkewich EL and F. M. Wolf, "Near-infrared spectroscopy for fetal assessment during labour," *Cochrane Database Syst. Rev.*, no. 3, 2000.

[34] D. M. Peebles *et al.*, "Relation between frequency of uterine contractions and human fetal cerebral oxygen saturation studied during labour by near infrared spectroscopy," *BJOG An Int. J. Obstet. \& Gynaecol.*, vol. 101, no. 1, pp. 44–48, 1994.

[35] A. J. Wolfberg and A. J. du Plessis, "Near-infrared spectroscopy in the fetus and neonate," *Clin. Perinatol.*, vol. 33, no. 3, pp. 707–728, 2006.

[36] F. Kovács, C. Horváth, Á. T. Balogh, and G. Hosszú, "Fetal phonocardiography—Past and future possibilities," *Comput. Methods Programs Biomed.*, vol. 104, no. 1, pp. 19–25, 2011.

[37] R. Jaros, R. Martinek, and R. Kahankova, “Non-adaptive methods for fetal ECG signal processing: a review and appraisal,” *Sensors*, vol. 18, no. 11, p. 3648, 2018.

[38] F. Kovács, M. Á. Goda, G. Hosszú, and T. Telek, “A Proposed Phonography-Based Measurement of Fetal Breathing Movement Using Segmented Structures with Frequency Splitting,” in *2020 42nd Annual International Conference of the IEEE Engineering in Medicine & Biology Society (EMBC)*, 2020, pp. 4483–4486.

[39] M. Á. Goda, T. Telek, and F. Kovács, “Novel Phonography-Based Measurement for Fetal Breathing Movement in the Third Trimester,” *Sensors* , vol. 21, no. 1. 2021.

[40] P. Chetlur Adithya, R. Sankar, W. A. Moreno, and S. Hart, “Trends in fetal monitoring through phonocardiography: Challenges and future directions,” *Biomed. Signal Process. Control*, vol. 33, pp. 289–305, 2017.

[41] M. Ruffo *et al.*, “Non-invasive foetal monitoring with combined ECG-PCG system,” *Biomed. Eng. Trends Electron. Commun. Softw.*, pp. 347–366, 2011.

[42] A. H. Khandoker, Y. Kimura, T. Ito, N. Sato, K. Okamura, and M. Palaniswami, “Antepartum non-invasive evaluation of opening and closing timings of the cardiac valves in fetal cardiac cycle.,” *Med. Biol. Eng. Comput.*, vol. 47, no. 10, pp. 1075–1082, Oct. 2009.

[43] F. Marzbanrad *et al.*, “Model-Based Estimation of Aortic and Mitral Valves Opening and Closing Timings in Developing Human Fetuses.,” *IEEE J. Biomed. Heal. informatics*, vol. 20, no. 1, pp. 240–248, Jan. 2016.

[44] F. Marzbanrad, A. H. Khandoker, Y. Kimura, M. Palaniswami, and G. D. Clifford, “Assessment of Fetal Development Using Cardiac Valve Intervals,” *Front. Physiol.*, vol. 8, 2017.

[45] R. M. Grivell, Z. Alfirevic, G. M. Gyte, and D. Devane, “Antenatal cardiotocography for fetal assessment,” *Cochrane Database Syst. Rev.*, no. 9, 2015.

[46] D. Ayres-de-Campos, C. Y. Spong, E. Chandraharan, and F. I. F. M. E. C. Panel, “FIGO consensus guidelines on intrapartum fetal monitoring: Cardiotocography,” *Int. J. Gynecol. Obstet.*, vol. 131, no. 1, pp. 13–24, Oct. 2015.

[47] D. Devane, J. G. Lalor, S. Daly, W. McGuire, A. Cuthbert, and V. Smith, “Cardiotocography versus intermittent auscultation of fetal heart on admission to labour ward for assessment of fetal wellbeing,” *Cochrane Database Syst. Rev.*, no. 1, 2017.

[48] A. Georgieva *et al.*, “Computer-based intrapartum fetal monitoring and beyond: A review of the 2nd Workshop on Signal Processing and Monitoring in Labor (October 2017, Oxford, UK),” *Acta Obstet. Gynecol. Scand.*, vol. 98, no. 9, pp. 1207–1217, Sep. 2019.

[49] M. G. Signorini, G. Magenes, S. Cerutti, and D. Arduini, “Linear and nonlinear parameters for the analysis of fetal heart rate signal from cardiotocographic recordings.,” *IEEE Trans. Biomed. Eng.*, vol. 50, no. 3, pp. 365–374, Mar. 2003.

[50] M. G. Signorini, N. Pini, A. Malovini, R. Bellazzi, and G. Magenes, “Integrating machine learning techniques and physiology based heart rate features for antepartum fetal monitoring,” *Comput. Methods Programs Biomed.*, vol. 185, p. 105015, 2020.

[51] P. Warrick, E. F. Hamilton, D. Precup, and R. E. Kearney, “Identification of the dynamic relationship between intrapartum uterine pressure and fetal heart rate for normal and hypoxic fetuses.,” *IEEE Trans. Biomed. Eng.*, vol. 56, no. 6, pp. 1587–1597, Jun. 2009.

[52] P. Warrick, E. Hamilton, R. Kearney, and D. Precup, “A Machine Learning Approach to the Detection of Fetal Hypoxia during Labor and Delivery,” *AI Mag.*, vol. 33, p. 79, Mar. 2012.

[53] M. Cesarelli, M. Romano, P. Bifulco, F. Fedele, and M. Bracale, “An algorithm for the recovery of fetal heart rate series from CTG data.,” *Comput. Biol. Med.*, vol. 37, no. 5, pp. 663–669, May 2007.

[54] M. Romano, P. Bifulco, M. Ruffo, G. Improta, F. Clemente, and M. Cesarelli, “Software for computerised analysis of cardiotocographic traces,” *Comput. Methods Programs Biomed.*, vol. 124, pp. 121–137, 2016.

[55] M. Romano, P. Bifulco, A. M. Ponsiglione, G. D. Gargiulo, F. Amato, and M. Cesarelli, “Evaluation of floatingline and foetal heart rate variability,” *Biomed. Signal Process. Control*, vol. 39, pp. 185–196, 2018.

[56] R. Kahankova *et al.*, “A Review of Signal Processing Techniques for Non-Invasive Fetal Electrocardiography,” *IEEE Rev. Biomed. Eng.*, vol. 13, pp. 51–73, 2020.

[57] D. Pani, C. Rabotti, M. G. Signorini, and L. Burattini, Eds., *Innovative Technologies and Signal Processing in Perinatal Medicine*, First. Springer, Cham, 2021.

[58] E. Sulas *et al.*, “A Novel Tool for Non-Invasive Fetal Electrocardiography Research: the NInFEA Dataset,” in *2020 42nd Annual International Conference of the IEEE Engineering in Medicine & Biology Society (EMBC)*, 2020, pp. 5631–5634.

[59] E. Sulas, M. Urru, R. Tumbarello, L. Raffo, R. Sameni, and D. Pani, “A non-invasive multimodal foetal ECG–Doppler dataset for antenatal cardiology research,” *Sci. Data*, vol. 8, no. 1, p. 30, 2021.

[60] E. Sulas, “Development of a Novel Dataset and Tools for Non-Invasive Fetal Electrocardiography Research.” University of Cagliari, 2020.

[61] L. Caserta *et al.*, “Two-dimensional fetal echocardiography: where we are,” *J. Prenat. Med.*, vol. 2, no. 3, pp. 31–35, Jul. 2008.

[62] R. Weber, D. Stambach, and E. Jaeggi, “Diagnosis and management of common fetal arrhythmias,” *J. Saudi Hear. Assoc.*, vol. 23, no. 2, pp. 61–66, Apr. 2011.

[63] J. F. Strasburger and R. T. Wakai, “Fetal cardiac arrhythmia detection and in utero therapy,” *Nat. Rev. Cardiol.*, vol. 7, no. 5, pp. 277–290, May 2010.

[64] I. Lakhno, “The impact of preeclampsia on fetal ECG morphology and heart rate variability,” *Arch. Perinat. Med.*, vol. Vol. 20, pp. 7–10, Mar. 2014.

[65] V. Smith, A. Nair, R. Warty, J. A. Sursas, F. da Silva Costa, and E. M. Wallace, “A systematic review on the utility of non-invasive electrophysiological assessment in evaluating for intra uterine growth restriction,” *BMC Pregnancy Childbirth*, vol. 19, no. 1, p. 230, 2019.

[66] A. Wacker-Gussmann, R. T. Wakai, and J. F. Strasburger, “Complex Fetal Care: Importance of Fetal Arrhythmias to the Neonatologist and Pediatrician,” *Neoreviews*, vol. 17, no. 10, pp. e568--e578, 2016.

[67] C. Kähler *et al.*, “The application of fetal magnetocardiography (FMCG) to investigate fetal arrhythmias and congenital heart defects (CHD).,” *Prenat. Diagn.*, vol. 21, no. 3, pp. 176–182, Mar. 2001.

[68] R. T. Wakai, “Assessment of fetal neurodevelopment via fetal magnetocardiography,” *Exp. Neurol.*, vol. 190, pp. 65–71, 2004.

[69] M. Cremer, “Ueber die direkte Ableitung der Aktionsstrome des menschlichen Herzens vom Oesophagus und uber das Elektrokardiogramm des Fotus,” *Munchen. Med. Wochenschr.*, vol. 53, pp. 811–813, 1906.

[70] A. Sacco, J. Muglu, R. Navaratnarajah, and M. Hogg, “ST analysis for intrapartum fetal monitoring,” *Obstet. Gynaecol.*, vol. 17, no. 1, pp. 5–12, 2015.

[71] I. Marcantoni *et al.*, “T-Wave Alternans Identification in Direct Fetal Electrocardiography,” in *2017 Computing in Cardiology (CinC)*, 2017, pp. 1–4.

[72] H. Norén *et al.*, “STAN in clinical practice—the outcome of 2 years of regular use in the city of Gothenburg,” *Am. J. Obstet. Gynecol.*, vol. 195, no. 1, pp. 7–15, 2006.

[73] I. Amer-Wåhlin *et al.*, "ST analysis of the fetal electrocardiogram during labor: Nordic observational multicenter study," *J. Matern. Neonatal Med.*, vol. 12, no. 4, pp. 260–266, 2002.

[74] K. G. Rosén, I. Amer-Wåhlin, R. Luzietti, and H. Norén, "Fetal ECG waveform analysis.," *Best Pract. Res. Clin. Obstet. Gynaecol.*, vol. 18, no. 3, pp. 485–514, Jun. 2004.

[75] A. Agostinelli *et al.*, "Quantification of Fetal ST-Segment Deviations," in *2017 Computing in Cardiology (CinC)*, 2017, pp. 1–4.

[76] D. J. Jagannath and A. I. Selvakumar, "Issues and research on foetal electrocardiogram signal elicitation," *Biomed. Signal Process. Control.*, vol. 10, pp. 224–244, 2014.

[77] R. Luzietti, R. Erkkola, U. Hasbargen, L. Å. Mattsson, J. M. Thoulon, and K. G. Rosén, "European Community Multi-Center Trial 'Fetal ECG Analysis During Labor': ST plus CTG analysis," vol. 27, no. 6, pp. 431–440, 1999.

[78] G. D. Clifford, I. Silva, J. Behar, and G. B. Moody, "Non-invasive fetal ECG analysis," *Physiol. Meas.*, vol. 35, no. 8, p. 1521, 2014.

[79] K. M. J. Verdurmen *et al.*, "A systematic review of prenatal screening for congenital heart disease by fetal electrocardiography.," *Int. J. Gynaecol. Obstet. Off. organ Int. Fed. Gynaecol. Obstet.*, vol. 135, no. 2, pp. 129–134, Nov. 2016.

[80] G. D. Clifford, R. Sameni, J. Ward, J. Robinson, and A. J. Wolfberg, "Clinically accurate fetal ECG parameters acquired from maternal abdominal sensors," *Am. J. Obstet. Gynecol.*, vol. 205, no. 1, pp. 47.e1-47.e5, 2011.

[81] J. Jezewski, A. Matonia, T. Kupka, D. Roj, and R. Czabanski, "Determination of fetal heart rate from abdominal signals: evaluation of beat-to-beat accuracy in relation to the direct fetal electrocardiogram," *Biomed. Tech. Eng.*, vol. 57, no. 5, pp. 383–394, 2012.

[82] J. Jezewski *et al.*, "Is Abdominal Fetal Electrocardiography an Alternative to Doppler Ultrasound for FHR Variability Evaluation? ," *Frontiers in Physiology* , vol. 8. p. 305, 2017.

[83] W. R. Cohen and B. Hayes-Gill, "Influence of maternal body mass index on accuracy and reliability of external fetal monitoring techniques.," *Acta Obstet. Gynecol. Scand.*, vol. 93, no. 6, pp. 590–595, Jun. 2014.

[84] N. Sänger *et al.*, "Prenatal Foetal Non-invasive ECG instead of Doppler CTG - A Better Alternative?," *Geburtshilfe Frauenheilkd.*, vol. 72, no. 7, pp. 630–633, Jul. 2012.

[85] D. Hoyer *et al.*, "Monitoring fetal maturation-objectives, techniques and indices of autonomic function.," *Physiol. Meas.*, vol. 38, no. 5, pp. R61–R88, May 2017.

[86] I. Lakhno, "The Use of Fetal Noninvasive Electrocardiography," *Scientifica (Cairo).*, vol. 2016, p. 5386595, 2016.

[87] I. Lakhno, "Fetal Non-invasive Electrocardiography Contributes to Better Diagnostics of Fetal Distress: A Cross-sectional Study Among Patients with Pre-eclampsia.," *Ann. Acad. Med. Singapore*, vol. 44, no. 11, pp. 519–523, Nov. 2015.

[88] C. L. Velayo, K. Funamoto, J. N. I. Silao, Y. Kimura, and K. Nicolaides, "Evaluation of Abdominal Fetal Electrocardiography in Early Intrauterine Growth Restriction ," *Frontiers in Physiology* , vol. 8. p. 437, 2017.

[89] J. A. Behar, L. Bonnemains, V. Shulgin, J. Oster, O. Ostras, and I. Lakhno, "Noninvasive fetal electrocardiography for the detection of fetal arrhythmias.," *Prenat. Diagn.*, vol. 39, no. 3, pp. 178–187, Feb. 2019.

[90] P.-C. Su, S. Miller, S. Idriss, P. Barker, and H.-T. Wu, "Recovery of the fetal electrocardiogram for morphological analysis from two trans-abdominal channels via optimal shrinkage.," *Physiol. Meas.*, vol. 40, no. 11, p. 115005, Dec. 2019.

[91] J. Behar, F. Andreotti, J. Oster, and G. D. Clifford, "A Bayesian filtering framework for accurate extracting of the non-invasive FECG morphology," in *Computing in Cardiology 2014*, 2014, pp. 53–56.

[92] E. C. Karvounis, M. G. Tsipouras, C. Papaloukas, D. G. Tsalikakis, K. K. Naka, and D. I. Fotiadis, "A non-invasive methodology for fetal monitoring during pregnancy," *Methods Inf. Med.*, vol. 49, no. 03, pp. 238–253, 2010.

[93] L. Su and H.-T. Wu, "Extract Fetal ECG from Single-Lead Abdominal ECG by De-Shape Short Time Fourier Transform and Nonlocal Median," *Front. Appl. Math. Stat.*, vol. 3, p. 2, 2017.

[94] I. Lakhno, J. A. Behar, J. Oster, V. Shulgin, O. Ostras, and F. Andreotti, "The use of non-invasive fetal electrocardiography in diagnosing second-degree fetal atrioventricular block," *Matern. Heal. Neonatol. Perinatol.*, vol. 3, no. 1, p. 14, 2017.

[95] R. Martinek *et al.*, "Non-Invasive Fetal Electrocardiogram Extraction Based on Novel Hybrid Method for Intrapartum ST Segment Analysis," *IEEE Access*, vol. 9, pp. 28608–28631, 2021.

[96] L. Noben, S.-A. Clur, J. O. E. H. van Laar, and R. Vullings, "Prenatal diagnosis of a bundle branch block based on the fetal ECG," *BMJ Case Rep.*, vol. 12, no. 7, p. e229998, Jul. 2019.

[97] I. Marcantoni, A. Sbrollini, L. Burattini, M. Morettini, S. Fioretti, and L. Burattini, "Automatic T-Wave Alternans Identification in Indirect and Direct Fetal Electrocardiography.," *Annu. Int. Conf. IEEE Eng. Med. Biol. Soc. IEEE Eng. Med. Biol. Soc. Annu. Int. Conf.*, vol. 2018, pp. 4852–4855, Jul. 2018.

[98] N. Widatalla, Y. Kasahara, Y. Kimura, and A. Khandoker, "Model based estimation of QT intervals in non-invasive fetal ECG signals," *PLoS One*, vol. 15, no. 5, p. e0232769, May 2020.

[99] J. Behar, F. Andreotti, S. Zaunseder, J. Oster, and G. D. Clifford, "A practical guide to non-invasive foetal electrocardiogram extraction and analysis," *Physiol. Meas.*, vol. 37, no. 5, pp. R1–R35, 2016.

[100] J. Behar, Z. Weiner, and P. Warrick, "Special Session on Computational Fetal Monitoring," in *2019 Computing in Cardiology (CinC)*, 2019, p. Page 1-Page 4.

[101] M. Mhajna *et al.*, "Wireless, remote solution for home fetal and maternal heart rate monitoring," *Am. J. Obstet. Gynecol. MFM*, vol. 2, no. 2, p. 100101, 2020.

[102] T. F. Oostendorp, A. van Oosterom, and H. W. Jongsma, "Electrical properties of tissues involved in the conduction of foetal ECG.," *Med. Biol. Eng. Comput.*, vol. 27, no. 3, pp. 322–324, May 1989.

[103] T. F. Oostendorp, A. Van Oosterom, and H. W. Jongsma, "The effect of changes in the conductive medium on the fetal ECG throughout gestation," *Clin. Phys. Physiol. Meas.*, 1989.

[104] E. Castillo, D. P. Morales, A. García, F. Martínez-Martí, L. Parrilla, and A. J. Palma, "Noise suppression in ECG signals through efficient one-step wavelet processing techniques," *J. Appl. Math.*, vol. 2013, 2013.

[105] R. Martinek, R. Kahankova, J. Nedoma, M. Fajkus, and K. Cholevová, "Fetal ECG Preprocessing Using Wavelet Transform," in *Proceedings of the 10th International Conference on Computer Modeling and Simulation*, 2018, pp. 39–43.

[106] R. Sameni, "Noninvasive Fetal Electrocardiography: Models, Technologies, and Algorithms BT - Innovative Technologies and Signal Processing in Perinatal Medicine: Volume 1," D. Pani, C. Rabotti, M. G. Signorini, and L. Burattini, Eds. Cham: Springer International Publishing, 2021, pp. 99–146.

[107] J. F. Cardoso, "Multidimensional independent component analysis," in *Proc. ICASSP*, 1998, vol. 4, pp. 1941–1944 vol.4.

[108] V. Zarzoso and A. K. Nandi, "Noninvasive fetal electrocardiogram extraction: blind separation versus adaptive noise cancellation," *IEEE Trans. Biomed. Eng.*, vol. 48, no. 1, pp. 12–18, 2001.

[109] R. Martinek *et al.*, “Comparative effectiveness of ICA and PCA in extraction of fetal ECG from abdominal signals: Toward non-invasive fetal monitoring,” *Front. Physiol.*, vol. 9, p. 648, 2018.

[110] J. Behar, J. Oster, and G. D. Clifford, “Combining and benchmarking methods of foetal ECG extraction without maternal or scalp electrode data,” *Physiol. Meas.*, vol. 35, no. 8, pp. 1569–1589, 2014.

[111] R. Sameni, C. Jutten, and M. B. Shamsollahi, “Multichannel Electrocardiogram Decomposition Using Periodic Component Analysis,” *IEEE Trans. Biomed. Eng.*, vol. 55, no. 8, pp. 1935–1940, 2008.

[112] F. Jamshidian-Tehrani, R. Sameni, and C. Jutten, “Temporally nonstationary component analysis; application to noninvasive fetal electrocardiogram extraction,” *IEEE Trans. Biomed. Eng.*, vol. 67, no. 5, pp. 1377–1386, 2019.

[113] F. Andreotti *et al.*, “Robust fetal ECG extraction and detection from abdominal leads.,” *Physiol. Meas.*, vol. 35, no. 8, pp. 1551–1567, Aug. 2014.

[114] R. Sameni, M. B. Shamsollahi, and C. Jutten, “Model-based Bayesian filtering of cardiac contaminants from biomedical recordings,” *Physiol. Meas.*, vol. 29, no. 5, pp. 595–613, 2008.

[115] R. Sameni, “Extraction of fetal cardiac signals from an array of maternal abdominal recordings.” Institut National Polytechnique de Grenoble-INPG; Sharif University of Technology (SUT), 2008.

[116] A. Khamene and S. Negahdaripour, “A new method for the extraction of fetal ECG from the composite abdominal signal.,” *IEEE Trans. Biomed. Eng.*, vol. 47, no. 4, pp. 507–516, Apr. 2000.

[117] H. Hassanpour and A. Parsaei, “Fetal ECG Extraction Using Wavelet Transform,” in *2006 International Conference on Computational Inteligence for Modelling Control and Automation and International Conference on Intelligent Agents Web Technologies and International Commerce (CIMCA’06)*, 2006, p. 179.

[118] E. Sulas, M. Urru, R. Tumbarello, L. Raffo, and D. Pani, “Systematic analysis of single- and multi-reference adaptive filters for non-invasive fetal electrocardiography,” *Math. Biosci. Eng.*, vol. 17, no. 1, pp. 286–308.

[119] R. Kahankova, R. Martinek, and P. Bilik, “Non-invasive fetal ECG extraction from maternal abdominal ECG using LMS and RLS adaptive algorithms,” in *International Afro-European conference for industrial advancement*, 2016, pp. 258–271.

[120] M. B. I. Reaz and L. S. Wei, “Adaptive linear neural network filter for fetal ECG extraction,” in *International Conference on Intelligent Sensing and Information Processing, 2004. Proceedings of*, 2004, pp. 321–324.

[121] M. A. Hasan, M. I. Ibrahimy, and M. B. I. Reaz, “Fetal ECG extraction from maternal abdominal ECG using neural network,” *J. Softw. Eng. Appl.*, vol. 2, no. 05, p. 330, 2009.

[122] W. Jia, C. Yang, G. Zhong, M. Zhou, and S. Wu, “Fetal ECG extraction based on adaptive linear neural network,” in *2010 3rd International Conference on Biomedical Engineering and Informatics*, 2010, vol. 2, pp. 899–902.

[123] M. Nasiri, K. Faez, and A. M. Nasrabadi, “A new method for extraction of fetal electrocardiogram signal based on adaptive nero-fuzzy inference system,” in *2011 IEEE International Conference on Signal and Image Processing Applications (ICSIPA)*, 2011, pp. 456–461.

[124] R. Li, M. G. Frasch, and H.-T. Wu, “Efficient Fetal-Maternal ECG Signal Separation from Two Channel Maternal Abdominal ECG via Diffusion-Based Channel Selection ,” *Frontiers in Physiology* , vol. 8. p. 277, 2017.

[125] E. H. Hon and S. T. Lee, “Noise reduction in fetal electrocardiography: II. Averaging techniques,” *Am. J. Obstet. Gynecol.*, vol. 87, no. 8, pp. 1086–1096, 1963.

[126] E. H. Hon and S. T. Lee, “Averaging techniques in fetal electrocardiography,” *Med. Electron. Biol.*

Eng., vol. 2, no. 1, pp. 71–76, 1964.

[127] T. Kao, K.-L. Wu, B. C. Yu, and J.-H. Hung, “Digital signal enhancement of the abdominal fetal ECG,” in *Images of the Twenty-First Century. Proceedings of the Annual International Engineering in Medicine and Biology Society,* 1989, pp. 771–772.

[128] X. B. Huang, J. A. Crowe, J. M. Herbert, and M. S. Woolfson, “A windows application for real-time fetal ECG analysis.,” *Comput. Biomed. Res.*, vol. 27, no. 6, pp. 419–433, Dec. 1994.

[129] C. Lempersz *et al.*, “The standardized 12-lead fetal electrocardiogram of the healthy fetus in mid-pregnancy: A cross-sectional study,” *PLoS One*, vol. 15, no. 4, p. e0232606, 2020.

[130] R. Vullings, B. de Vries, and J. W. M. Bergmans, “An Adaptive Kalman Filter for ECG Signal Enhancement,” *IEEE Trans. Biomed. Eng.*, vol. 58, no. 4, pp. 1094–1103, 2011.

[131] M. Kotas, J. Jezewski, K. Horoba, and A. Matonia, “Application of spatio-temporal filtering to fetal electrocardiogram enhancement,” *Comput. Methods Programs Biomed.*, vol. 104, no. 1, pp. 1–9, 2011.

[132] E. Fotiadou, J. O. E. H. van Laar, S. G. Oei, and R. Vullings, “Enhancement of low-quality fetal electrocardiogram based on time-sequenced adaptive filtering.,” *Med. Biol. Eng. Comput.*, vol. 56, no. 12, pp. 2313–2323, Dec. 2018.

[133] E. Fotiadou, T. Konopczyński, J. Hesser, and R. Vullings, “Deep Convolutional Encoder-Decoder Framework for Fetal ECG Signal Denoising,” in *2019 Computing in Cardiology (CinC)*, 2019, p. Page 1-Page 4.

[134] E. Fotiadou, T. Konopczyński, J. Hesser, and R. Vullings, “End-to-end trained encoder-decoder convolutional neural network for fetal electrocardiogram signal denoising,” *Physiol. Meas.*, vol. 41, no. 1, p. 15005, Feb. 2020.

[135] E. Fotiadou and R. Vullings, “Multi-Channel Fetal ECG Denoising With Deep Convolutional Neural Networks ,” *Frontiers in Pediatrics* , vol. 8. p. 508, 2020.

[136] M. Ma, N. Wang, and S.-Y. Lei, “Extraction of FECG based on time frequency blind source separation and wavelet de-noising,” in *2009 3rd International Conference on Bioinformatics and Biomedical Engineering*, 2009, pp. 1–3.

[137] B. Rivet, V. Vigneron, A. Paraschiv-Ionescu, and C. Jutten, “Wavelet de-noising for blind source separation in noisy mixtures,” in *International Conference on Independent Component Analysis and Signal Separation*, 2004, pp. 263–270.

[138] M. Shayesteh and J. Fallahian, “Using wavelet transformation in blind sources separation of the fetal electrocardiogram,” *Majlesi J. Electr. Eng.*, vol. 5, no. 3(18), pp. 33–37, 2011.

[139] R. Swarnalatha and D. V. Prasad, “Maternal ECG Cancellation in Abdominal Signal Using ANFIS and Wavelets,” *J. Appl. Sci.*, vol. 10, no. 11, pp. 868–877, 2010.

[140] V. Vigneron, A. Paraschiv-Ionescu, A. Azancot, O. Sibony, and C. Jutten, “Fetal electrocardiogram extraction based on non-stationary ICA and wavelet denoising,” in *Seventh International Symposium on Signal Processing and Its Applications, 2003. Proceedings.*, 2003, vol. 2, pp. 69–72.

[141] Y. Wang, Y. Fu, and Z. He, “Fetal Electrocardiogram Extraction Based on Fast ICA and Wavelet Denoising,” in *2018 2nd IEEE Advanced Information Management,Communicates,Electronic and Automation Control Conference (IMCEC)*, 2018, pp. 466–469.

[142] G. Baldazzi *et al.*, “Wavelet-Based Post-Processing Methods for the Enhancement of Non-Invasive Fetal ECG,” in *2019 Computing in Cardiology (CinC)*, 2019, pp. 1–4.

[143] R. Jaros, R. Martinek, R. Kahankova, and J. Koziorek, “Novel Hybrid Extraction Systems for Fetal Heart Rate Variability Monitoring Based on Non-Invasive Fetal Electrocardiogram,” *IEEE Access*, vol. 7, pp. 131758–131784, 2019.

[144] M. Ahmadi, M. Ayat, K. Assaleh, and H. Al-Nashash, “Fetal ECG Signal Enhancement using Polynomial Classifiers and Wavelet Denoising,” in *2008 Cairo International Biomedical Engineering Conference*, 2008, pp. 1–4.

[145] F. N. Jamaluddin, Z. A. K. Bakti, M. Kamal, and A. Aminudin, “Wavelet analysis on FECG detection using two electrodes system device,” *Int. J. Integr. Eng.*, vol. 5, no. 3, 2013.

[146] V. Ionescu, “Fetal ECG extraction from multichannel abdominal ECG recordings for health monitoring during labor,” *Procedia Technol.*, vol. 22, pp. 682–689, 2016.

[147] Y. Ishikawa, H. Horigome, A. Kandori, H. Toda, and Z. Zhang, “Noise reduction by perfect-translation-invariant complex discrete wavelet transforms for fetal electrocardiography and magnetocardiography,” *Int. J. Wavelets, Multiresolution Inf. Process.*, vol. 12, no. 04, p. 1460008, 2014.

[148] N. Ivanushkina, K. Ivanko, E. Lysenko, I. Borovskiy, and O. Panasiuk, “Fetal electrocardiogram extraction from maternal abdominal signals,” in *2014 IEEE 34th International Scientific Conference on Electronics and Nanotechnology (ELNANO)*, 2014, pp. 334–338.

[149] M. S. H. Jadhav and M. D. N. Dhang, “Extraction of Fetal ECG from Abdominal Recordings Combining BSS-ICA & WT Techniques,” *Int. J. Eng. Res. Technol.*, vol. 10, no. 1, 2017.

[150] S. H. Jothi and K. H. Prabha, “Fetal electrocardiogram extraction using adaptive neuro-fuzzy inference systems and undecimated wavelet transform,” *IETE J. Res.*, vol. 58, no. 6, pp. 469–475, 2012.

[151] F. Mochimaru, Y. Fujimoto, and Y. Ishikawa, “The fetal electrocardiogram by independent component analysis and wavelets,” *Jpn. J. Physiol.*, vol. 54, no. 5, pp. 457–463, 2004.

[152] C.-Y. Lin, L. Su, and H.-T. Wu, “Wave-Shape Function Analysis,” *J. Fourier Anal. Appl.*, vol. 24, no. 2, pp. 451–505, 2018.

[153] M. Gavish and D. L. Donoho, “Optimal shrinkage of singular values,” *IEEE Trans. Inf. Theory*, vol. 63, no. 4, pp. 2137–2152, 2017.

[154] K. N. Chaudhury and A. Singer, “Non-local Euclidean medians,” *IEEE Signal Process. Lett.*, vol. 19, no. 11, pp. 745–748, 2012.

[155] C.-Y. Lin, A. Minasian, X. J. Qi, and H.-T. Wu, “Vector nonlocal Euclidean median: principal bundle captures the nature of patch space,” *arXiv Prepr. arXiv1611.05073*, 2016.

[156] I. Kononenko and M. Kukar, “Chapter 12 - Cluster Analysis,” I. Kononenko and M. B. T.-M. L. and D. M. Kukar, Eds. Woodhead Publishing, 2007, pp. 321–358.

[157] N. H. Spencer, *Essentials of multivariate data analysis*. CRC press, 2013.

[158] F. Jamshidian-Tehrani and R. Sameni, “Fetal ECG extraction from time-varying and low-rank noninvasive maternal abdominal recordings,” *Physiol. Meas.*, vol. 39, no. 12, p. 125008, 2018.

[159] J. Behar, A. Johnson, G. D. Clifford, and J. Oster, “A Comparison of Single Channel Fetal ECG Extraction Methods,” *Ann. Biomed. Eng.*, vol. 42, no. 6, pp. 1340–1353, 2014.

[160] J. M. Leski, “Robust weighted averaging of biomedical signals,” *IEEE Trans. Biomed. Eng.*, vol. 49, no. 8, pp. 796–804, 2002.

[161] A. Matonia *et al.*, “Fetal electrocardiograms, direct and abdominal with reference heartbeat annotations,” *Sci. Data*, vol. 7, no. 1, p. 200, 2020.

[162] G. Baldazzi, E. Sulas, M. Urru, R. Tumbarello, L. Raffo, and D. Pani, “Annotated real and synthetic datasets for non-invasive foetal electrocardiography post-processing benchmarking,” *Data Br.*, vol. 33, p. 106399, 2020.

[163] R. Sameni, “The Open-Source Electrophysiological Toolbox (OSET), version 3.14.” 2018.

[164] M. J. O. Taylor *et al.*, "Non-invasive fetal electrocardiography in singleton and multiple pregnancies.," *BJOG*, vol. 110, no. 7, pp. 668–678, Jul. 2003.

[165] H. Nadila, D. Danudirdjo, and H. Zakaria, "Fetal Heart Rate Detection Algorithm from Noninvasive Fetal Electrocardiogram," in *2021 IEEE International Biomedical Instrumentation and Technology Conference (IBITeC)*, 2021, pp. 71–76.

[166] G. Baldazzi, E. Sulas, M. Urru, R. Tumbarello, L. Raffo, and D. Pani, "Wavelet Denoising as a Post-Processing Enhancement Method for Non-Invasive Foetal Electrocardiography," *Comput. Methods Programs Biomed.*, vol. 195, p. 105558, 2020.

[167] D. L. Donoho and J. M. Johnstone, "Ideal spatial adaptation by wavelet shrinkage," *Biometrika*, vol. 81, no. 3, pp. 425–455, 1994.

[168] D. L. Donoho, "De-noising by soft-thresholding," *IEEE Trans. Inf. theory*, vol. 41, no. 3, pp. 613–627, 1995.

[169] M. Han, Y. Liu, J. Xi, and W. Guo, "Noise Smoothing for Nonlinear Time Series Using Wavelet Soft Threshold," *Signal Process. Lett. IEEE*, vol. 14, no. 1, pp. 62–65, 2007.

[170] M. Misiti, Y. Misiti, G. Oppenheim, and J.-M. Poggi, *Wavelets and their Applications*, vol. 330. Wiley Online Library, 2007.

[171] S. Mallat, *A wavelet tour of signal processing*. Elsevier, 1999.

[172] M. Unser and A. Aldroubi, "A review of wavelets in biomedical applications," *Proc. IEEE*, vol. 84, no. 4, pp. 626–638, 1996.

[173] L. Sörnmo and P. Laguna, *Bioelectrical signal processing in cardiac and neurological applications*, vol. 8. Academic Press, 2005.

[174] I. M. Johnstone and B. W. Silverman, "Wavelet threshold estimators for data with correlated noise," *J. R. Stat. Soc. Ser. B (statistical Methodol.*, vol. 59, no. 2, pp. 319–351, 1997.

[175] S. Almagro, M. M. Elena, M. J. Bastiaans, and J. M. Quero, "A new mother wavelet for fetal electrocardiography, to achieve optimal denoising and compressing results," in *2006 Computers in Cardiology*, 2006, pp. 157–160.

[176] R. R. Coifman and D. L. Donoho, "Translation-invariant de-noising," in *Wavelets and statistics*, Springer, 1995, pp. 125–150.

[177] G. P. Nason and B. W. Silverman, "The stationary wavelet transform and some statistical applications," in *Wavelets and statistics*, Springer, 1995, pp. 281–299.

[178] J.-C. Pesquet, H. Krim, and H. Carfantan, "Time-invariant orthonormal wavelet representations," *IEEE Trans. signal Process.*, vol. 44, no. 8, pp. 1964–1970, 1996.

[179] D. B. Percival and A. T. Walden, *Wavelet methods for time series analysis*, vol. 4. Cambridge university press, 2006.

[180] A. T. Walden and A. Contreras Cristan, *The phase-corrected undecimated discrete wavelet packet transform and its application to interpreting the timing of events*, vol. 454. 1998.

[181] D.-D. Ţarălungă, G.-M. Ungureanu, I. Gussi, R. Strungaru, and W. Wolf, "Fetal ECG extraction from abdominal signals: a review on suppression of fundamental power line interference component and its harmonics," *Comput. Math. Methods Med.*, vol. 2014, 2014.

[182] J. A. Apolinario JR, *QRD-RLS Adaptive Filtering*. Springer, 2009.

[183] D. Pani, S. Argiolas, and L. Raffo, "A DSP algorithm and system for real-time fetal ECG extraction," in *2008 Computers in Cardiology*, 2008, pp. 1065–1068.

[184] D. Pani, G. Barabino, and L. Raffo, "NInFEA: an embedded framework for the real-time evaluation

of fetal ECG extraction algorithms," *Biomedizinische Technik/Biomedical Engineering*, vol. 58. p. 13, 2013.

[185] M. G. Signorini, G. Lanzola, E. Torti, A. Fanelli, and G. Magenes, "Antepartum fetal monitoring through a wearable system and a mobile application," *Technologies*, vol. 6, no. 2, p. 44, 2018.

[186] P. Kligfield *et al.*, "Recommendations for the standardization and interpretation of the electrocardiogram: part I: the electrocardiogram and its technology a scientific statement from the American Heart Association Electrocardiography and Arrhythmias Committee, Council on Clin," *J. Am. Coll. Cardiol.*, vol. 49, no. 10, pp. 1109–1127, Mar. 2007.

[187] J. P. Martinez, R. Almeida, S. Olmos, A. P. Rocha, and P. Laguna, "A wavelet-based ECG delineator: evaluation on standard databases," *IEEE Trans. Biomed. Eng.*, vol. 51, no. 4, pp. 570–581, 2004.

[188] A. Gaikwad and M. S. Panse, "Extraction of FECG from Non-Invasive AECG signal for Fetal Heart Rate Calculation," *Int. J. Sci. Res. Netw. Secur. Commun.*, vol. 5, no. 3, pp. 16–19, 2017.

[189] B. De Moor, P. De Gersem, B. De Schutter, and W. Favoreel, "DAISY: A database for identification of systems," *J. A*, vol. 38, pp. 4–5, 1997.

[190] A. L. Goldberger *et al.*, "PhysioBank, PhysioToolkit, and PhysioNet: components of a new research resource for complex physiologic signals," *Circulation*, vol. 101, no. 23, pp. e215–e220, 2000.

[191] I. Silva *et al.*, "Noninvasive Fetal ECG: the PhysioNet/Computing in Cardiology Challenge 2013.," in *2013 Computing in Cardiology (CInC)*, 2013, vol. 40, pp. 149–152.

[192] Y. Ishikawa, "Wavelet Analysis for Clinical Medicine (in Japanese) with MEM Software on CD-ROM," *Med. Publ.*, pp. 154–163, 305–308, 2000.

[193] M. V Wickerhauser, *Adapted Wavelet Analysis: From Theory to Software*. Wellesley, MA: Peters, Ltd, 1994.

[194] F. Mochimaru, Y. Fujimoto, and Y. Ishikawa, "Detecting the fetal electrocardiogram by wavelet theory-based methods," *Prog. Biomed. Res.*, vol. 7, pp. 185–193, 2002.

[195] Z. F. Issa, J. M. Miller, and D. P. Zipes, *Clinical Arrhythmology and Electrophysiology. A Companion to Braunwald's Heart Disease*, 1st ed. Philadelphia: Saunders, Elsevier, 2009.

[196] D. Durham and L. I. G. Worthley, "Cardiac arrhythmias: diagnosis and management. The tachycardias.," *Crit. care Resusc. J. Australas. Acad. Crit. Care Med.*, vol. 4, no. 1, pp. 35–53, Mar. 2002.

[197] B. A. Koplan and W. G. Stevenson, "Ventricular Tachycardia and Sudden Cardiac Death," *Mayo Clin. Proc.*, vol. 84, no. 3, pp. 289–297, Mar. 2009.

[198] D. Fu, "Cardiac arrhythmias: diagnosis, symptoms, and treatments," *Cell Biochem. Biophys.*, vol. 73, no. 2, pp. 291–296, 2015.

[199] C. T. Pedersen *et al.*, "EHRA/HRS/APHRS expert consensus on ventricular arrhythmias," *EP Eur.*, vol. 16, no. 9, pp. 1257–1283, 2014.

[200] C. Antzelevitch and A. Burashnikov, "Overview of basic mechanisms of cardiac arrhythmia," *Card. Electrophysiol. Clin.*, vol. 3, no. 1, pp. 23–45, 2011.

[201] A. Natale and O. M. Wazni, *Handbook of cardiac electrophysiology*. London, UK: Informa Healthcare, 2007.

[202] L. Gaztañaga, F. E. Marchlinski, and B. P. Betensky, "Mechanisms of cardiac arrhythmias.," *Rev. Esp. Cardiol. (Engl. Ed).*, vol. 65, no. 2, pp. 174–185, Feb. 2012.

[203] J. C. Nielsen *et al.*, "European Heart Rhythm Association (EHRA)/Heart Rhythm Society (HRS)/Asia Pacific Heart Rhythm Society (APHRS)/Latin American Heart Rhythm Society (LAHRS) expert consensus on risk assessment in cardiac arrhythmias: use the right tool for the right outcome," *EP*

Eur., vol. 22, no. 8, pp. 1147–1148, Aug. 2020.

[204] J. Goldberger and J. Ng, *Practical Signal and Image Processing in Clinical Cardiology*. Springer, London, 2010.

[205] J. M. T. de Bakker, “Electrogram recording and analyzing techniques to optimize selection of target sites for ablation of cardiac arrhythmias,” *Pacing Clin. Electrophysiol.*, vol. 42, no. 12, pp. 1503–1516, Dec. 2019.

[206] S. K. S. Huang and J. M. Miller, *Catheter Ablation of Cardiac Arrhythmias*, 4th ed. Elsevier, 2019.

[207] F. S. Ng, C. Roney, C. D. Cantwell, and N. S. Peters, “Fundamentals of Cardiac Mapping,” in *Cardiac Mapping*, Fifth Edit., John Wiley & Sons, Ltd, 2019, pp. 70–83.

[208] F. E. Marchlinski, J. D. Callans, C. D. Gottlieb, and Z. Erica, “Linear Ablation Lesions for Control of Unmappable Ventricular Tachycardia in Patients With Ischemic and Nonischemic Cardiomyopathy,” *Circulation*, vol. 101, no. 11, pp. 1288–1296, Mar. 2000.

[209] M. Moreno, N. Perez-Castellano, and J. Villacastin, “Pacemapping,” *Indian Pacing Electrophysiol. J.*, vol. 5, no. 1, pp. 35–42, Jan. 2005.

[210] B. Schaeffer and W. G. Stevenson, “Entrainment mapping: Theoretical considerations and practical implementation.,” *J. Cardiovasc. Electrophysiol.*, vol. 29, no. 1, pp. 204–213, Jan. 2018.

[211] Z. Aziz and R. Tung, “Novel Mapping Strategies for Ventricular Tachycardia Ablation,” *Current Treatment Options in Cardiovascular Medicine*. 2018.

[212] M. Shenasa and A. Al-Ahmad, “Historical perspectives on cardiac mapping and ablation,” *Card. Electrophysiol. Clin.*, vol. 11, no. 3, pp. 405–408, 2019.

[213] D. Bhakta and J. M. Miller, “Principles of electroanatomic mapping,” *Indian Pacing Electrophysiol. J.*, vol. 8, no. 1, pp. 32–50, Feb. 2008.

[214] W. G. Stevenson, “Ventricular scars and ventricular tachycardia,” *Trans. Am. Clin. Climatol. Assoc.*, vol. 120, pp. 403–412, 2009.

[215] J. M. T. de Bakker *et al.*, “Reentry as a cause of ventricular tachycardia in patients with chronic ischemic heart disease: electrophysiologic and anatomic correlation.,” *Circulation*, vol. 77, no. 3, pp. 589–606, Mar. 1988.

[216] J. M. T. de Bakker *et al.*, “Slow conduction in the infarcted human heart. ‘Zigzag’ course of activation.,” *Circulation*, vol. 88, no. 3, pp. 915–926, Sep. 1993.

[217] A. G. Kléber and M. J. Janse, “Fibrosis and arrhythmogenesis,” in *Cardiac Mapping*, Fifth Edit., John Wiley & Sons, Ltd, 2019, pp. 375–382.

[218] E. J. Ciaccio *et al.*, “Structure and function of the ventricular tachycardia isthmus.,” *Hear. Rhythm*, Aug. 2021.

[219] H. H. Hsia, D. Lin, W. H. Sauer, D. J. Callans, and F. E. Marchlinski, “Anatomic characterization of endocardial substrate for hemodynamically stable reentrant ventricular tachycardia: identification of endocardial conducting channels.,” *Hear. Rhythm*, vol. 3, no. 5, pp. 503–512, May 2006.

[220] S. Kyoko, S. W. G, S. J. L, S. A. P, C. Gregory, and E. L. M, “Endocardial and epicardial radiofrequency ablation of ventricular tachycardia associated with dilated cardiomyopathy,” *J. Am. Coll. Cardiol.*, vol. 43, no. 10, pp. 1834–1842, May 2004.

[221] A. Natale *et al.*, “Venice Chart International Consensus document on ventricular tachycardia/ventricular fibrillation ablation.,” *J. Cardiovasc. Electrophysiol.*, vol. 21, no. 3, pp. 339–379, Mar. 2010.

[222] R. Martin, M. Hocini, M. Haïsaguerre, P. Jaïs, and F. Sacher, “Ventricular tachycardia isthmus characteristics: insights from high-density mapping,” *Arrhythmia Electrophysiol. Rev.*, vol. 8, no. 1,

p. 54, 2019.

[223] R. Martin *et al.*, “Characteristics of Scar-Related Ventricular Tachycardia Circuits Using Ultra-High-Density Mapping,” *Circ. Arrhythmia Electrophysiol.*, vol. 11, no. 10, p. e006569, Oct. 2018.

[224] W. G. Stevenson *et al.*, “Exploring postinfarction reentrant ventricular tachycardia with entrainment mapping.,” *J. Am. Coll. Cardiol.*, vol. 29, no. 6, pp. 1180–1189, May 1997.

[225] C. de Chillou *et al.*, “Isthmus characteristics of reentrant ventricular tachycardia after myocardial infarction.,” *Circulation*, vol. 105, no. 6, pp. 726–731, Feb. 2002.

[226] P. I. Gardner, P. C. Ursell, J. J. J. Fenoglio, and A. L. Wit, “Electrophysiologic and anatomic basis for fractionated electrograms recorded from healed myocardial infarcts.,” *Circulation*, vol. 72, no. 3, pp. 596–611, Sep. 1985.

[227] W. G. Stevenson *et al.*, “Fractionated endocardial electrograms are associated with slow conduction in humans: evidence from pace-mapping.,” *J. Am. Coll. Cardiol.*, vol. 13, no. 2, pp. 369–376, Feb. 1989.

[228] E. Anter, C. M. Tschabrunn, A. E. Buxton, and M. E. Josephson, “High-Resolution Mapping of Postinfarction Reentrant Ventricular Tachycardia,” *Circulation*, vol. 134, no. 4, pp. 314–327, Jul. 2016.

[229] D. Z. Kocovic, T. Harada, P. L. Friedman, and W. G. Stevenson, “Characteristics of electrograms recorded at reentry circuit sites and bystanders during ventricular tachycardia after myocardial infarction.,” *J. Am. Coll. Cardiol.*, vol. 34, no. 2, pp. 381–388, Aug. 1999.

[230] O. A. Ajijola, R. Tung, and K. Shivkumar, “Ventricular tachycardia in ischemic heart disease substrates.,” *Indian Heart J.*, vol. 66 Suppl 1, no. Suppl 1, pp. S24-34, 2014.

[231] S. Nakahara *et al.*, “Distribution of late potentials within infarct scars assessed by ultra high-density mapping,” *Hear. Rhythm*, vol. 7, no. 12, pp. 1817–1824, 2010.

[232] S. Nakahara *et al.*, “Characterization of the arrhythmogenic substrate in ischemic and nonischemic cardiomyopathy implications for catheter ablation of hemodynamically unstable ventricular tachycardia.,” *J. Am. Coll. Cardiol.*, vol. 55, no. 21, pp. 2355–2365, May 2010.

[233] Y. Komatsu *et al.*, “Electrophysiologic characterization of local abnormal ventricular activities in postinfarction ventricular tachycardia with respect to their anatomic location,” *Hear. Rhythm*, vol. 10, no. 11, pp. 1630–1637, 2013.

[234] E. Anter *et al.*, “Infarct-Related Ventricular Tachycardia: Redefining the Electrophysiological Substrate of the Isthmus During Sinus Rhythm.,” *JACC. Clin. Electrophysiol.*, vol. 4, no. 8, pp. 1033–1048, Aug. 2018.

[235] A. Frontera *et al.*, “High-Density Characterization of the Ventricular Electrical Substrate During Sinus Rhythm in Post-Myocardial Infarction Patients.,” *JACC. Clin. Electrophysiol.*, vol. 6, no. 7, pp. 799–811, Jul. 2020.

[236] R. Tung *et al.*, “Freedom from recurrent ventricular tachycardia after catheter ablation is associated with improved survival in patients with structural heart disease: An International VT Ablation Center Collaborative Group study,” *Hear. Rhythm*, vol. 12, no. 9, pp. 1997–2007, Sep. 2015.

[237] K.-H. Kuck *et al.*, “Catheter ablation of stable ventricular tachycardia before defibrillator implantation in patients with coronary heart disease (VTACH): a multicentre randomised controlled trial.,” *Lancet (London, England)*, vol. 375, no. 9708, pp. 31–40, Jan. 2010.

[238] B. K. Martinez *et al.*, “Systematic review and meta-analysis of catheter ablation of ventricular tachycardia in ischemic heart disease,” *Hear. Rhythm*, vol. 17, no. 1, pp. e206–e219, 2020.

[239] J. L. Sapp *et al.*, “Ventricular Tachycardia Ablation versus Escalation of Antiarrhythmic Drugs,” *N. Engl. J. Med.*, vol. 375, no. 2, pp. 111–121, May 2016.

[240] L. Di Biase, P. Santangeli, D. J. Burkhardt, and A. Natale, “Ventricular Tachycardia Ablation as First Line Therapy: Are We There Yet?,” *J. Cardiovasc. Electrophysiol.*, vol. 24, no. 5, pp. 530–533, 2013.

[241] S. G. Priori *et al.*, “2015 ESC Guidelines for the management of patients with ventricular arrhythmias and the prevention of sudden cardiac death: The Task Force for the Management of Patients with Ventricular Arrhythmias and the Prevention of Sudden Cardiac Death of the Europe,” *Eur. Heart J.*, vol. 36, no. 41, pp. 2793–2867, Nov. 2015.

[242] K. Shivkumar, “Catheter ablation of ventricular arrhythmias,” *N. Engl. J. Med.*, vol. 380, no. 16, pp. 1555–1564, 2019.

[243] G. S. Guandalini, J. J. Liang, and F. E. Marchlinski, “Ventricular Tachycardia Ablation: Past, Present, and Future Perspectives.,” *JACC. Clin. Electrophysiol.*, vol. 5, no. 12, pp. 1363–1383, Dec. 2019.

[244] E. M. Cronin *et al.*, “2019 HRS/EHRA/APHRS/LAHRS expert consensus statement on catheter ablation of ventricular arrhythmias,” *Hear. Rhythm*, vol. 21, no. 8, pp. 1143–1144, Aug. 2019.

[245] S. R. Dukkipati, J. S. Koruth, S. Choudry, M. A. Miller, W. Whang, and V. Y. Reddy, “Catheter Ablation of Ventricular Tachycardia in Structural Heart Disease: Indications, Strategies, and Outcomes—Part II,” *J. Am. Coll. Cardiol.*, vol. 70, no. 23, pp. 2924–2941, 2017.

[246] V. Y. Reddy *et al.*, “Prophylactic catheter ablation for the prevention of defibrillator therapy,” *N. Engl. J. Med.*, vol. 357, no. 26, pp. 2657–2665, 2007.

[247] Y. Komatsu, “Substrate-based approach for ventricular tachycardia in structural heart disease: Tips for mapping and ablation,” *J. Arrhythmia*, vol. 30, no. 4, pp. 272–282, 2014.

[248] M. E. Josephson and E. Anter, “Substrate mapping for ventricular tachycardia: assumptions and misconceptions,” *JACC Clin. Electrophysiol.*, vol. 1, no. 5, pp. 341–352, 2015.

[249] R. Tung, “Substrate Mapping in Ventricular Arrhythmias.,” *Card. Electrophysiol. Clin.*, vol. 11, no. 4, pp. 657–663, Dec. 2019.

[250] P. Santangeli and F. E. Marchlinski, “Substrate mapping for unstable ventricular tachycardia.,” *Hear. Rhythm*, vol. 13, no. 2, pp. 569–583, Feb. 2016.

[251] D. F. Briceño *et al.*, “Substrate ablation of ventricular tachycardia: late potentials, scar dechanneling, local abnormal ventricular activities, core isolation, and homogenization,” *Card. Electrophysiol. Clin.*, vol. 9, no. 1, pp. 81–91, 2017.

[252] T. Kitamura *et al.*, “Substrate Mapping and Ablation for Ventricular Tachycardia in Patients with Structural Heart Disease: How to Identify Ventricular Tachycardia Substrate.,” *J. Innov. Card. Rhythm Manag.*, vol. 10, no. 3, pp. 3565–3580, Mar. 2019.

[253] J. Romero *et al.*, “Substrate Ablation for Ventricular Tachycardia in Structural Heart Disease,” in *Cardiac Mapping*, Fifth Edit., 2019, pp. 881–893.

[254] A. Nogami *et al.*, “JCS/JHRS 2019 guideline on non-pharmacotherapy of cardiac arrhythmias,” *J. Arrhythmia*, vol. 37, no. 4, pp. 709–870, Aug. 2021.

[255] A. Arenal *et al.*, “Ablation of electrograms with an isolated, delayed component as treatment of unmappable monomorphic ventricular tachycardias in patients with structural heart disease.,” *J. Am. Coll. Cardiol.*, vol. 41, no. 1, pp. 81–92, Jan. 2003.

[256] P. Vergara *et al.*, “Late Potentials Abolition as an Additional Technique for Reduction of Arrhythmia Recurrence in Scar Related Ventricular Tachycardia Ablation,” *J. Cardiovasc. Electrophysiol.*, vol. 23, no. 6, pp. 621–627, Jun. 2012.

[257] D. M. Cassidy *et al.*, “Endocardial catheter mapping in patients in sinus rhythm: relationship to underlying heart disease and ventricular arrhythmias.,” *Circulation*, vol. 73, no. 4, pp. 645–652, Apr. 1986.

[258] P. Santangeli, F. Infusino, G. A. Sgueglia, A. Sestito, and G. A. Lanza, “Ventricular late potentials: a critical overview and current applications.,” *J. Electrocardiol.*, vol. 41, no. 4, pp. 318–324, 2008.

[259] J. Silberbauer *et al.*, “Noninducibility and late potential abolition: a novel combined prognostic procedural end point for catheter ablation of postinfarction ventricular tachycardia,” *Circ. Arrhythmia Electrophysiol.*, vol. 7, no. 3, pp. 424–435, 2014.

[260] S. E. Mountantonakis *et al.*, “Relationship Between Voltage Map ‘Channels’ and the Location of Critical Isthmus Sites in Patients With Post-Infarction Cardiomyopathy and Ventricular Tachycardia,” *J. Am. Coll. Cardiol.*, vol. 61, no. 20, pp. 2088–2095, 2013.

[261] P. Jaïs *et al.*, “Elimination of local abnormal ventricular activities: a new end point for substrate modification in patients with scar-related ventricular tachycardia,” *Circulation*, vol. 125, no. 18, pp. 2184–2196, 2012.

[262] F. Sacher *et al.*, “Substrate mapping and ablation for ventricular tachycardia: the LAVA approach.,” *J. Cardiovasc. Electrophysiol.*, vol. 26, no. 4, pp. 464–471, Apr. 2015.

[263] A. Berruezo *et al.*, “Scar Dechanneling,” *Circ. Arrhythmia Electrophysiol.*, vol. 8, no. 2, pp. 326–336, Apr. 2015.

[264] W. S. Tzou *et al.*, “Core isolation of critical arrhythmia elements for treatment of multiple scar-based ventricular tachycardias.,” *Circ. Arrhythm. Electrophysiol.*, vol. 8, no. 2, pp. 353–361, Apr. 2015.

[265] L. Di Biase *et al.*, “Endo-epicardial homogenization of the scar versus limited substrate ablation for the treatment of electrical storms in patients with ischemic cardiomyopathy.,” *J. Am. Coll. Cardiol.*, vol. 60, no. 2, pp. 132–141, Jul. 2012.

[266] P. Santangeli, D. S. Frankel, and F. E. Marchlinski, “End points for ablation of scar-related ventricular tachycardia.,” *Circ. Arrhythm. Electrophysiol.*, vol. 7, no. 5, pp. 949–960, Oct. 2014.

[267] F. Bourier *et al.*, “Is it feasible to offer ‘targeted ablation’ of ventricular tachycardia circuits with better understanding of isthmus anatomy and conduction characteristics?,” *EP Eur.*, vol. 21, no. Supplement_1, pp. i27–i33, Feb. 2019.

[268] D. Tsiachris *et al.*, “Electroanatomical voltage and morphology characteristics in postinfarction patients undergoing ventricular tachycardia ablation: pragmatic approach favoring late potentials abolition.,” *Circ. Arrhythm. Electrophysiol.*, vol. 8, no. 4, pp. 863–873, Aug. 2015.

[269] H. M. Haqqani *et al.*, “Fundamental differences in electrophysiologic and electroanatomic substrate between ischemic cardiomyopathy patients with and without clinical ventricular tachycardia.,” *J. Am. Coll. Cardiol.*, vol. 54, no. 2, pp. 166–173, Jul. 2009.

[270] F. Bogun *et al.*, “Electrogram Characteristics in Postinfarction Ventricular Tachycardia,” *J. Am. Coll. Cardiol.*, vol. 46, pp. 667–674, Aug. 2005.

[271] B. Campos, M. E. Jauregui, F. E. Marchlinski, S. Dixit, and E. P. Gerstenfeld, “Use of a novel fragmentation map to identify the substrate for ventricular tachycardia in postinfarction cardiomyopathy,” *Hear. Rhythm*, vol. 12, no. 1, pp. 95–103, Jan. 2015.

[272] C.-Y. Lin *et al.*, “Simultaneous amplitude frequency electrogram transformation (SAFE-T) mapping to identify ventricular tachycardia arrhythmogenic potentials in sinus rhythm,” *JACC Clin. Electrophysiol.*, vol. 2, no. 4, pp. 459–470, 2016.

[273] K. Kuroki *et al.*, “New Substrate-Guided Method of Predicting Slow Conducting Isthmuses of Ventricular Tachycardia: Preliminary Analysis to the Combined Use of Voltage Limit Adjustment and Fast-Fourier Transform Analysis,” *Circ. Arrhythmia Electrophysiol.*, vol. 11, no. 4, p. e005705, Apr. 2018.

[274] V. Mor-Avi and S. Akselrod, “Spectral analysis of canine epicardial electrogram. Short-term variations in the frequency content induced by myocardial ischemia.,” *Circ. Res.*, vol. 66, no. 6, pp. 1681–1691, Jun. 1990.

[275] G. Sierra, M. de Jesús Gómez, P. Le Guyader, B. Soucy, P. Savard, and R. Nadeau, "Spectral analysis of electrograms during ventricular tachycardia in a canine model: Relation with epicardial isochronal maps," *J. Electrocardiol.*, vol. 30, no. 3, pp. 225–237, 1997.

[276] C. Cabo, J. M. Wharton, P. D. Wolf, R. E. Ideker, and W. M. Smith, "Activation in unipolar cardiac electrograms: a frequency analysis.," *IEEE Trans. Biomed. Eng.*, vol. 37, no. 5, pp. 500–508, May 1990.

[277] F. Pannizzo and S. Furman, "Frequency spectra of ventricular tachycardia and sinus rhythm in human intracardiac electrograms-application to tachycardia detection for cardiac pacemakers," *IEEE Trans. Biomed. Eng.*, vol. 35, no. 6, pp. 421–425, 1988.

[278] K. Minami, H. Nakajima, and T. Toyoshima, "Real-time discrimination of ventricular tachyarrhythmia with Fourier-transform neural network.," *IEEE Trans. Biomed. Eng.*, vol. 46, no. 2, pp. 179–185, Feb. 1999.

[279] J. Morellato *et al.*, "Quantitative spectral assessment of intracardiac electrogram characteristics associated with post infarct fibrosis and ventricular tachycardia," *PLoS One*, vol. 13, no. 10, p. e0204997, Oct. 2018.

[280] V. Luther *et al.*, "A Prospective Study of Ripple Mapping the Post-Infarct Ventricular Scar to Guide Substrate Ablation for Ventricular Tachycardia," *Circ. Arrhythmia Electrophysiol.*, vol. 9, no. 6, p. e004072, Jun. 2016.

[281] H. Launer, T. Clark, T. Dewland, C. A. Henrikson, and B. Nazer, "An automated fractionation mapping algorithm for mapping of scar-based ventricular tachycardia," *Pacing Clin. Electrophysiol.*, vol. 42, no. 8, pp. 1133–1140, 2019.

[282] C. Martin *et al.*, "Use of Novel Electrogram 'Lumipoint' Algorithm to Detect Critical Isthmus and Abnormal Potentials for Ablation in Ventricular Tachycardia," *JACC Clin. Electrophysiol.*, vol. 5, Mar. 2019.

[283] K. Zeppenfeld, P. Kiès, M. C. E. F. Wijffels, M. Bootsma, L. van Erven, and M. J. Schalij, "Identification of successful catheter ablation sites in patients with ventricular tachycardia based on electrogram characteristics during sinus rhythm.," *Hear. Rhythm*, vol. 2, no. 9, pp. 940–950, Sep. 2005.

[284] D. Gupta, J. Hashemi, S. Akl, and D. Redfearn, "A novel method for automated fractionation detection in ventricular tachycardia," in *2016 Computing in Cardiology (CinC)*, 2016, pp. 925–928.

[285] D. Gupta, M. H. Shariat, M. Baetz-Dougan, J. Hashemi, S. Akl, and D. Redfearn, "Novel automated paced fractionation detection algorithm for ablating ventricular tachycardia," *J. Biomed. Sci. Eng.*, vol. 9, no. 10, p. 488, 2016.

[286] M. Orini *et al.*, "Evaluation of the reentry vulnerability index to predict ventricular tachycardia circuits using high-density contact mapping," *Hear. Rhythm*, vol. 17, no. 4, pp. 576–583, 2020.

[287] F. O. Campos *et al.*, "Characterizing the clinical implementation of a novel activation-repolarization metric to identify targets for catheter ablation of ventricular tachycardias using computational models," *Comput. Biol. Med.*, vol. 108, pp. 263–275, 2019.

[288] M. Masjedi *et al.*, "A novel algorithm for 3-D visualization of electrogram duration for substrate-mapping in patients with ischemic heart disease and ventricular tachycardia," *PLoS One*, vol. 16, no. 7, p. e0254683, Jul. 2021.

[289] N. Jackson *et al.*, "Decrement Evoked Potential Mapping," *Circ. Arrhythmia Electrophysiol.*, vol. 8, no. 6, pp. 1433–1442, Dec. 2015.

[290] A. Porta-Sánchez *et al.*, "Multicenter Study of Ischemic Ventricular Tachycardia Ablation With Decrement-Evoked Potential (DEEP) Mapping With Extra Stimulus.," *JACC. Clin. Electrophysiol.*, vol. 4, no. 3, pp. 307–315, Mar. 2018.

[291] A. Bhaskaran, J. Fitzgerald, N. Jackson, S. Gizurarson, K. Nanthakumar, and A. Porta-Sánchez, “Decrement Evoked Potential Mapping to Guide Ventricular Tachycardia Ablation: Elucidating the Functional Substrate,” *Arrhythmia Electrophysiol. Rev.*, vol. 9, no. 4, pp. 211–218, Dec. 2020.

[292] Z. Aziz *et al.*, “Targeted Ablation of Ventricular Tachycardia Guided by Wavefront Discontinuities During Sinus Rhythm,” *Circulation*, vol. 140, no. 17, pp. 1383–1397, Oct. 2019.

[293] J. Acosta *et al.*, “Elucidation of hidden slow conduction by double ventricular extrastimuli: a method for further arrhythmic substrate identification in ventricular tachycardia ablation procedures.,” *Eur. Eur. pacing, arrhythmias, Card. Electrophysiol. J. Work. groups Card. pacing, arrhythmias, Card. Cell. Electrophysiol. Eur. Soc. Cardiol.*, vol. 20, no. 2, pp. 337–346, Feb. 2018.

[294] J. Acosta *et al.*, “Long-term outcomes of ventricular tachycardia substrate ablation incorporating hidden slow conduction analysis,” *Hear. Rhythm*, vol. 17, no. 10, pp. 1696–1703, 2020.

[295] C. Pandozi *et al.*, “Mapping of ventricular tachycardia in patients with ischemic cardiomyopathy: Current approaches and future perspectives,” *Clin. Cardiol.*, vol. 42, no. 10, pp. 1041–1050, 2019.

[296] E. Wissner, W. G. Stevenson, and K.-H. Kuck, “Catheter ablation of ventricular tachycardia in ischaemic and non-ischaemic cardiomyopathy: where are we today? A clinical review,” *Eur. Heart J.*, vol. 33, no. 12, pp. 1440–1450, 2012.

[297] A. J. Graham, M. Orini, and P. D. Lambiase, “Limitations and Challenges in Mapping Ventricular Tachycardia: New Technologies and Future Directions.,” *Arrhythmia Electrophysiol. Rev.*, vol. 6, no. 3, pp. 118–124, Aug. 2017.

[298] J. W. Cheung, “Targeting Abnormal Electrograms for Substrate-Based Ablation of Ventricular Tachycardia: Can We Ablate Smarter?” American College of Cardiology Foundation Washington DC, 2020.

[299] G. Heinzel, A. Rüdiger, and R. Schilling, “Spectrum and spectral density estimation by the Discrete Fourier transform (DFT), including a comprehensive list of window functions and some new flat-top windows,” *Max Plank Inst*, vol. 12, Jan. 2002.

[300] A. Phinyomark, S. Thongpanja, H. Hu, P. Phukpattaranont, and C. Limsakul, “The Usefulness of Mean and Median Frequencies in Electromyography Analysis,” in *Computational Intelligence in Electromyography Analysis - A Perspective on Current Applications and Future Challenges*, 2012, pp. 195–220.

[301] W. J. Conover and R. L. Iman, “On multiple-comparisons procedures,” *Los Alamos Sci. Lab. Tech. Rep. LA-7677-MS*, vol. 1, p. 14, 1979.

[302] W. J. Conover, *Practical nonparametric statistics*, 3rd ed. Hoboken, NJ: John Wiley & Sons, 1999.

[303] R. Tung, M. E. Josephson, J. S. Bradfield, and K. Shivkumar, “Directional Influences of Ventricular Activation on Myocardial Scar Characterization,” *Circ. Arrhythmia Electrophysiol.*, vol. 9, no. 8, p. e004155, Aug. 2016.

[304] M. Beheshti *et al.*, “Determinants of atrial bipolar voltage: Inter electrode distance and wavefront angle.,” *Comput. Biol. Med.*, vol. 102, pp. 449–457, Nov. 2018.

[305] T. Yamaguchi, A. Fukui, and K. Node, “Bipolar Voltage Mapping for the Evaluation of Atrial Substrate: Can We Overcome the Challenge of Directionality?,” *J. Atr. Fibrillation*, vol. 11, no. 5, p. 2116, 2019.

[306] M. Strzelecki and P. Badura, “Machine Learning for Biomedical Application,” *Applied Sciences* , vol. 12, no. 4. 2022.

[307] G. Baldazzi, M. Orrù, M. Matraxia, G. Viola, and D. Pani, “Supervised Classification of Ventricular Abnormal Potentials in Intracardiac Electrograms,” in *2020 Computing in Cardiology (CinC)*, 2020, pp. 1–4.

[308] G. Baldazzi, M. Orrù, M. Matraxia, G. Viola, and D. Pani, "Automatic Recognition of Ventricular Abnormal Potentials in Intracardiac Electrograms," in *2019 Computing in Cardiology (CinC)*, 2019, pp. 1–4.

[309] F. Zaraket *et al.*, "P1129 Bipolar voltage cut-off validation in electroanatomical voltage mapping to identify scar and conduction channels in ventricular tachycardia ablation: need for new cut-off in NICM," *EP Eur.*, vol. 22, no. Supplement_1, pp. euaa162-341, 2020.

[310] C. D. Cantwell, C. H. Roney, F. S. Ng, J. H. Siggers, S. J. Sherwin, and N. S. Peters, "Techniques for automated local activation time annotation and conduction velocity estimation in cardiac mapping," *Comput. Biol. Med.*, vol. 65, pp. 229–242, Oct. 2015.

[311] M. Masé and F. Ravelli, "Automatic reconstruction of activation and velocity maps from electro-anatomic data by radial basis functions," in *2010 Annual International Conference of the IEEE Engineering in Medicine and Biology*, 2010, pp. 2608–2611.

[312] S. E. Williams *et al.*, "OpenEP: a cross-platform electroanatomic mapping data format and analysis platform for electrophysiology research," *Front. Physiol.*, vol. 12, p. 160, 2021.

[313] G. Chandrashekar and F. Sahin, "A survey on feature selection methods," *Comput. Electr. Eng.*, vol. 40, no. 1, pp. 16–28, 2014.

[314] M. Radovic, M. Ghalwash, N. Filipovic, and Z. Obradovic, "Minimum redundancy maximum relevance feature selection approach for temporal gene expression data," *BMC Bioinformatics*, vol. 18, no. 1, pp. 1–14, 2017.

Appendix A

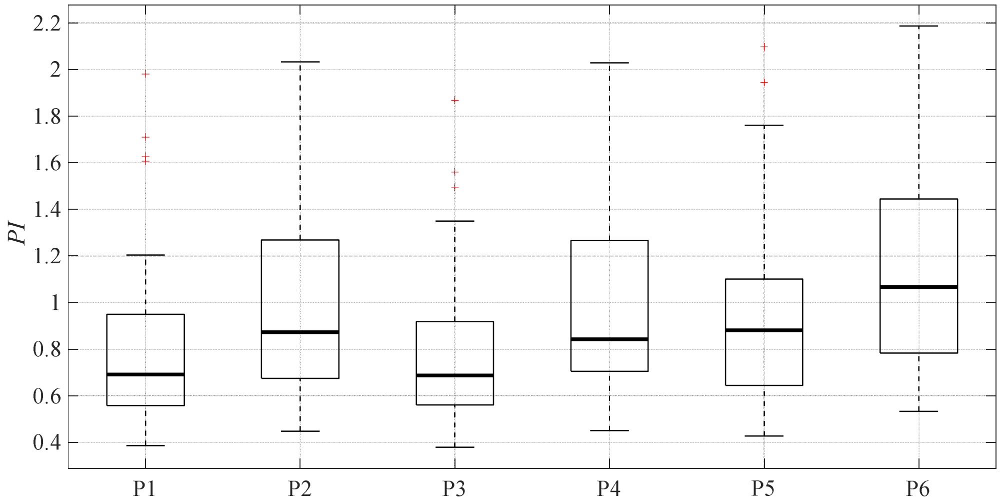

Figure 5A.1. PI distributions obtained for the different parameterizations analysed for the Ahmadi et al. algorithm [144], involving DWT, 6-level decomposition and Universal threshold with: P1) coif4 mother wavelet and hard thresholding, P2) coif4 mother wavelet and soft thresholding, P3) sym8 mother wavelet and hard thresholding, P4) sym8 mother wavelet and soft thresholding, P5) db8 mother wavelet and hard thresholding, P6) db8 mother wavelet and soft thresholding.

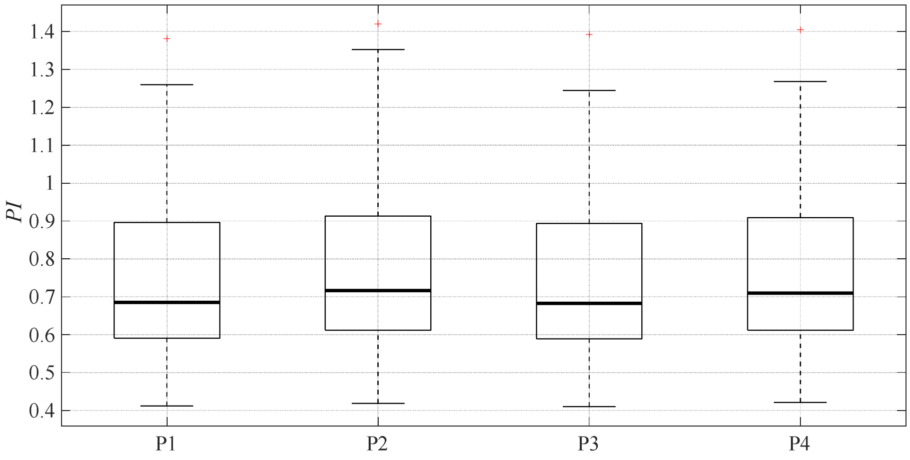

Figure 5A.2. PI distributions obtained for the different parameterizations analysed for the Ivanushkina et al. algorithm [148], involving DWT, 6-level decomposition, a custom thresholding and: P1) bior2.6 mother wavelet with Rigrsure threshold, P2) bior2.6 mother wavelet with the Han et al. threshold, P3) sym6 mother wavelet with Rigrsure threshold, P4) sym6 mother wavelet with Han et al. threshold.

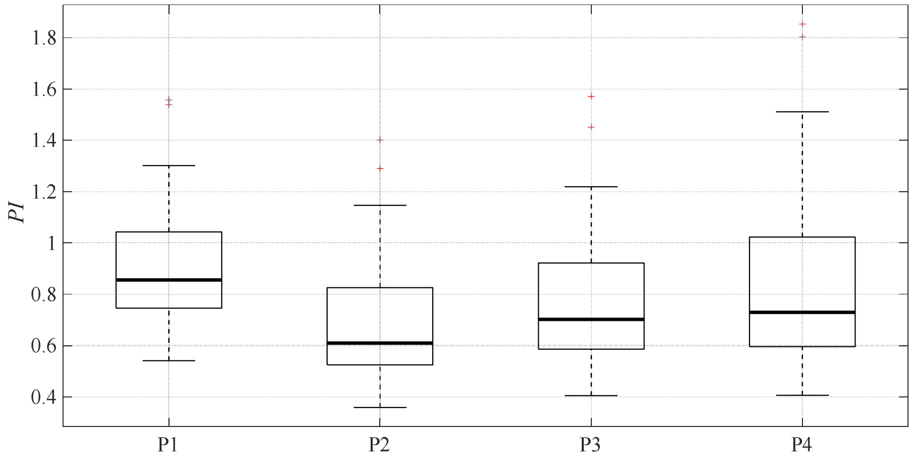

Figure 5A.3. PI distributions obtained for the different parameterizations analysed for the Jadhav and Dhang algorithm [149], employing DWT, coif5 mother wavelet, 6-level decomposition and: P1) Rigrsure threshold with hard thresholding, P2) Han et al. threshold with hard thresholding, P3) Rigrsure threshold with soft thresholding, P4) Han et al. threshold with soft thresholding.

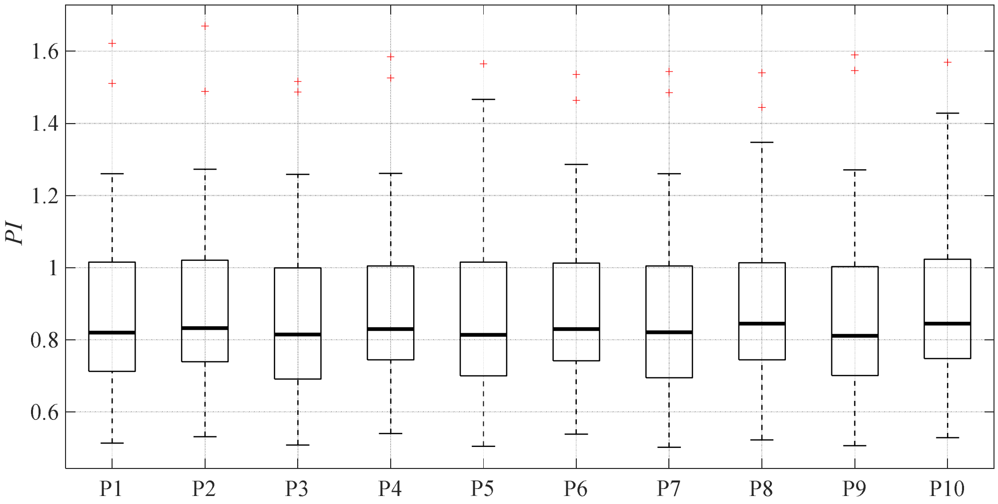

Figure 5A.4. PI distributions obtained for the different parameterizations analysed for the Shayesteh and Fallahian algorithm [138], assuming DWT, Rigrsure threshold and hard thresholding with: P1) bior1.1 mother wavelet and 6-level decomposition, P2) bior1.1 mother wavelet and 7-level decomposition, P3) db3 mother wavelet and 6-level decomposition, P4) db3 mother wavelet and 7-level decomposition, P5) db4 mother wavelet and 6-level decomposition, P6) db4 mother wavelet and 7-level decomposition, P7) db5 mother wavelet and 6-level decomposition, P8) db5 mother wavelet and 7-level decomposition, P9) db6 mother wavelet and 6-level decomposition, P10) db6 mother wavelet and 7-level decomposition.

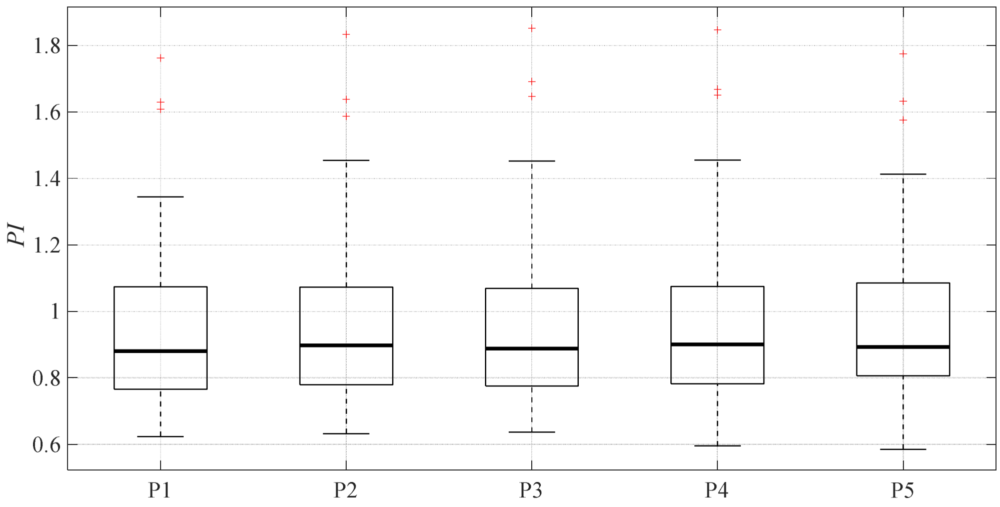

Figure 5A.5. PI distributions obtained for the different parameterizations analysed for the Swarnalatha and Prasad algorithm [139], involving DWT, 5-level decomposition, and a custom thresholding approach with: P1) coif1 mother wavelet, P2) coif2 mother wavelet, P3) coif3 mother wavelet, P4) coif4 mother wavelet, P5) coif5 mother wavelet.

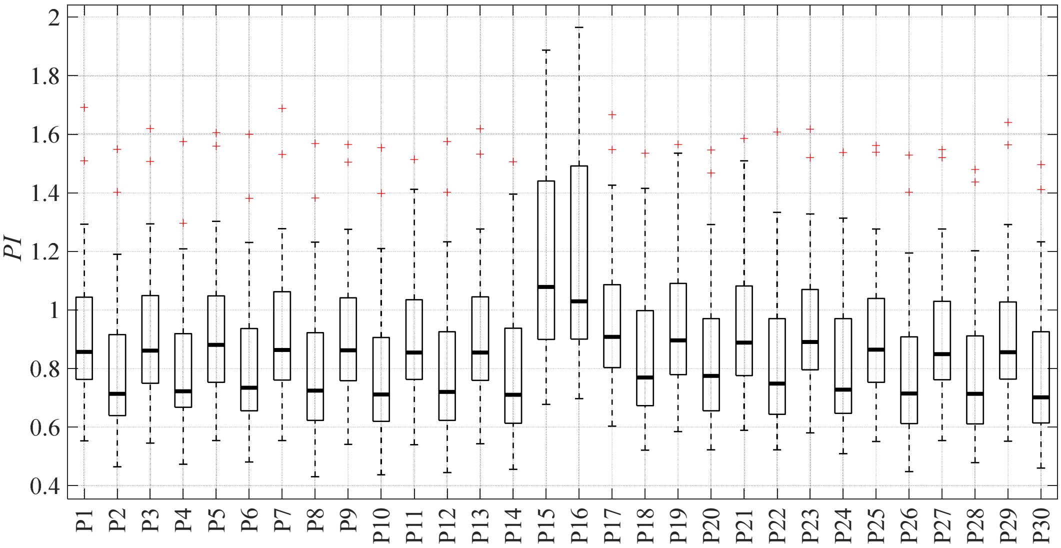

Figure 5A.6. PI distributions obtained for the different parameterizations analysed for the Vigneron et al. algorithm [140], involving DWT, 7-level decomposition, Rigrsure threshold and: P1) bior1.1 mother wavelet with hard thresholding, P2) bior1.1 mother wavelet with soft thresholding, P3) bior1.3 mother wavelet with hard thresholding, P4) bior1.3 mother wavelet with soft thresholding, P5) bior1.5 mother wavelet with hard thresholding, P6) bior1.5 mother wavelet with soft thresholding, P7) bior2.2 mother wavelet with hard thresholding, P8) bior2.2 mother wavelet with soft thresholding, P9) bior2.4 mother wavelet with hard thresholding, P10) bior2.4 mother wavelet with soft thresholding, P11) bior2.6 mother wavelet with hard thresholding, P12) bior2.6 mother wavelet with soft thresholding, P13) bior2.8 mother wavelet with hard thresholding, P14) bior2.8 mother wavelet with soft thresholding, P15) bior3.1 mother wavelet with hard thresholding, P16) bior3.1 mother wavelet with soft thresholding, P17) bior3.3 mother wavelet with hard thresholding, P18) bior3.3 mother wavelet with soft thresholding, P19) bior3.5 mother wavelet with hard thresholding, P20) bior3.5 mother wavelet with soft thresholding, P21) bior3.7 mother wavelet with hard thresholding, P22) bior3.7 mother wavelet with soft thresholding, P23) bior3.9 mother wavelet with hard thresholding, P24) bior3.9 mother wavelet with soft thresholding, P25) bior4.4 mother wavelet with hard thresholding, P26) bior4.4 mother wavelet with soft thresholding, P27) bior5.5 mother wavelet with hard thresholding, P28) bior5.5 mother wavelet with soft thresholding, P29) bior6.8 mother wavelet with hard thresholding, P30) bior6.8 mother wavelet with soft thresholding.

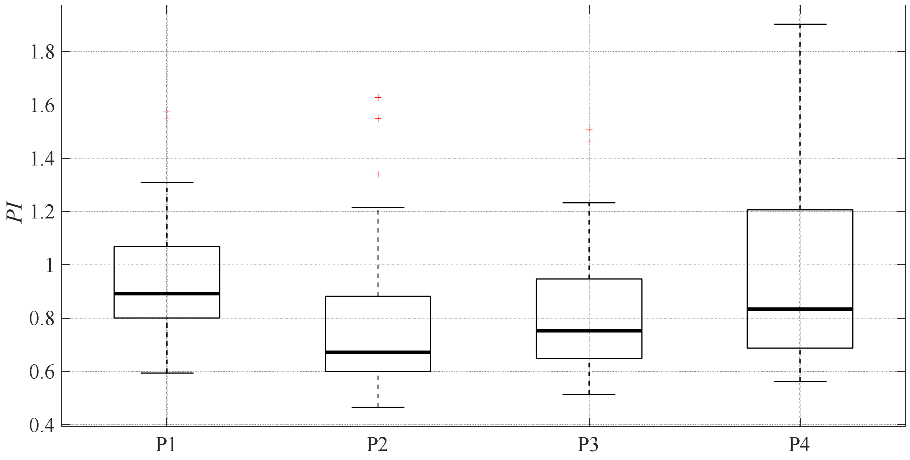

Figure 5A.7. PI distributions obtained for the different parameterizations analysed for the Wang et al. algorithm [141], involving DWT, bior5.5 mother wavelet, 7-level decomposition and: P1) Rigrsure threshold with hard thresholding, P2) Han et al. threshold and hard thresholding, P3) Rigrsure threshold with soft thresholding, P4) Han et al. threshold and soft thresholding.

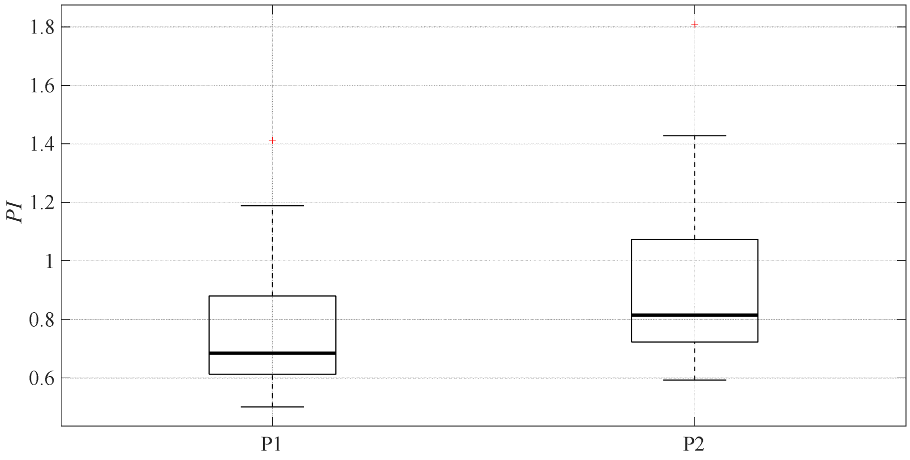

Figure 5A.8. PI distributions obtained for the different parameterizations analysed for the Mochimaru et al. algorithm [151], assuming DWT, coif24 mother wavelet, 12-level decomposition and a custom threshold with : P1) hard thresholding, P2) soft thresholding.

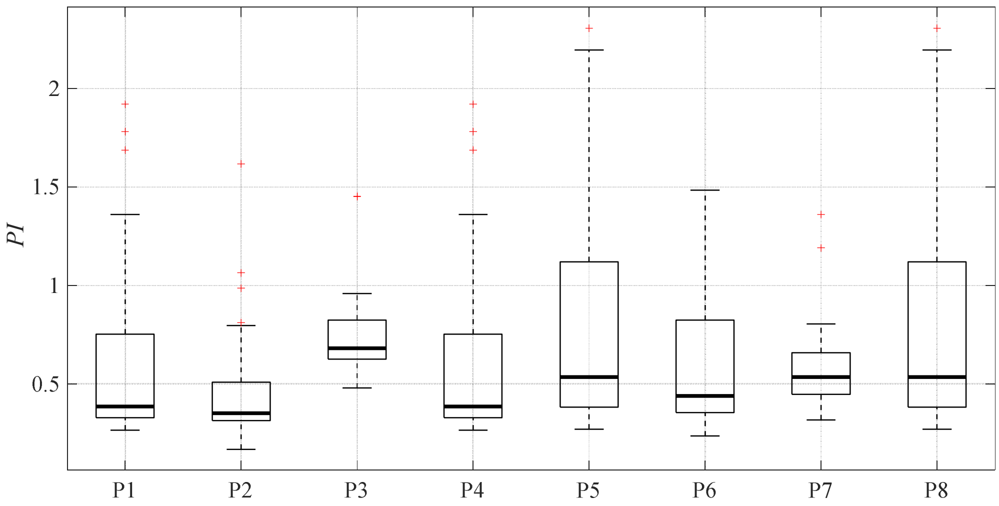

Figure 5A.9. PI distributions obtained for the different parameterizations analysed for the Ionescu algorithm [146], involving SWT, bior4.4 mother wavelet, 9-level decomposition with: P1) Universal threshold and hard thresholding, P2) Minimax threshold and hard thresholding, P3) Rigrsure threshold and hard thresholding, P4) Heursure threshold and hard thresholding, P5)Universal threshold and soft thresholding, P6) Minimax threshold and soft thresholding, P7) Rigrsure threshold and soft thresholding, P8) Heursure threshold and soft thresholding.

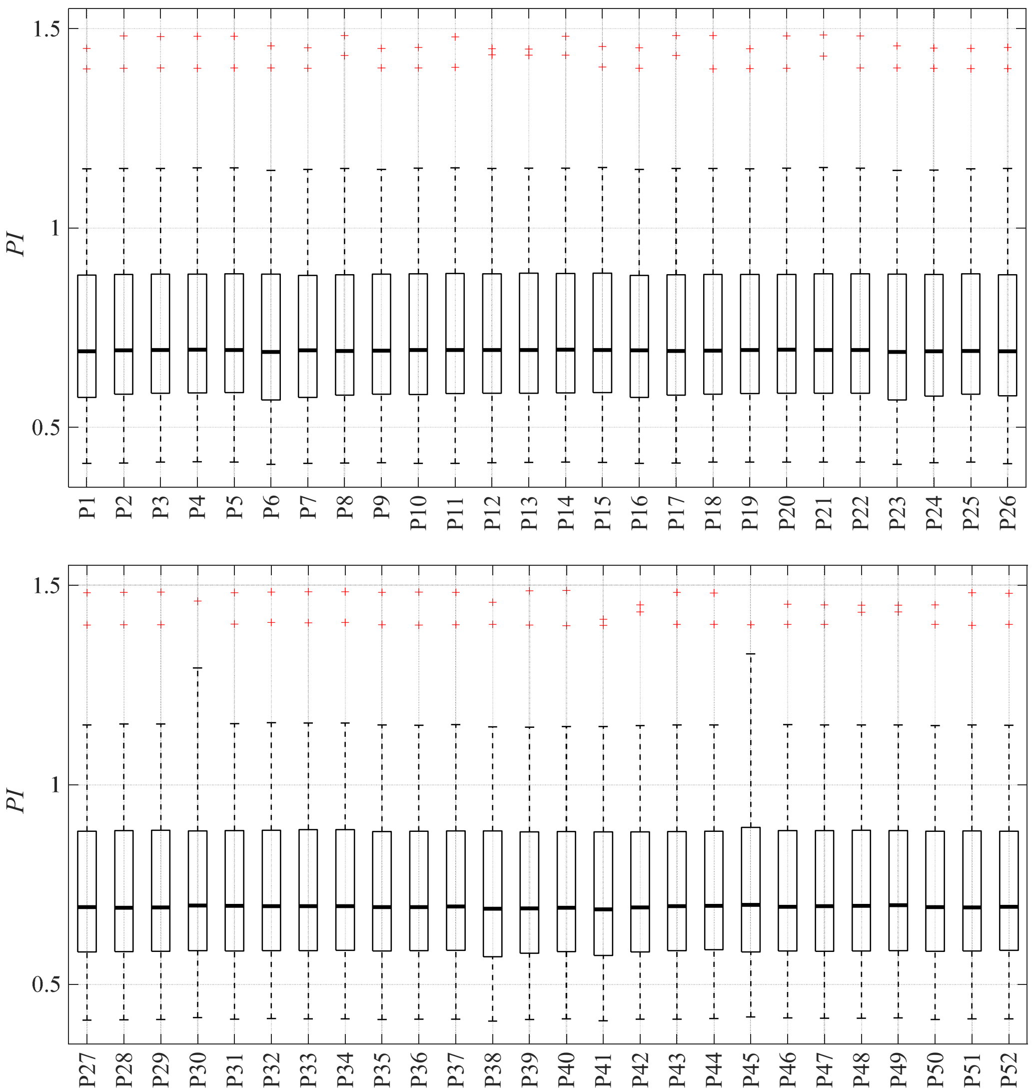

Figure 5A.10. PI distributions obtained for the different parameterizations analysed for the Jothi and Prabha algorithm [150], involving SWT, 3-level decomposition, Rigrsure threshold, hard thresholding and: P1) coif1 mother wavelet, P2) coif2 mother wavelet, P3) coif3 mother wavelet, P4) coif4 mother wavelet, P5) coif5 mother wavelet, P6) db1 mother wavelet, P7) db2 mother wavelet, P8) db3 mother wavelet, P9) db4 mother wavelet, P10) db5 mother wavelet, P11) db6 mother wavelet, P12) db7 mother wavelet, P13) db8 mother wavelet, P14) db9 mother wavelet, P15) db10 mother wavelet, P16) sym2 mother wavelet, P17) sym3 mother wavelet, P18) sym4 mother wavelet, P19) sym5 mother wavelet, P20) sym6 mother wavelet, P21) sym7 mother wavelet, P22) sym8 mother wavelet, P23) bior1.1 mother wavelet, P24) bior1.3 mother wavelet, P25) bior1.5 mother wavelet, P26) bior2.2 mother wavelet, P27) bior2.4 mother wavelet, P28) bior2.6 mother wavelet, P29) bior2.8 mother wavelet, P30) bior3.1 mother wavelet, P31) bior3.3 mother wavelet, P32) bior3.5 mother wavelet, P33) bior3.7 mother wavelet, P34) bior3.9 mother wavelet, P35) bior4.4 mother wavelet, P36) bior5.5 mother wavelet, P37) bior6.8 mother wavelet, P38) rbior1.1 mother wavelet, P39) rbior1.3 mother wavelet, P40) rbior1.5 mother wavelet, P41) rbior2.2 mother wavelet, P42) rbior2.4 mother wavelet, P43) rbior2.6 mother wavelet, P44) rbior2.8 mother wavelet, P45) rbior3.1 mother wavelet, P46) rbior3.3 mother wavelet, P47) rbior3.5 mother wavelet, P48) rbior3.7 mother wavelet, P49) rbior3.9 mother wavelet, P50) rbior4.4 mother wavelet, P51) rbior5.5 mother wavelet, P52) rbior6.8 mother wavelet.

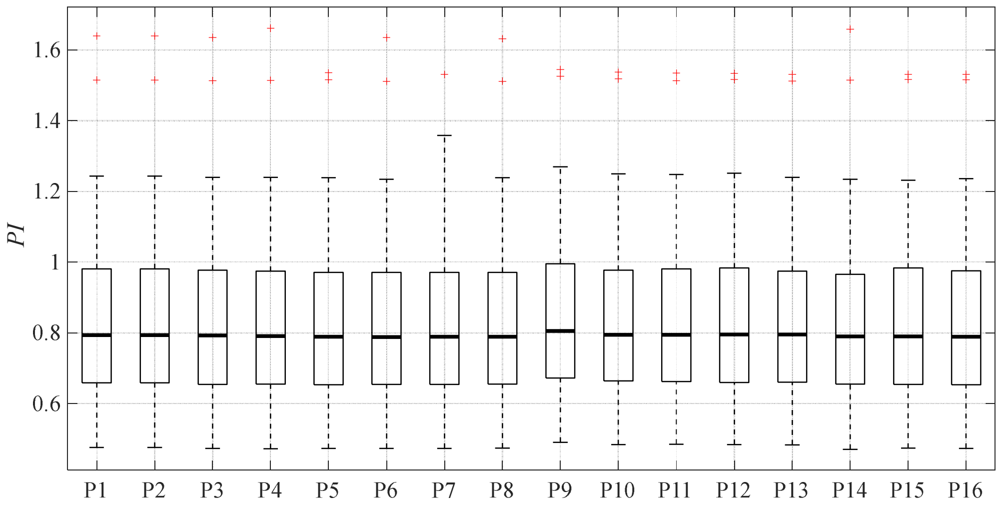

Figure 5A.11. PI distributions obtained for the different parameterizations analysed for the Rivet et al. algorithm [137], involving SWT, 6-level decomposition, Rigrsure threshold and hard thresholding with: P1) Haar mother wavelet, P2) bior1.1 mother wavelet, P3) bior1.3 mother wavelet, P4) bior1.5 mother wavelet, P5) bior2.2 mother wavelet, P6) bior2.4 mother wavelet, P7) bior2.6 mother wavelet, P8) bior2.8 mother wavelet, P9) bior3.1 mother wavelet, P10) bior3.3 mother wavelet, P11) bior3.5 mother wavelet, P12) bior3.7 mother wavelet, P13) bior3.9 mother wavelet, P14) bior4.4 mother wavelet, P15) bior5.5 mother wavelet, P16) bior6.8 mother wavelet.

Appendix B

Table 9B.1. Absolute power contents obtained for all EGM types in the different spectral ranges. Values are reported in 10^{-4} mV^2 in terms of medians (in bold) and 5^{th} and 95^{th} percentiles (in brackets).

Frequency range (Hz)	Border	Scar	LP1	LP2	EP
0 – 20	**27.21** [4.43 ; 97.92]	**4.06** [0.27 ; 21.47]	**14.32** [1.51 ; 66.99]	**4.68** [0.97 ; 27.95]	**5.68** [0.37 ; 62.20]
20 – 40	**23.98** [5.84 ; 105.39]	**1.93** [0.12 ; 10.18]	**17.73** [1.94 ; 97.39]	**5.16** [0.83 ; 48.35]	**6.43** [0.55 ; 94.46]
40 – 60	**2.92** [0.20 ; 25.13]	**0.05** [0.01 ; 1.28]	**2.38** [0.15 ; 81.73]	**1.71** [0.15 ; 24.70]	**1.98** [0.04 ; 10.36]
60 – 80	**0.67** [0.03 ; 14.63]	**0.03** [0.00 ; 0.45]	**0.63** [0.07 ; 23.25]	**0.65** [0.09 ; 6.30]	**0.62** [0.06 ; 6.84]
80 – 100	**0.39** [0.03 ; 7.71]	**0.01** [0.00 ; 0.21]	**0.34** [0.04 ; 7.89]	**0.32** [0.03 ; 4.29]	**0.36** [0.03 ; 4.40]
100 – 120	**0.19** [0.01 ; 4.99]	**0.01** [0.00 ; 0.16]	**0.18** [0.01 ; 2.05]	**0.16** [0.01 ; 3.90]	**0.21** [0.01 ; 4.14]
120 – 140	**0.13** [0.00 ; 3.00]	**0.00** [0.00 ; 0.13]	**0.09** [0.01 ; 0.92]	**0.10** [0.01 ; 3.31]	**0.19** [0.01 ; 3.62]
140 – 160	**0.10** [0.01 ; 1.76]	**0.00** [0.00 ; 0.10]	**0.06** [0.01 ; 1.28]	**0.07** [0.01 ; 2.02]	**0.07** [0.00 ; 2.02]
160 – 180	**0.04** [0.01 ; 1.36]	**0.00** [0.00 ; 0.08]	**0.05** [0.00 ; 2.68]	**0.07** [0.01 ; 1.44]	**0.07** [0.01 ; 1.51]
180 – 200	**0.03** [0.00 ; 0.99]	**0.00** [0.00 ; 0.03]	**0.04** [0.01 ; 3.20]	**0.04** [0.00 ; 0.90]	**0.06** [0.00 ; 1.57]
200 – 220	**0.02** [0.00 ; 0.99]	**0.00** [0.00 ; 0.03]	**0.03** [0.00 ; 2.86]	**0.01** [0.00 ; 0.36]	**0.04** [0.00 ; 1.39]
220 – 240	**0.02** [0.00 ; 0.74]	**0.00** [0.00 ; 0.01]	**0.02** [0.00 ; 1.40]	**0.02** [0.00 ; 0.45]	**0.05** [0.00 ; 1.01]
240 – 260	**0.01** [0.00 ; 0.48]	**0.00** [0.00 ; 0.01]	**0.02** [0.00 ; 0.44]	**0.02** [0.00 ; 0.30]	**0.03** [0.00 ; 0.83]
260 – 280	**0.01** [0.00 ; 0.25]	**0.00** [0.00 ; 0.01]	**0.01** [0.00 ; 0.22]	**0.01** [0.00 ; 0.20]	**0.03** [0.00 ; 0.62]
280 – 300	**0.01** [0.00 ; 0.22]	**0.00** [0.00 ; 0.01]	**0.01** [0.00 ; 0.38]	**0.01** [0.00 ; 0.17]	**0.02** [0.00 ; 0.61]
300 – 320	**0.01** [0.00 ; 0.18]	**0.00** [0.00 ; 0.01]	**0.01** [0.00 ; 0.34]	**0.01** [0.00 ; 0.18]	**0.02** [0.00 ; 0.40]

Table 9B.2. Relative power contents obtained for all EGM types in the different spectral ranges. Percentage values are reported as medians (in bold) and 5th and 95th percentiles (in brackets).

Frequency range (Hz)	Border	Scar	LP1	LP2	EP
0 – 20	**43.56** [15.46 ; 70.20]	**67.93** [29.52 ; 83.74]	**40.09** [10.26 ; 59.73]	**34.14** [7.24 ; 67.71]	**34.42** [6.32 ; 65.22]
20 – 40	**44.46** [12.10 ; 60.18]	**28.08** [13.44 ; 54.13]	**43.97** [20.66 ; 55.76]	**35.02** [15.68 ; 58.63]	**35.50** [11.15 ; 60.28]
40 – 60	**4.59** [0.39 ; 25.07]	**1.09** [0.22 ; 10.97]	**6.10** [1.71 ; 33.78]	**9.52** [2.48 ; 25.29]	**8.72** [2.33 ; 31.05]
60 – 80	**0.70** [0.06 ; 15.56]	**0.65** [0.14 ; 5.40]	**1.80** [0.60 ; 10.20]	**4.84** [0.87 ; 14.24]	**3.53** [0.56 ; 16.07]
80 – 100	**0.42** [0.04 ; 12.60]	**0.21** [0.05 ; 2.40]	**1.06** [0.23 ; 4.23]	**2.38** [0.23 ; 11.83]	**1.95** [0.34 ; 12.85]
100 – 120	**0.29** [0.03 ; 7.93]	**0.13** [0.04 ; 1.20]	**0.48** [0.06 ; 4.37]	**1.39** [0.17 ; 8.78]	**1.19** [0.15 ; 8.35]
120 – 140	**0.14** [0.01 ; 5.13]	**0.09** [0.01 ; 0.67]	**0.18** [0.04 ; 2.20]	**0.83** [0.08 ; 6.17]	**1.03** [0.09 ; 5.20]
140 – 160	**0.10** [0.02 ; 2.80]	**0.05** [0.01 ; 0.60]	**0.15** [0.01 ; 1.96]	**0.49** [0.05 ; 4.67]	**0.60** [0.08 ; 5.52]
160 – 180	**0.05** [0.01 ; 2.27]	**0.07** [0.01 ; 0.72]	**0.10** [0.02 ; 3.74]	**0.45** [0.05 ; 2.92]	**0.45** [0.06 ; 4.16]
180 – 200	**0.04** [0.00 ; 1.96]	**0.05** [0.01 ; 0.45]	**0.09** [0.02 ; 4.38]	**0.24** [0.03 ; 2.13]	**0.37** [0.05 ; 3.79]
200 – 220	**0.03** [0.00 ; 1.52]	**0.05** [0.01 ; 0.31]	**0.08** [0.01 ; 3.95]	**0.11** [0.02 ; 1.25]	**0.22** [0.02 ; 2.84]
220 – 240	**0.02** [0.00 ; 0.85]	**0.03** [0.01 ; 0.27]	**0.06** [0.01 ; 1.44]	**0.13** [0.02 ; 0.84]	**0.25** [0.04 ; 2.18]
240 – 260	**0.02** [0.00 ; 0.56]	**0.04** [0.00 ; 0.27]	**0.05** [0.01 ; 0.59]	**0.11** [0.02 ; 0.71]	**0.19** [0.02 ; 1.87]
260 – 280	**0.01** [0.00 ; 0.49]	**0.02** [0.01 ; 0.30]	**0.04** [0.00 ; 0.45]	**0.08** [0.01 ; 0.83]	**0.18** [0.02 ; 1.64]
280 – 300	**0.01** [0.00 ; 0.41]	**0.03** [0.00 ; 0.25]	**0.04** [0.00 ; 0.61]	**0.07** [0.01 ; 0.53]	**0.15** [0.02 ; 1.23]
300 – 320	**0.01** [0.00 ; 0.27]	**0.02** [0.00 ; 0.31]	**0.04** [0.00 ; 0.55]	**0.08** [0.01 ; 0.97]	**0.12** [0.02 ; 1.12]

List of publications

Journal publications:

A. Spanu, M. Taki, G. Baldazzi, A. Mascia, P. Cosseddu, D. Pani A.Bonfiglio, “Epidermal electrodes with ferrimagnetic/conductive properties for biopotential recordings”, Bioengineering, MDPI, 2022.

G. Baldazzi, M. Orrù, G. Solinas, M. Matraxia, G. Viola, and D. Pani, “Spectral characterization of ventricular intracardiac potentials in human post-ischemic bipolar electrograms”, Scientific Reports, 2022.

A. Spanu, A. Mascia, G. Baldazzi, B. F. Salerno, F. Torrisi, G. Viola, A. Bonfiglio, P. Cosseddu, and D. Pani, “Parylene C-based, breathable tattoo electrode for high-quality biopotential measurements”, Frontiers in Bioengineering and Biotechnology, 2022.

G. Baldazzi, G. Solinas, M. Urru, J. del Valle, M. Barbaro, S. Micera, L. Raffo and D. Pani, “Systematic analysis of wavelet denoising methods for neural signal processing”, Journal of Neural Engineering, 2020.

G. Baldazzi, E. Sulas, M. Urru, R. Tumbarello, L. Raffo and D. Pani, “Annotated real and synthetic datasets for non-invasive foetal electrocardiography post-processing benchmarking”, Data in Brief, Elsevier, 2020.

G. Baldazzi, E. Sulas, M. Urru, R. Tumbarello, L. Raffo and D. Pani, “Wavelet Denoising as a Post-Processing Enhancement Method for Non-Invasive Foetal Electrocardiography”, Computer Methods and Programs in Biomedicine, Elsevier, 2020.

E. Gusai, A. Zedda, M. Caruso, S. Bertuletti, G. Baldazzi, S. Spanu, A. Spanu, D. Riboni, A. Pibiri, M. Monticone, A. Cereatti, D. Pani, “Development of a home-based neuromotor telerehabilitation system for mildly impaired patients with stroke: the DoMoMEA Project”, IEEE Journal of Biomedical and Health Informatics, 2022. (under review)

R. Coa, S. M. La Cava, G. Baldazzi, L. Polizzi, G. Pinna, C. Conti, G. Defazio, D. Pani, M. Puligheddu, “Estimated EEG functional connectivity and aperiodic component induced by vagal nerve stimulation in patients with drug-resistant epilepsy”, Scientific Reports, 2022. (under submission)

G. Baldazzi, E. Sulas, M. Urru, R. Tumbarello, L. Raffo, R. Vullings, D. Pani, “Automatic signal quality assessment of raw trans-abdominal biopotential recordings for non-invasive fetal electrocardiography”, Frontiers in Bioengineering and Biotechnology, Research topic “Biomedical Engineering Technologies and Methods in Antenatal Medicine”, 2022. (accepted abstract, under submission)

G. Baldazzi, D. Pani, H.-T. Wu, “Fetal ECG extraction from non-invasive multichannel recordings by nonlocal median and optimal shrinkage”, Frontiers in Bioengineering and Biotechnology, Research topic “Biomedical Engineering Technologies and Methods in Antenatal Medicine”, 2022. (under submission)

Conference publications:

G. Baldazzi, A. Spanu, A. Mascia, G. Viola, A. Bonfiglio, P. Cosseddu and D. Pani, “Validation of A Novel Tattoo Electrode for ECG Monitoring”, Computing in Cardiology (CinC), 2021.

E. Gusai, A. Zedda, S. Spanu, G. Baldazzi, M. Caruso, S. Bertuletti, A. Pibiri, M. Monticone, A. Cereatti and D. Pani, “DoMoMEA – A Neuromotor Telerehabilitation System for Post-Stroke Patients”, Live Demonstration at IEEE Biomedical Circuits and Systems Conference (BIOCAS), 2021 (*in press*).

R. Coa, S. M. La Cava, G. Baldazzi, A. Ledda, L. Polizzi, G. Pinna, C. Conti, D. Pani, M. Fraschini, M. Puligheddu, “Vagal nerve stimulation in patients with drug-resistant epilepsy acts differently on the electroencephalographic aperiodic components of responder patients compared with non-responders”, American Epilepsy Society (AES), 2021 (a*bstract contribution*).

E. Gusai, A. Zedda, G. Baldazzi, S. Spanu, M. Caruso, S. Bertuletti, A. Pibiri, D. Riboni, M. Monticone, A. Cereatti and D. Pani, “The DoMoMEA telerehabilitation system for post-stroke patients: first usability assessment”, XXI Congresso della Società Italiana di Analisi del Movimento in Clinica (SIAMOC), 2021. (*in press*)

G. Baldazzi, M. Orrù, M. Matraxia, G. Viola and D. Pani, “Supervised classification of ventricular abnormal potentials in intracardiac electrograms”, Computing in Cardiology (CinC), 2020.

E. Sulas, G. Pili, E. Gusai, G. Baldazzi, M. Urru, R. Tumbarello, L. Raffo and D. Pani, “A Novel Tool for Non-Invasive Fetal Electrocardiography Research: the NInFEA Dataset”, Engineering in Medicine and Biology Society (EMBC), 2020, 42nd Annual International Conference of the IEEE.

A. Zedda, E. Gusai, M. Caruso, S. Bertuletti, G. Baldazzi, S. Spanu, D. Riboni, A. Pibiri, M. Monticone, A. Cereatti and D. Pani, “DoMoMEA: a Home-Based Telerehabilitation System for Stroke Patients”, Engineering in Medicine and Biology Society (EMBC), 2020, 42nd Annual International Conference of the IEEE.

G. Baldazzi, G. K. Masciavè, E. Gusai, A. Zedda, S. Spanu, E. Sulas, L. Raffo and D. Pani, “A Plantar Pressure Biofeedback M-Health System for Stroke Patients”, 2020 IEEE International Symposium on Medical Measurements and Applications (MeMeA 2020).

A. Zedda, E. Gusai, M. Caruso, S. Bertuletti, S. Spanu, G. Baldazzi, G. K. Masciavè, A. Pibiri, M. Monticone, A. Cereatti, L. Raffo and D. Pani, “DoMoMEA: a home neuromotor telerehabilitation system for stroke patients”, GNB Proceedings 2020.

G. Baldazzi, E. Sulas, E. Brungiu, M. Urru, R. Tumbarello, L. Raffo and D. Pani, “Wavelet-Based Post-Processing Methods for the Enhancement of Non-Invasive Fetal ECG”, Computing in Cardiology (CinC), 2019.

G. Baldazzi, M. Orrù, M. Matraxia, G. Viola and D. Pani, “Automatic Recognition of Ventricular Abnormal Potentials in Intracardiac Electrograms”, Computing in Cardiology (CinC), 2019.

G. Barabino, G. Baldazzi, E. Sulas, C. Carboni, L. Raffo and D. Pani, “Comparative evaluation of different wavelet thresholding methods for neural signal processing”, Engineering in Medicine and Biology Society (EMBC), 2017, 39th Annual International Conference of the IEEE.

G. Baldazzi, D. Pani and H.-T- Wu, “Extraction algorithm for morphologically preserved non-invasive multi-channel fetal ECG”, Computing in Cardiology (CinC), 2022. (under submission)

G. Baldazzi, M. Orrù, M. Matraxia, G. Viola and D. Pani, “Efficacy of spectral signatures for the automatic classification of ventricular abnormal potentials in substrate-guided mapping procedures”, Computing in Cardiology (CinC), 2022. (under submission)

A. Pitzus, G. Baldazzi, M. Orrù, A. Valdes Rey, M. Matraxia, G. Viola, P. Djuric and D. Pani, "Exploring transfer learning for ventricular tachycardia electrophysiology studies", Computing in Cardiology (CinC), 2022. (under submission)

N. Mandas, M. Mollura, G. Baldazzi, M. Figorilli, M. Puligheddu, D. Pani and R. Barbieri, "Characterization of Autonomic Dysfunction in REM Sleep Behavior Disorder", Computing in Cardiology (CinC), 2022. (under submission)